HAL open science

Characterization of nuclear mechanics with physical models in fluorescence image microscopy

Yekta Kesenci

To cite this version:

Yekta Kesenci. Characterization of nuclear mechanics with physical models in fluorescence image microscopy. Quantitative Methods [q-bio.QM]. Sorbonne Université, 2023. English. NNT : 2023SORUS648 . tel-04586173

HAL Id: tel-04586173

https://theses.hal.science/tel-04586173

Submitted on 24 May 2024

HAL is a multi-disciplinary open access archive for the deposit and dissemination of scientific research documents, whether they are published or not. The documents may come from teaching and research institutions in France or abroad, or from public or private research centers.

L'archive ouverte pluridisciplinaire **HAL**, est destinée au dépôt et à la diffusion de documents scientifiques de niveau recherche, publiés ou non, émanant des établissements d'enseignement et de recherche français ou étrangers, des laboratoires publics ou privés.

Thèse préparée à l'Institut Pasteur de Paris et
delivrée par Sorbonne Université

École Doctorale Informatique, Télécommunications, Électronique de Paris n°130

Unité d'Analyse d'Images Biologiques

Characterization of nuclear mechanics with physical models in fluorescence image microscopy

Caractérisation de la mécanique nucléaire avec des modèles physiques en microscopie d'image de fluorescence

Par Yekta KESENCI

Thèse de doctorat d'Informatique

Dirigée par Jean-Christophe OLIVO-MARIN
et co-encadrée par Aleix Boquet-Pujadas

Présentée et soutenue publiquement le 20 décembre 2023
devant un jury composé de

Benoît LADOUX	Président du jury, Rapporteur
Arrate MUÑOZ BARRUTIA	Rapporteuse
Dominique BÉRÉZIAT	Examinateur
Jean-Yves TINEVEZ	Examinateur
Sandrine ÉTIENNE-MANNEVILLE	Invitée
Isabelle TARDIEUX	Invitée
Aleix BOQUET-PUJADAS	Co-encadrant
Jean-Christophe OLIVO-MARIN	Directeur de thèse

Abstract

Abstract: We propose a set of computational imaging methods to characterize the mechanical properties of a cell nucleus under fluorescence imaging. Each is stated as the solution to a continuum mechanics problem under low quasistatic stress. In this framework, the nucleus behaves like a linearly elastic isotropic material, and the desired physical quantities observe regularity properties imposed by the theory of elliptic operators. We first compute the displacement field of the nuclear material from images of its deformation. To do this, we developed a new variational optical flow method, penalized by the mixed nuclear norm of the Hessian of the displacement field. These displacements are then processed to compute other physical quantities of interest. The strain and stress tensors, and the boundary traction forces, are obtained as the solutions of an optimization problem constrained by the partial differential equations of linear elasticity. Young's moduli are computed by the finite element resolution of elliptic partial differential equations that we introduce. We show that these methods respect the expected regularity properties from linear elasticity theory, and experiments validate both their accuracy and practical interest. We apply these frameworks to study two configurations of interest: the deformation of the nuclei of migrating glioblastoma cells; and the boundary traction forces exerted on the nucleus of the parasite Toxoplasma gondii during host-cell invasion.

Keywords: Mechanobiology, optical flow, Hessian Schatten-norm, inverse problems, continuum mechanics, adjoint method, imaging, biophysics.

Résumé: Nous proposons un ensemble de méthodes d'imagerie computationnelle pour caractériser les propriétés mécaniques d'un noyau cellulaire sous imagerie par fluorescence. Chacune s'énonce comme la solution à un problème de mécanique des milieux continus sous faible contrainte quasistatique. Dans ce cadre, le noyau se conduit tel un matériau élastique, isotrope et linéaire, et les champs désirés observent des propriétés de régularité édictées par la théorie des opérateurs elliptiques. Nous calculons d'abord le champ de déplacement du matériel nucléaire à partir d'images de sa déformation. Nous développons pour ce faire une nouvelle méthode variationnelle de flux optique, pénalisée par la norme mixte nucléaire de l'Hessien du déplacement. Ces déplacements sont ensuite traités pour calculer d'autres grandeurs physiques d'intérêt. Les tenseurs de déformation, de contrainte, et la force de traction aux bords, sont obtenus tels les solutions d'un problème d'optimisation sous contrainte d'équations différentielles élastiques. Les modules de Young sont calculés par résolution d'équations différentielles elliptiques que nous introduisons. Nous montrons que ces méthodes respectent les propriétés de régularité de la théorie d'élasticité linéaire, et des expérimentations en valident l'acuité tout comme l'intérêt pratique. Nous appliquons ces méthodes pour étudier deux configurations d'intérêt : la déformation des noyaux des cellules de glioblastome migrantes; et les forces de traction exercées sur noyau du parasite Toxoplasma gondii durant l'invasion de cellules hôtes.

Mots clés: Mécanobiologie, flux optique, norme Schatten de l'Hessienne, problèmes inverses, mécanique des milieux continus, méthode adjointe, imagerie, biophysique.

Remerciements

Je remercie Jean-Christophe Olivo-Marin d'avoir accepté de diriger ma thèse au sein de son unité. C'est chose malaisée que de piloter un laboratoire. Il faut pourvoir à mille nécessités, surmonter bien des malheurs, suivre les dernières idées de la science, veiller à ce que son équipe dirige tous ses efforts vers les entreprises les plus prometteuses... Bref, œuvrer à ce que ses chercheurs puissent constamment travailler dans les meilleures conditions, celles qui feront advenir les découvertes futures. Je sens bien la chance qu'il y a à collaborer avec quelqu'un qui a une idée si nette de sa mission, de ses exigences, et pourtant la remplit avec libéralité, accorde à ses doctorants sa confiance, aussi bien en leurs idées, qu'en leurs démarches. Je t'exprime pour tout cela ma sincère gratitude. Mes collègues ne s'y trompent pas non plus.

Je remercie ensuite Pascal Bochet. Mais de quoi ? Tu es, bien sûr, celui qui m'as introduit à ce laboratoire, à une époque d'errance où j'ignorais à quoi aspirer. Mais il n'est par ailleurs pas une période de ma vie estudiantine (lycée, classes préparatoires, thèse) qui n'ait bénéficié de ton concours. À ce compte les enfants devraient remercier leurs parents de les avoir fait naître. Et quand bien même je t'aurais remercié de tout cela, que je ne serais pas quitte de ce que je te dois. Tu m'as offert durant ces trois années le plus beau modèle de ce que pouvait être un homme de science : ouvert à toutes les idées, défiant vis-à-vis des siennes, et surtout, incapable de la moindre dose d'orgueil. Que le monde serait beau si la moitié des scientifiques étaient seulement capables de cela... "Faisons bien et laissons dire", professait d'Artagnan. Et laissons les gens sérieux se ridiculiser eux-mêmes. J'espère à l'avenir pouvoir te ressembler un peu.

Je remercie chaleureusement les membres de mon jury de thèse : Benoît Ladoux, Arrate Muñoz Barrutia, Dominique Béréziat, Jean-Yves Tinevez, Sandrine Étienne-Manneville, Isabelle Tardieux. Il est heureux, et tout à l'honneur de la communauté scientifique, que de si éminents professionnels, requis pourtant par tant d'obligations, prennent le temps d'étudier les essais d'un jeune aspirant à la science, de lui partager ses remarques, et de lui accorder *in fine* le titre qui le consacre parmi eux.

Merci à mes collaborateurs biologistes : Emma van Bodegraven, Luis Vigetti, Isabelle Tardieux, Elvire Infante, Matthieu Gélin, Sandrine Étienne-Manneville, sans qui nous serions tous au chômage, et nos travaux tellement plus ternes. Vous contribuez chaque jour à un peu mieux comprendre le monde du vivant. Vous assister est un honneur et notre vraie mission.

Je remercie tous les membres de mon laboratoire : Maria Manich, pour être la plus vivante et sémillante personne au monde ; Elisabeth Labruyère, pour ta complicité et nos moments de rire ; Giacomo Nardi, pour ton élégance et ton goût ; Marie-Anne Lin, pour ta gentillesse et ton constant secours ; Stéphane Dallongeville, pour ta patience et ta disponibilité ; Daniel Felipe González, pour ta camaraderie et tes mots encourageants ; Marion Louveaux, pour m'avoir écouté dans mes moments de doute ; Lucie, pour ta sincérité et ton amitié ; Vannary Meas-Yedid, pour ta conversation ; Nancy Guillen, pour ton franc-parler ; Rituparna Sarkar and Suvadip Mukherjee, for being to me (and to so many other PhD

students as well) the kind, reassuring, familiar figures in my darkest hours during my thesis – I wish you and Raaya the happiest lives ever.

Je remercie (par "ordre d'apparition") tous les doctorants du laboratoire : Diana Mandache et Alexandre Bouyssoux, mes devanciers et mes idoles, Samuel Kubler, mon fidus Achates et compagnon de la première heure, Erwan Dereure et Antoine Habis, mangaphile et roi du badminton, Benjamin Dorra et Mounib Mohamed Benimam, les plus courageux d'entre nous, Raphaël Rème, mon seul rival aux échecs, Thomas Tréport, biologiste et pourtant très sympa, et Thomas Musset qui, bien que développeur, fait partie de la bande. Je ne m'étends pas sur tout ce que j'éprouve pour vous, ce sont des sentiments trop affectueux pour être placés devant des équations différentielles partielles. Vous eussé-je rencontré ailleurs, à une autre époque, en d'autres circonstances, que ça n'aurait rien changé à ce fait irréfragable : vous êtes mes amis et vous le resterez toujours.

Je remercie Thibault Lagache d'avoir fait de moi un indécrotable anarchiste-de-droite-ultra-libertarien-pourfendeur-de-l'Etat-obèse-afuera, et plus sérieusement d'être le plus sincère et bienveillant interlocuteur qui se puisse désirer. C'est en te côtoyant que j'ai appris qu'il ne faut jamais déguiser ses opinions – ceux qui s'y adonnent finissent toujours par mourir un peu. Puissé-je rester fidèle à tes préceptes... Ah oui, merci aussi d'avoir relu mes slides : grâce à tes conseils, de nulles, elles sont devenues médiocres.

Merci à mon tuteur Florian Muller pour les nombreuses conversations détendues autour d'un café sur mon travail de recherche et mes projets professionnels, ses conseils, et surtout sa grande et fraternelle gentillesse.

Merci au docteur Philippe Azria, qui me soigne et conseille depuis tout petit, pour m'avoir dit ce que j'avais besoin d'entendre au moment le plus critique de ma thèse. Je n'exagère pas en disant que, sans vous, je n'aurais pas fini ce travail. Merci encore.

Je remercie toute ma famille de m'avoir soutenu, encouragé, félicité, aidé, défendu, applaudi, épaulé, vanté dans tout ce que j'ai pu faire de bien ou de mal durant cette thèse, et ce sans avoir la plus petite idée de ce dont il s'agissait. Cela vous inclut aussi, les Gouraud.

La coutume veut que les encadrants soient remerciés juste après les directeurs de thèse. Je m'excuse donc auprès d'Aleix Boquet-Pujadas, mais ce qu'il fut pour moi le place bien plus près de ma famille que de l'encadrement. Je n'ai qu'admiration pour toi, tu es le grand frère auquel je veux ressembler, et je regarde notre rencontre comme l'une des grandes chances de ma vie.

Merci à Clara, que j'aime de tout mon cœur.

Merci à Mozart et Jean-Sébastien Bach, au système de numération indo-arabe, aux cafés parisiens, aux tableaux de Frans Hals, aux rues de Londres, aux aires d'autoroute, à la révolution copernicienne, à Michel de Montaigne, aux ports d'Istanbul, to The Red Wheelbarrow, à l'abbaye de Noirlac, to Flaco the owl. Et enfin merci à moi-même pour n'avoir jamais eu peur du ridicule.

List of Figures

I.1 Main nuclear components and their cytoskeletal associations 2
I.2 Human dermal fibroblasts from laminopathy patients 8
I.3 Pelger-Huet anomaly 9
I.4 Cancer cells' nuclei 11
I.5 The three types of mechanical models 13
I.6 Strain definitions and limitations of probing methods for measuring mechanical properties of the nucleus 16
I.7 Strain definitions and limitations of confinement-based methods for measuring mechanical properties of the nucleus 18
I.8 Strain definitions and limitations of suspension-based methods for measuring mechanical properties of the nucleus 20

II.1 General principles of isotropic linear elastic materials 26
II.2 Sobolev embedding theorems, definition of the trace operator 34
II.3 Overview of our data creation framework 40
II.4 Overview of the Finite Element Method 41
II.5 Delaunay triangulation 42

III.1 Variational optical flow problems enforce the brightness constancy assumption and fix the aperture problem 51
III.2 Two cases where optical flow fails: illumination change and occlusion 53
III.3 Large displacement estimation in optical flow: a multiresolution strategy 55
III.4 Total Variation optical flow sharply delineates objects' boundaries 57
III.5 Proximal operator, Legendre-Fenchel conjugate, Soft-thresholding 58
III.6 Overview of Large Displacement Optical Flow 61
III.7 An example of deep-learning based optical flow method: recurrent all-pairs field transform. 64
III.8 FISTA and ADMM 75
III.9 Axial and lateral displacements of optical flow methods and ours for a linear elastic material with two stiff inclusions 79
III.10 Axial and lateral strain components of the strain of optical flow methods and ours for a linear elastic material with two stiff inclusions 80
III.11 Displacement and strain profiles. Stability against regularisation parameters 81
III.12 Axial and lateral displacements of optical flow methods and ours for a linear elastic nucleus 83
III.13 Axial and lateral strain components of the strain of optical flow methods and ours for a linear elastic nucleus 84
III.14 Segmentation of invading glioblastoma cells' nuclei 86
III.15 Displacement and strain of an glioblastoma nucleus 88
III.16 Statistical comparison of the mean of the Frobenius norm of the strain tensor of glioblastoma nuclei with or without knocked out intermediate filaments 89

IV.1 General experimental setting for elastography techniques 95

IV.2 Symmetric axial deformation reduces to 1D deformations 96
IV.3 Reconstructed Young's modulus of the cell and its nucleus 98
IV.4 Examples of simulated experimental settings in elastography 102
IV.5 Classical elastography reconstruction methods against our Mixed PDE..... 103
IV.6 Profile of the elastography reconstruction methods for a varying number of inclusions 104
IV.7 Whole pipeline evaluation with heterochromatin gathering at the nuclear pore complexes . 106
IV.8 Whole pipeline evaluation with heterochromatin gathering at a nucleolus within the nuclear interior..... 107
IV.9 Application of our elastography method on real images of deforming nuclei 110
IV.10 Simulation and computation of the displacement, stress and boundary traction..... 114
IV.11 Accuracy of the retrieved quantities for each experiment 115
IV.12 Presentation of Toxoplasma gondii 117
IV.13 Time evolution of the deformation of *Toxoplasma gondii* 118
IV.14 Time evolution of perimeter, surface, curvature, and of the mean of the Frobenius norm of the strain of three invading *Toxoplasma gondii* cells..... 119
IV.15 Super resolution of the time evolution of an invading Toxoplasma gondii cell along with its deviatoric strain and boundary traction..... 120

A.1 General principles of fluorescence Microscopy. 126
A.2 Photobleaching..... 128
A.3 General principles of Brillouin microscopy 129

B.1 Illustration of the staircasing effect with the Rudin-Osher-Fatemi problem. 135

C.1 **Différents niveaux de modélisation mécanique des noyaux**. (a) Modèle 1D de Jeffrey d'un noyau, où les ressorts et les amortisseurs sont assemblés en série ou en parallèle pour donner une représentation viscoélastique ; (b) Modélisation en mécanique des milieux continus, où la géométrie de la cellule est précisément déterminée par segmentation, puis maillée par une triangulation, et où les grandeurs physiques d'intérêt sont calculées le plus souvent par les éléments finis ; (c) 140
C.2 **Illustration des étapes de création de données synthétiques à partir des équations d'élasticité régissant le noyau**. 141
C.3 **Comparaison des méthodes de flux optique dans le calcul des déplacements et de la déformation axiale**. 143
C.4 **Application des méthodes de flux optique dans l'étude de l'influence des filaments intermédiaires dans la migration des glioblastomes**. (a) Champ de déplacement d'un noyau de glioblastome ; (b) Norme de Frobenius du tenseur de déformation du même champ de déformation ; (c) Comparaison de la déformation des noyaux de glioblastomes meneurs, avec ou sans filaments intermédiaires, avec une différence dans la moyenne significative ; (d) Comparaison de la déformation des noyaux de glioblastomes suiveurs, avec ou sans filaments intermédiaires, sans différence significative de la moyenne. 144
C.5 **Reconstitution de la valeur absolue du moduel de Young du noyau**. Chaque ligne indique une simulation de déformation de noyau, avec des rayons de noyaux grandissants. Chaque colonne indique la méthode de flux optique utilisée. Les méthodes de flux optique de l'état de l'art sont appariées avec une méthode indirecte pour uen meilleure stabilité dans la reconstitution. Notre méthode de flux optique (Hessian) est appariée à une méthode d'élastographie directe. Non seulement la reconstruction est plus exacte dans notre cas, mais beaucoup plus rapide..... 146
C.6 **Application à des données réelles de notre méthode d'élastographie relative**..... 147

C.7 **Application de notre méthodologie pour le calcul des déformations déviatoriques et des forces de traction au bord d'un noyau de Toxoplasma gondii durant l'invasion**. (a) Première image de l'invasion ; (b) Seconde image de l'invasion ; (c) Champ du tenseur de déformation déviatorique ; (d) Forces de traction au bord. 148

List of Tables

II.1 Values of Lamé parameters of different materials. 31

III.1 RMSE of the reconstructions of the displacement field and strain field for experiments with varying stretching conditions. 82

IV.1 Mean and standard deviation of the accuracy of the reconstruction for each evaluation metric. 97
IV.2 RMSE of the elastography reconstruction methods with true displacements as input for experiments with varying stretching conditions 105
IV.3 Runtime of our Mixed-PDE method compared to indirect reconstruction. 105
IV.4 Quantitative evaluation of the whole pipeline for the two real-like configurations 108

Contents

List of Figures **i**

List of Tables **iii**

Contents **iv**

Outline **vii**

I Motivation **1**
- I.1 Nuclear mechanics ... 1
  - I.1.1 Nuclear architecture ... 1
    - I.1.1.1 Nuclear components ... 1
    - I.1.1.2 The cell's nucleus and mechanotransduction ... 6
  - I.1.2 Diseases induced by mechanical defects ... 7
    - I.1.2.1 Laminopathies ... 7
    - I.1.2.2 Pelger-Huët Anomaly ... 8
    - I.1.2.3 Cancer ... 9
  - I.1.3 Mechanical modeling of the nucleus ... 11
- I.2 Measuring mechanical properties ... 14
  - I.2.1 Imaging methods ... 14
  - I.2.2 Experimental settings ... 15
  - I.2.3 Drawbacks of existing methods ... 22

II Modelization of the nucleus **25**
- II.1 Elasticity of the nucleus ... 25
  - II.1.1 Equations of linear elasticity ... 25
    - II.1.1.1 Equations of equilibrium ... 25
    - II.1.1.2 Constitutive equations ... 28
    - II.1.1.3 Equations of linear elasticity ... 31
  - II.1.2 Regularity requirements ... 32
    - II.1.2.1 Sobolev spaces ... 32
    - II.1.2.2 Existence, unicity, and regularity of the solutions ... 35
- II.2 Formulation of the three problems to solve ... 38
- II.3 Data creation ... 39
  - II.3.1 Tessellation ... 39
  - II.3.2 Variational formulation ... 42
  - II.3.3 Finite element definitions ... 44
  - II.3.4 Discretization, assembly, solve and warping ... 46

III Measuring displacements from images **49**
- III.1 State of the art of optical flow techniques ... 49

III.1.1 Brightness constancy ... 49
III.1.2 Horn Schunck ... 52
III.1.3 TV-L1 ... 56
III.1.4 Large Displacement Optical Flow ... 60
III.1.5 eFOLKI ... 62
III.1.6 Deep-Learning methods ... 63
III.1.7 Some remarks on the staircasing effect ... 64
III.2 Proposed optical flow method ... 65
III.2.1 Higher order regularization ... 65
III.2.2 Polynomial-time approximation ... 68
III.2.3 Proposed optical flow problem, minimization procedure ... 70
III.2.3.1 Regularity properties of the solution. ... 70
III.2.3.2 Numerical resolution. ... 71
III.2.4 Numerical evaluation ... 77
III.3 Application 1: influence of vimentin intermediate filaments on the deformations of glioblastoma nuclei during invasion ... 85

IV Estimation of physical quantities from displacements **91**
IV.1 State of the art ... 91
IV.2 Proposed elastography methods ... 94
IV.2.1 Computation of the absolute values of the Young's modulus ... 94
IV.2.2 A mixed PDE framework for the computation of relative Young's modulus ... 99
IV.3 Application 2: estimation of the relative stiffness distribution of deforming cardiomyocytes and SKOV3 cells' nuclei ... 109
IV.4 Proposed method for measuring stress and boundary traction forces ... 111
IV.5 Application 3: temporal evolution of the forces and stress within the nucleus of Toxoplasma gondii during invasion ... 116

Conclusion and perspectives **121**

A Microscopy techniques **125**
A.1 Fluorescence microscopy ... 125
A.2 Brillouin microscopy ... 128

B Staircasing effect **131**
B.1 Perimeter, jump sets, co-area formula ... 131
B.2 The Euler-Lagrange equations ... 133
B.3 The equivalent level-sets problem, existence of the staircasing the effect ... 134

C Adjoint method **137**

French summary **139**
C.1 Motivation ... 139
C.2 Modélisation du noyau cellulaire ... 140
C.3 Mesure des déplacements à partir d'images ... 141
C.4 Calcul des champs physiques à partir des déplacements ... 145
C.5 Conclusion et perspective ... 148

Bibliography **151**

Outline

Chapter I of this thesis motivates the problems under study. Section I.1. reviews the mechanical properties of the nucleus. After exposing its architecture and its main constituents, we show how each interacts with one another to fulfill physiological functions of interest, such as mechanotransduction and migration. We then explain how some alterations in the complex mechanical machinery of the nucleus may cause a wide range of diseases, from laminopathies to cancer. Once we understand the biological importance of nuclear mechanics, we end the section by exposing the physical models that biologists use to study them. Section I.2. presents several experimental settings that biologists deploy to measure physical quantities of interest, and mentions the chief strengths and limitations of each of them. It ends with an argument in favor of the necessity of computational imaging tools to compute physical quantities in biological configurations that remain intractable with the actual experimental methods.

Chapter II recasts the biological and mechanical problem of the previous chapter into a mathematical one. Section II.1. establishes the equations ruling the nuclear domain, namely the equations of nonlinear elasticity, and shows why we may assume in many cases that these can be simplified into equations of isotropic linear elasticity. It also derives several hypothesis drawn from the nuclear architecture exposed in Chapter I, and deduces necessary regularity properties that the physical quantities must observe in our configuration. Given these equations, and these necessary properties, Section II.2. states in mathematical terms the three problems our methods will need to solve in the following chapters. Finally section II.3. describes how we may numerically approximate, with the finite element method, the solutions of the equations ruling the nuclear domain, and use these simulations to create synthetic images of deforming cells' nuclei with underlying known mechanical quantities, to serve as a benchmark for later evaluation.

Chapter III exposes how we estimate displacement fields from images of a deforming nucleus. We rely here on a method called optical flow. Section III.1 reviews the main principles underlying it and presents several state-of-the-art optical flow techniques. It shows that these methods, while efficient for estimating real-life 3D motion, do not observe the regularity properties that we set forth in chapter II, and are therefore inoperative in our context. We also show that they suffer from a well-known image artifact called the "staircasing effect" that is particularly detrimental in the derivation of physical quantities. We offer our remedy to these problems in Section III.2, namely our own optical flow method, endowed with a new regularisation term. After underlying the necessity of a higher order regularization method, it proves that our optical flow technique observes the improved regularity properties in the continuous setting and overcomes the staircasing effect. An efficient numerical resolution method is given and evaluated thanks to the data creation framework we presented in section II.3. Although the obtained displacement fields are meant to be further processed, section III.3. shows they can be already used as such to prove important biological properties, namely the influence of vimentin filaments on the deformation of glioblastoma nuclei during invasion.

Chapter IV shows how we estimate the physical quantities of interest from the computed displacement field. Section IV. 1. exposes the state of the art on the computation of the stress, traction and

Young's modulus. Section IV. 2. presents two methods we developed to compute the distribution of the Young's modulus within the cell. In the first one, the boundary traction forces are supposed to be known, and the absolute values of the Young's modulus is derived thanks to the accuracy of our optical flow method presented in chapter III. In the second one, the boundary traction forces are not known, and we retrieve the relative values of the Young's modulus through a novel Mixed PDE of the stiffness within the nucleus. Both are systematically evaluated following the data creation frameworks in section II.3. Section IV. 3 shows an application of the proposed elastography methods, for which we estimate the relative stiffness distribution of deforming cardiomyocytes and SKOV3 cells' nuclei. Section IV. 4. assumes that the Young's modulus and the Poisson's parameter are known, and explains our framework to compute the stress tensor field within the nucleus and the boundary traction forces. Section IV. 5. presents an application of this method by establishing the temporal evolution of the forces and the stress within the nucleus of Toxoplasma gondii during invasion.

Chapter I

Motivation

This chapter shows the physiological relevance of nuclear mechanics. A brief exposition of the nuclear architecture is given, and of the complex relations entangling its numerous components, within and outside the nuclear domain. We expose how some alterations in the healthy layout of this architecture occasion diseases. From there, we rule out those components that do not partake in the mechanical machinery of the domain, and come by degrees to more abstract physical models of the nucleus. We then explain how biologists rely on these models to build probing tools that measure the desired mechanical properties of the nucleus, and why these are inconsistent with many biological configurations of interest.

I.1 Nuclear mechanics

The nucleus houses most of the genomic activity of the cell, and has mostly been studied as such. This is somewhat an unfair statement, since the pioneering work of Lionel Beale (1828–1906), to whom we owe the discovery of the relationship between abnormal nuclear morphology and cancer, largely predates those on the functionality of the genome [1]. But the interest in the topic has been upstaged by the discovery of the DNA at the end of the nineteenth century and by the ensuing explorations of the genome during the twentieth. We have to wait up until the 1980s, when the introduction of the first traction force microscopy enabled biologists to probe the nucleus in a sufficiently precise way [2], to witness a rekindling of the subject that concerns us here. Interestingly, the investigations of cellular genomics set forth a number of nuclear components previously unknown in the nineteenth century (for example the nuclear lamina), of which a portion fulfill mechanical roles as well. It is because of this ambivalence that the biochemical and mechanical properties of the cell intertwine, and the reason why mechanical defects are used today as diagnostic and prognosis tools.

I.1.1 Nuclear architecture

I.1.1.1 Nuclear components

The majority of eukaryotic cells contain a single nucleus. While some blood cells contain none [3], and syncytia [4] and coenocytes [5] contain several, these will be regarded as the exceptions confirming the rule. It is difficult to state a typical size of the nucleus, which may span from 1 μm to 20 μm [6], with wide variability in the nuclear-to-cytoplasmic ratio [7]. But we may assume without prejudice that it is the largest organelle of the cell [8]. The nucleus might be roughly divided into two, the nuclear envelope and the interior [9] (see Figure I.1).

Nuclear envelope. The *outer nuclear membrane*, a phospholipid bilayer, occupies the periphery of the nucleus [11]. Lipid bilayers are found likewise around all cells and all membrane-bound organelles [12]. They are a few nanometers thick, and are impermeable to hydrophilic molecules, which makes it

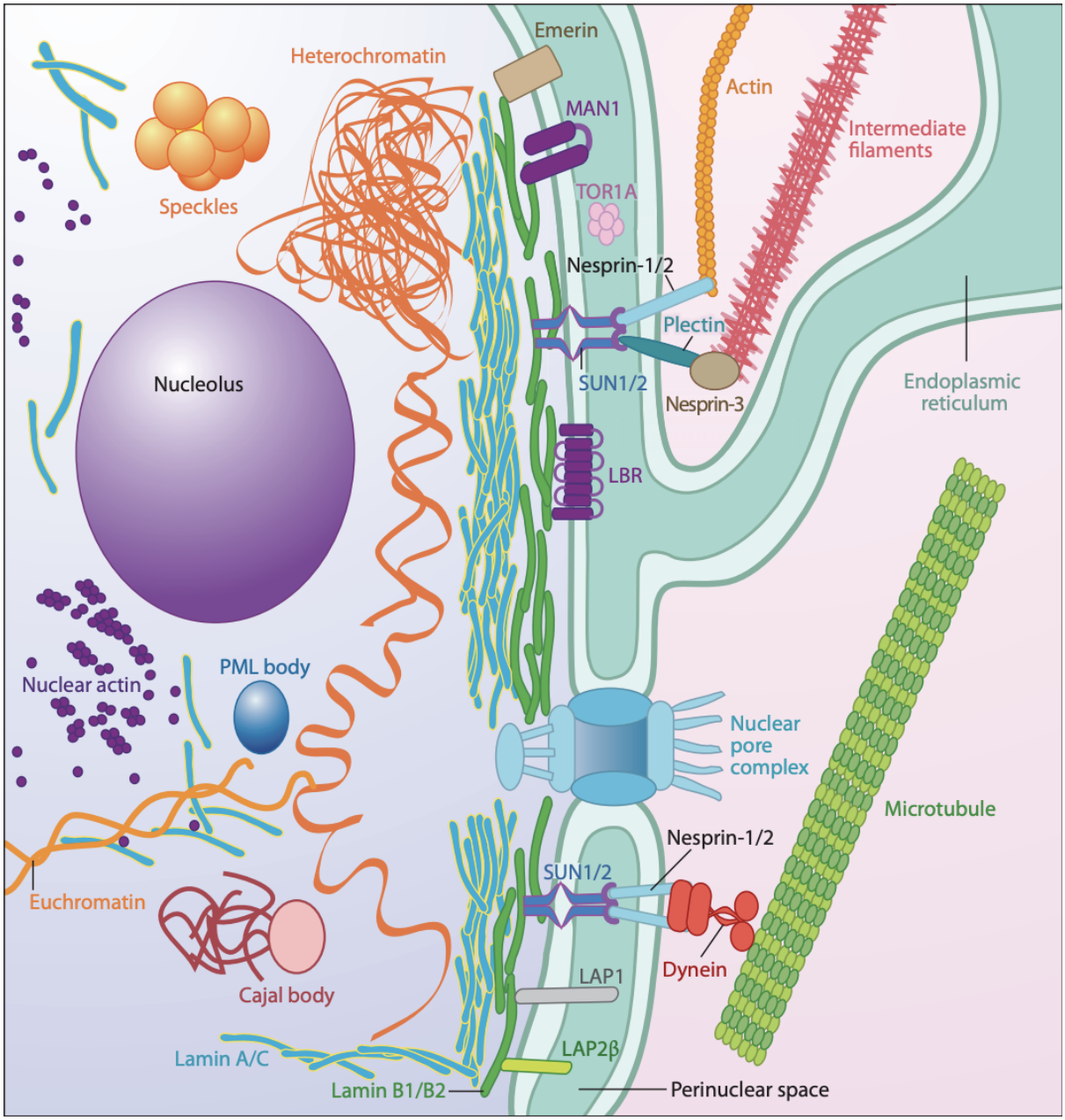

Figure I.1: Main nuclear components and their cytoskeletal associations. (from [10]).

impossible for most external elements to cross them. The outer nuclear membrane also contains all four isoforms of nesprin [13], which as we will see play a key role in the mechanotransduction of the cell. It is continuously attached to the *endoplasmic reticulum*, an organelle of its own. The endoplasmic reticulum is composed of corrugated membranes called cisternae [14]. We may discern two parts of it, with distinctive biochemical functions: the rough endoplasmic reticulum (RER), and the smooth endoplasmic reticulum (SER). The RER is so named because it contains ribosomes throughout its surface [15]. These particles come and go to depose proteins, which are then folded and modified through post-translational procedures. The SER contains the exit sites of the proteins [16], but it has increasingly been remarked that it also plays prominent roles in lipid synthesis, calcium storage, and detoxification of drugs and toxins [17]. Beneath the outer nuclear membrane comes the *perinuclear space*, a 10 to $50\ nm$ thick space mainly composed of solutes [18]. Besides being a transitory region for proteins, biologists doubt whether it fills any additional role, though very recent studies seem to maybe suggest otherwise [19]. Next comes the inner nuclear membrane, a phospholipid bilayer as well. Its structure differs not extensively from the one of the outer nuclear membrane, but because it is supported by the nuclear lamina beneath [20], it contains related proteic structures such as emerin, lamin B receptors, lamin-associated proteins (LAP), or SUN proteins. The inner and outer nuclear membranes are not free to slide on one another. Rather they are firmly attached through multiple (between 30 to 50) *nuclear pore complexes* that spans through the perinuclear space [21]. These 5 to $12nm$ diameter structures are intricate organizations of nucleoporins and are homogeneously studded accross the nuclear envelope [22]. They act as selective gateways for proteins entering or exiting the nuclear domain. While small particles (up to 30 or $60kDa$) diffuse without hindrance through them, bigger proteins, such as RNA, DNA polymerase, signaling molecules, or ribosomal proteins, undergo a selection and transportation process executed by nuclear transport receptors (NTR) [23]. Above 30 of such NTRs are currently identified, but their whole spectrum is difficult to pin down because of the variety and dynamism of the cargo transportation signaling pathways [24], [25]. The *nuclear lamina* is attached below the inner nuclear membrane. It is a regular fibrillar meshwork made of proteins called lamins [26]. While mostly localized in the envelope, lamins are likewise found in the nuclear interior in solute forms, but their function there yet escapes the latest investigations [27]. Lamins are classified as type V intermediate filaments (IF) and are in fact the only IF in the nucleus [28]. As such, they share the common structure of all IF proteins [29], that is: an N-terminal domain at its head, a rod domain in its center composed of four alpha-helical domains that are separated by linker regions, and a globular C-terminal domains at its tail, that contains lamin-specific motifs such as nuclear localization signal, immunoglobin fold motif, and the C-terminal CaaX. We will see that this peculiar assembly plays a role in the overall mechanism of the nucleus. Despite this uniformity of structure, one may discern two distinct types of lamins: A-type lamins (the lamins A and C that result from the LMNA gene), and B-type lamins (lamins B1 and B2/B3, encoded by the LMNB gene) [30]. Numerous studies, starting with the ones on the *Xenopus* oocytes [31], prove that these two types of lamins are found in equal amount, and that they form separate networks within the nuclear lamina. It is also shown that the loss of either lamin A or B does not impede the organization of its counterpart, and that they cannot supply against the lack of their counterpart either [32]. For these reasons studies of the properties of the lamina tend to be divided in two, and an increasing body of evidence suggests that lamins A and B fulfill different nuclear functions as well [33]. It was shown for instance that knocking out the LMNA gene prompted abnormal nuclear shape [34], and that knocking out the LMNB gene didn't – instead, this last knockout impeached proper positioning of the nucleus during migration [35], [36]. It is consistently proven that lamins interact with over 30 transcriptional regulators, such as retinoblastoma proteins, c-Fos, Gcl, Mok2, and SREBP-1 [37]. Lamin B1 for instance sequesters Oct-1 within the nuclear envelope, ruling whenever this transcriptional may play its part [38], which is testimony of a direct mediation in the transcriptional process. Lamins are also shown to regulate signaling pathways [39]. More interestingly for our purpose, the lamina constitutes in many ways an interacting platform within and outside the nucleus. But we will delve on this point once the reader holds a complete overview of the nuclear architecture.

Nuclear interior. *Chromatin* is the packaged state of DNA [40]. It is composed of nucleosomes, which are 147 pairs of DNA wrapped around an octomer of four core histones (H3, H4, H2A, H2B). These assemble into $30nm$ thick chromatin fibers. Chromatin may be found in two states: heterochromatin and euchromatin [41]. The heterochromatin is a dense, trancriptionaly silent, gene poor region, mostly situated at the periphery of the nucleus, and at the centromeres and telomeres of chromosomes [42]. We know from experimentation that it fulfills at least two biological functions, a structural one and a gene silencing one [43]. It is now growingly accepted that the heterochromatin comes in two forms which separately operate these two functions: the facultative heterochromatin [44], and the constitutive heterochromatin [45]. The separation between one state and the other is usually ruled by the quantity of methylation on lysine-9 in histone H3 [46]. The constitutive heterochromatin is permanently condensed throughout all the cell cycle, almost completely transcriptionally inactive, and was shown to prevent chromosomal rearrangements. The facultative, on the other hand, can switch intermittently between a condensed and looser state, depending on the cell cycle. In the latter case it becomes active, and partakes in the gene silencing activity. Conversely, euchromatin is a light, transcriptionally active region of the chromatin structure, usually found toward the nuclear interior and near nuclear pores [47]. The openness of its structure allows free replication and repair of DNA [48]. Recent electron microscopy experiments showed that both heterochromatin and euchromatin display a fractal, knot-free organization [49]. Interestingly, this topology is not only a natural consequence of the tightening requirements of the long DNA strands, but also a prerequisite for proper gene expression [50] - a good illustration of how fractals can conceive spaces that are both dense at one scale and open at another. For experiments that operate at this level of accuracy, it was for instance proven that the fractal dimension of the organization can be used as an effective prognosis tool of the malignancy of cell carcinomas of the pancreas [51]. We now come to the description of the interchromatin space. It is a profoundly complex and dynamic environment. While every year seems to bring forth new components that describe its organization, we will circumscribe our presentation to the most established elements only. The *nucleolus* is the biggest of these elements. Its high density and high refractive index [52] makes it noticeable even through simple light microscopy [53]. We know for certain that it is located where the ribosomes are produced, [54], which corresponds to a precise nucleolus organizing region found on a select number of chromosomes [55]. It is yet unclear what determines which chromosome will contain it or not. The nucleolus may be divided in two regions: pars fibrosa, which contains proteins required for transcription, and pars granulosa which contains ribosomal precursors [56]. Although this may indicate that the nucleolus is prominent in the creation of ribosomes [57], it is very much doubted that it sustains by itself the whole ribogenesis – in large eukaryotic cells, for instance, it was shown that the endoplasmic reticulum partakes this task as well [58]. *Nuclear speckles*, also called interchromatin granule clusters, are membraneless organelles, generally 25 to 50 in each nucleus, showing wide variability in structure according to the genetic activity of the cell [59]. They gather concentrated amounts of snRNPs and non-snRNPs protein splicing factors and it was observed through electron microscopy that their localizations also harbour most of the splicing operations [60]. Recent studies suggest that it furthermore participates in mRNA production [61]. *Cajal bodies* are likewise membraneless organelles [62]. They mostly contain coiled threads of the marker protein coilin [63], involved in the post-transcriptional modification processes of RNAs. This protein also attaches the Cajal bodies unto the nucleolus. In fact, we know that the nucleolus and Cajal bodies frequently exchange this protein, but to what purpose remains unclear [64]. It also counts a significant amount of survival of motor neuron (SMN) protein, [65], responsible of the modification and assembly of U snRNPs, [66], engaged in the spliceosome [67]. *Promyelocytic leukemia nuclear bodies* (PML-NB) share their name with the PML proteins that constitute them [68]. They are rather thick (0.2 to $1\mu m$ in diameter), and can be as many as 30 in a nucleus, according to the differentiation stage. The very versatile PML protein, also found in the cytoplasm, plays mostly here a role of tumour suppressor along with Sp100 and DAXX, which are permanently found within its interior [69]. But PML-NB further hosts a number of transitory proteins, which makes it a key actor in functions as diverse as apoptosis [70], senescence [71], proliferation inhibition [72], genomic stabilization [73] and antiviral responses

[74]. Mostly, it is regarded as a hub for posttranslational modification and frequently serves as protein depot [75].

Nucleoskeleton. We end this presentation of the nuclear architecture with a few considerations about the "nucleoskeleton" [76]. We employ quotation marks here as its very existence is debated. A significant portion of the mechanobiological community is seduced with the idea of an intranuclear structure that supplies mechanical support and functional organization within the nucleus – something like the nuclear equivalent of the cytoskeleton in the cytoplasm. Several analysis of salt extraction procedures of the nucleus concluded favorably on the existence of residual protein structures, to the point of establishing the notion of a "nuclear matrix" in the 1970s [77]. Later on, the existence of actin, a protein that forms microfilaments in the cytoskeleton, was disclosed within the chromatin interspace [78]. At the same time, epigenetic studies rigorously established the partition of chromosomes into a unique and stable topography, implying the presence of a central organizational scaffold that would orchestrate their position [79]. But many arguments come to cross these hints. It was for instance doubted that the residual protein structures issued from the nuclear composition, but rather was artificially precipitated because of the harsh extraction method. Furthermore, as we just said, the interchromatin space is filled with ribonucleoproteins and numerous nuclear bodies: it is very questionable that any dynamic structure could move easily within it. While striking, the presence of actin does not directly imply the presence of a skeleton. First, it was proven that most of it is G actin, in other words in a solute form, and that only a minor fraction of it is polymeric [80]. Secondly, no one revelead yet the existence of phalloidin, which is required for signaling potential filaments [81]. Rather, it was proven that actin took part in several non structuring roles, by providing assistance in transcription, mRNA processing and exportation, as well as chromatin remodeling [82]. Overall, at the present time, only the nuclear lamina can pretend a kindred resemblance to the cytoskeleton [83]. As we will see next, it maintains nuclear shape, decides the positions of nuclear pore complexes within the envelope, and is studded with actin binding sites. But the opinion of the biologists on the matter is evolving, and a certain number of proteins seem to stand as good candidates in a possible nucleoskeleton machinery. *Titin*, for instance, is the main component of striated muscle cells, and provides stiffness to them [84]. It was recently discovered within the chromatin interspace, both with actin and lamin binding sites on one hand, [85], and with low weight proteins shared with H2A, H3 and H4 histones on the other [86], suggesting a mechanical transmission role between the chromosome and the envelope. *Nuclear mitotic apparatus protein 1* (NuMa) form spindle poles in mitosis [87]. When absent, nuclear fragmentation may be observed [88]. It was only recently established that this didn't occur because of the spindle poles, but rather because its disruption may not impeach chromosomal binding at mitotic exit [89]. *Spectrins* repeat were already known to be present in the cytoplasm and the plasma membrane [90]. They would appear in large structural proteins like dystrophin, α-actinin and spectrin itself. In the past two decades, several experiments revealed their presence in structuring proteins of the interchromatin space of the nucleus as well [91]. It is nowadays well attested that *Nonerythroid αII-spectrin* recruits repairing proteins to the damaged sites of DNA ICLs – both, as it seems, to genomic and telomeric regions [92]. More interestingly for us here, it recently transpired that this protein could very well likewise fulfill a scaffolding role, as it binds to lamin, emerin, actin, protein 4.1, nuclear myosin, and SUN proteins – which we will see are essential in the mechanical machinery of the nucleus [93]. To the point of questioning biologists whether Fanconi anemia, that were known to be produced by their deficiency, rather ensued from mechanical failure, than lack of genomic repair [94]. We may also mention the presence of spectrin repeats in $\beta SpectrinIV\Sigma 5$, that associates with all of the aforementioned PML bodies, *Bpag 1*, derived from the large family of plakins, that appears in the nucleus of C2C12 myoblasts and co-aligns, presumably for a scaffolding role, with actin stress fibers, or even $MAKAP$, a large cardiac ion channel, yet only found in the nuclear envelope of heart and cultured myocytes, that induces calcium release from intracellular calcium ion stores [95].

I.1.1.2 The cell's nucleus and mechanotransduction

As stated in the introduction of this thesis, mechanotransduction is the process by which a cell converts mechanical signals into biochemical ones [96]. We know from the last two decades that it is the nuclear envelope that transmits forces from the cytoskeleton to the nuclear interior [97]. Its participation and biochemical reactions have been established for three important functions: nuclear migration [98], organization of the chromatin [99] (hence the nucleoskeleton discussion at the end of the previous section), and chromosome pairing [100]. This remarkable variety relies on the presence of two families of bridging protein regions, called SUN (Sad1p and UNC-84) and KASH (Klarsicht, ANC-1 and Syne/Nesprin homology) [101]. These are nowadays regrouped in what is termed the LINC (linker of nucleoskeleton and cytoskeleton) complex model [102]. Though some SUN3 and *Spag4* domain proteins are found in the cytoplasm, only SUN1 and SUN2 are in the nucleus [103]. Nevertheless, they all possess in common one trans-membrane domain. SUN1 and SUN2 proteins are located in the inner nuclear membrane, and their trans-membrane domain pokes out within the perinuclear space [104]. The precise signaling procedures that localize the SUN domain proteins in the nuclear envelope is not well understood [105]. Their N-terminal nucleoplasmic domains, for instance, do contain the chemical signaling needed for localization, but their mutation did not seem to hinder their positioning. Likewise it was posited that the lamin interaction may influence its localization, but not all SUN domain proteins interact with lamin, and yet they are precisely localized [101]. In any case, it is shown that the presence of SUN domain proteins is stable and well strewn across the inner nuclear membrane – a fact we will leverage in the last section of this chapter [106]. KASH domain proteins all contain a C-terminal domain that spans within membranes [107]. Their localization is precisely determined by a lumen domain and an N-terminal domain within the cytoplasm. We previously mentioned the four families of nesprins, located in the outer nuclear membrane: they all contain this C-terminal KASH domain [108]. Interestingly, they all require interactions with different SUN domain proteins to perform the previously mentioned functions. For instance, during migration, the cytoplasmic domains of the KASH protein UNC-83, Nesprin-4 and Syne/Nesprin-2, bind the KLC-2 light chain of kinesin-1 and three regulators of dynein, in conjunction with the anchoring functionality of the SUN domain protein UNC-84 [109]. Likewise, nuclear anchorage to microtubules involves both the KASH protein ZYG-12, which interacts with dynein, and the SUN protein matefin to ensure proper spacing of nuclei in gonads [107]. Intermediate filaments are linked to actin filaments thanks to the plakin protein named plectin, which is shown to interact with KASH protein Nesprin-3, which is localized in the outer nuclear membrane by expressions Sun1 and Sun2 [110]. These are just a few examples of what seems to be a ubiquitous collaboration of the LINC complex. Other instances of conjunctions include roles in: maintaining the spacing between inner and outer nuclear membranes (nesprin-2 giant and Sun1), preventing clustering of nuclear pore complexes (nesprin-1 and Sun1), maintaining nuclear size and architecture (nesprin-2 giant and Sun1), tilting polarization during migration (Zyg-12 and Sun1, Sun2, or regulating the organization of the cytoskeleton (ANC-1 and Syne/Nesprin-1 and -2)). Regarding this last point, a whole body of research investigates the influence of the LINC complex in mechanosensing [111]. This important cellular function involves the mediation of myosin-like actin-associated motor proteins to adapt the cytoskeletal tension to the extracellular stiffness. Cytoskeletal rearrangement through ANC-1 and Syne/Nesprin-1 and -2 interactions are of course very important in that respect, but recent studies suggest that the nucleus itself can be used as a mechanosenor organelle, since dominant-negative versions of nesprin and sun proteins were shown to impede stretch-induced proliferation [112]. Finally, the Zyg-12 along with Sun1/Matefin are paired to allow Dynein-mediated transport along microtubules for rapid chromosome movements during meiotic prophase 1 [113]. The same dynein regulation is involved for the recruiting of IKNM during neurogenesis. We see that many of these proteins appear in very different phenomena. In this light, the subject of LINC redundancy has challenged the enquiries of the biologists for a long time: mice deficient in either SUN1 and SUN2 are viable, but not when they are deprived of both; mice deficient in Nesprin-4 have normal epithelial and pancreatic secretions properties, but not when Nesprin-1 and Nesprin-2 are absent

as well; on the other hand, mice deficient in Sun1 are infertile and develop early onset hearing loss, with or without the presence of Sun2 [114]. All these force-transmitting proteins are shown to interact with other proteins found within the inner nuclear membrane, namely emerin, MAN1, LBR, lamina-associated polypeptids (LAP1, LAP2β), which in turn are bound to the nuclear lamina, suggesting an influence of the cytoskeletal force to the genetic state of the nucleus. It is unknown how the interaction of lamin-A and emerin affects the genotype, but we will see in the next section that its absence causes serious diseases. It shares, along with MAN1 and LAP2, a 43-residue N-terminal motif termed the LEM domain, shown to mediate interaction with the DNA associated protein Barrier-to-Autointegration Factor (BAF) [115]. MAN1 further binds the tail domains of pre-lamin A and mature lamin B1 [116]. LAP1 shares functional links to Torsin A/B [117], and Lap2α regulates cell proliferation by affecting the activity of retinoblastoma protein [118]. As we can see, the precise roles of each SUN and KASH domain proteins, along with associated inner membrane proteins, are ample, intertwined, and not fully elucidated, and we hope to have given the reader, after this short overview, a taste of the biochemical complexity of the mechanical properties of the nucleus. We now show how extinction of some nuclear components, or some perturbations within their interactions, may result in diseases.

I.1.2 Diseases induced by mechanical defects

I.1.2.1 Laminopathies

Mutations in the LMNA and LMNB genes have been associated with over 15 diseases [119]. Some are overlapping, and it is common to proceed to some unification. Mutations in the LMNA gene are predominant, and are proven to cause the following groups of affections: premature aging syndromes such as the very rare but lethal Hutchinson-Gilford progeria syndrome (HGPS) [120], striated muscle diseases such as Emery-Dreifuss Muscular Dystrophy, limb-girdle muscular dystrophy or dilated cardiomyopathy, lipodystrophy syndromes including the Dunningan type, and finally peripheral neuropathy. Mutations in LMNB genes are more rare. Experiments suggest an involvement of the duplication of the LMNB1 gene in leukodystrophy, and LMNB2 mutations partially cause lipodystrophy. These diseases are dire: progeria, although rare, is a hastened senescence procedure, that makes the concerned patients look older, and kills them during their mid teenage years or early twenties [121]. Muscular dystrophy affects the muscles used for movement [122]. It deforms the joint into a tight organization called contractures, which little by little restricts the movements of the elbows, ankles and neck, and results in heart abnormalities through a corruption of the electrical signals that pulsate the heartbeat. Patients suffering from either of lipodystrophy syndromes are unable to produce and maintain healthy fat tissues, causing failures in insuring insulin resistance, and preventing hypertriglyceridemia and non-alcoholic fatty liver diseases [123]. As its name suggests, peripheral neuropathy affects the peripheral nerves, responsible for signal transmission between the central nervous system and the rest of the body, resulting in sensations of numbness and tingling, loss of coordination, muscle weakness, or crippling pain. Leukodystrophy concerns the white matter of the brain [124]. People suffering from it display abnormally low levels of myelin, a fatty sheath surrounding the nerve fibers and allowing proper signal transmission, and witness an impairment of their motor abilities, a cognitive and developmental delay, as well as speech difficulties. These extremely different phenotypes are occasioned from the corruption of both the structural functions of lamin and its epigenetic state regulation properties. For instance, skeletal muscle fibers of patients suffering from Emery Dreifuss muscular dystrophy contain multiple fragmented nuclei (see Figure I.2). These nuclei also display less resistance to force. A lack of nesprin-1 and nesprin-2 are commonly observed in this kind of affection, as well as a mislocalization of SUN2 proteins [125]. Cultured mouse embryonic fibroblasts deficient in lamin A not only have more fragile nuclei, but also reduced ability in the stiffnening of their cytoskeleton. More precisely, the knock out of genes encoding both nesprins-1 and nesprins-2 results in Emery Dreifuss muscular dystrophy, and the sole disruption of their KASH domain causes muscular dystrophy in mice [126]. Similar perturbations of the LMNA gene proved damaging for the perinuclear actin, and knock-out of emerin in

some experiments separated the microtubule organizing center from the nucleus. Structural changes are also witnessed in fibroblasts of patients suffering from Hutchinson-Gilford progeria syndrome [127]: modifications of nuclear shape, nuclear reorganization, thickening of the nuclear lamina, loss of heterochromatin, are all observed. Most are associated with the spreading of the mutant protein progerin out of the inner nuclear membrane, which causes, by unwanted associations, several nuclear membrane ruptures and DNA damage. The precise biochemical mechanism behind this affection is not clear, although it has been reported that loss of lamin A caused it, and that additional lamin B1 expression may partly counter it [128]. It remains for instance intriguing to see that some HGPS patients do not suffer from muscular diseases. We see that the challenges of laminopathies lie in the wide variety of the phenotypes, to the point of studying mutations of the LMNA gene down to the amino acid level: in particular, it was shown that the displacement of T528 could either cause, depending on its position, Emery Dreifuss muscular dystrophy, familial partial lipodystrophy, or atypical HGPS [129]. And these mutations are not linked to a single chemical phenomena: familial partial lipodystrophy is caused by a compromised interaction of the lamin Ig-fold with SREBP-1, whereas Emery Dreifuss muscular dystrophy are caused by major up-endings in the lamina organization; HGPS patients, on the other hand, witness only partial reorganization of their lamina meshwork, the one responsible of nucleocytoplasmic transport of Ran GTPase, Ubc9, and the TPR nucleoporin.

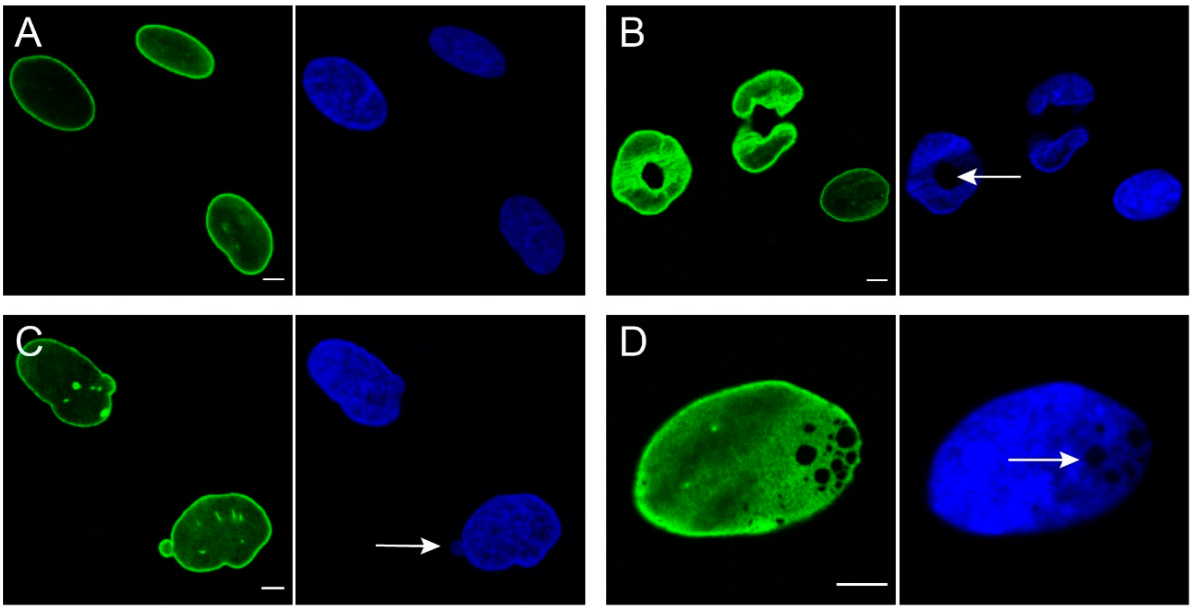

Figure I.2: Human dermal fibroblasts from laminopathy patients. The staining applies on lamin A/C. (A) Healthy nuclei; (B) abnormally shaped nuclei, with abnormal lamin repartition ; (C) nuclear blebbing: nuclear herniations with increased lamin A/C expression ; (D) honeycomb structures. Bars represent 5 μm (from [130]).

I.1.2.2 Pelger-Huët Anomaly

The Pelger-Huët Anomaly classifies as a laminopathy as well, but its cause originates from a dysfunctioning of the lamin B receptor [131]. It is characterized by unusual shapes of the nuclei of their neutrophils (see Figure I.3), a type of white blood cell that are involved in the identification and destruction of certain bacteria, fungi, and invasive microorganisms. The affection seems to appear during granulopoiesis, where the induction of lamin B receptor expression is required. Instead of being hyperlobulated, neutrophils' nuclei in a patient suffering from Pelger-Huët anomaly are either bilobed, dumbbell-shaped, or even appear as a single round nuclei. Unlike the aforementioned diseases, Pelger-Huët is benign and does not seem to significantly deteriorate the immune system of the patient, unless

left unchecked for too long: some rare reports mention a subsequent appearance of blood cancer in some cases, and some individuals suffer from developmental delay, epilepsy and skeletal abnormalities, in the case of a completely ovid nuclei for some homozygous carriers. But the biological consequences are worthy of study. The Pelger-Huët anomaly is inherited in an autosomal dominant manner, in other words that a single copy of the mutated gene transferred from non-sex chromosomes is sufficient to cause the it. In practice, this concerns half the offsprings of the patients presenting the anomaly. Peripheral blood smears examinations prove, along the distorted nucleus, the presence of a coarse chromatin. During chemotaxis, for instance, hypolobulated nuclei have proven to be less able to cross filters with small pore size. *In vitro* experimentation of these neutrophils also showed less capability of the LBR to migrate through membranes.

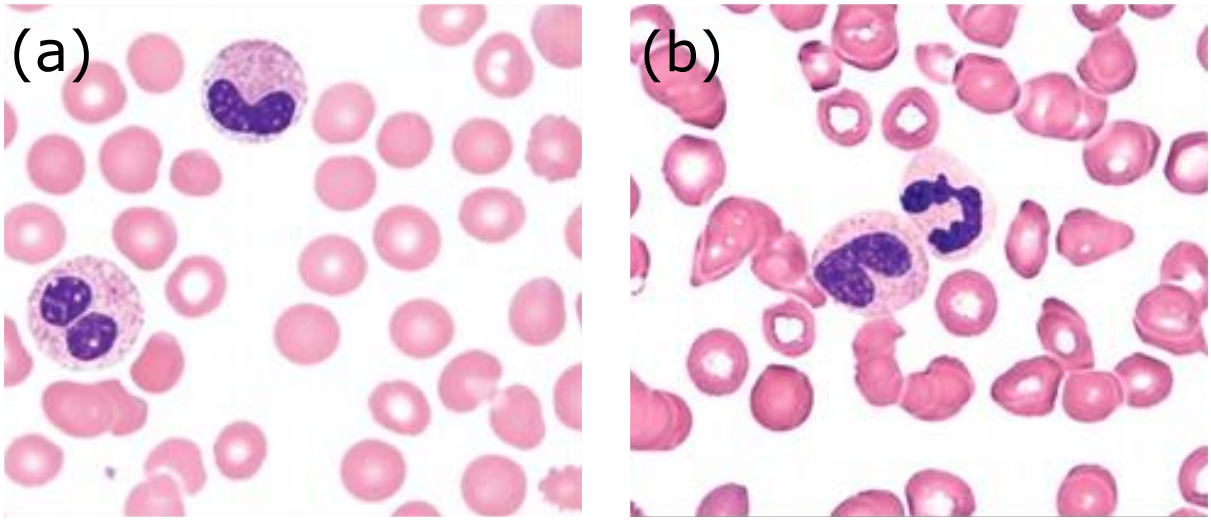

Figure I.3: Pelger-Huët anomaly. (a) Bilobed polymorphonuclear leukocyte on left and indented variant on right. (b) Indented variant on left and typical bilobed polymorphonuclear leukocyte on right, with darker staining indicative of high chromatin compaction (from [132]).

I.1.2.3 Cancer

However, the question of nuclear mechanics and migration is of great importance for another disease of great concern: cancer. By cancer medical practitioners mean a body of several disorders that disrupt the proper cycle of growth, division, and death in cells [133]. When cells divide and grow abnormally, they form a stiff lump in the tissue called a tumor. Tumors might be either benign or malignant. In the former case, the tumor is well circumscribed and does not invade the surrounding tissues. An apt medical doctor may remove it without altering the good functionality surrounding tissue. A malignant tumor, however, has no clear defined boundaries, invades the surrounding tissues, and can even spread to the entire body. This last phenomenon is called metastasis, and commonly precedes the death of the patient. As mentioned in the beginning of this chapter, nuclear morphology assessments were widely used to detect cancers onset on the microscope. The Papanicolaou test, for instance, evaluates the size and regularity of the nuclei of cells in the cervix [134]. These can generally be related to loss of nuclear domains, chromatin decompaction or compaction, and nucleolar irregularities. Further studies indicate that these changes in shape are more a symptom indicative of an ability of cells to migrate fast in the surrounding tissues, but the precise biochemical mechanisms underpinning it are yet not precisely understood. **This is where the mechanics of the nucleus become important for studying cancer cell migrations**. Several of many of the nuclear components previously presented serve as cancer biomarkers. In the interchromatin space, for example, urine tests suggest that the presence of NMP22 (NUMA) protein is highly correlated to the presence of bladder cancers [135], and nucleophosmin (NPM)/B23, a protein of the nucleolus, is overexpressed during breast cancer proliferation [136].

Likewise, lamin-B are highly upregulated during the differentiation of tumors in the prostate, and more specifically lamin B1 shows similar correlation for hepatocellular carcinomas [137]. On the other hand, lamin B is downregulated in gastrointestinal and lung cancer. Lamin A is overexpressed in skin and ovarian cancers. Conversely, it is scarcer in lymphomas and leukemias [138]. The metastasis of the tumors in the colon into the peritoneum are known to be poorly prognosised. One prognosis tool that seems promising, although debated, is the observation of the peritoneal involvement. For the proponents of this prognosis, characterising elastic lamina invasion can significantly be correlated to a pathologic stage 3 tumors without regional lymph node metastasis [139]. Several studies', involving the use of reverse transcription-polymerase chain reaction, western blots conclude in a downregulation of lamin A/C and related proteic expressions during histological differentiation in primary gastric carcinoma. This correlation pattern repeats with colorectal cancer tumors and gastric carcinomas. While there are good grounds to use the regulation of both lamins A/C and B as prognosis tools, it is yet unclear why these might prove relevant for each individual cancer type and differentiation stages. Numerous studies try to track the explanation in the proteic expressions related to the abnormal regulations of lamins, whether as a direct or indirect consequence of it. But another body of research, which concerns us here, also tries to understand the mechanical consequences of these oddities. These are to be paralleled with the mechanical properties of the invaded tissues as well. The idea is to state that these changes in the conformation of nuclear bodies alter the stiffness, or deformability, of the largest organelle of the cell. For instance, small cell lung carcinomas show denser compaction of chromatin, which result in higher nuclear stiffness (see Figure I.4). Because this alteration allows the nucleus to undergo a higher amount of stress, it also makes it more competitive to enter tight tissues that are otherwise non permissive to alien elements. This would also explain how cancer cells are able to enter the lymphatic system to spread throughout the body. We will see that both explanations work. In some cases, more deformable nuclei coincide with a better ability of cells to squeeze into tight spaces. In other, the rigidity of the nucleus allows it to resist distortion during the deformation of the extracellular matrix. Indeed, in breast cancer cells for instance, the invadopodia, a specialized F-actin rich protrusion, are known to exert significant forces on the nucleus to invade tissues, together with ECM degradation [140]. These two simple schemes might explain how both downregulation (softer nuclei) and upregulation (stiffer nuclei) of the lamina meshwork are witnessed. But the precise reason why one mode is preferred against the other according to the cancer type, subtype, and stage differentiation, remains to be elucidated. This short presentation should not overshadow the fact that lamins, whose epigenetic roles are now well exposed, could very well play a role before invasion, during tumorgenesis. For instance, the telomeric protein AKTIP is well known to be enriched at the nuclear lamina. Downregulation of the lamin A/C directly relates to the level of AKTIP expression in the nucleus, which shares some similarity with the tumor susceptibility gene TSG101 [141]. This image of the mechanics of the nucleus is even more complicated when considering that the lamina also alters the chromatin compaction levels, which may be directly related to cancer progressions as well, or even proteic productions. SATB1 and SATB2 are two families of proteins that are well known to interfere with the higher order organization of the chromatin structure. During tumor relapse and metastasis, SATB1 expression also happens to generate some cellular and molecular heterogeneities necessary for good tumor progression [142]. Conversely, SATB 2 expression suppresses the progression of colorectal cancer cells via inactivation of MEK 5/ERK 5 signaling. Also, the modification of lamins and chromatin structures might directly affect the cytoskeleton composition, as we saw. One recent body of research focuses on the expression of intermediate filaments in many types of cancer invasions, including lung, pancreatic, and nervous system related ones. In the last chapter of this thesis, we take part in an original research proving that overexpression of vimentin intermediate filaments, which belong to the nuclear domain, are crucial during the invasion of immunoglioblastoma nuclei in the ECM, and show that knocking out the specific genes regulating it might prove sufficient to stop cancer progression. These filaments ensure that the nucleus is sturdy enough during invasion of tight three dimensional spaces by degradation with metalloproteinase.

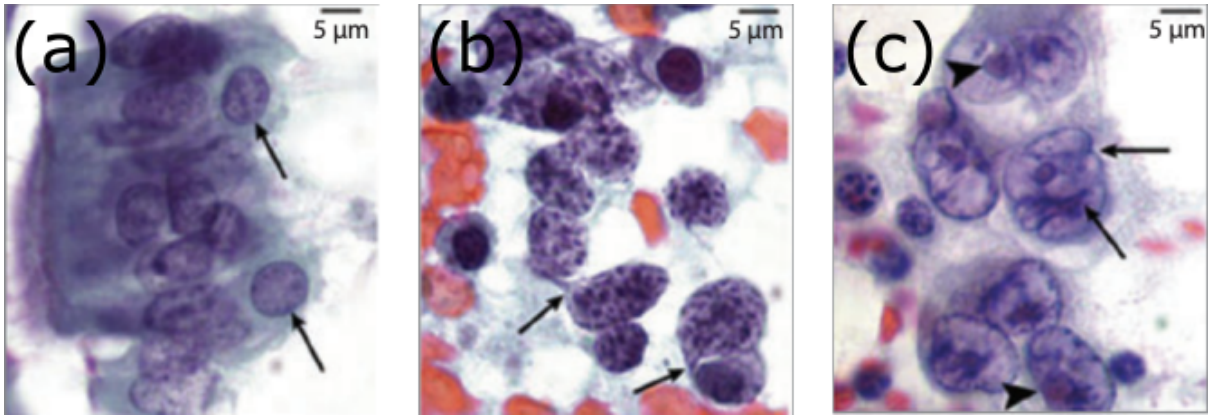

Figure I.4: Cancer cells' nuclei. (a) Normal basal cells of bronchial epithelium ; (b) Small cell lung carcinomas show denser compaction of chromatin ; (c) Large cell lung carcinomas display abnormal shaped nuclei (from [143]).

We hope that, at the end of this short overview, the reader may perceive how many different phenotypes might be related to the single question of nuclear mechanics. While the causes linking the mechanical properties of the nucleus to these affections is multifaceted and complex, **the need for developing new tools to measure them is eagerly required to tackle yet unanswered questions**. In light of the preceding presentation, we consider the mechanical properties of each components of the nucleus, and which ones are foremost in the overall force-deformation chain. We will then examine which exact physical model best describes their behavior. This is the first step of our modelization procedure, where we switch our biological description of the nuclear domain into a mechanical one.

I.1.3 Mechanical modeling of the nucleus

We follow the opinion of Hobson in [144], who classifies the mechanical models of the nucleus in three categories: one-dimensional models, molecular dynamics models, and continuum mechanics models (see figure C.1). Each applies to specific components of the nuclei, then combine to give an overview of the whole nuclear mechanics. Of the three, we will chose the last one, but we nevertheless present the other two to justify our choice. We will show in the next section that most experimental settings that measure the mechanical properties of the nucleus assume either a one-dimensional modeling of the nucleus (in most cases) or a molecular dynamics one (in some rare instances). It is in light of this choice of modelization that we pretend that our image-processing tools are, in many respects, superior to the existing ones. But we must first reduce the complexity of our problem, and select only those elements of the nucleus that are foremost in the whole domain's behavior. We state readily that we will only keep two: the nuclear lamina, and the chromatin. Indeed, the outer and inner nuclear membranes are mostly phospholipid bilayers. While under some varying temperature the stiffness of the phospholipid bilayers may vary, their rigidity generally vanishes in front of the intermediate filaments of the nuclear lamina. Also, the nuclear bodies' sizes are too small compared to that of the chromatic domain, and even the nucleolus, which is the largest of them, proved to be more like a liquid-like component. On the other hand, micropipette aspiration proved the linear lamina to behave like a stiff infinitely thin linearly elastic shell. Both lamins A/C and B1/B2 seem to follow the same behaviors, although sometimes with different stiffness properties [145]. Rheological experiments seem to indicate that the nuclear lamina may depend on the time-scale deformation as well, indicating a viscoelastic response to induced forces [146]. This would also correspond to the polymer-like structure of the lamina, which is well known to represent viscoelastic material. Likewise, the chromatin structure can be represented as an elastic material as well under small deformation. This has to be put in light with the process of mechanotransduction. As stated earlier, long stretches of applied forces might very well induce changes in the conformation of the

chromatin, but under small deformations its structure seems very stable. While the nuclear bodies do not seem to have their own stiffness, their fluid-like behaviors might very well change the mechanical response of the nuclear interior into a viscoelastic-like mode of deformation, like that of the nuclear lamina, although with different rheological parameters [147]. More precise modeling rather prefer the poroelastic model, which depicts the nuclear interior as an elastic material with pores through which fluid can pass. Because of the presence of nuclear pore complexes, the nuclear lamina is tighlty attached to the nuclear interior. **Overall, we may state that the nucleus can be modeled as a viscoelastic infinitely thin shell wrapped around the likewise viscoelastic interior, without sliding between them**. Under quasistatic deformation, meaning small and slow forces, these behaviors reduce to purely elastic deformations. We will hereafter suppose that we are in this configuration, although we will suggest how one may adapt our techniques to take the viscous response of the lamina and the chromatin as well.

One-dimensional models. These reduce the physical quantities of importance, namely stress, strain, displacement, the stiffness, the viscosity, and time, to single values of interest. Just like electrical systems, the mechanical constituents are represented with springs and dashpots. Springs are 1D models of elastic materials, i.e. objects that resist deformation, and that resume their shape when the applied forces on them are removed (think of a tennis ball or a real spring). Their deformation δx is linearly correlated with the applied force F, through the equation $F = -k\delta x$. Here, k is the stiffness constant, or Young's modulus. Dashpots on the other hand are 1D models of viscous materials, i.e. objects that resist time varying deformation (think of honey, for a high viscosity material, and water, for a low viscosity one). Their rate of expansion and compression $\delta\dot{x}$ are linearly correlated to the applied force F, through the equation $F = -\eta\delta\dot{x}$. Here, η is the viscosity constant. These springs and dashpots can be combined in series or in parallel, in which case, their force response can be adapted according to each constants of importance. In figure C.1 we may see for instance Jeffreys model, where a spring and dashpot have been paralleled, and altogether serialized with a second dashpot, and was used in micropipette experiments to prove that lamina contribute to the overall viscosity and rigidity in mouse embryonic fibroblasts. Other combinations are of course possible. Some of these were joined with other experimental settings to prove isolated chondrocyte nuclei are stiffer and more viscous that intact chondrocytes. Overall, these models are advantageous when the nuclear components behave homogeneously, meaning when their mechanical properties are so extremely established that they seem to cancel all other mechanical phenomena. We may likewise easily understand the limitations. We showed for instance that the chromatin can be found in two states: euchromatin and heterochromatin, both with very different compaction, and hence stiffness values. One-dimensional models suppose their heterogeneity does not matter, which it actually does in many biological functions of interest. Likewise, the geometry of the nucleus matter a great deal. We saw that nuclear shape may be indicative of certain disorders, the first one of them being cancer. Likewise, the nuclear geometry, as we will see in the last section of this chapter, imposes some crucial regularity properties of the deformation and the stress functions. The simplifications of the one-dimensional models overlook some key information of interest in that respect. The modelization is actually so abstract that they do not depend on the nuclei at all, but on proximal values (such as the nuclear perimeter, its surface, etc.) taken on them. This will become forcibly clear in the next section of this chapter.

Molecular Dynamics models. We may find, at the other end of the spectrum, molecular dynamics models [150]. Here the nuclei are divided into proteic, sometimes molecular components. Each component is then linked through specific equations derived by Newton's laws of motion. These molecules assemble into a polymeric chain whose entire reaction hinges on the specific properties of each of these linkers. These form further assemble into chromatin fibers or intermediate filaments meshwork of the nuclear lamina. This depiction embraces very closely the actual structures of both the lamina and the chromatin. The practitioner is able to ascribe precise viscosity and elasticity values at the subcomponent level. This is an ideal method to determine the role of the application of cytoskeletal traction forces at

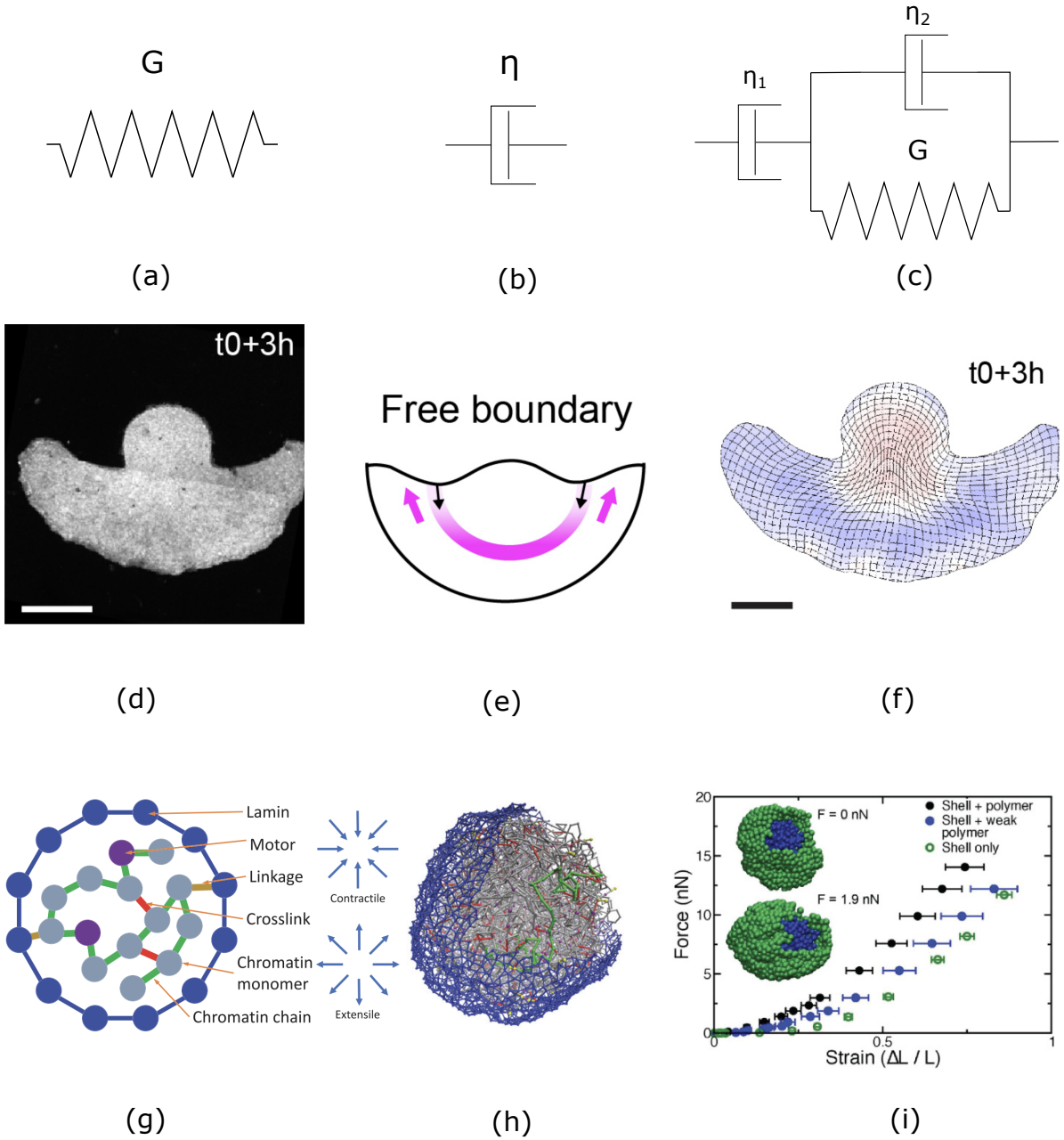

Figure I.5: The three types of mechanical models. First line: 1D models ; (a) Spring with force deformation relation $f = -kdx$; (b) Dashpot with force deformation rate relation $f = -\eta d\dot{x}$; (c) Jeffrey rheological characterisation of a viscoelastic material, especially used for fluids with shear-thinning behavior. Second line: Continuum mechanics models ; (d) brightfield image of a posterior epiblast half ; (e) Definition of the boundary conditions ; (f) Magnitude of the velocity field obtained after finite element resolution of the non-linear Stokes models with boundary velocity fields obtained from PIV techniques (adapted from [148]). Third line: molecular dynamics models ; (g) Definition of the number of monomers and the crosslinks tying them for each modeled nuclear components ; (h) 3D representations of all the monomers and their cross-links ; (i) Force/strain relations established after molecular dynamics simulations (Adapted from [149]).

the periphery of the nuclear membrane. It also allows the depiction of complex reactions that would be wiped off by overwhelmingly simplified models. For instance, some molecular dynamics modelizations ascribed some precise interaction properties at the polymeric levels, and the overall assembly into the precise lamina and chromatic architecture resulted in strain-stiffening behavior that was not predicted beforehand. Finally, contrary to one-dimensional models, the heterogeneity of each substructure is given with the greatest details. But we may likewise understand the chief limitation of this fantastical modeling. First, the computation power. It is in this case exacting, to the point of being scarcely applicable in many modestly endowed biological laboratories around the world. Also, the idea of modeling exactly the forces behind molecules is misleading. Often the model has to recourse to coarse-graining simplifications, meaning regrouping smaller polymeric components into larger entities. In this downscaling process, accuracy is lost, to the point of questioning the computational necessity of such undertaking. Finally, the greatest strength of molecular dymamics modelisation, namely its ability to let rise microscopic level phenomena from polymeric-level interactions, also hide a drawback, namely that of impeaching the analyst to ascribe precise overall response that are well attested for nuclear components.

Continuum mechanics models. We believe that continuum mechanics models are best adapted for the analysis of the mechanical properties in microscopy imaging [151]. Their chief assumption is that the nuclear domain is continuous. Which is not true, but allowed for two reasons. First, as we will see in the next section, fluorescence microscopy techniques operate at limited resolution. This smoothes out the irregularity of the lamina meshwork, as well as of the fractal-like configuration of the chromatin. Regarding this last point, we saw that the interchromatin space is filled with numerous nuclear bodies, to the point of making the idea of a nucleoskeleton highly unlikely (actin filaments cannot freely move in this jammed space). This further supports the possibility of representing the nuclear interior as a continuous domain. Once this assumption admitted, continuum mechanics models ascribe precise partial differential equations to the physical values of interest. Once solved, these yield space- and time-dependent estimations of the displacement, strain, stress, forces, and the stiffness and viscosity parameters. We refrain for telling more here, since this topic will be amply explored in the last section of this chapter.

I.2 Measuring mechanical properties

I.2.1 Imaging methods

It is not our design to provide a complete overview of current microscopy techniques in mechanobiology. Rather we wish to lay out the underlying physical principles of two techniques of interest, fluorescence microscopy [152] and Brillouin microscopy [153], without dwelling on the various technical configurations. We declare right here that of the two, we will exclusively use the first one. The second operates under very different physical configurations, and is outright incompatible with the proposed techniques in the following chapters. However we cannot deny it enjoys a soaring popularity amid the mechanobiological community [154], and we feel bound to discuss its promises as well as appearing limitations in regard of what we are to propose. Brightfield microscopy on the other hand, with its many phase shifting variants [155], has proven sufficiently precise to sharply delineate the boundary of the cell's nucleus. As such it is a precious tool for many image computational topics related to the biological motion of the cell, from segmentation [156] to cell tracking [157]. The reader will easily perceive that it might very well be applied to several of the different probing configurations exposed in the next section. However we are entitled to doubt its texture accuracy in the nuclear domain. The reasons are long known and well established, and can be summarised by the low contrast, out-of-focus blurring, and magnification limitations [158]. We propose in the following chapters several frameworks to compute many physical quantities of interest (displacement, strain, stress, etc.) that are defined within the nuclear interior. All rely on the faithfulness of an optical flow technique of our own which, as it will be

explained, is very sensitive to texture accuracy. It is actually the only requirement we have regarding the microscope, and we justify how current fluorescent microscopy techniques are sufficient for our purpose. We refer to Annex A for further details.

I.2.2 Experimental settings

We review here several of the experimental settings used in the past to evaluate the mechanical properties of the cell's nucleus. All apply *in vitro* deformations and, despite their diversity, all rely on the same principles. A known force is applied, often through a probing tool, to a certain part of the nuclear surface or interior. A single proxy value of interest is defined to evaluate the induced deformation. This deformation value is computed through simple shape descriptors derived from the images of the deformation –unlike for our method, a simple brightfield imaging modality may suffice here. This proxy value is linked through a 1D simplified relation to the applied forces to derive mechanical quantities of importance, such as the stiffness of the nucleus. The reader will easaily recognize that these methods all range in the categories of 1D mechanical models, previously introduced. We follow the presentation of [159] who, in our opinion, provided a complete taxonomy of currently applied methods.

Probing methods (see Figure I.6). These apply a known force to a limited portion of the nuclear boundary. The faithfulness of these methods rely on the accuracy in measurements of the applied forces. Their main drawbacks regard the precise measurement of the poked surface, and the risk of drilling through the nuclear interior (recall that a certain force quantity applied to a limited surface results in high pressure). In *Atomic Force Microscope*, a probing tip of precisely known dimension is attached to a cantilever, sturdily hafted to a xyz drive, and eventually to a piezoelectric element for periodic forces [160]. Above the cantilever is a detector that measures the cantilever deflection over time. Several configurations for the detector exist, some based on interferometry, other optical levers or even STM-based detectors. In the beam-deflection method for instance, a superluminescent diode shines a laser light over the back of the cantilever, which deflects it according to different angles when it bends. These deflections are recorded by two quadrant photodiodes. This setting is now extremely precise, and accounts for angstrom-scale cantilever deflections. Because the geometry of the probe is very well characterised, the applied force might be directly related to the bending of the cantilever. In some simple instances, the probe might be approximated by a spring of constant k, determined by the following relation:

$$k = \frac{Ewt^3}{4L^3},$$

where E is the Young's modulus of the cantilever material, w the cantilever width, t the cantilever thickness, and L the cantilever length. Others try to improve the accuracy of this estimate by taking into account the precise geometry of the tip. Overall, current atomic force microscopy techniques can faithfully measure forces of the range of tens of pN to hundreds of nN. The deformation is measured by the recorded probing of the cantilever tip on the nucleus. Reportedly, the local surface curvature, the perimeter differences, as well as the surface differences, are used as proxy for the induced strain. The stretch modulus γ, for instance, is recovered through these two simple one dimensional formulas:

$$\begin{aligned} \nabla \cdot \mathbf{S} + \mathbf{F}_V &= 0 \\ \mathbf{S} \cdot \mathbf{n} &= -\frac{\gamma}{A}\mathbf{u}, \end{aligned} \tag{I.1}$$

where F is the measured volume force, $\mathbf{S}$ is the stress tensor, $\mathbf{n}$ the vector normal to the surface, A is the contact surface, and u is the displacement field, determined through geometrical approximation of the aforementioned strain. Despite its accuracy in the force measurement system, atomic force microscopy cannot apply stretching forces, but only compressive forces. Furthermore, it is shown, in some instances where the applied force is high, that the deformation of the gel on which the cell is laid down can overestimate the induced mechanical deformations. The first of these drawbacks is tackled by *micromanipulation* experiments [161]. With these, a single (or a pair) of pipette is attached to one end of the material

	Experimental setting	Strain definition	Limitations
AFM	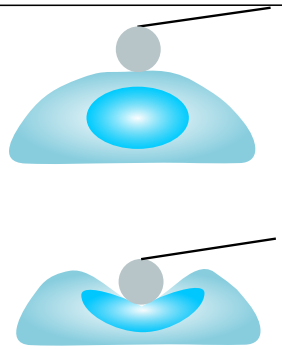	- Local curvature - Perimeter variation - Surface variation	- Applied surface measurement - High pressure, rupture risk - Only compressive forces
Micromanipulation	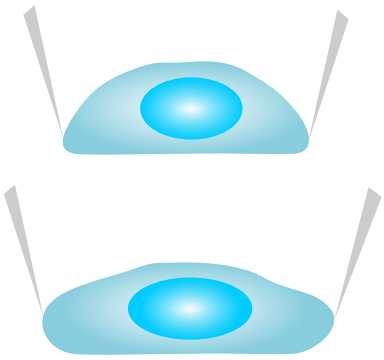	- Diameter variation - Height variation - Surface variation	- Large force applications - Complex pipette modelisation
Tweezers	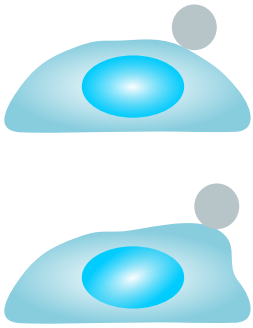	- Diameter variation - Height variation - Surface variation	- Large local force applications - Complex retrieval of the exact forces

Figure I.6: Strain definitions and limitations of probing methods for measuring mechanical properties of the nucleus.

of interest. Nowadays sturdy mechanical settings allow a very firm maintenance of the micropipette through micropipette holders. These allow programs of movement in the micrometer scales, and are generally paired with a microforce sensor that transforms the movement in a precise voltage, which is then converted to force. Some complex relationships entangle the geometry of the pipette (pipette cunning for the opening size), its filling (with biochemicals at both ends of the pipette to allow proper attachment), and loading. Since the applied force is mechanically determined at the onset of the system, the measurements are generally very reliable. Like in atomic force microscopy, the measurements of the deformation comes from fluorescence imaging of the material, and requires likewise shape descriptors of interest to fill a simplistic one dimensional model. Generally speaking, both methods require large deformation values to be properly accounted to, which may cause problems since, as we outlined in the part of this chapter regarding mechanotransduction, the chromatin conformation may change through sustained high value of forces. It is with this issue in mind that some came with the idea of developing

optical and magnetic tweezers to apply small-scale forces. They coat polystyrene beads of variable size with specific membrane proteins to attach them at the surface of the nucleus – we say that the bead is "trapped". Like for atomic force microscopy, a quadrant detector photodiode detector is carefully placed to measure bead thermal fluctuations. These are in turn analyzed to compute the trap stiffness and the position detector's conversion factor. Note that some debates exist about the proper determination of these two in biological materials, since studies have consistently proven that these might depend as well of the viscoelastic properties of the nucleus as well. In some instances, it might be relevant to take into account the force ruling the molecular bond between the bead and the nucleus. For instance, the rupture force F_r may be retrieved through:

$$F_r(r) = \frac{k_B T}{x_\beta} \ln\left(\frac{r x_\beta}{k^0_{\text{off}} k_B T}\right),$$

where k^0_{off} is the unloaded dissociation rate, k_B is Boltzmann's constant, T is the absolute temperature, x_β is the distance between the bound state and transition state along the reaction coordinate.

Once known, a strong laser beam with a very high electric field is applied to the studded beads, which results in a known force determined by the following relation:

$$F = -k_{\text{trap}} \delta x$$

where δx is the induced displacement and k_{trap} the trap stiffness. The measured force is of the order of nN, and mechanical figures of interest can be retrieved through the simplified formula. For instance, in the case of the Young's modulus E:

$$E = \frac{3(1-\nu^2)}{4\sqrt{R\delta x}} \frac{dF}{d\delta x}$$

where ν is Poisson's ratio and R the radius of the beam. Magnetic tweezers rely on the sample principles, except that they control directly the applied magnetic field, allowing for more complex movements such as the rotation of the beads. While locally applied large deformations might impair the nucleus, one may consider to apply larger deformations to a greater surface of boundary. This can achieved with *confinement-based methods* (see Figure I.7). Take for instance *micropipette aspiration* methods [162]. Like micromanipulation experiments, they attach the bounds of an open pipette with precisely determined geometry to the surface of the nucleus. This time, the pipette is not filled, but hollow. A suction pressure (typically of the order of tens of N) aspires the nuclear material within the interior of the pipette, until an equilibrium is found. Three regimes may qualify this equilibrium: when the length of the protrusion of the nucleus is less than the radius of the pipette, when it is equal, and when it is superior. The forces applied at the surface of the nuclear boundary is derived according to precise mechanical models we ascribe to the nucleus. When applied for the cytoplasm, for instance, a liquid drop model is admitted, for which the law of Laplace provides a convenient characterisation of the pressure:

$$\Delta P = 2N\left(\frac{1}{R_{\text{pro}}} - \frac{1}{R_{\text{cell}}}\right),$$

where ΔP is the applied pressure difference, N the surface tension, R_{pro} and R_{cell} the radii of the cell and the protrusion respectively. All these quantities are thoroughly recorded with phase-contrast bright-field microsocpy techniques, which are known to capture neat boundaries, despite their poor internal texture rendering. Since the precise geometrical description of the nucleus is very simple (an ellipsoïd with precise surface contact), the whole setting might be represented with finite element methods to allow proper continuous computation of the nucleus. Although this mix has been applied in the past, we feel cautious to apply simplistic geometric modeling of the nucleus (which can be actually quite complex) with this very precise modeling tools. We will see later that it can be better paired with image processing frameworks. Like the previously mentioned methods, micropipette aspiration probes

	Experimental setting	Strain definition	Limitations
Micropipette aspiration	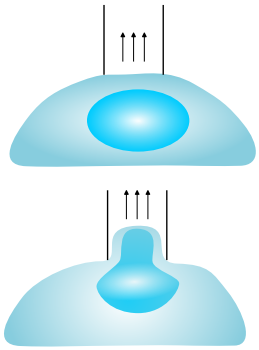	- Aspired length - Radius variations	- Applies only to circular or ellipsoid nucleus - Pipette diameter depends on nuclear size - Single nucleus
Plate compression	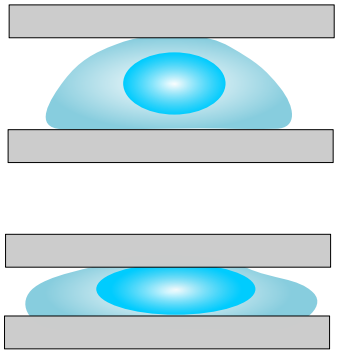	- Minimal height - Plate distances - Minimal surface	- Large force applications - Parallelizable, but doesn't distinguish deformation of each nuclei
Confined migration	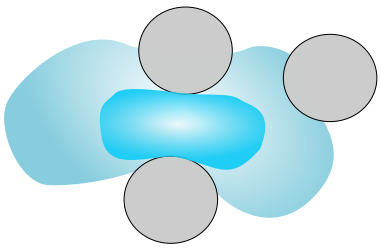	- Local curvature - Perimeter variation - Surface variation	- Cannot isolate nucleus - Compressive forces only - Applied force hard to determine

Figure I.7: Strain definitions and limitations of confinement-based methods for measuring mechanical properties of the nucleus

.

one nucleus at a time, and it can be preferred, for statistical conveniences, to apply a known force to several individuals of interest. *Plate compression* experiments seem like the easiest of the alternatives [163]. These consist of two plates controlled by a compressive setup that allows micrometer wide space between them. Cells' are first isolated and cultured up until they reach a desired state of growth, for instance within a stainless steel pressure vessel, then placed in suspension within a buffer solution to maintain their viability. Because the plates are generally large, these can squeeze entire monolayers of cell at once. They may be coated with binding proteins, often found in the extracellular matrix, such as fibronectin, collagen or laminin, to allow proper fixing with the plates. In this regard, the good execution of the suspension step after the cell culture is crucial to maintain good adhesion properties – sometimes, a certain amount of incubation time may be observed so that proper adhesion has time to form. They afterwards draw to one another, squeezing the nuclei up until a desired deformation. This deformation,

like for the previously mentioned techniques, is generally monitored through correlative fluorescence microscopy. Some strain proxies include the height of the resulting nuclei or simply the distance between two plates. Others embed the nuclei with fiducial markers to propose a particle-like tracking of each nucleus. The applied stress is easily retrieved as a measure of the mechanical forces over the known plate area. Other configurations with periodic excitements are also found in the literature. Because they allow great parallelization, and because they are simple to use, plate compression methods offer a handy alternative to measure overall induced deformations to multiple nuclei, but they remain subpar for the measurement of individual nuclei deformation. As of such they prove to be a tool of choice for statistical studies of the deformations of whole populations of nuclei. One may complain that the presented methods require complex *in vitro* settings that poorly mimick *in vivo* deformation. Biologists concerned with the study of migration of cells had this issue in mind when they conceived several of the many confinement based methods of deformation. In a nutshell, these consist in replicating the extracellular environment, with its many tight interstitial spaces, and to monitor how cells and their nuclei navigate through them. *Microfluidic devices* are issued through the creation of a three-dimensional constricting space, of polydimethylsiloxane (PDMS) material for instance [164]. A technique of choice for generating the spacing is using a silicon wafer through photolithography. The PDMS replicate is then cut into several "chips" which usually contain several of the microfluidic devices. These microfluidic devices respect certain regularly spaced geometries, allegedly representing the varying tight holes found in the ECM. Before seeding, the devices are cleansed, then punctured through biopsy punches to create the holes that will welcome the cell. The whole device is rinsed, dried with pressurized air, cleaned with a plasma cleaner, seared with a hot plate. Then only it may be coated, again with fibronectin or collagen, and receive the suspended cells by a pipette. The coating respect a peculiar process to allow a chemoattracting gradient that will spur the various nuclei throughout the maze. The material should not allow deflection, and can be sturdily placed into a brightfield microscope incubation chamber. The camera may then monitor several types of displacements per devices.

The *Boyden chamber assay* works in a similar way, but its architecture is different [165]. Instead of a regularly spaced maze through which the nuclei will have to pass through, it consists of two compartments, or chambers, separated by a porous membrane, the mechanical properties of which is precisely determined. The cells are first placed in the top chamber, and a chemotaxis stimulus is likewise added to the bottom chamber, and the whole ensuing migration is orthogonally captured with a fluorescent microscope. Some even employ *3D collagen matrices* to create the interstices of their devices [166]. These are generated by the *in vitro* assembly of selected collagen monomers, and are supposedly to be less regular than their previously mentioned counterparts. In all cases, the deformations incurred by migration is defined through image processing shape descriptors, for instance the local curvature or the variation in the nuclear perimeter. It is through these experiments that the nucleus really appeared as a rate limiting factor during cellular movement. Unlike the previous methods, however, constriction assays cannot apply on isolated nuclei (a nucleus moves along its cytoplasm) to the point of making it sometimes difficult to measure the relevant part of the deformation that can be ascribed to the overall cell or to the nuclear domain only. Also, these assays apply compressive forces only, and not extension. This last point rises from the immobility of the environment, and it can be overcome by moving the environment itself (see Figure I.8). *Osmotic shock* leverages the Boyle Van't Hoff relation, which states that the cell volume is inversely proportional to osmolarity, or the concentration of solute particles in a solution [167]. By downregulating the osmolarity of the extracellular medium, the cell naturally expands through the spanning pressure gradients. Because the concentration of the surrounding media is precisely known, Boyle Van't Hoff law offers a nonlinear relation between the volume of the nucleus and the boundary pressure. The volume of the nucleus is tracked through confocal spinning disk fluorescence microscopy techniques. The resulting pressure can be likewise inputted into an inversion scheme to yield the stiffness of the lamina meshwork at the boundary of the nucleus. Note that the osmotic concentration can be modulated in both ways (hypo-osmotic and hyper-osmotic shocks), and that

	Experimental setting	Strain definition	Limitations
Environment	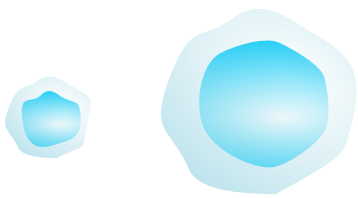	- Perimeter variations - Surface variations - Volume variations	- Unanticipated physiological reaction to osmotic changes - Nucleus/cytoplasm separation inaccurate
Substrate strain	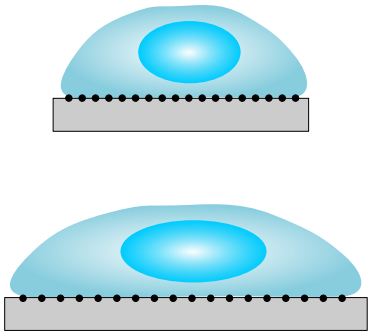	- Minimal height - Diameter variation - Substrate strain	- Uniaxial strain - Nucleus/cytoplasm separation inaccurate
Suspension	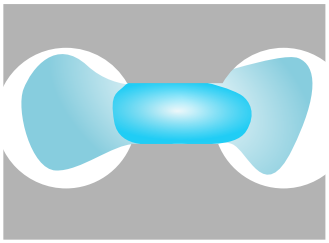	- Time to pass	- Only hydrostatic forces - Inaccurate parallelization

Figure I.8: Strain definitions and limitations of suspension-based methods for measuring mechanical properties of the nucleus

both stretching and shrinking of the nucleus may be precisely applied. These devices were for instance particularly useful when paired with micropipette aspiration settings to show the compressibility of the nucleus. However, in general, cells are exposed to stable osmotic environment, and modifying the concentration of solutes might distress its normal physiological reaction. Also, while the precise gradient of pressure might be accurately modeled, it is difficult to regulate the speed of extension, or shrinking, in these processes – making the viscous parts of the deformation sometimes more prominent than the elastic one. Taking the volume as an input is generally simplistic, and it is very well probable that shape descriptors are required to compute the proper osmotic reaction of the cell to deformations. Finally, as underlined in methods with constrictive migration, it is difficult to separate the deformations pertaining precisely to the nucleus rather than the cytoplasm alone. Another way to change the environment to induce deformation is to alter its stiffness. *Substrate alterations* can be made in two ways: either by changing its topography, or by changing its composition [168]. This has the advantage of showing

how cells and their nuclei react to the restructuring of its environment. Pre-polymerized polyacrylamide (PAA) hydrogels with precise stiffness may be manufactured and coated to receive certain cell lines. Gradually varying amount of these gels are then cast on a flat coverslip. The cell lines are introduced within a chamber containing these gels with different stiffnesses, and their shapes are monitored through brightfield microscopy. The stiffness of the surrounding material generally incurs more or less greater deformation within the cell and its nucleus through the binding forces of the fibronectin. The same system might be adapted to alter the precise topography of the gel, or to lay precise coating to favor certain paths during migration. In both cases, precise deformation schemes might be understood through the use of classical shape descriptors. However, one has to consider that the interaction between a cell and its surrounding matrix is all but simple. Often, the cell deforms as much its environment as it deforms itself, and the simplistic relationship binding the first to the second is more complicated than it looks. Also, it is troublesome to mend this inconveniency through a simple upgrade of the theoretical formula, as the strain within the gel is not always precisely monitored – we may mention the settings of traction force microscopy, which studs the gel with fluorescently labeled beads, to track the induced displacement through known image-based techniques, as an exception to this rule. Furthermore, in this context, the engendered deformation is most of the time anisotropic, which might trigger specific reactions of the mechanical properties of the cytoskeleton, as we will see in the next section. Finally, cells are known to adapt to their environment, and this setting does not allow long stretches of deformation, unless we wish to witness changes of physiological modalities. An easier view of tackling this problem might be to induce *substrate stretch* [169]. The deformations are most of the time isotropic, and sometimes reduce to a simple ax. Cells are grown on elastomeric sheets to form monolayers. These cells are then laid down on a rectangular transparent silicone channel tethered at both ends to piezoelectric translators. The whole system is inputted in the chamber of a confocal microscope which records both the movement of the cell and, optionally, the deformation of the environment. Because the Young's modulus of the plate is exactly known, an homogeneous approximation of the applied stress might be inferred. Again, the strain is defined through variations of the nuclear shape descriptors. Recent assays also incorporate the use of circular distortions, and others account for periodic excitation, although the relationship to the ensued nuclear deformation is more complicated to interpret. In any case, the deformations in theses settings is rather simplistic, and to complicate it, one may resort to the bending of micropillar arrays. These replace the substrate with microneedle-like posts. The geometry of the posts can be carefully engineered to allow various indentation within the cell and its nucleus. Some experiments solely monitor the bending of these posts through cellular interaction. Brightfield images of the bending catche the distance spanned by the stained end of each post. An undeformed grid marking the initial configuration of the tips is used as reference points, and the images are inputted to compute the new coordinates of each tip after deformation. The difference in coordinates are then simply multiplied by the values of the spring constants to obtain the applied forces. It is in this manner possible to reconstitute applied forces to the resolution of the posts throughout the cell adhesion surface. Once a position of equilibrium is reached, the biologist can deform the nucleus by opposing a known magnetic field to the posts. Because the Maxwell laws are precisely known, the applied magnetic field can be easily converted into an applied force field. The resulting displacement of the posts can this time be used as a resistance to external stress, and some simplified version of the Young's modulus at the boundary can be computed. However, the reader will easily perceive that despite the astuteness of the device, the deformations merely apply at the cell's surface, and to account for nuclear deformations would require large forces transmitted through mechanotransduction. Because the forces would be indirect, it is dubious to relate the applied magnetic field to any deformation within the nucleus, yet alone to the computation of any nuclear stiffness. However, newly developed assays seem to adapt to the specific domain of the nucleus, and look very promising in this regard. There remains to develop the computational powers to measure incurred deformation and the stress field, which we will present in the remaining of this thesis. The final category of deformation methods are what we may term suspension methods. *Confined cell perfusion* stages the fabrication of microfluidic devices consisting of several chambers connected through single tight connection [170].

Unlike previous devices, the chambers contain a select fluid the flow of which can be controlled. Once elaborated, the cell, or a small cluster of cells, is placed into a determinate chamber, again using adhesive patterns or, in some cases, cell traps. A syringe pump, or any pressure-driven system, suck the fluid from one chamber to the next, and the cell along with it. Here, the strain is defined as the time it gets for a cell to pass through a specific hole of known dimension. Because the nucleus is the largest and stiffest organelle, the overall deformation of the cell can be assimilated to the sole deformation of the nucleus. The whole device can be easily inputted into a microscope chamber, allowing the leverage of shape descriptors of the nucleus as well. Like the previously mentioned tweezers, *optical stretching* methods apply an intensive laser light on the cell's surface [171]. Because of the difference in the refractive index of the cell and its surrounding material, a gradient of optical forces is generated that pushes the cell toward the center of the beam. The applied force is measured by computation of the displacements of studded beans within the nuclear interior. However, the applied stress remains hydrostatic in this setting, and to compute deviatoric deformation, one may resort to *hydrodynamic shearing* [172]. The setting ressembles that of the confined cell perfusion, but the microchannels are this time arranged to allow flow parallel to the boundary of the cytoplasm. Through similar pumping techniques, the fluid strokes the surface of the cytoplas, or the isolated nucleus, generating a known force obtained through the vorticity of its displacement field.

I.2.3 Drawbacks of existing methods

We hope that, by the end of this shot overview, the reader will have an idea of the variety of experimental setups that apply and measure deformations within the nucleus. Despite their diversity, we may put forth the following drawbacks of the currently applied settings:

- *Simplistic values of the strain*. Because all the proposed models are 1D models, the definition of the strain is very simplistic. Often times, biologists struggle to extend this 1D definition of the strain to a continuum mechanics one. This can only be done by sacrificing either the deformation procedure, or the theoretical laws that relates the deformation to the applied forces. We argue that only a continuum mechanics model can bypass these issues. More precisely, our method should be an image-based one. The deformation should be likewise captures by 2D or 3D videos of a cell's nucleus, and the displacement field computed at each point within the nuclear domain. It is only when we have obtained this displacement field that we can derive further measures of the strain tensor field, which can be inputted to compute mechanical values of interest. As the next section will prove, the required displacement field has to follow some precise regularity properties dictated by the architecture of the cell's nucleus as described previously.

- In vitro *deformation*. Regardless of the astuteness of some of the recently engineered migration devices, the deformations procedure remain simplistic in nature. This is due mainly to the previously made point: since the biologists may only rely on debased versions of the strain tensor, they have to simplify the distortion configuration to fit a well-grounded physical model. For real migration for instance, the intersticial holes vary a lot in size, and are inhomogeneously dispatched within the extracellular matrix. There seems to be no shortcuts to it: if one wants to understand *in vivo* deformations, one would ultimately need to compute the deformations of a nucleus through imaging of *in vivo* deformations, and not realistic-looking *in vitro* ones.

- *Large deformations*. This does not concern tweezer methods. But for the rest, it appears that, to set a visible distortion of the nucleus, one has to apply considerable stress. If applied for a long time, this might change the chromosomal configuration of the nucleus, as laid out in the previous section. On the other hand, the small deformation regime of the nucleus bears some significant physiological interest.

We now assume the prerequisites of continuum mechanics for our nucleus. We will show in the next chapter the exact partial differential equations that it follows, as well as some necessary regularity properties of the solutions. Chapter 3 will show how we may compute the displacement field at each point of the nucleus with fluorescence microscopy images.

Chapter II

Modelization of the nucleus

This chapter states in mathematical terms the problems of nuclear mechanics. We establish the equations of nonlinear elasticity, then simplify them into the equations of isotropic linear elasticity, which applies under small deformations and quasi static loading. We show how the specific architecture of the nucleus implies necessary regularity properties of the involved physical quantities. With these constraints in mind, we state the three problems that our image processing tools in the next two chapters will have to solve. The chapter ends with a framework to create synthetic images of deforming nuclei with known underlying elastic parameters.

II.1 Elasticity of the nucleus

II.1.1 Equations of linear elasticity

We heretofore establish the partial differential equations ruling the nuclear domain. Our goal is to extend the 1D relations of linear elasticity used in most biological settings to 2D and 3D deformations (see Figure II.1). We follow the presentation of Ciarlet in [173], synthesized in [174]. We first derive the equations of equilibrium from the stress principle of Euler and Cauchy, then the constitutive equations from the axiom of material frame-indifference. The equations of linear elasticity are then obtained by adding proper boundary conditions to the two. We refer to the very commendable works of [175], [176] and [177] for the proofs of the main theorems. Other approaches are found likewise to establish the same results. For an energy-based one, see [178].

II.1.1.1 Equations of equilibrium

We suppose the nucleus fills a bounded domain $\Omega \subset \mathbb{R}^3$, named the *reference configuration*. When loads are applied to its boundary and to its interior, deformations occur, until it reaches static equilibrium. The nucleus then occupies another domain called the *deformed configuration* or *placement*. We define it as the image Ω_d of a vector valued function $\Phi : \Omega \to \mathbb{R}^3$ termed *deformation*. To single out the number of placement candidates, we impose Φ to be bijective and differentiable – actually, we may even content ourselves with the sole injective and orientation preserving properties. The displacement field is the difference between the deformed configuration and the reference configuration, i.e. $\mathbf{u} := \Phi - \mathbf{Id}$, where $\mathbf{Id}$ is the identity map. Note that the displacement field is *not* what we call deformation. A falling coin or a spinning ball might register a great deal of displacement, without deforming the least. These are examples of what we call *rigid motion*.

We suppose that volumetric forces, such as gravity, are non-existent, and note $\mathbf{g_d} : \Gamma_{d,t} \to \mathbb{R}^3$ the boundary forces, where $\Gamma_{d,t}$ is a subset of the boundary Γ_d of the deformed configuration. The stress principle of Euler and Cauchy states that the forces applied on a linear elastic body are met at every

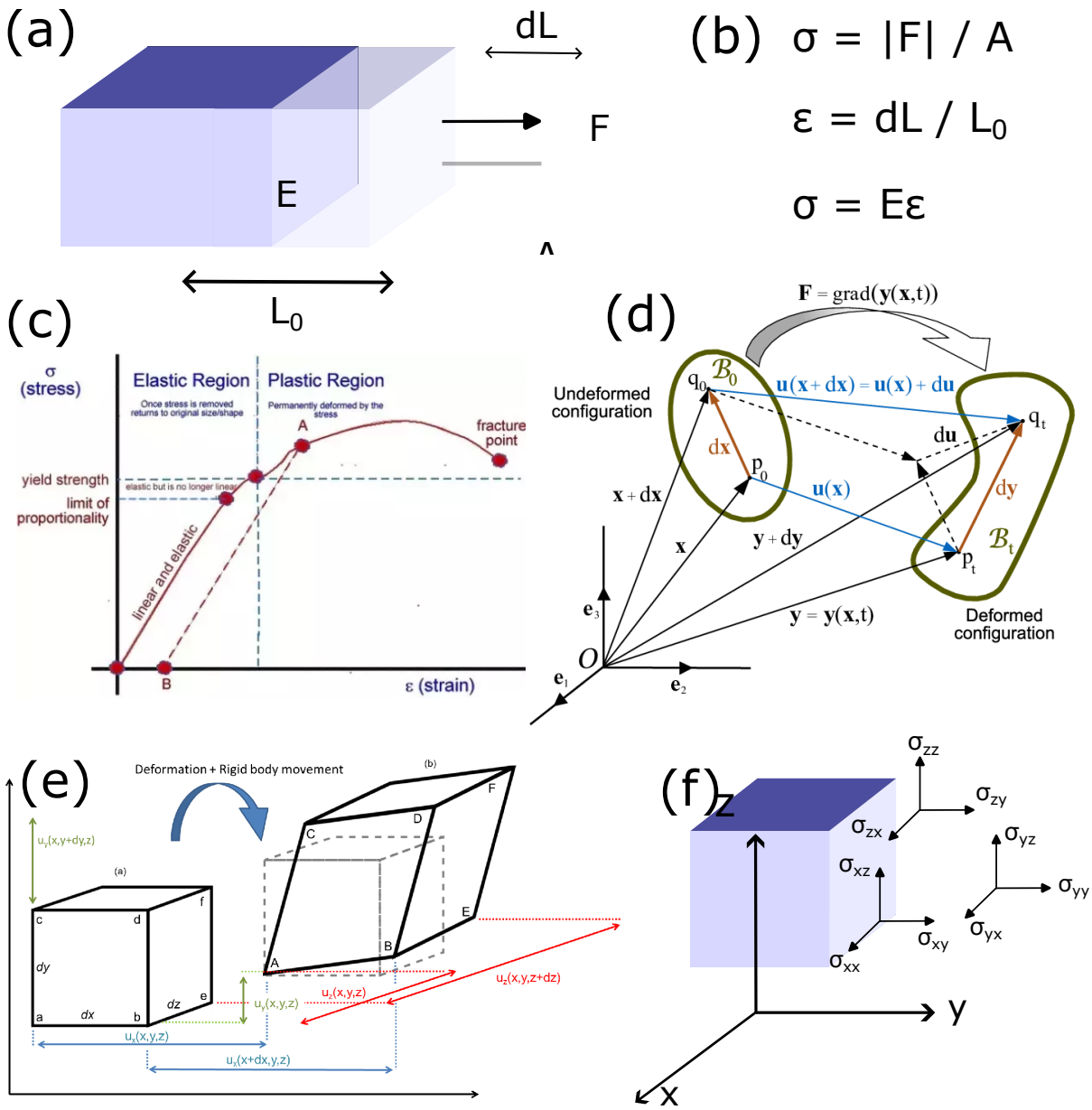

Figure II.1: General principles of isotropic linear elastic materials (a) 1D or axial deformations of an elastic body. The Young's modulus E defines the stiffness of the material, an homogeneous force F stretches it to the right, inducing an elongation dL added to its original length L_0 ; (b) In 1D, the sress tensor σ divides the applied force with the surface A on which this force applies, the strain ϵ is the ratio of deformation over the initial length, and both these 1D quantities are linearly linked by the Young's modulus (in linear elasticity) ; (c) A linear elastic body is only linear for small deformations. Beyond a certain amount of force, it enters a non-linear regime, and after a plastic deformation regime from which it will not find its initial shape, even after the removal of the force ; (d) in 3D, the dispalcement field is defined by mapping each point from an undeformed configuration to a deformed configuration which are the domains the elastic body fills during static equilibrium ; (e) all linear elastic movement is a composition of rigid body and deformation, where this last notion quantifies how much two points of the body draws or stretches from one another ; (f) in 3D, the stress and strain tensors contains nine components, which quantifies the force in each direction of a small cubic volume centered around a certain point.

point by a counteracting force, equal in magnitude and opposite in direction. It is the elastic equivalent of the newtonian mechanical equilibrium.

Theorem II.1.1 (Stress principle of Euler and Cauchy)**.** . *The body Ω_d is in equilibrium if there exists a vector field $\mathbf{t} : \Omega_d \times S^2 \to \mathbb{R}^3$ such that, for all domains $A_d \subset \Omega_d$,*

$$\begin{aligned} \int_{\partial A_d} \mathbf{t}(x_d, \mathbf{n}(x_d)) da_d &= \mathbf{0}, \\ \int_{\partial A_d} x_d \wedge \mathbf{t}(x_d, \mathbf{n}(x_d)) da_d &= \mathbf{0}, \\ \mathbf{t}(x_d, \mathbf{n}(x_d)) &= \mathbf{g_d}(x_d), \quad \text{for } \partial\Omega_d\text{-almost all } x_d \in \partial A_d \cap \Gamma_d \end{aligned} \tag{II.1}$$

where $\mathbf{n}(x_d)$ is the exterior normal unit vector at x_d. The vector field $\mathbf{t}$ is called the stress function.

Cauchy provides a linearity theorem which states that the stress function can be further decomposed into:

$$\mathbf{t}(x_d, \mathbf{n}(x_d)) = \mathbf{T_d}(x_d)\mathbf{n}(x_d), \tag{II.2}$$

for all point $x_d \in \Omega$, where $\mathbf{T_d} : \Omega_d \to \mathbb{R}^{3\times 3}$ is a $\mathcal{C}^1$ matrix field. Inputting (II.2) into (II.1), the Stokes' formula yield the following equations of equilibrium in the deformed configuration.

Theorem II.1.2 (Equations of equilibrium in the deformed configuration)**.** *The linearized stress field $\mathbf{T_d}$ follows these equations:*

$$\begin{aligned} -\mathbf{div}\, \mathbf{T_d}(x_d) &= \mathbf{0}, \forall\, x_d \in \Omega_d \\ \mathbf{T_d}(x_d)\mathbf{n}(x_d) &= \mathbf{g_d}(x_d), \forall\, x_d \in \Gamma_{d,t} \\ \mathbf{T_d}(x_d) &\in \mathbb{S}^3, \forall\, x_d \in \Omega_d. \end{aligned} \tag{II.3}$$

Computational imaging methods relying on a Lagrangian point of view can easily rely on this formulation for their purpose. But we will advocate in the following chapter for Eulerian methods that could not operate on the deformed configuration. Rather they constantly refer their physical quantities to a grid of interest (in our case the first image of a video). This is the reason why we reframe these equations in the reference configuration.

Denote x the antecedent of x_d through Φ. This change of variables dictates us the expression of the unit surface area and the boundary forces in the reference configuration:

$$\begin{aligned} \mathbf{n_d}(x_d) da_d &= \det(\nabla\Phi(x))\nabla\Phi(x)^{-T}\mathbf{n}(x) da \\ \mathbf{g_d}(x_d) da_d &= \mathbf{g}(x) da \end{aligned} \tag{II.4}$$

where the letters without subscripts designate their subscripted counterparts in the reference configuration. Substituting the first of this relation into equation (II.1), we may naturally come to the following definition.

Definition II.1.1 (First Piola-Kirchhoff stress tensor)**.** *We define the first Piola-Kirchhoff stress tensor field $\mathbf{T}$ for all $x \in \Omega$ by:*

$$\mathbf{T}(x) := \mathbf{T_d}(\Phi(x)) \det(\nabla\Phi(x))\nabla\Phi(x)^{-T} \tag{II.5}$$

Unlike the linearized stress field in the deformed configuration, this stress tensor is not symmetric. This is why we introduce the following definition.

Definition II.1.2 (Second Piola-Kirchhoff stress tensor)**.** *We define the second Piola-Kirchhoff stress tensor field* $\mathbf{\Sigma}$ *for all* $x \in \Omega$ *by:*

$$\mathbf{\Sigma}(x) := \nabla\Phi(x)^{-1}T(x) \tag{II.6}$$

This second tensor field is symmetric. When inputted in the equations of equilibrium in the deformed configuration, we get the equations of equilibrium in the reference configuration.

Theorem II.1.3 (Equations of equilibrium in the reference configuration)**.** *The second Piola-Kirchhoff stress tensor respects the following equations:*

$$\begin{aligned} \mathbf{div}\,(\nabla\Phi(x)\Sigma(x)) &= \mathbf{0}, \forall\, x \in \Omega \\ (\nabla\Phi(x)\Sigma(x))\mathbf{n}(x) &= g(x), \forall\, x \in \Gamma_t \end{aligned} \tag{II.7}$$

These equations, as they stand, present two unknowns, Φ and Σ. To be solvable, they need first to be supplied with additional equations relating these fields. The constitutive equations of elasticity will serve that purpose.

II.1.1.2 Constitutive equations

The previous equations were derived from the equilibrium of the laws of motion. Up until now, the specific material characteristic of the domain were not taken into account. Here we will show that the previously established stress tensor that the elastic body opposes to boundary forces depends on a *strain* tensor field that quantifies material deformation, and on the Lamé parameters that quantify its stiffness and compressibility properties.

The theory of continuum mechanics rely on an axiom named the *principle of determinism for the stress*, which states that the stress of a body is determined by the history of the motion of that body. We defined in the previous section elastic materials as those objects that resist forces that are applied to it, and that resume their shape once the same force is removed. In this light, the stress of an elastic material depends solely on its deformation gradient and the point on which it is applied, which translates into the following mathematical definition.

Definition II.1.3 (Elastic material)**.** *We say that a material is elastic if it observes either of the following equivalent properties:*

- *There exists a function* $\mathbf{T}^* : \overline{\Omega} \times \mathbb{M}^3_+ \to \mathbb{M}^3$ *defined for all* $x \in \Omega$ *as* $\mathbf{T}(x) = \mathbf{T}^*(x, \nabla\Phi(x))$.
- *There exists a function* $\mathbf{\Sigma}^* : \overline{\Omega} \times \mathbb{M}^3_+ \to \mathbb{S}^3$ *defined for all* $x \in \Omega$ *as* $\mathbf{\Sigma}(x) = \mathbf{\Sigma}^*(x, \nabla\Phi(x))$.

Functions $\mathbf{T}^*$ and $\mathbf{\Sigma}^*$ are called *response functions*. Note that the second definition is more restrictive as it does require symmetry of the image matrix. This symmetry comes in help when we adjoin it another important axiom of continuum physics, the axiom of material frame-indifference. This axiom states that any observable quantity is stable against any changes in the orthogonal basis in which it is expressed. To further exploit this property, let us first remind the reader of polar decomposition.

Theorem II.1.4 (Polar decomposition)**.** *There exists, for any square invertible real matrix* $\mathbf{A}$*, a unique unitary matrix* $\mathbf{U}$ *such that* $\mathbf{A} = \mathbf{U}(\mathbf{A}\mathbf{A}^{\mathbf{T}})^{1/2}$.

Then, given any deformation gradient $\nabla\mathbf{\Phi}$, the response function $\mathbf{\Sigma}^*$ that follows the axiom of material frame-indifference observes the following restrictive property:

$$\mathbf{\Sigma}^*(x, \nabla\mathbf{\Phi}(x)) = \mathbf{\Sigma}^*(x, \mathbf{C}^{1/2}) \tag{II.8}$$

where $\mathbf{C}$ is the square of the semi-definite positive square root of $\nabla\mathbf{\Phi}$. This new matrix bears a name: the Cauchy-Green deformation tensor.

Definition II.1.4 (Cauchy-Green deformation tensor)**.** *The Cauchy-Green deformation tensor field is defined through the deformation gradient for all $x \in \Omega$ by $\mathbf{C}(x) = \nabla\mathbf{\Phi}^T(x)\nabla\mathbf{\Phi}(x)$.*

We derive from this tensors three invariant scalars that are independent of the elastic material intrinsic properties.

Definition II.1.5 (Principal invariants)**.** *Given a Cauchy-Green deformation tensor $\mathbf{C}$, the three principal invariants I_1, I_2, I_3 are defined for all $x \in \Omega$ by:*

- $I_1(x) = \text{tr } \mathbf{C}(x)$
- $I_2(x) = \text{tr } Cof\mathbf{C}(x)$
- $I_3(x) = \det \mathbf{C}$

One may keep in mind the following loose physical interpretation. The first invariant quantifies hydrostatic, meaning the volumetric, deformation of the material. The second relates to the deviatoric part of the deformation. The final invariant relates to the compressibility of the material: if close to one, it means the material conserves its volume, and is incompressible.

We will thereon consider the deformations to be "small", as we saw that greater deformations applied for a sufficiently long time corrupts the healthy layout of the mechanical properties of the nucleus. In this case, it is sometimes more convenient to express the Cauchy-Green tensor in terms of the displacement field $\mathbf{u}$, rather than with the deformation function.

Definition II.1.6 (Green-St Venant strain tensor)**.** *The Green-St Venant strain tensor $\mathbf{E}$ is the second-order tensor defined at every point $x \in \Omega$ by:*

$$\mathbf{E}(x) = \frac{1}{2}(\nabla\mathbf{u}^T(x) + \nabla\mathbf{u}(x) + \nabla\mathbf{u}^T(x)\nabla\mathbf{u}(x))$$

The Cauchy-Green deformation tensor can be simply expressed at every point $x \in \Omega$ by:

$$\mathbf{C}(x) = \mathbb{1} + 2\mathbf{E}(x) \tag{II.9}$$

where $\mathbb{1}$ denotes the second-order identity tensor.

Besides, we will suppose that the cell's nucleus is isotropic, an hypothesis that applies for all the nuclei we will study. Note that this assumption may possibly need a reevaluation for striated muscle cells.

Definition II.1.7. *An elastic material is said to be isotropic if its response function is the same when the reference configuration is rotated by any orthogonal matrix.*

The isotropy of a material greatly simplifies the expression of its stress tensor. In a sense, it reduces its expression to a decomposition of its hydrostatic, deviatoric and compressibility parts. Rivlin and Ericksen proved this remarkable property in the following theorem which marshalls the previously defined principal invariants [179].

Theorem II.1.5 (Rivlin-Ericksen theorem)**.** *Denote $\mathbf{I}(x)$ for any $x \in \Omega$ the triplet of the principle invariants $(I_1(x), I_2(x), I_3(x))$. For any isotropic elastic material, there exist three real functions β_0, β_1, β_2 defined over $\Omega \times \mathbb{R}^3$ such that:*

$$\Sigma(x) = \beta_0(x, \mathbf{I}(x))\mathbb{1} + \beta_1(x, \mathbf{I}(x))\mathbf{C}(x) + \beta_2(x, \mathbf{I}(x))\mathbf{C}^2(x),$$

for all $x \in \Omega$

This theorem is valid for any deformation, and its converse is true. For small deformations, the three invariants can be simplified through Taylor expansions:

$$\begin{aligned} \mathrm{tr}\mathbf{C}(x) &= 3 + 2\mathrm{tr}\mathbf{E}(x), \\ \mathrm{tr}(\mathrm{Cof}\mathbf{C}(x)) &= 3 + 4\mathrm{tr}\mathbf{E}(x) + o(|\mathbf{E}(x)|) \\ \det\mathbf{C}(x) &= 1 + 2\mathrm{tr}\mathbf{E}(x) + o(|\mathbf{E}(x)|), \\ \mathbf{C}^2(x) &= 1 + 4\mathbf{E}(x) + o(|\mathbf{E}(x)|) \end{aligned} \tag{II.10}$$

for all $x \in \Omega$. When inputted in the previous relation, we get the following simplified theorem.

Theorem II.1.6 (Linearized Rivlin-Ericksen theorem)**.** *For an isotropic linear elastic material under small deformations, there exists two scalar functions λ and μ defined through the following relation:*

$$\mathbf{\Sigma}(x) = \mathbf{\Sigma}^*(x, \mathbb{1}) + \lambda(x)\mathrm{tr}\mathbf{E}(x)\mathbb{1} + 2\mu\mathbf{E}(x) + o(|\mathbf{E}(x)|)$$

for all $x \in \Omega$. The functions λ and μ are called the Lamé parameters

We will heretofore consider that the body is in a *natural state*, in which case the first term in the above equation vanishes. The ensuing linearity dependence is captured by the elasticity tensor.

Definition II.1.8 (Elasticity tensor)**.** *The fourth-order elasticity tensor $\mathcal{C}$ relates the Green-St Venant strain tensor to the stress for every $x \in \Omega$:*

$$\mathbf{\Sigma}(x) = \mathcal{C} \cdot \mathbf{E}(x) \tag{II.11}$$

where the dot product here applies between tensors of different ranks.

Definition II.1.9 (Homogeneity)**.** *We say that an isotropic linear elastic material is homogeneous if the Lamé parameters are constant over Ω.*

It is clear that a cell's nucleus cannot be considered in any sense as an homogeneous material. Instead, the Lamé parameters are expected to take very different values whenever they are evaluated on the lamin domain, heterochromatin domain, or euchromatin domain. On the other hand, the first Lamé parameter λ can very well represent the overall compressibility of the nucleus. Indeed, remark that when $\lambda(x) \to +\infty$ for any point in the domain, $\mathrm{tr}\mathbf{E}(x)$ necessarily tends to 0. In other words, the volume of the material remains invariant around that point. Instead of the Lamé parameters, some prefer the

Material	λ	μ
Steel	65 GPa	80 GPa
Glass	30 GPa	25 GPa
Rubber	10 MPa	1 MPa
Gelatin	40 kPa	35 kPa
Nucleus (overall)	200-1000 Pa	100 – 1000 Pa

Table II.1: Values of Lamé parameters of different materials.

equivalent definitions of the Young's modulus E, or stiffness, and Poisson's ratio ν, or compressibility, expressed for all $x \in \Omega$ through the following relations:

$$\begin{aligned} \lambda(x) &= \frac{\nu E(x)}{(1+\nu)(1-2\nu)}, \\ \mu(x) &= \frac{E(x)}{2(1+\nu)} \end{aligned} \tag{II.12}$$

Although there is no theoretical restrictions to prove it, several experiments consistently show the Lamé parameters to be positive. To give the reader a glimpse of its range, we consign here in Table II.1 a certain number of values of reference.

When under no external forces, the relationship between deformation and stress remains. Revisiting the previous decomposition in that light, we naturally come to the following constitutive equation.

Definition II.1.10 (Constitutive equation)**.** *The constitutive equation of an isotropic linear elasticy material is given for any $x \in \Omega$ by:*

$$\Sigma(x) = \lambda(x)\mathrm{tr}\mathbf{E}(x)\mathbb{1} + 2\mu\mathbf{E}(x).$$

This equation is likewise invertible:

$$\mathbf{E}(x) = \frac{1}{2\mu(x)}\mathbf{\Sigma}(x) - \frac{\nu}{E(x)}(\mathrm{tr}\mathbf{\Sigma}(x))\mathbb{1}$$

We now pair this equation along the equation of equilibrium with proper boundary conditions, then linearize them to get the equations ruling the nuclear domain.

II.1.1.3 Equations of linear elasticity

Denote $\Gamma_u = \partial\Omega - \Gamma_t$ the portion of the boundary that isn't subjected to any traction or compression forces. We suppose the nucleus is clamped on this part, i.e. its displacement field vanishes. Because the restriction directly affects the displacement field, we say that it is a *Dirichlet* type of boudary condition. Γ_t, which constrains the derivative of the displacement field, is called a *Neumann* type boundary condition. Keep in mind that one can easily extend the following results to non-zero boundary displacements $\mathbf{u_0}$ by substituting $\mathbf{u}$ with $\mathbf{u} - \mathbf{u_0}$.

Definition II.1.11 (Nonlinear equations of elasticity)**.** *Given an elastic body with response function $\mathbf{\Sigma}^*$, the nonlinear equations of elasticity are given by:*

$$\begin{aligned} \operatorname{div} \mathbf{T}(x) &= \mathbf{0}, \quad x \in \Omega, \\ \mathbf{\Phi}(x) &= x, \quad x \in \Gamma_0, \\ \mathbf{T}(x)\mathbf{n}(x) &= \mathbf{g}(x), \quad x \in \Gamma_1, \end{aligned} \tag{II.13}$$

where $\mathbf{T}(x) = \nabla\mathbf{\Phi}(x)\mathbf{\Sigma}^*(x, \nabla\mathbf{\Phi}(x))$ for all $x \in \Omega$.

When the nucleus is under small deformations, we may posit $\mathbf{\Phi}(x) = x + \mathbf{u}(x)$ for $x \in \Omega$. The derivatives of the displacement being small, the second order terms in the Green-St Venant strain tensor vanishes, yielding what we call the engineering definition of the strain.

Definition II.1.12 (Engineering strain)**.** *The engineering strain ϵ is the second-order tensor defined at every point $x \in \Omega$ by:*

$$\epsilon(x) = \frac{1}{2}(\nabla\mathbf{u}(x) + \nabla\mathbf{u}^T(x)). \tag{II.14}$$

One can recognize the symmetric part of the Jacobian of the displacement field. We readily recover the engineering strain by Taylor expansion of the stress tensor. Provided that the material is isotropoic, we have for every $x \in \Omega$:

$$\begin{aligned} \mathbf{T}(x) &= \nabla\mathbf{\Phi}(x)\mathbf{\Sigma}(x) \\ &= (\mathbb{1} + \nabla\mathbf{u}(x))\,(\lambda(\mathrm{tr}\mathbf{E}(x))\mathbb{1} + 2\mu\mathbf{E}(x)) \\ &= \lambda\mathrm{tr}(\epsilon(x))\mathbb{1} + 2\mu\epsilon(x) + o(|\nabla\mathbf{u}|) \end{aligned} \tag{II.15}$$

The non-negligible term defines the *linear stress*. Therefore, the equations of linear elasticity for an isotropic material can be expressed as:

Definition II.1.13 (Equations of linear elasticity)**.** *The equations of an isotropic linearly elastic material are given as:*

$$\begin{cases} \nabla \cdot \varsigma = 0, & \text{in } \Omega \\ \varsigma(\mathbf{u}) = \lambda\mathrm{tr}(\varepsilon(\mathbf{u}))\mathbb{1} + 2\mu\varepsilon(\mathbf{u}), & \text{in } \Omega \\ \varepsilon(\mathbf{u}) = \frac{1}{2}(\nabla\mathbf{u} + \nabla\mathbf{u}^{\mathrm{T}}), & \text{in } \Omega \\ \mathbf{u} = \mathbf{0}, & \text{on } \Gamma_u \\ \varsigma \cdot \mathbf{n} = \mathbf{T}, & \text{on } \Gamma_t, \end{cases} \tag{II.16}$$

Remind that the Lamé parameters λ and μ vary across the domain of the nucleus, depending on which nuclear element it is evaluated on. In the next section, we establish the existence and regularity of the solutions of these equations. These are paramount, as the image processing tools we will develop in the following chapters aim at constraining the computed displacement fields to the right Banach spaces endowed with these regularity properties.

II.1.2 Regularity requirements

II.1.2.1 Sobolev spaces

We first recall some basic definitions and properties about Sobolev spaces which befit the study of the solutions of partial differential equations. Note that the concepts we will develop here are valid for any Hilbert space of finite dimension. Denote $L^p(\Omega)$ for any integer p the associated Lebesgues space

on Ω, $L^p_{\text{loc}}(\Omega)$ its local counterpart, and $\mathcal{D}(\Omega) = C_c^\infty(\Omega)$ the set of infinitely differentiable functions with compact support. From now on, we will consider derivatives in the weak sense, which we define within the frame of distribution theory.

Definition II.1.14 (Weak derivative)**.** *Let $u \in L^1_{\text{loc}}(\Omega)$ and α a multi-index. We say that it admits a weak derivative of order α if and only if there exists $v \in L^1_{\text{loc}}(\Omega)$ such that, for all $\varphi \in C_c^\infty(\Omega)$, the following relation holds:*

$$\int_\Omega u D^\alpha \varphi dx = (-1)^{|\alpha|} \int_\Omega v \varphi dx, \tag{II.17}$$

where $D^\alpha \varphi = \frac{\partial^{|\alpha|}\varphi}{\partial x_1^{\alpha_1} x_2^{\alpha_2} x_3^{\alpha_3}}$. We say that v is the αth-weak derivative of u and we denote it $D^\alpha u$.

Sobolev spaces extend the definition of the $L^p(\Omega)$ spaces to functions that are weakly differentiable and their derivatives.

Definition II.1.15 (Sobolev spaces)**.** *Let $k \in \mathbb{N}$, $1 \leq p \leq +\infty$. The Sobolev space $W^{k,p}(\Omega)$ is defined as:*

$$W^{k,p}(\Omega) = \{u \in L^p(\Omega) | D^\alpha(u) \in L^p(\Omega), \forall |\alpha| \leq k\}. \tag{II.18}$$

It is naturally equipped with the following norm:

$$\forall f \in W^{m,p}(\Omega), \quad ||f||_{W^{m,p}(\Omega)} = \left(\int_\Omega (f(x)^p + \sum_{|\mathbf{k}| \leq m} |\partial^{\mathbf{k}} f(x)|^p) dx \right)^{1/p} \tag{II.19}$$

If $p = 2$, we use the notation $H^k = W^{k,2}(\Omega)$. We denote $W_0^{k,p}(\Omega)$ the closure of $\mathcal{D}(\Omega)$ in $W^{k,p}(\Omega)$.

Definition II.1.16 (Dual of Sobolev spaces)**.** *Let $k \in \mathbb{N}$, $1 \leq p \leq +\infty$, $p^* \in \mathbb{N}$ such that $\frac{1}{p} + \frac{1}{p^*} = 1$. We denote $W^{-k,p}$ the dual of the Sobolev space W^{k,p^*}*

We are to solve boundary value problems. It is not evident to determine whether the restriction of an element of $W^{k,p}$ belongs to a Sobolev space, since the Lebesgues measure of the boundary vanishes. The trace theorem helps us in circumventing this conundrum.

Theorem II.1.7 (Trace theorem in $H^1(\Omega)$)**.** *Suppose the boundary Γ to be Lipschitz continuous. We define the mapping $\gamma_0 : \mathcal{D}(\bar{\Omega}) \to L^2(\Gamma)$ by:*

$$\forall \varphi \in \mathcal{D}(\bar{\Omega}), \quad \gamma_0(\varphi) = \varphi_{|\Gamma}.$$

Then this mapping can be extended to a linear and bounded operator $\gamma : H^1(\Omega) \to L^2(\Gamma)$.

Definition II.1.17 (The Space $H^{1/2}(\Gamma)$)**.** *We denote $H^{1/2}(\Gamma) = \gamma_0(H^1(\Omega, \mathbb{R}^3))$ the trace space on the boundary Γ. Its dual space is denoted $H^{-1/2}(\Gamma)$.*

Definition II.1.18 (The space $H(\text{div}, \Omega)$)**.** *We define $H(\text{div}, \Omega)$ to be the following space:*

$$H(\text{div}, \Omega) = \left\{ \tau \in \left[L^2(\Omega)\right]^3 | \quad \text{div}(\tau) \in L^2(\Omega) \right\}$$

Theorem II.1.8 (Normal Trace of $H(\text{div}, \Omega)$)**.** *There exists a linear, bounded, and surjective operator $\gamma_{\mathbf{n}} : H(\text{div}, \Omega) \to H^{-1/2}(\Gamma)$ such that for each $\tau \in \left[H^1(\Omega)\right]^3$, $\gamma_{\mathbf{n}}(\tau)$ is identified, through the inner product of $L^2(\Gamma)$, with $\gamma_u(\tau) \cdot \mathbf{n}$.*

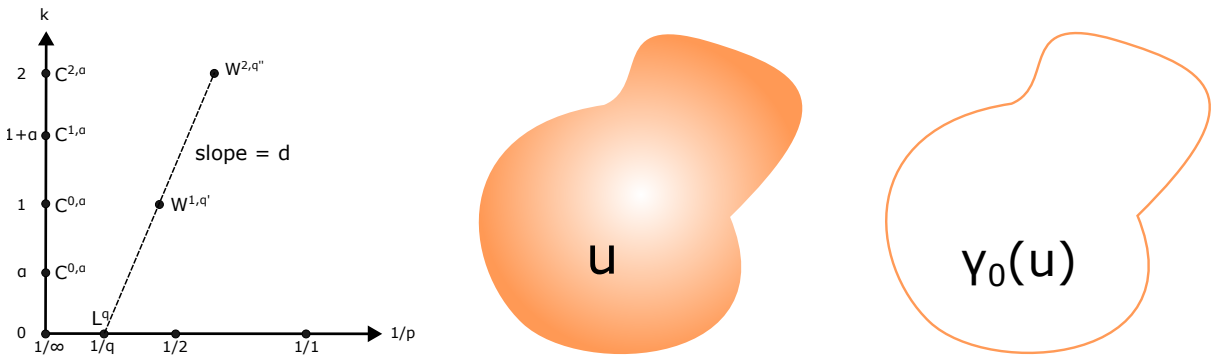

Figure II.2: Sobolev embedding theorems, definiion of the trace operator. The Sobolev embedding theorems can be graphically represented on the left. Here, $W^{2,q''}$ is continuously embedded in $W^{1,q'}$ which is continuously embedded in L^q, where q, q' and q'' lie on the a line of slope the space dimension d. On the middle and the right, the trace operator $\gamma_0$of a weakly differentiable u function restricts this function to the boundary ; the trace theorems show that this restriction satisfies weak differentiability properties as well.

The Sobolev spaces with imposed boundary values are then properly defined.

Definition II.1.19 (Sobolev spaces with constrained boundary)**.** *Given $p \in \mathbb{N}$, we define $W_0^{1,p}(\Omega)$ and $W_0^{2,p}(\Omega)$ in the following way:*

$$\begin{aligned} W_0^{1,p}(\Omega) &= \{u \in W^{1,p}(\Omega) | \gamma(u) = 0\} \\ W_0^{2,p}(\Omega) &= \{u \in W^{2,p}(\Omega) | \gamma(u) = 0\} \end{aligned} \tag{II.20}$$

It is of the utmost importance to understand how Sobolev spaces relate to one another. We will prove in the next chapter that not only current optical flow methods that compute the displacement field do not constrain it to the right Sobolev space, but furthermore that they constrain it to a Sobolev space that is not continuously embedded by the desired Sobolev space (see Figure II.2).

Definition II.1.20 (Continuous and compact embeddings)**.** *Let X and Y be two normed vector spaces. We say that Y is continuously embedded in X if and only if the identity function $\mathbf{Id} : Y \to X$ is continuous (i.e. bounded). If it is furthermore a compact operator, we say that Y is compactly embedded in X.*

Using this definition, and thanks to the Riesz representation theorem, we easily infer that $L^p(\Omega)$ is continuously embedded in $W^{-s,p}(\Omega)$. The following two embedding theorems are more involved.

Theorem II.1.9 (Rellich's embedding theorem)**.** *Let $1 \leq p < n$ and $p^* \in \mathbb{N}$ such that $\frac{1}{p^*} = \frac{1}{p} - \frac{1}{n}$. Then $W^{1,p}(\Omega)$ is continuously embedded in $L^{p^*}(\Omega)$ and compactly emmbedded in $L^q(\Omega)$ for any $1 \leq q < p^*$.*

Theorem II.1.10 (Kondrachov's embedding theorem)**.** *Suppose Ω is compact with C^1 boundary. Then if $k > l$ and $k - n/p > l - n/q$ then $W^{k,p}(\Omega)$ is compactly embedded in $W^{q,l}(\Omega)$.*

Theorem II.1.11 (Hölder embedding theorem)**.** *Let $k \geq 0$ and $0 < \alpha \leq 1$. Denote $C^{r,\alpha}(\Omega)$ the Hölder space of functions whose r^{th} derivatives are Hölder continuous of order α. If $kp > 3$ and $r + \alpha = k - \frac{n}{p}$, then $W^{k,p}(\Omega)$ is continuously embedded in $C^{r,\alpha}(\Omega)$.*

We are now geared with all the necessary notions to prove the existence, unicity and regularity of the solutions of the equations ruling the nuclear domain.

II.1.2.2 Existence, unicity, and regularity of the solutions

This section is divided into two. In the first part, we establish the existence and unicity of the equations of linear elasticity under general assumptions. In the second part, we summarize, based on the preceding presentation of the nuclear architecture, some further hypothesis we can make on the problem, and derive additional regularity properties of the solution. These two parts involve somewhat different arguments in their proofs. The first relies on the classical Lax-Milgram formula and the all-important Korn's inequalities. The second musters the theory of Schauder estimates on elliptic operators. These results are not new, but, to the best of our knowledge, their application to biological setting is, and requires as such a rigorous exposition. We refer the reader to [175] for complete proofs of the theorems, to which we owe the knowledge of the following report. We only keep the intermediate results necessary to the intelligence of our upcoming discussions.

It is very seldom that one can determine the exact solutions of a partial differential equation, or even guarantee their existence. Often it is sufficient to prove the existence of weak solutions which pertains to a related strongly coercive elliptic problem. Here we obtain it by multiplying the linear elasticity equations with a test function $\mathbf{v} \in H^1_{\Gamma_u}(\Omega)$.

Definition II.1.21 (Weak solutions of the linear elasticity problem)**.** *We say that any vector field* $\mathbf{u}$ *is a weak solution of the linear elasticity equations if it follows the following equality:*

$$\int_\Omega \varsigma(\mathbf{u}) : \varepsilon(\mathbf{v}) dx = \int_{\Gamma_t} \mathbf{g} \cdot \mathbf{v} \tag{II.21}$$

where $\mathbf{v} \in H^1_{\Gamma_u}(\Omega, \mathbb{R}^3)$.

The existence and unicity of solutions to these problems are generally assured thanks to the Lax-Milgram theorems, of which we give here a particular instance.

Definition II.1.22 (Strong coercivity)**.** *Let* $(H, \langle\cdot\rangle)$ *be a real Hilbert space with induced norm* $||\cdot||$*, and let* $B : H \times H \to \mathbb{R}$ *be a bilinear form. We say that* B *is strongly coercive if there exists a constant* $\alpha > 0$ *such that:*

$$B(x, x) \geq \alpha ||x||^2 \quad \forall v \in H.$$

Theorem II.1.12 (Lax-Milgram)**.** *Let* $(H, \langle\cdot,\cdot\rangle)$ *be a Hilbert space with induced norm* $||\cdot||$ *and let* $B : H \times H \to \mathbb{R}$ *be a bounded bilinear form. Assume that* B *is strongly coercive. Then, for each* $F \in H'$*, there exists a unique* $u \in H$ *such that:*

$$B(u, v) = F(v) \quad \forall v \in H$$

and

$$||u|| \leq \frac{1}{\alpha} ||F||.$$

We see that the stronger the ellipticity is, i.e. the higher the constant value α is, the stabler the solutions are. Indeed, given two solutions u_1 and u_2, we have $||u_1 - u_2|| \leq \frac{1}{\alpha}||F_1 - F_2||$.

In the beginning of the previous section, we said that there are movements without deformation, and we took the examples of rigid translations and rotations to prove our point. Actually, the following lemma shows that non-deforming bodies are necessarily undergoing a combination of translation and rotation, a property we will remind our reader when presenting optical flow techniques. This is a natural consequence of the identity $\partial_{ij}\mathbf{u}_k = \partial_i \varepsilon_{jk}(\mathbf{u}) + \partial_j \varepsilon_{ik}(\mathbf{u}) - \partial_k \varepsilon_{ij}(\mathbf{u})$, and that any vanishing second-order derivatives in the sense of distribution implies that the antiderivative is affine.

Lemma II.1.1 (Infinitesimal rigid displacement lemma)**.** *Let* $\mathbf{u} \in H^1(\Omega, \mathbb{R}^3)$*. If* $\varepsilon(\mathbf{u}) = 0$*, then* $\mathbf{u}(x) = \mathbf{A}x + \mathbf{b}$*, where* $\mathbf{b} \in \mathbb{R}^3$ *and* $\mathbf{A} \in \mathbb{M}$*.*

This lemma, along another one we owe to Jacques-Louis Lions, and Rellich's embedding theorem which we stated earlier, is at the heart of the proof of the following theorem.

Theorem II.1.13 (Korn's inequality)**.** *Let* Ω *be a domain in* $\mathbb{R}^3$ *and let* $\Gamma_u \subset \partial\Omega$*. Suppose that and that* $\mathbf{g} \in L^{4/3}(\Omega, \mathbb{R}^3)$*. Then there exists a constant* C *such that for all* $\mathbf{u} \in H^1_{\Gamma_\mathbf{u}}(\Omega, \mathbb{R}^3) = \{\mathbf{u} \in H^1(\Omega, \mathbb{R}^3) | \mathbf{u} = \mathbf{0} \text{ on } \Gamma_u\}$*:*

$$||\varepsilon(\mathbf{u})||_{L^2(\Omega, \mathbb{S}^3)} \geq C||\mathbf{u}||_{H^1(\Omega, \mathbb{R}^3)}.$$

A similar inequality may be established for problems where pure traction forces apply. None of the biological settings we will study checks this configuration. We nevertheless consign it here, lest the need be felt.

Theorem II.1.14 (Korn's inequality with no clamped boundaries)**.** *Let* Ω *be a bounded domain in* $\mathbb{R}^3$ *and* $\mathrm{Rig}(\Omega, \mathbb{R}^3)$ *the set of rigid displacements. Then there exists a constant* C *such that:*

$$||\varepsilon(\mathbf{u})||_{L^2(\Omega, \mathbb{S}^3)} \geq C \inf_{w \in \mathrm{Rig}(\Omega, \mathbb{R}^3)} ||\mathbf{u} + \mathbf{w}||_{H^1(\Omega, \mathbb{R}^3)}$$

for all $\mathbf{u} \in H^1(\Omega, \mathbb{R}^3)$

The first of these two inequalities allows us to check the first hypothesis of the Lax-Milgram formula. Given $\mathbf{u} \in H^1_{\Gamma_u}(\Omega, \mathbb{R}^3)$, there exists a constant C such that:

$$\int_\Omega \varsigma(\mathbf{u}) : \varepsilon(\mathbf{u}) dx = \int_\Omega (\lambda \mathrm{tr}(\varepsilon(\mathbf{u}))^2 + 2\mu ||\varepsilon(\mathbf{u})||^2) dx \geq 2\mu \int_\Omega ||\varepsilon(\mathbf{u})||^2 dx \geq C||\mathbf{u}||^2_{H^1(\Omega, \mathbb{R}^3)}$$

The bilinear form is bounded thanks to the boundedness of the derivatives of all elements in $H^1_{\Gamma_u}(\Omega, \mathbb{R}^3)$. We just proved that the variational problem (II.21) admits a unique solution $u \in H^1_{\Gamma_u}(\Omega, \mathbb{R}^3)$.

Since the beginning of this subsection, we did not consider the biological configuration of our problem. This brings forth a list of hypothesis which, taken into account, amount to a few regularity properties. Recall that:

- The nuclear lamina is a regular meshwork of intertwined lamins A and B that supports the inner nuclear membrane. While the lipid bilayers composing the inner and outer nuclear membranes are very well capable of admitting sharp distortions under certain thermal conditions, we saw that the nuclear envelope's overall stiffness is ruled by the nuclear lamina. Given its established rigidity, we may assume smoothness of the domain boundary: $\Gamma \in C^\infty$.
- Probing assays apply piecewise constant forces. Both the KASH domain proteins, SUN domain proteins, and LINC complexes, which link the force-transmitting cytoskeleton to the nucleus, are homogeneously allocated within the envelope. Binding proteins such as laminin and fibronectin are continuously dispatched in the extracellular matrix during migration. Therefore, we may posit that $\mathbf{T} \in H^{1/2}(\Omega, \mathbb{R}^3)$.
- Chromatin has a fractal-like configuration, so $E \in L^1(\Omega, \mathbb{R})$. However we saw that the inter-chromatin space is filled with nuclear bodies, that all may contribute, to a lesser extent, for sure, to the intranuclear stiffness. Besides, we saw that the confocal microscopes we will use operate at limited resolution, and smoothes out the nanometric details. It is therefore possible to lay the stronger assumption that $E \in H^2(\Omega, \mathbb{R})$.

- We saw that the idea of a nucleoskeleton is highly debated. At the utmost, if there is an organizing structure within the nuclear interior, it operates slowly. We suppose it operates slowly enough to not be taken into account during quasi static deformations. In other words, no volumetric forces apply.
- Several experiments concluded to a constant value of Poisson's ratio throughout the nuclear domain. We will take the approved value of $\nu = 0.33$, which accounts for a high compressibility.
- The inner and outer nuclear membranes are separated by the perinuclear space. The nucleus is clamped through laminin contact, operated beneath the inner nuclear membrane. Therefore we may suppose that $\Gamma_u \cap \Gamma_t = \emptyset$.

Given these assumptions, we remind several results for the theory of linear elastic materials that the displacements ruling the nuclear domain necessarily belong to $H^2(\Omega, \mathbb{R}^3)$.

Denote $\mathcal{C}$ the fourth-order elasticity tensor in the linearized configuration. Boundary conditions apart, a strong solution $\mathbf{u}$ of the established linear elasticity equations verifies $\text{div}(\mathcal{C} \cdot \nabla \mathbf{u}) = \mathbf{0}$. Denote A the scalar operator defined for every $\mathbf{u}$ by $A\mathbf{u} = \text{div}(\mathcal{C} \cdot \nabla \mathbf{u})$. Denote $H^2_\partial(\Omega, \mathbb{R}^3)$ the space composed of elements $\mathbf{u} \in H^2(\Omega, \mathbb{R}^3)$ such that:

$$\begin{aligned} \mathbf{u} = \mathbf{0} \quad &\text{on} \quad \Gamma_\mathbf{u} \\ (\mathcal{C} \cdot \mathbf{u}) \cdot \mathbf{n} = \mathbf{t} \quad &\text{on} \quad \Gamma_\mathbf{t} \end{aligned} \tag{II.22}$$

We suppose the elasticity tensor to be hyperelastic, meaning $\mathcal{C}^{ijkl} = \mathcal{C}^{klij}$. We also suppose that it is strongly elliptic, i.e. that there exists a constant $\alpha > 0$ such that:

$$\mathcal{C}^{ijkl}(x)\xi_i\xi_k\eta_j\eta_l \geq \alpha||\xi||^2||\eta||^2$$

for every $\xi, \eta \in \mathbb{R}^3$ and $x \in \Omega$.

Now, because of the positivity and the assumed regularity of the Lamé parameters, Schauder theory assures us of the existence of the following sample elliptic estimate.

Theorem II.1.15 (Sample elliptic estimate)**.** *Given $\mathbf{u} \in H^2_\partial(\Omega, \mathbb{R}^3)$, there exists a constant Λ such that for every $k \geq 2$:*

$$||\mathbf{u}||_{H^k(\Omega,\mathbb{R}^3)} \leq \Lambda \left(||A(\mathbf{u})||_{H^{k-2}(\Omega,\mathbb{R}^3)} + ||\mathbf{u}||_{L^k(\Omega,\mathbb{R}^3)} \right).$$

The previous result holds even for non-homogeneous values of the Lamé parameters. We only need them to be bounded from below, which we can easily assume thanks to their positivity.

We are interested in the kernel of A, which regroups the solutions of the problem we wish to solve. Given an element $\mathbf{u} \in kerA$, the above equation shows that $||\mathbf{u}||_{H^2(\Omega,\mathbb{R}^3)} \leq \Lambda||\mathbf{u}||_{L^2(\Omega,\mathbb{R}^3)}$. From Rellich's compactness theorem, which we stated previously, we deduce that the unit ball of $kerA$ is compact, and therefore finite dimensional. We refer to [175] to see that the range of A is closed in $L^2(\Omega, \mathbb{R}^3)$. Now, we are fit to understand the following fundamental result.

Theorem II.1.16 (Weak solutions are strong solutions)**.** *Let $\mathbf{u} \in L^2(\Omega, \mathbb{R}^3)$. We suppose that $\mathbf{u}$ is a weak solution of the linear elasticity equations, that is, for every test function $\mathbf{v} \in H^2_\partial(\Omega, \mathbb{R}^3)$:*

$$\langle \mathbf{u}, A\mathbf{v} \rangle = 0.$$

Then $\mathbf{u} \in H^2_\partial(\Omega, \mathbb{R}^3)$ and $A\mathbf{u} = 0$.

These theorems are at the heart of the proof of the following fundamental theorem.

Theorem II.1.17 (Fredholm Alternative)**.** *We have the following orthogonal decomposition:*

$$L^2(\Omega, \mathbb{R}^3) = rgA \oplus kerA.$$

The Fredholm alternative allows us to determine the solutions up to elements of ker A. Again, the proof is quite intricate, and can be found in Ciarlet [173]. For full traction problems, it reads as the following theorem.

Theorem II.1.18 (Regularity of the solutions for pure traction problems)**.** *Suppose that* $\Gamma_t = \partial\Omega$ *and* $\int_{\Gamma_t} \mathbf{g} \cdot \mathbf{v} da = 0$ *for all rigid displacement fields* $\mathbf{v} \in H^1(\Omega, \mathbb{R}^3)$*, i.e. satisfying* $\varepsilon(\mathbf{v}) = \mathbf{0}$*. If* $\mathbf{g} \in W^{m+1-1/p,p}(\Gamma_t, \mathbb{R}^3)$*, and* $\partial\Omega$ *is of class* $\mathcal{C}^{m+2}$*, where* m *and* p *are two positive integers satisfying* $1 < p < +\infty$ *and* $p \geq \frac{6}{5+2m}$*, then any solution* $\mathbf{u}$ *to the linear elasticity equations belongs to the space* $W^{m+2,p}(\Omega, \mathbb{R}^3)$ *and there exists a constant* C *such that:*

$$||\mathbf{u}||_{W^{m+2,p}(\Omega,\mathbb{R}^3)/\text{Rig}(\Omega,\mathbb{R}^3)} \leq C||\mathbf{g}||_{W^{m+1-1/p,p}(\partial\Omega,\mathbb{R}^3)}$$

In our case, with our hypothesis, this would mean that $\mathbf{u} \in H^2(\Omega, \mathbb{R}^3)$ up to any rigid displacement.

We have exposed the mathematical problem we are to solve, and we laid out some important regularity properties of some of its mechanical values ruling the behavior of the nuclear domain. We now summarize all our hypothesis and state clearly our image processing goal.

II.2 Formulation of the three problems to solve

Given two (possibly 3D) fluorescence images of a nucleus, one before deformation, the other after deformation, we wish to compute the displacement field $\mathbf{u}$, the strain field ε, the stress field ς and the Young's modulus E, as well as the traction forces $\mathbf{T}$ at the boundary, at each point (in the image resolution limit) of the nuclear domain. Unfortunately this problem is ill-posed, as certain quantities are required for the computation of others. This dependency is testified by the previously established equations of linear elasticity:

$$\begin{cases} \nabla \cdot \varsigma = 0, & \text{in } \Omega \\ \varsigma(\mathbf{u}) = \lambda \text{tr}(\varepsilon(\mathbf{u}))\mathbb{1} + 2\mu\varepsilon(\mathbf{u}), & \text{in } \Omega \\ \varepsilon(\mathbf{u}) = \frac{1}{2}(\nabla\mathbf{u} + \nabla\mathbf{u}^{\mathrm{T}}), & \text{in } \Omega \\ \mathbf{u} = \mathbf{0}, & \text{on } \Gamma_u \\ \varsigma \cdot \mathbf{n} = \mathbf{T}, & \text{on } \Gamma_t, \end{cases}$$

To make it tractable, we would like to divide our problem in three sub-problems:

- **Problem 1**. Given two fluorescence images of a nucleus, one before deformation, the other after deformation, compute the displacement and strain fields $\mathbf{u}$ and $\varepsilon(\mathbf{u})$ at each point of the nuclear domain. We saw that the displacement field belongs to $H^2(\Omega, \mathbb{R}^3)$, and that consequently the strain field belongs to $H^1(\Omega, \mathbb{R}^3)$. Chapter 3 tackles this problem by presenting a novel optical flow technique to compute the displacement field within a better Sobolev space.
- **Problem 2**. Given images of a nucleus before and after deformation, compute the relative values of the Young's modulus distribution or, in case the boundary traction forces are supplied, compute the absolute value of the Young's modulus. This is a famous problem in medical imaging called

"elastography". To our knowledge, no one offered yet a complete depiction of the heterogeneity of the Young's modulus within the nucleus. We pioneer this work by solving a novel mixed-PDE elliptic system of differential equations of the stiffness of the nucleus. Again, it relies on the regularity assumption $E \in H^2(\Omega, \mathbb{R})$ we supposed in the previous section.

- **Problem 3**. Given the Young's modulus distribution E of the nucleus, its Poisson's ratio, and images before and after deformation of the nucleus, compute the stress field ς and the boundary traction $\mathbf{T}$. These two quantities naturally arise from the computation of the displacement field from Problem 1. We will see that the stress field and the boundary tractions are best reconstructed through a PDE-constrained optimization framework that projects the optical flow solution to the kernel of the elasticity operator.

II.3 Data creation

The framework of this section is summarized in Figure C.2. We first create an initial image of a nucleus before deformation. To do so, we prescribe the geometry of the nuclear domain, set randomly the intensity values, then smooth them out with Gaussian filtering to better catch the textural properties of fluorescence microscopy. From this first image, we then create a second image of the nucleus, but this time after deformation. We define the deformation beforehand by choosing some boundary conditions, both Neumann and Dirichlet. Given a linear elastic body filling a domain Ω and some boundary conditions, how can we compute the resulting displacement field? Generally speaking, unless under very simplistic geometries, we cannot. If we are allowed to make some assumptions, we may at most prove the existence and regularity of the solutions – which we did in our case in chapter I. However, we may determine, on a related space of finite dimension, some approximation of the solution. This is the finite element method. Once we possess the displacement fields, we use them to warp the first image to create our second image. We now detail each of these steps, starting with the finite element resolution.

The finite element method does not apply *per se* on the image space. It may be divided into five steps [180]: first, segmentation of the nuclear domain to define the coordinates of its boundary points; second, tessellation of the resulting domain, which means definition of a mesh of finite elements (triangles or quadrilaterals, for instance); third, variational formulation of the partial differential equations to solve, and definition of the finite-dimensional Hilbert spaces on which they will be solved; fourth, discretization of this variational formulation on the finite-dimensional Hilbert spaces defined in the second step, and assembly of a sparse system of linear equations, the solution of which is the vector of the displacement field at each node of the finite elements; fifth, solve of the system of equations and eventual post-processing procedures (see Figure II.4).

II.3.1 Tessellation

Because the boundary of the nuclear domain is smooth, we may resort to simple triangular elements for creating the mesh. One method of interest for this purpose is the Delaunay algorithm [181]. A Delaunay mesh defines a set of N points $V = \{v_1, ..., v_N\}$, called *nodes* in the Eucledian space. The nodes are assumed to not be all colinear. The set of edges E regroups the $\binom{N}{2}$ segments stringing one point to another into triangles. Delaunay meshing assumes two hypothesis. First, there are no *properly intersecting* edges, meaning that edges only intersect at their endpoints. Second, the circumcircle of any triangle in the triangulation contains no point of V in its interior. We find it easier to understand the cause of this last property by introducing Voronoi diagrams [182]. For a given $i \in \{1, ..., N\}$, we define the *Voronoi polygon associated with the node* v_i as the set $V(i) = \{x \in \mathbb{R}^n \mid d(x, v_i) \leq d(x, v_j),\ j = 1, ..., N\}$. In other words, it is the set of points closer to v_i than to any other node. The set of Voronoi polygons define a partition of the nuclear domain, named a *Voronoi diagram*, as illustrated in II.5. We heretofore adopt the point of view of Lee in [183]. Suppose each Voronoi polygon as the result of a

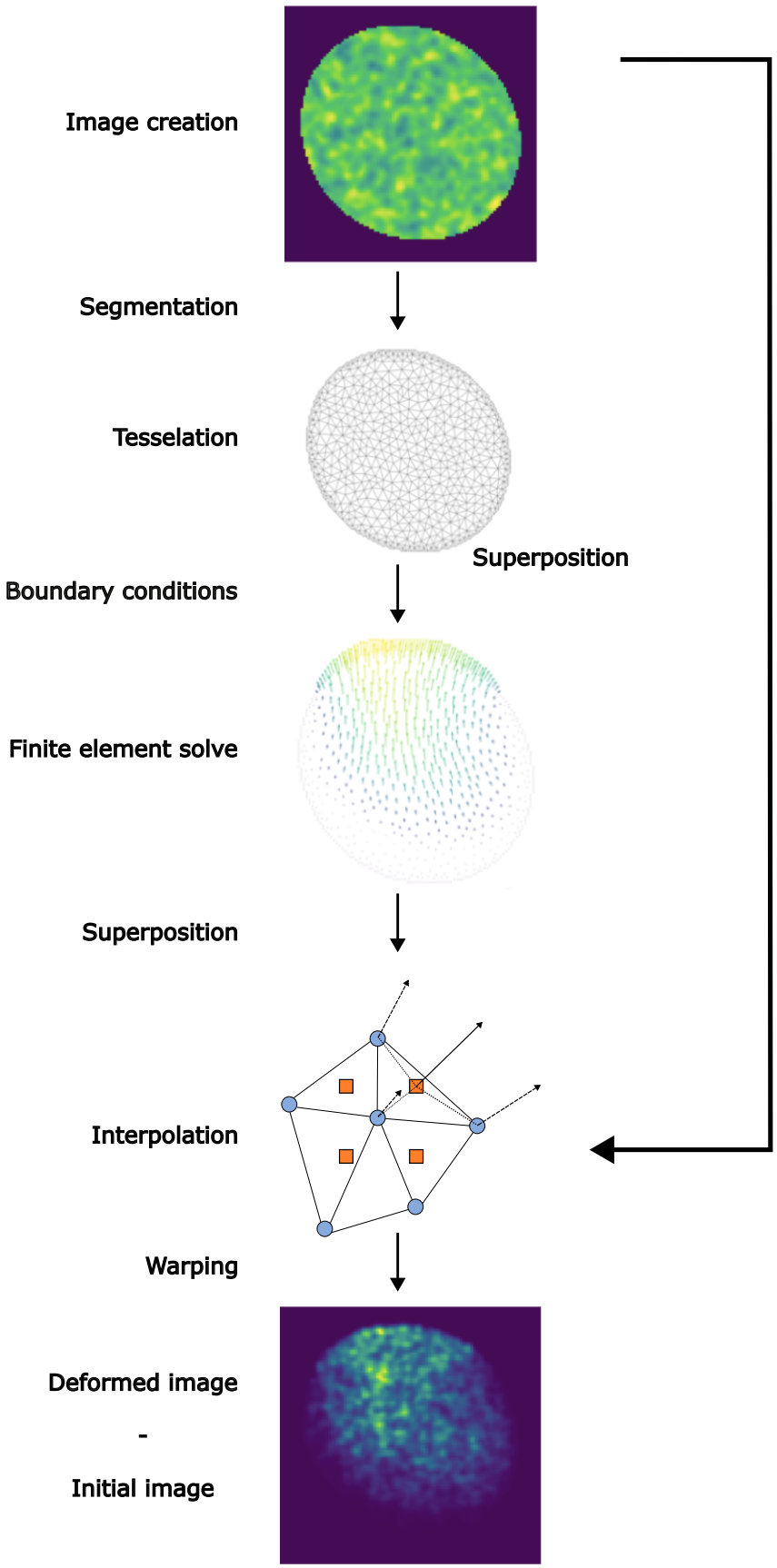

Figure II.3: Overview of our data creation framework.

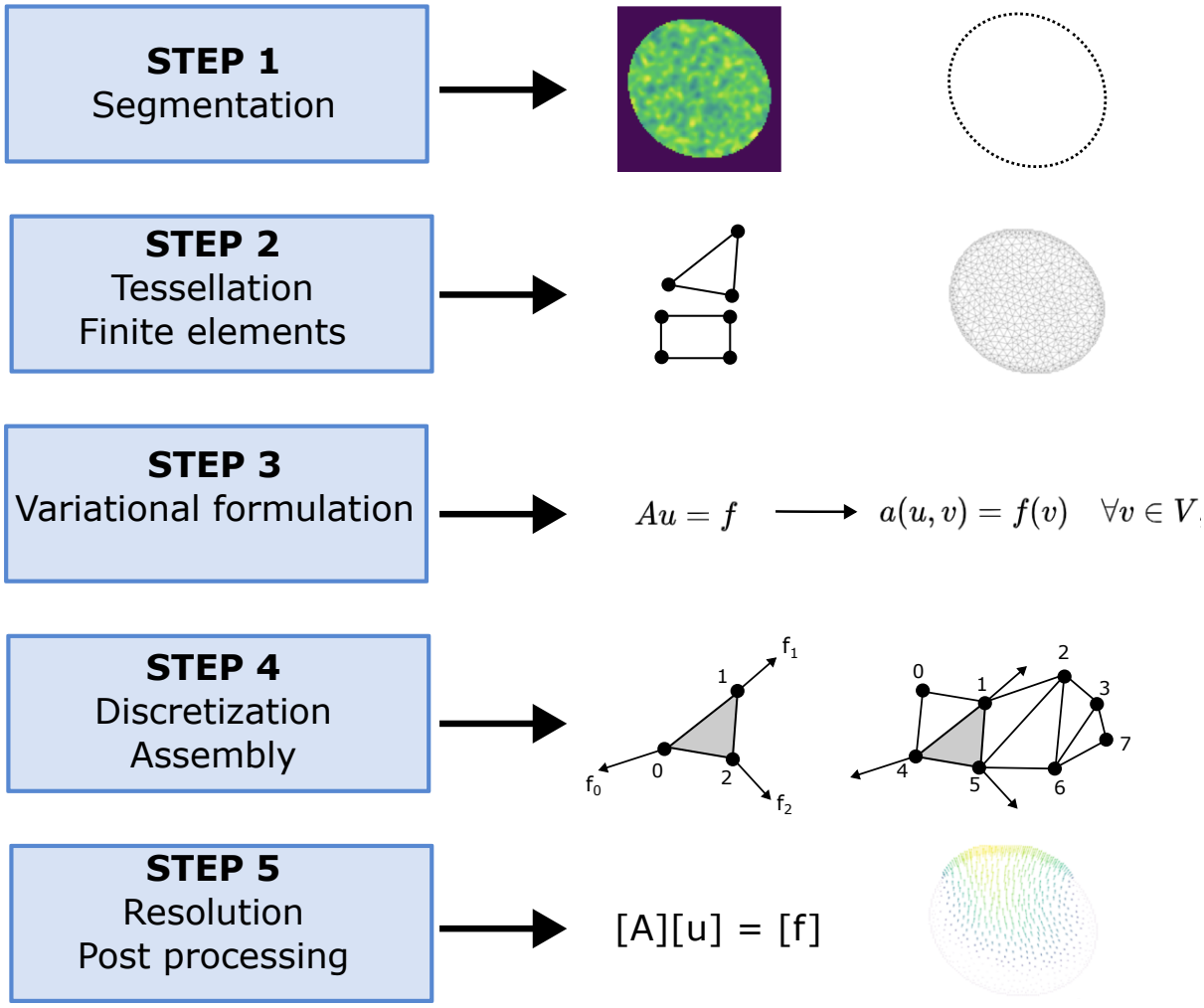

Figure II.4: Overview of the Finite Element Method.

growing process. Each node defines initially a cell that, over time, stretches farther and farther to its neighborhood. Once a cell meets another one, both stop growing at that juncture point. Eventually, the junction enlarges to the point of forming a segment. This segment in turn stops elongating once it meets the frontiers of another cell. The intersecting point is called a *Voronoi point*. This is, in an nutshell, the heuristic behind the construction of Voronoi diagrams. Though simplistic, it underlines some particular properties of interest. First, we understand that the initial point of contact between two cells is necessarily at the midsection of the two nodes of interest. We also see that every point of the "edge of contact" between two Voronoi polygons must be at equidistant of the centers of the polygons. It follows naturally that the *Voronoi point* of three polygons is necessarily equidistant of each corresponding node. In other words, the Voronoi point of three polygons is the circumcenter of each of their nodes.

We may find several Delaunay triangulations for a given set of points V. However, one might prove that each of these triangulations share the same number of triangles and the same number of edges. An induction argument also shows that the Voronoi paritioning of a set of points define a triangulation where neither of the circumcircle of each triangle contains another node [185]. In other words, we just recovered the initial properties of Delaunay triangles (see Figure II.5). We say that the Delaunay triangulation and the Voronoi diagrams are dual to one another. We call this property the *circle criterion*. Other equivalent geometrical properties may define a Delaunay triangulation as well [186]. For instance, the *MAX-MIN angle criterion* states that the minimum measure of angles of all the triangles

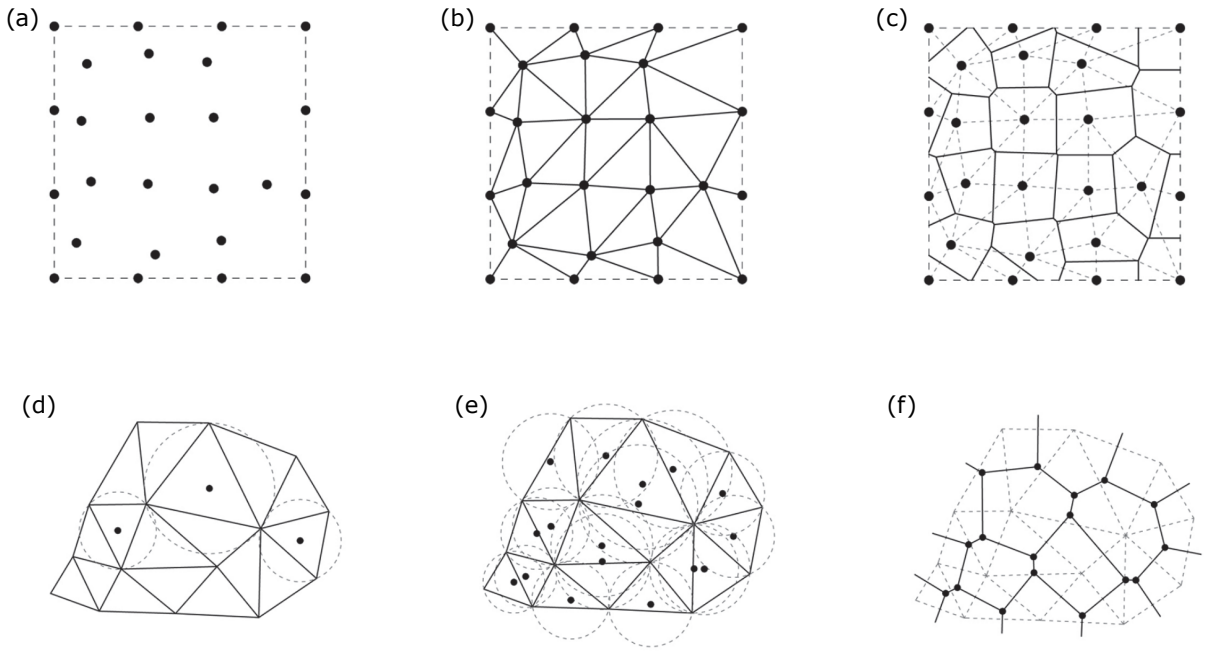

Figure II.5: Delaunay triangulation. (a) Random creation of a set of points within the selected domain ; (b) There are no properly interecting edges in a Delaunay triangulation ; (c) corresponding Voronoi diagram for the given points ; (d) Each Voronoi point is the center of a triangle ; (e) the ensuing triangulation satisfies the circumcircle property ; (f) the centers of the circles determine the vertices of the dual polygon (from [184].

shall be maximized [187]. This criterion as others might be used as a defining yardstick for tessellation algorithms. In this thesis, we resorted to the CGAL library for generating Delaunay triangulation [188]. This software is known for its robustness and it successfully excluded all singularities in any simulation we had to undertake so far. It relies on a "divide-and-conquer" algorithm, which has been shown to have a complexity of $O(N\ln N)$ [189]. This is, at the moment, the algorithm with the lowest computational price [190]. It is sufficiently fast in quasistatic deformation, even in 3D, since, as the reader will see in the following section, we only need to build one mesh for our computation. However, shall we extend the presented work to time-dependent deformations, such as is the case in a viscoelstic modeling, we would need to compute $T-1$ of such meshes, where T is the number of frames monitoring the movement. The computation would still be tractable, but perhaps too long for ergonomic requirements: a biologist would have difficulty using our algorithms on its own. One idea would be to implement an arbitrary Eulerian-Lagrangian method [191], [192], [193], in order to deform the initial mesh over time with the computed displacement field.

II.3.2 Variational formulation

We remind some basic notions of the Ladyzhenskaya–Babuska–Brezzi theory [194] before exposing the variational formulation of our problem. This allows us to ensure of the existence and unicity of the linear elasticity equations once we adopt a mixed formulation [195].

Definition II.3.1 (Continuous inf-sup condition)**.** *Let H and Q be two finite-dimensional real Hilbert spaces with associated norms $||\cdot||_H$ and $||\cdot||_Q$. We say that a bilinear operator $b : H \times Q \to \mathbb{R}$ satisfies the continuous inf-sup condition if there exists a constant $\beta > 0$ such that:*

$$\inf_{\substack{\nu\in Q\\ \nu\neq 0}} \sup_{\substack{\tau\in H\\ \tau\neq 0}} \frac{b(\tau,\nu)}{||\tau||_H||\nu||_Q} \geq \beta.$$

This definition is at the heart of the characterization of the existence and unicity of the solutions of mixed variational problems.

Definition II.3.2 (Mixed variational problem)**.** *Let H and Q be two finite-dimensional Hilbert spaces with associated norms $||\cdot||_H$ and $||\cdot||_Q$. Let $a : H \times H \to \mathbb{R}$ and $b : H \times Q \to \mathbb{R}$ be two bounded bilinear forms, and $F \in H'$ and $G \in Q'$ be two linear forms. The problem that consists in finding $(\sigma, u) \in H \times Q$ such that:*

$$\begin{aligned} a(\sigma,\tau) + b(\tau,u) &= F(\tau),\ \forall \tau \in H, \\ b(\sigma,\nu) &= G(\nu),\ \forall \nu \in Q. \end{aligned}$$

is called a mixed variational problem.

Theorem II.3.1 (Existence and unicity of a mixed variational problem)**.** *Consider a mixed variational problem with the notation as above. Suppose that:*

- *a is α coercive on the kernel of b, meaning:*

$$a(\tau,\tau) \geq \alpha ||\tau||_H^2,$$

  for all τ such that $b(\tau,\nu) = 0$ for all $\nu \in Q$,

- *b satisfies the inf-sup condition,*

then there exists a unique solution (τ,ν) of the mixed variational problem. Moreover, there exists a constant C such that this solution respects the following inequality:

$$||\sigma||_H + ||\tau||_Q \leq C\left(||F||_{H^*} + ||G||_{Q^*}\right)$$

Our goal now is to derive, from the linear elasticity equations ruling the nuclear domain, a mixed variational problem that checks these conditions. A simpler finite element method would work in the compressible setting. In the incompressible setting, however, the Lamé parameter λ tends to infinity. To ensure finiteness of the stress tensor ς, the hydrostatic strain field $\mathrm{tr}(\varepsilon(\mathbf{u}))$ has to tend to 0. In other words, the "volume" of the material is conserved – and hence we find again the intuitive idea behind incompressibility. Numerically, however, this means that the constitutive equation stages the multiplication of a very high number with a very low number: in other words, there is, at each point of the domain, occasions for both overflow and underflow approximation [196]. To avoid that, mixed finite elements seek to compute two figures of interest, the displacement field per se, and some rotational value, which relates to the volumetric deformation.

Remind the equations established at the end of the previous section. We seek to find a displacement field $\mathbf{u} \in H^2(\Omega, \mathbb{R}^3)$ such that:

$$\begin{cases} \nabla \cdot \varsigma = \mathbf{0}, & \text{in } \Omega \\ \varsigma(\mathbf{u}) = \lambda \mathrm{tr}(\varepsilon(\mathbf{u}))\mathbb{1} + 2\mu\varepsilon(\mathbf{u}), & \text{in } \Omega \\ \varepsilon(\mathbf{u}) = \frac{1}{2}(\nabla\mathbf{u} + \nabla\mathbf{u}^{\mathrm{T}}), & \text{in } \Omega \\ \mathbf{u} = \mathbf{0}, & \text{on } \Gamma_u \\ \varsigma \cdot \mathbf{n} = \mathbf{T}, & \text{on } \Gamma_t, \end{cases}$$

For any Hilbert space X, denote $\mathbf{X} = X^3$, $\mathbb{X} = X^{3\times 3}$, $\mathbb{X}(\text{div}, \Omega) = \{\tau \in \mathbb{L}^2(\Omega) \ : \text{div}\tau \in \mathbf{L}^2(\Omega)\}$. This last space is endowed with the norm $||\tau||_{\text{div},\Omega} = \left\{||\tau||^2 + ||\text{div}\tau||^2\right\}^{1/2}$. Given these notations, one may say we wish to retrieve two variables, $\mathbf{u} \in H^2(\Omega, \mathbb{R}^3)$ and $\varsigma \in L^1(\Omega, \mathbb{R}^9)$ such that:

$$\begin{cases} \varsigma = \mathcal{C} \cdot \varepsilon(\mathbf{u}), & \text{in } \Omega \\ \nabla \cdot \varsigma = \mathbf{0}, & \text{in } \Omega \\ \mathbf{u} = \mathbf{0}, & \text{on } \Gamma_u \\ \varsigma \cdot \mathbf{n} = \mathbf{T}, & \text{on } \Gamma_t, \end{cases} \tag{II.23}$$

where $\mathcal{C}$ is the elasticity tensor defined in (II.1.8). This strain tensor ε is the symmetric part of the Jacobian of the displacement field. We denote ε_s its skew-symmetric counterpart, defined as:

$$\varepsilon_s(\mathbf{u}) = \nabla \mathbf{u} - \varepsilon(\mathbf{u}).$$

This tensor catches the rotational properties of the nucleus. The elasticity tensor is invertible. Multiplying the first equation of (II.23) by a test function $\tau \in \mathbb{H}(\text{div}, \mathbf{\Omega})$, one gets the following variational problem by integration and application of Green's identity:

$$\int_\Omega \mathcal{C}^{-1}\varsigma : \tau = -\int_\Omega \mathbf{u} \cdot \text{div}\tau + \langle \gamma_n(\tau), \gamma_0(\mathbf{u})\rangle - \int_\Omega \varepsilon_s(\mathbf{u}) : \tau, \tag{II.24}$$

where $\gamma_\mathbf{n}$ is the normal trace operator defined in (II.1.8). Denote $\xi = -\gamma_0(\mathbf{u})$. We have $\xi = 0$ on $\Gamma_\mathbf{u}$. The previous equation simplifies into the following:

$$\begin{aligned} &a(\varsigma, \tau) + b(\tau, (\mathbf{u}, \varepsilon_s, \chi)) = F(\tau), \quad \forall \tau \in \mathbb{H}(\text{div}, \Omega) \\ &b(\varsigma, (\mathbf{v}, \eta, \chi)) = G(\mathbf{v}, \eta, \xi), \quad \forall (\mathbf{v}, \eta, \xi) \in \mathbf{L}^2(\Omega) \times \mathbb{L}^2_{\text{skew}}(\Omega) \times \mathbf{H}_0^{1/2}(\Gamma_\mathbf{t}), \end{aligned} \tag{II.25}$$

where $\mathbb{L}^2_{\text{skew}}(\Omega)$ denotes the space of the skew-symmetric matrix fields, $H_0^{1/2}(\Gamma_\mathbf{t})$ the space of trace operator that vanishes at $\Gamma_\mathbf{u}$, and a, b, F and G the following bounded bilinear and linear operators:

$$\begin{aligned} a(\varsigma, \tau) &= \int_\Omega \mathcal{C}^{-1}\varsigma : \tau = \frac{1}{2\mu}\int_\Omega \varsigma : \tau - \frac{\lambda}{4\mu(\lambda+\mu)}\int_\Omega \text{tr}(\varsigma)\text{tr}(\tau) \\ b(\tau, (\mathbf{v}, \eta, \chi) &= \int_\Omega \mathbf{v} \cdot \text{div}\ \tau + \int_\Omega \eta : \tau + \langle \gamma_\mathbf{n}(\tau)|_{\Gamma_t}, \chi\rangle_{\Gamma_t} \end{aligned} \tag{II.26}$$

for all $(\tau, (\mathbf{v}, \eta, \chi)) \in \mathbb{H}(\text{div}, \Omega) \times (\mathbf{L}^2(\Omega) \times \mathbb{L}^2_{\text{skew}}(\Omega) \times \mathbf{H}_0^{1/2}(\Gamma_\mathbf{t}))$, $F \in H'$, and $G \in Q'$ is given by:

$$G(\mathbf{v}, \eta, \chi) = -\int_\Omega \mathbf{f} \cdot \mathbf{v} + \langle \mathbf{g}, \chi\rangle_{\Gamma_t}, \quad \forall (\mathbf{v}, \eta, \chi) \in \mathbf{L}^2(\Omega) \times \mathbb{L}^2_{\text{skew}}(\Omega) \times \mathbf{H}_0^{1/2}(\Gamma_\mathbf{t}). \tag{II.27}$$

Proving that the inf-sup condition here is satisfied requires some technical tactics to circumvent the difficulty arising with the natural boundary conditions that arise in linear functional b. We refer to [197] for a full proof of this inequality. In the meantime, we can say that, thanks to the Babuska-Brezzi theorem, there exists a unique pair $(\varsigma, (\mathbf{u}, \varepsilon_s, \chi))$ such that equation II.25 is satisfied.

II.3.3 Finite element definitions

Now, the previous equation is infinitely dimensional, and in order to solve it, the finite element method solves the variational problem in a discrete subspace. This is where the polygonal definition arising from the Delaunay triangulation comes handy. Ciarlet defines a finite element as a triple in the following way [198].

Definition II.3.3 (Finite element)**.** *A finite element is defined by a triplet* $(T, \mathcal{V}, \mathcal{L})$ *where:*

- *The domain T is a bounded, closed subset of $\mathbb{R}^d$, $d \in \{2,3\}$, with non-empty interior and piecewise smooth boundary.*
- *The space $\mathcal{V} = \mathcal{V}(T)$ is a finite dimensional function space on T of dimension n.*
- *The set of degrees of freedom (nodes) $\mathcal{L} = \{l_1, ..., l_n)$ is a basis for the dual space $\mathcal{V}'$, that is, the space of bounded linear functions on $\mathcal{V}$.*

In our case, the domain T will be the triangles defined by the previously outlined meshing algorithm. We will resort to the Brezzi-Douglas-Marini element, which relies on the definition of the Raviart-Thomas elements and Nédelec H(curl) elements (NED). We transcribe here the definition of each of these elements, as laid out in [199]. But first, we remind the reader the definition of the H(curl) space.

Definition II.3.4 (H(curl))**.** *Given a bounded domain Ω with Lipschitz continuous domain, the H(curl) space is defined in the following way:*

$$H(\text{curl}, \Omega) = \left\{ u \in L^2(\Omega) | \text{ curl u} \in L^2(\Omega) \right\}$$

Definition II.3.5 (Raviart-Thomas)**.** *The Raviart-Thomas element (RT_q) is defined for $q = 1, 2, ...$ by:*

- $T \in \{\text{triangle,tetrahedron}\}$,
- $\mathcal{V} = [\mathcal{P}_{q-1}(T)]^d + x\mathcal{P}_{q-1}(T)$,
- $\mathcal{L} = \begin{cases} \int_f v \cdot n \; p \; ds, & \text{for a set of basis functions } p \in \mathcal{P}_{q-1}(f) \text{ for each facet e,} \\ \int_T v \cdot p dx, & \text{for a set of basis functions } p \in [\mathcal{P}_{q-2}(T)]^d, \text{ for } q \geq 2 \end{cases}$

Definition II.3.6 (Nédélec)**.** *For $q = 1, 2, ...$, define the space:*

$$\mathcal{S}_q(T) = \{ s \in [\mathcal{P}_q(T)]^d : \; s(x) \cdot x = 0, \;\; \forall x \in T \}$$

The Nédélec element of the second kind (NED_q^2) is defined for $q = 1, 2, ...$ in two dimensions by:

- *T = triangle,*
- $\mathcal{V} = [\mathcal{P}_{q-1}(T)]^2 + \mathcal{S}_q(T)$,
- $\mathcal{L} = \begin{cases} \int_e v \cdot t \; p \; ds, & \text{for a set of basis functions } p \in \mathcal{P}_{q-1}(e) \text{ for each edge e,} \\ \int_T v \cdot p dx, & \text{for a set of basis functions } p \in [\mathcal{P}_{q-2}(T)]^2, \text{ for } q \geq 2 \end{cases}$

where t is the edge tangent, and in three dimensions by:

- *T = tetrahedron,*
- $\mathcal{V} = [\mathcal{P}_q(T)]^3$,
- $\mathcal{L} = \begin{cases} \int_e v \cdot t \; p \; dl, & \text{for a set of basis functions } p \in \mathcal{P}_q(e) \text{ for each edge e,} \\ \int_f v \cdot p dx, & \text{for a set of basis functions } p \in \text{RT}_{q-1}(T), \text{ for } q \geq 2 \\ \int_T v \cdot p dx, & \text{for a set of basis functions } p \in \text{RT}_{q-2}(T), \text{ for } q \geq 3 \end{cases}$

Definition II.3.7 (Brezzi-Douglas-Marini element)**.** *The Brezzi-Douglas-Marini element (BDM_q) is defined for $q = 1, 2, ...$ by:*

- $T \in \{\text{triangle,tetrahedron}\}$,
- $\mathcal{V} = [\mathcal{P}_q(T)]^d$,
- $\mathcal{L} = \begin{cases} \int_f v \cdot n\, p\, ds, & \text{for a set of basis functions } p \in \mathcal{P}_q(f) \text{ for each edge facet f,} \\ \int_T v \cdot p dx, & \text{for a set of basis functions } p \in \text{NED}^1_{q-1}(T), \text{ for } q \geq 2 \end{cases}$

Theorem II.3.2 (Dimension of RT, NED and BDM elements)**.** *The respective dimensions of Raviart=Thomas. Nédélec and Brezzi-Douglas-Marini elements are:*

- $d_{\text{RT}_q} = \begin{cases} q(q+2), & \text{if T be a triangle,} \\ \frac{1}{2}q(q+1)(q+3), & \text{if T be a tetrahedron} \end{cases}$
- $d_{\text{NED}_q} = \begin{cases} (q+1)(q+2), & \text{if T be a triangle,} \\ \frac{1}{2}(q+1)(q+2)(q+3), & \text{if T be a tetrahedron} \end{cases}$
- $d_{\text{BDM}_q} = \begin{cases} (q+1)(q+2), & \text{if T be a triangle,} \\ \frac{1}{2}(q+1)(q+2)(q+3), & \text{if T be a tetrahedron} \end{cases}$

Given a function in $H(\text{curl})$ or $H(\text{div})$, it can be interpolated on each of these finite dimensional elements. The interpolation errors are given in the following theorem.

Theorem II.3.3 (Interpolation error)**.** *Given a function $u \in H(\text{div})$, the Raviart-Thomas and Brezzi-Douglas-Marini interpolators $\Pi^{q,T}_{\text{RT}}$ and $\Pi^{q,T}_{\text{BDM}}$ admit the following respective error bounds:*

- $||u - \Pi^{q,T}_{\text{RT}}||_{H(\text{div})(T)} \leq Ch^q_T |u|_{H^{q+1}(T)}$,
- $||u - \Pi^{q,T}_{\text{RT}}||_{L^2(T)} \leq Ch^q_T |u|_{H^q(T)}$
- $||u - \Pi^{q,T}_{\text{BDM}}||_{H(\text{div}(T)} \leq Ch^q_T |u|_{H^{q+1}(T)}$
- $||u - \Pi^{q,T}_{\text{BDM}}||_{L^2(T)} \leq Ch^{q+1}_T |u|_{H^{q+1}(T)}$

Given a function $u \in H(\text{curl})$, the Nédélec H(curl) interpolator $\Pi^{q,T}_{\text{NED}}$ admits the following error bounds:

- $||u - \Pi^{q,t}_{\text{NED}} u||_{H(\text{curl})(T)} \leq Ch^q_T |u|_{H^{q+1}(T)}$
- $||u - \Pi^{q,t}_{\text{NED}} u||_{L^2(T)} \leq Ch^{q+1}_T |u|_{H^{q+1}(T)}$

II.3.4 Discretization, assembly, solve and warping

We define the finite element subspaces of $\mathbb{H}(\text{div}, \Omega)$, $\mathbf{L}^2(\Omega)$, and $\mathbb{L}^2_{\text{skew}}(\Omega)$, denoted $\mathbb{H}_h(\text{div}, \Omega)$, $\mathbf{L}^2_h(\Omega)$, and $\mathbb{L}^2_{\text{skew},h}(\Omega)$ using the Delaunay triangulation $\mathcal{T}_h$ of the domain Ω, the reunion of BDM elements for $\mathbb{H}_h(\text{div}, \Omega)$, Lagrange elements for $\mathbf{L}^2_h(\Omega)$, and symmetric Lagrange elements for $\mathbb{L}^2_{\text{skew},h}(\Omega)$. Using the basis functions mentioned in the previous subsection, one can express the solution $(\varsigma, (\mathbf{u}, \varepsilon_s, \chi))$

as a linear combination of these basis functions, which, when inputted in the finite dimensional variational formulation, can be assembled into a sparse system:

$$AU = b \tag{II.28}$$

where A is a multilinear form, U a vector of lexicographically ordered nodal values of $(\varsigma, (\mathbf{u}, \varepsilon_s, \chi))$, and b a vector of lexicographically ordered nodal values of the linear form defined in (II.26). This assembly algorithm is implemented in an efficient way in the FEniCS [200] and dolfin libraries [201]. The system can be solved directly through an inversion technique with LU factorization for preconditioning. For stability reasons, we resort to the GMRES krylov subspace method, with again LU preconditioning. Again, FEniCS offers a fast implementation of these solvers. We refer to [202] for further details on the computational aspects.

Chapter III

Measuring displacements from images

This chapter shows how we estimate the intranuclear motion from images of a deforming nucleus. It answers the first problem stated in the second section of chapter 2. We rely on a well-known technique called optical flow [203]. We first review some of the most popular state-of-the-art variational optical flow techniques, and show they do not check the necessary regularity properties stated in chapter 2. We also show that they occasion a detrimental staircasing artifact. We then propose our own optical flow framework. We show that this framework effectively embeds the solution with the right regularity properties in the continuous setting, and circumvents staircasing. We then offer an efficient numerical method to compute it rapidly in the discrete setting. Our optical flow method is systematically evaluated numerically, then applied to study the influence of vimentin filaments on the deformation of glioblastoma nuclei during invasion (this paper is currently under review, see the preprint in [204]).

III.1 State of the art of optical flow techniques

The term *optical flow* was issued for the first time by the American psychologist James J. Gibson [205]. Optical flow then meant the perception of patterns of motion that the environment submits to an observer. For instance, the apparent radial expansion of a field for a man walking straight to it, or the translation of a static scene when he turns his head. While the subsequent debates regarding affordance perception remained in the remit of the psychologist, this very idea of *apparent motion pattern* made its way into the image processing community. A self-driving car, for instance, is bound to evaluate very frequently the optical flow observed by some of its cameras in order to stop in time whenever an "apparent motion" (an oblivious child, for instance) crosses its trajectory [206]. Optical flow has proven also useful in the study of fluid movements, for instance in particle image velocimetry [207] or weather monitoring [208]. However one has to tread carefully: while some components of currently developed optical flow techniques remain useful in our case, the apparent 3D rigid motion of the real world is very different from the elastic deformation of a nucleus, and a simple application of what is available to biological data will simply fail.

III.1.1 Brightness constancy

Denote $I : (\mathbf{x}, t) \to I(\mathbf{x}, t)$ the image intensity function of a video sequence, where t is the discrete variable referring to the frame number, and $t \to \mathbf{x}(t)$ the (eventually 3D) trajectory of each point of the image. The brightness constancy assumption states that the intensity of the image remains constant over time:

$$\frac{dI}{dt} = 0. \tag{III.1}$$

If we suppose the displacement between two frames small enough, the trajectories are differentiable. We may then rightly apply a Taylor expansion around the null vector:

$$\frac{\partial I}{\partial t} + \nabla I \cdot \mathbf{u} = 0, \tag{III.2}$$

where $\mathbf{u} = d\mathbf{x}/dt$ is the velocity field and ∇I the image gradient (see Figure III.1). We call this relation the *optical flow equation*. Now, we made two assumptions: one regarding image intensity, the brightness constancy assumption, and one regarding the displacement field, namely its being close to $\mathbf{0}$. Are we allowed to assume them in our case? We proved in the previous chapter that the physical phenomena ruling the excitation of fluorophores in fluorescence microscopy imaging were deterministic enough to rely on a constancy of each pixel intensity. We also mentioned photobleaching, which could reduce the overall image intensity, but in an homogeneous way, and after proper normalization over time, we may assume that the image intensity remains constant (see Figure III.2). As to the second point, many interesting biological properties are best derived in a linearly elastic mode of deformation, since large deformation might impair, through the mechanisms of mechanotransduction, the mechanical configuration of the nucleus. So we can assume in a sense that the second property is valid as well. However we feel the need to account for larger deformations can be useful, and we will describe shortly after a pyramidal approach to compute larger displacements.

We only have one of it, and yet 2 (or 3) times as much unknowns (the components of the displacement field). This is called the *aperture problem*. Given this constraint alone, we can at best estimate the motion at the gradient direction through the following relation:

$$\mathbf{u} = -\frac{\partial I}{\partial t}\frac{\nabla I}{|\nabla I|^2}. \tag{III.3}$$

There are several way to overcome the *aperture problem*. Block-matching methods, for instance, divide the images into regular patches [209]. A feature extractor like SIFT [210] then assigns a descriptive vector to each of those. These vectors are then paired from one image to another based on a similarity metric tailored with the requirements of the image processing. Once the matching is done, the flow can be recovered through bicubic interpolation [211]. Feature-based methods proceed somewhat similarly, but their features are computed throughout the whole images, and include a variety of information, such as keypoint matches or edges [212]. Others, named phase-based methods, discard the brightness constancy assumption altogether, and instead compute the Fourier transforms of each image [213]. The phase difference between corresponding frequency components is reckoned, and used to reconstruct the flow. But among these classes of methods, one stands above all in popularity and practicality. Horn and Schunck are celebrated for introducing the all-popular variational formulation of optical flow [203]. Instead of solving directly the equations, they change it into a minimization problem by adding a Tikhonov-like regularisation parameter. We will follow the same approach here, and adapt it to our purpose.

The minimization problem is most of the time presented as the sum of two terms: a data term, linked to the optical flow equation, which insures proper warping of the second image unto the first one, and a regularisation term, which penalizes the irregularity of the displacement field in order to single out the number of candidates. Provided these two observe some satisfying regularity properties, the optical flow problem becomes a question of calculus of variation:

$$\mathbf{u} = \underset{\mathbf{u}\in\mathcal{F}(\Omega_I,\mathbb{R}^2)}{\operatorname{argmin}} \quad E_{\text{data}}(\mathbf{u}) + \alpha E_{\text{reg}}(\mathbf{u}), \tag{III.4}$$

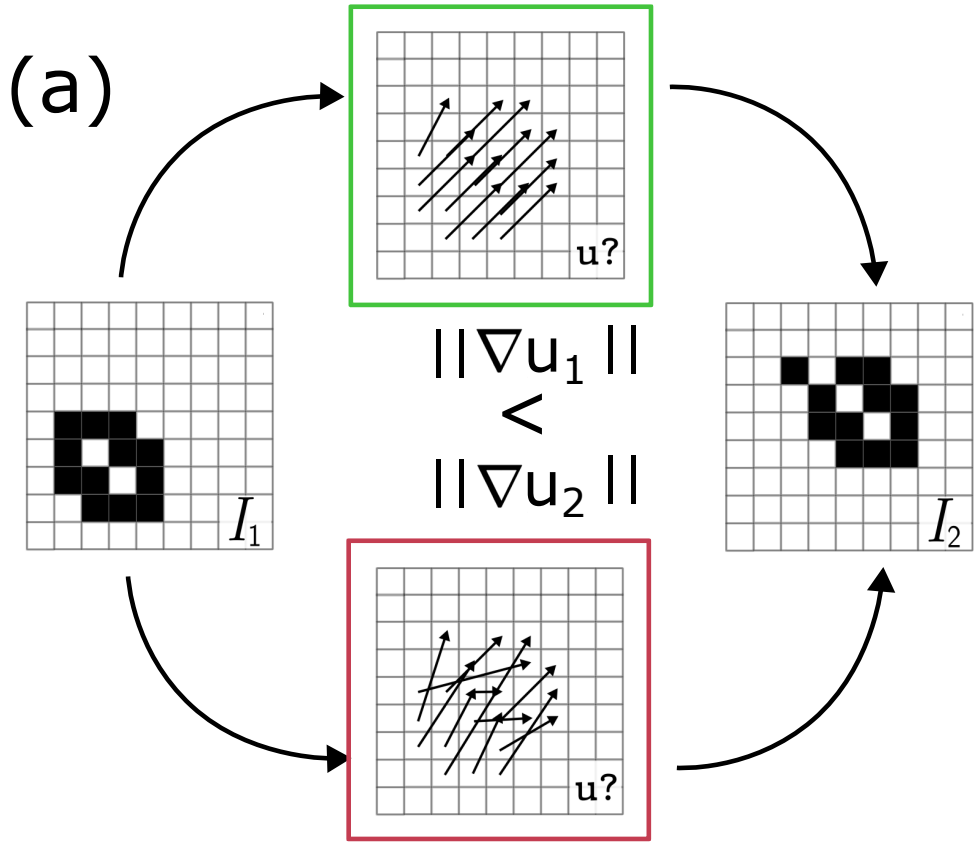

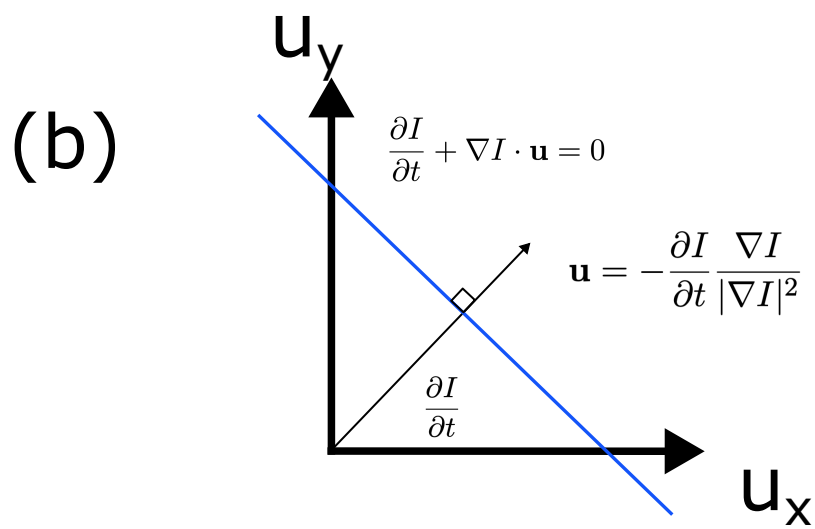

Figure III.1: Variational optical flow problems enforce the brightness constancy assumption and fix the aperture problem. (a) The brightness constancy states that each pixel from the first image on the left will be found likewise on the second image on the right, but there are infinitely many displacement fields that may warp one to the other ; variational optical flow enforces the smoothest displacement fields, here the one in green (adapted from [214]) (b) Linearization of the brightness constancy assumption constrains the optical flow field to a hyperplane in the space of the displacement fields, but it alone cannot determine it entirely (*aperture problem*) except for all the flow that is perpendicular to the isophotes.

where Ω_I is the domain of the image, $\mathcal{F}(\Omega_I, \mathbb{R}^2)$ is the space of real vector valued functions defined over the image domain, and α is a regularisation constant setting a trade-off between regularisation and warping accuracy. Since their introduction, variational frameworks witnessed an extraordinary flourishing of innovations, to the point of making it impossible to present a synthesizing framework that would regroup them all [215]. We wish here to confine our presentation to the exposition of the most popular ones.

We start with the seminal method of Horn and Schunck (HS) which.

III.1.2 Horn Schunck

The HS method proposes to minimize the following functional:

$$J_{HS}(\mathbf{u}) = \int_{\Omega_I} \left(\nabla I \cdot \mathbf{u} + \frac{\partial I}{\partial t} \right)^2 + \alpha ||\nabla \mathbf{u}||^2_{\mathbb{S}_2}, \tag{III.5}$$

where $||\nabla \mathbf{u}||^2_{\mathbb{S}_2}$ is the Frobenius norm of the Jacobian of the displacement field, defined for every $\mathbf{u} = (u, v, w) \in \mathbb{R}^3$ by:

$$||\nabla \mathbf{u}||^2_{\mathbb{S}_2} = ||\nabla u||^2_2 + ||\nabla v||^2_2 + ||\nabla w||^2_2, \tag{III.6}$$

where $||\cdot||_2$ is the L_2 eucledian norm. As always with quadratic terms in minimization problems, the data is expected to follow a Gaussian distribution. This makes the method particularly sensitive to outliers, for instance at object boundaries where the motion plunges at edges. This is the main reason why the subsequent methods prefer other more robust norms. However we will see that the HS method does not have it so bad in the context of linear elasticity – for instance, it does not suffer from the staircasing effect, but this is the discussion of the next section. Because of the regularity properties of the appearing norms, one may derive easily the Euler-Lagrange equations, which in 3D read:

$$\begin{aligned}
\frac{\partial I}{\partial x}^2 u_x + \frac{\partial I}{\partial x}\frac{\partial I}{\partial y} u_y + \frac{\partial I}{\partial x}\frac{\partial I}{\partial z} u_z &= \alpha \operatorname{div}(\nabla u_x) - \frac{\partial I}{\partial x}\frac{\partial I}{\partial t} \\
\frac{\partial I}{\partial x}\frac{\partial I}{\partial y} u_x + \frac{\partial I}{\partial y}^2 u_y + \frac{\partial I}{\partial y}\frac{\partial I}{\partial z} u_z &= \alpha \operatorname{div}(\nabla u_y) - \frac{\partial I}{\partial y}\frac{\partial I}{\partial t} \\
\frac{\partial I}{\partial x}\frac{\partial I}{\partial z} u_x + \frac{\partial I}{\partial y}\frac{\partial I}{\partial z} u_y + \frac{\partial I}{\partial z}^2 u_z &= \alpha \operatorname{div}(\nabla u_z) - \frac{\partial I}{\partial z}\frac{\partial I}{\partial t}
\end{aligned} \tag{III.7}$$

The Laplacian at $\mathbf{u}$ measures how much the average value of $\mathbf{u}$ over a small sphere surrounding it differs from the the actual value of $\mathbf{u}$. Noting $\overline{u}_i$ for $i = x, y, z$ their respective local average, we may write:

$$\begin{aligned}
\operatorname{div}(\nabla u) &\approx \overline{u} - u, \\
\operatorname{div}(\nabla v) &\approx \overline{v} - v, \\
\operatorname{div}(\nabla w) &\approx \overline{w} - w.
\end{aligned} \tag{III.8}$$

After proper rearrengement, the iterative solution appears clearly by repetitive application of this relation. The value of the displacement field at iteration k is determined by:

$$\begin{aligned}
u^{k+1} &= \overline{u}^k - \frac{\frac{\partial I}{\partial x}\left(\frac{\partial I}{\partial x}\overline{u}^k + \frac{\partial I}{\partial y}\overline{v}^k + \frac{\partial I}{\partial z}\overline{w}^k + + \frac{\partial I}{\partial t}\right)}{\alpha + \frac{\partial I}{\partial x}^2 + \frac{\partial I}{\partial y}^2 + \frac{\partial I}{\partial z}^2}, \\
v^{k+1} &= \overline{v}^k - \frac{\frac{\partial I}{\partial y}\left(\frac{\partial I}{\partial x}\overline{u}^k + \frac{\partial I}{\partial y}\overline{v}^k + \frac{\partial I}{\partial z}\overline{w}^k + + \frac{\partial I}{\partial t}\right)}{\alpha + \frac{\partial I}{\partial x}^2 + \frac{\partial I}{\partial y}^2 + \frac{\partial I}{\partial z}^2}, \\
w^{k+1} &= \overline{w}^k - \frac{\frac{\partial I}{\partial z}\left(\frac{\partial I}{\partial x}\overline{u}^k + \frac{\partial I}{\partial y}\overline{v}^k + \frac{\partial I}{\partial z}\overline{w}^k + + \frac{\partial I}{\partial t}\right)}{\alpha + \frac{\partial I}{\partial x}^2 + \frac{\partial I}{\partial y}^2 + \frac{\partial I}{\partial z}^2}.
\end{aligned} \tag{III.9}$$

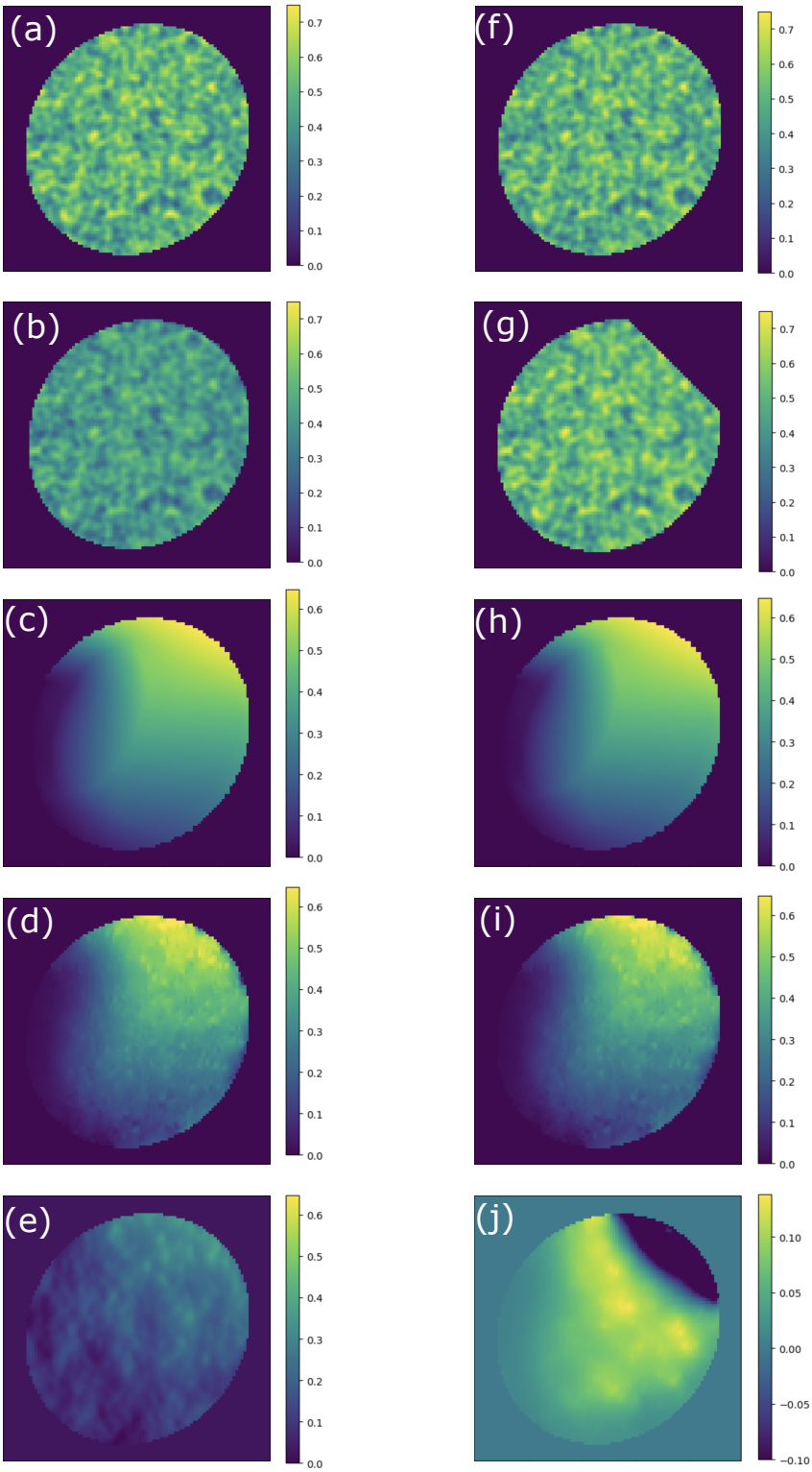

Figure III.2: Two cases where optical flow fails: illumination change and occlusion.
Left column: optical flow computation with simulated photobleaching. (a) First image before deformation ; (b) Second image after finite element deformations (see first section of chapter 3) and after illumination attenuation to simulate photobleaching ; (c) true displacement field in y ; (d) y-component of the displacement field obtained Horn-Schunck optical flow when photobleaching isn't simulated (e) y-component of the displacement field obtained Horn-Schunck optical flow when photobleaching is simulated. Right column: optical flow computation with simulated occlusion. (f) First image before deformation ; (g) second image after finite element deformations and with occluded tip ; (h) true y-coomponent of the displacement field ; (i) y-component of the displacement field obtained by Horn-Schunck optical flow without simulated occlusion ; (j) y-component of the displacement field obtained by Horn-Schunck optical flow with simulated occlusion

We also mention the finite difference filters employed by Horn and Schunck. While many methods used centered first order derivatives of the second image for computing the image gradient, we find that their seminal scheme produces more accurate results. This is probably due to the smoothing over time that they incorporate, which is lacking in other configurations. Since we are to use it consistently during our implementation, we detail it here once and for all. Given a four dimensional point $(\mathbf{x}, t)$, the image derivative at this point is computed as the mean of the forward first order finite differences in each dimension:

$$\begin{aligned}
\frac{\partial I}{\partial x}(x,y,z,t) \approx \frac{1}{8}(&I_{x+1,y,z,t} - I_{x,y,z,t} + I_{x+1,y+1,z,t} - I_{x,y+1,z,t} \\
&+ I_{x+1,y,z,t+1} - I_{x,y,z,t+1} + I_{x+1,y+1,z,t+1} - I_{x,y+1,z,t+1} \\
&+ I_{x+1,y,z+1,t} - I_{x,y,z+1,t} + I_{x+1,y+1,z+1,t} - I_{x,y+1,z+1,t} \\
&+ I_{x+1,y,z+1,t+1} - I_{x,y,z+1,t+1} + I_{x+1,y+1,z+1,t+1} - I_{x,y+1,z+1,t+1}) \\
\frac{\partial I}{\partial y}(x,y,z,t) \approx \frac{1}{8}(&I_{x,y+1,z,t} - I_{x,y,z,t} + I_{x+1,y+1,z,t} - I_{x+1,y,z,t} \\
&+ I_{x,y+1,z+1,t+1} - I_{x,y,z+1,t+1} + I_{x+1,y+1,z+1,t+1} - I_{x+1,y,z+1,t+1} \\
&I_{x,y+1,z+1,t} - I_{x,y,z+1,t} + I_{x+1,y+1,z+1,t} - I_{x+1,y,z+1,t} \\
&+ I_{x,y+1,z+1,t+1} - I_{x,y,z+1,t+1} + I_{x+1,y+1,z+1,t+1} - I_{x+1,y,z+1,t+1}) \\
\frac{\partial I}{\partial z}(x,y,z,t) \approx \frac{1}{8}(&I_{x,y,z+1,t} - I_{x,y,z,t} + I_{x+1,y,z,t} - I_{x,y,z,t} \\
&+ I_{x,y,z+1,t+1} - I_{x,y,z,t+1} + I_{x+1,y,z+1,t+1} - I_{x+1,y,z,t+1} \\
&+ I_{x,y+1,z+1,t} - I_{x,y+1,z,t} + I_{x+1,y+1,z,t} - I_{x,y+1,z,t} \\
&+ I_{x,y+1,z+1,t+1} - I_{x,y,z,t+1} + I_{x+1,y+1,z+1,t+1} - I_{x+1,y+1,z,t+1}) \\
\frac{\partial I}{\partial t}(x,y,z,t) \approx \frac{1}{8}(&I_{x,y,z,t+1} - I_{x,y,z,t} + I_{x+1,y,z,t+1} - I_{x+1,y,z,t} \\
&+ I_{x,y+1,z,t+1} - I_{x,y+1,z,t} + I_{x+1,y+1,z,t+1} - I_{x+1,y+1,z,t} \\
&+ I_{x,y,z+1,t+1} - I_{x,y,z+1,t} + I_{x+1,y,z+1,t+1} - I_{x+1,y,z+1,t} \\
&+ I_{x,y+1,z+1,t+1} - I_{x,y+1,z+1,t} + I_{x+1,y+1,z+1,t+1} - I_{x+1,y+1,z+1,t})
\end{aligned} \tag{III.10}$$

The local averages are estimated from the immediate neighboring pixels. The pixels on the diagonal are taken to be farther away in order to emulate a Euclidean-like distance. Unlike with image derivatives, the Laplace operator is estimated spatially only. We have then for any point $(\mathbf{x}, t)$:

$$\begin{aligned}
\overline{u}_{x,y,z,t} = &\frac{1}{6}\left(u_{x-1,y,z,t} + u_{x+1,y,z,t} + u_{x,y-1,z,t} + u_{x,y+1,z,t} + u_{x,y,z-1,t} + u_{x,y,z+1,t}\right) \\
&+ \frac{1}{12}\left(u_{x-1,y-1,z,t} + u_{x+1,y+1,z,t} + u_{x-1,y+1,z,t} + u_{x+1,y-1,z,t}\right) \\
&+ \frac{1}{24}\left(u_{x-1,y-1,z-1,t} + u_{x+1,y+1,z+1,t} + u_{x-1,y+1,z-1,t} + u_{x+1,y-1,z-1,t}\right),
\end{aligned} \tag{III.11}$$

and the same goes as well for $\overline{v}$ and $\overline{w}$.

The initial Horn-Schunck optical flow did not account for large displacements motions – typically above one pixel. Yet it is easily adaptable to a multi-scale strategy, detailed first in [216] (see Figure III.3). In this case, the brightness constancy equation (III.1) can be replaced with a nonlinear counterpart:

$$I(\mathbf{x}, t_1) - I(\mathbf{x} + \mathbf{u}, t_2) = 0, \tag{III.12}$$

for every four dimensional point $(\mathbf{x}, t)$. Should $\mathbf{u}$ be small, we could linearize $I(\mathbf{x} + \mathbf{u}, t_2)$ through Taylor expansions, and obtain again the optical flow equations (III.2). However this is not allowed for

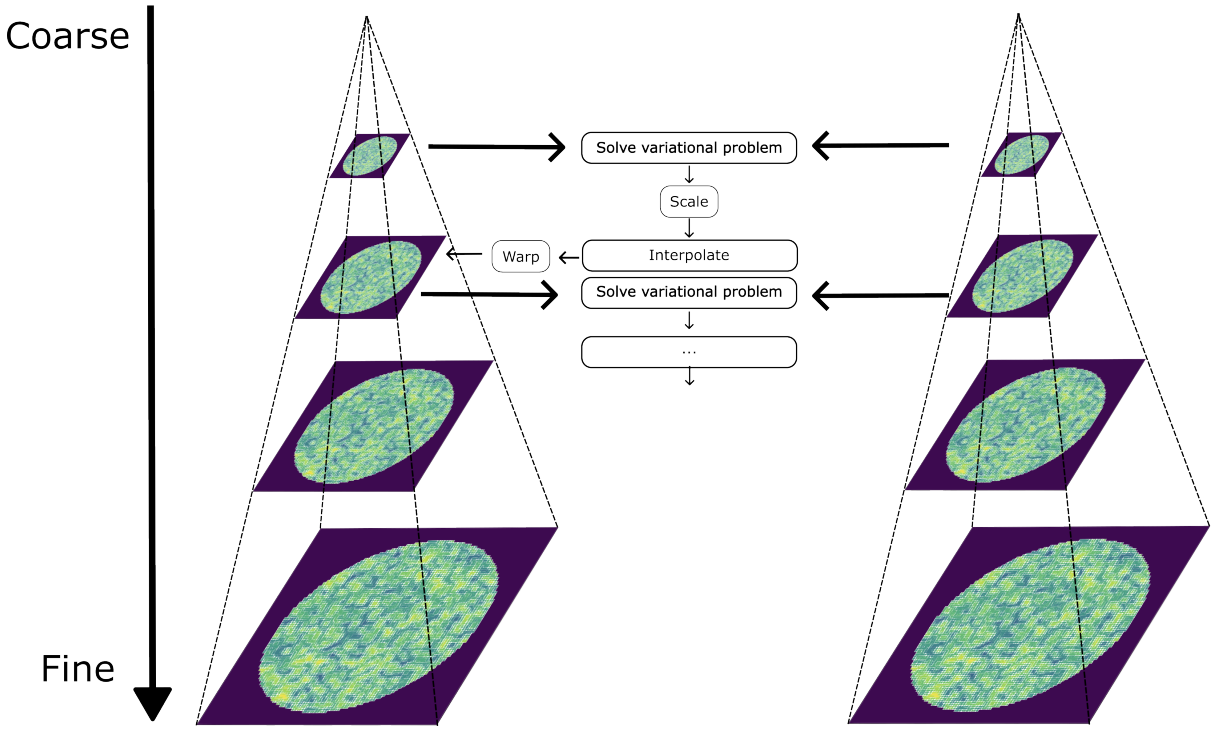

Figure III.3: Large displacement estimation in optical flow: a multiresolution strategy. Images before and after deformations are blurred and downsampled successively until the obtained coarse images monitor 1-pixel motions ; the optical flow is then solved iteratively from the coarsest level to the finest, with scaling between each level for initialization.

large motions. But if by any chance we had some motion estimation $\mathbf{u}^*$ close to $\mathbf{u}$, we could linearize it around this point, and the energy to be minimized reads:

$$J_{HS}(\mathbf{u}) = \int_{\Omega_I} \left(I(\mathbf{x}, t_1) - I(\mathbf{x} + \mathbf{u}^*, t_2) \cdot (\mathbf{u} - \mathbf{u}^*) + \nabla I(\mathbf{x} + \mathbf{u}^*, t_2)(\mathbf{u} - \mathbf{u}^*)\right)^2 + +\alpha ||\nabla \mathbf{u}||^2_{\mathbb{S}_2} \tag{III.13}$$

Now, how to get this motion estimation $\mathbf{u}^*$? Suppose that some pixels within the images move significantly, say ten pixels. If you downsample the images, larger pixels will replace the original pixels, and the same motion can be accounted with less but bigger pixels, say seven. Repeat this process of downsampling enough times, and eventually you will find images where the pixels are so large that the motion you try to estimate is at subpixel level. More precisely, given an image pair $I(\mathbf{x}, t_1)$, $I(\mathbf{x}, t_2)$, one creates for each an image pyramid by downsampling by a factor of $\eta \in]0, 1[$. To avoid aliasing, one first blurs the images, so that image $I^s(\eta\mathbf{x}, \mathbf{t^1})$ at scale s follow:

$$\begin{aligned} I^s(\eta\mathbf{x}, t_1) &= G_\sigma * I^{s-1}(\mathbf{x}, t_1) \\ I^s(\eta\mathbf{x}, t_2) &= G_\sigma * I^{s-1}(\mathbf{x}, t_2), \end{aligned} \tag{III.14}$$

where the images are sampled using bicubic interpolation. Note that the sampling and the smoothing should be matched according to a Gaussian distribution. Indeed, if the downsampling factor is close to 1, then the smoothing should be minimal, whereas if it is close to 0, it should be consequential. Given the standard deviation σ of the gaussian kernel, we may chose:

$$\sigma(\eta) = \sigma_0 \sqrt{\eta^{-2} - 1}, \tag{III.15}$$

where $\sigma_0 = 0.6$ is an empirically justified choice [217].

Once in the possession of the two image pyramids, we first compute the motion field $\mathbf{u}^0$ at the coarsest level using the previously detailed iteration steps. We then rescale this motion field to the next coarser level with:

$$\mathbf{u}^1 = \frac{1}{\eta}\mathbf{u}^0(\eta\mathbf{x}), \tag{III.16}$$

and use the motion $\mathbf{u}^1$ as initialization for the scale of the image pyramid. This process is repeated down to the finest scales, and overall the algorithm yields accurate estimation of large displacements.

One of the downsize of the Horn Schunck optical flow estimation method is that it penalizes quadratic functions of the displacement fields. One can easily show, by the continuity of both the data term and the regularisation term, that the resulting flow field belongs to $H^1(\Omega, \mathbb{R}^2)$. This means the flow cannot admit sharp discontinuities, even at the boundaries of objects. The total variation was precisely introduced to overcome this inconveniency.

III.1.3 TV-L1

It is with this requirement on the regularity property in mind that we introduce the following definition of the total variation.

Definition III.1.1 (Total Variation)**.** *The total variation of a scalar function $u \in L^1_{loc}(\Omega, \mathbb{R})$ is defined by duality:*

$$\mathrm{TV}(u) = \sup\left\{-\int_{\Omega_I} u \,\mathrm{div}\phi \, dx : \ \phi \in C_c^\infty(\Omega, \mathbb{R}^3), |\phi(x)| \leq 1, \ \forall x \in \Omega\right\} \tag{III.17}$$

This duality definition allows us to restrict the solution to the space of bounded variations, which is the space containing every locally integrable functions with $\mathrm{TV}(u) < +\infty$. But we may retrieve the simple primal formulation in the case where $u \in W^{1,1}(\Omega)$. Then the weak gradient is correctly defined and we have by duality:

$$-\int_{\Omega_I} u \,\mathrm{div}\, \phi dx = \int_{\Omega_I} \nabla u \phi dx \tag{III.18}$$

which we see gives $\mathrm{TV}(u) = \int_{\Omega_I} |\nabla u| dx$.

The total variation is defined as the sup of linear forms. Given $u \in L^1(\Omega, \mathbb{R})$ and a sequence $(u_n)_{n\in\mathbb{N}}$ of bounded variations converging weakly to it in $L^1(\Omega, \mathbb{R})$, we have that:

$$\mathrm{TV}(u) \leq \liminf_{n\to+\infty} \mathrm{TV}(u_n) \tag{III.19}$$

Likewise, we may show that it is *convex*, *one-homogeneous* and *rotation invariant*. In other words, it does not depend on the frame of reference, and if inputted into a variational framework as a regulariser it is ensured to converge to a unique solution, provided the data term follows similar properties.

Therefore, the TV-L1 optical flow method minimizes the following functional to compute the displacement field between two frames:

$$J_{\mathrm{TV}}(\mathbf{u}) = \int_{\Omega_I} |I(\mathbf{x}, t_1) - I(\mathbf{x} + \mathbf{u}, t_2)| + \alpha(\mathrm{TV}(u) + \mathrm{TV}(v) + \mathrm{TV}(w)), \tag{III.20}$$

where $\mathbf{u} = (u, v, w)$ is the displacement field, t_1 and t_2 the time point of the frames, and α a regularisation constant. Just like in the Horn Schunck method, the data term is destined to be linearized and imbedded in a multiscale strategy to account for larger displacement fields. It has, unlike it, the additional property of estimating sharp discontinuities at the nucleus' boundary (see Figure III.4)

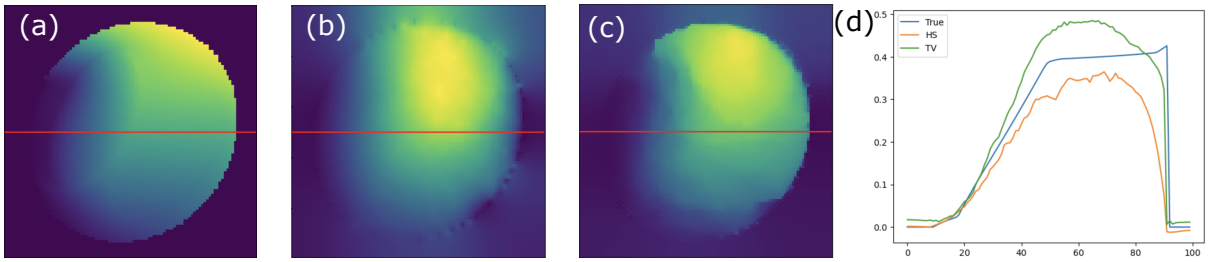

Figure III.4: Total Variation optical flow sharply delineates objects' boundaries. The total variation regulariser constrains the displacement field to belong to the space of functions of bounded variations, which admit discontinuities at objects' boundaries. (a) Simulated y-component of the true displacement field ; (b) y-component of the displacement field obtained with Horn-Schunck optical flow ; (c) y-component of the displacement field obtained with TV-L1 optical flow ; (d) Displacement profiles following the red line.

We now detail its minimization procedure, as some key notions will be used for our own optical flow method. Contrary to the Horn Schunck method, neither the data term nor the regularisation term are differentiable. However the problem can be rearranged into a saddle-point formulation. Given two Hilbert spaces $\mathcal{X}, \mathcal{Y}$, two proper convex lower-semicontinuous functions $G : \mathcal{X} \to [0, +\infty[$, $F^* : \mathcal{Y} \to [0, +\infty[$, a continuous linear operator $K : \mathcal{X} \to \mathcal{Y}$, these optimization problems are of the form:

$$\min_{x \in \mathcal{X}} \max_{y \in \mathcal{Y}} \langle Kx, y \rangle + G(x) - F^*(y). \tag{III.21}$$

They are efficiently solved through a primal-dual gradient method proposed by Chambolle and Pock (see Algorithm (1)) [218]. It consists of an ascend step in the dual variable, and a descent step in the primal variable, with a relaxation parameter of the primal variable to allow convergence.

In our case, because the total variation is defined in a dual way, the saddle-point formulation naturally comes as:

$$\min_{\mathbf{u} \in L^1(\Omega_I, \mathbb{R}^2)} \max_{\mathbf{p} \in L^1(\Omega_I, \mathbb{R}^4)} \langle \nabla \mathbf{u}, p \rangle_{L^1(\Omega_I, \mathbb{R}^4)} + \frac{1}{\alpha} |I(\mathbf{x}, t_1) - I(\mathbf{x} + \mathbf{u}, t_2)| - \delta_P(\mathbf{p}), \tag{III.22}$$

where the vector space $L^1(\Omega_I, \mathbb{R}^4)$ is endowed with the natural inner product $\langle p, q \rangle_{L^1(\Omega_I, \mathbb{R}^4)} = \int_{\Omega_I} p_1 q_1 + p_2 q_2 + p_3 q_3 + p_4 q_4 dx$, $P = \{p \in L^1(\Omega_I, \mathbb{R}^4) : \ ||p||_\infty \leq 1\}$ is its unit ball for the infinity norm, and δ_P the indicator functions of the set P (taking an infinity value outside of it).

Although neither of the terms are differentiable, the second and the third ones admit an explicit proximal operator (see Figure III.5.a.).

Definition III.1.2 (Proximal operator)**.** *Given a proper, lower semi-continuous, and convex real-valued function f defined on $\mathbb{R}^3$, and $\lambda \in \mathbb{R}$ a constant, its proximal operator is the function defined for every $\mathbf{v} \in \mathbb{R}^3$ as:*

$$\text{prox}_f(\mathbf{v}) = \underset{\mathbf{u} \in \mathbb{R}^3}{\text{argmin}} \left(f(\mathbf{u}) + \frac{1}{2\lambda} ||\mathbf{u} - \mathbf{v}||_2^2 \right). \tag{III.23}$$

Note that this definition extends easily to Hilbert spaces (and even to general Banach spaces, if we are ready to make some concessions in the optimization scheme [219]). The proximal operator is known to be a generalization of the orthogonal projection (see figure III.5). Indeed, if you take the indicator function of any set $X \subset \mathbb{R}^N$:

$$\chi_X(u) = \begin{cases} 0, & \text{if } u \in X \\ +\infty, & \text{if } u \notin X \end{cases} \tag{III.24}$$

then its proximal becomes naturally the orthogonal projection on the said set X. Most of the functions we wish to optimize are based on norms, which are for many separable. In this case, the proximal can

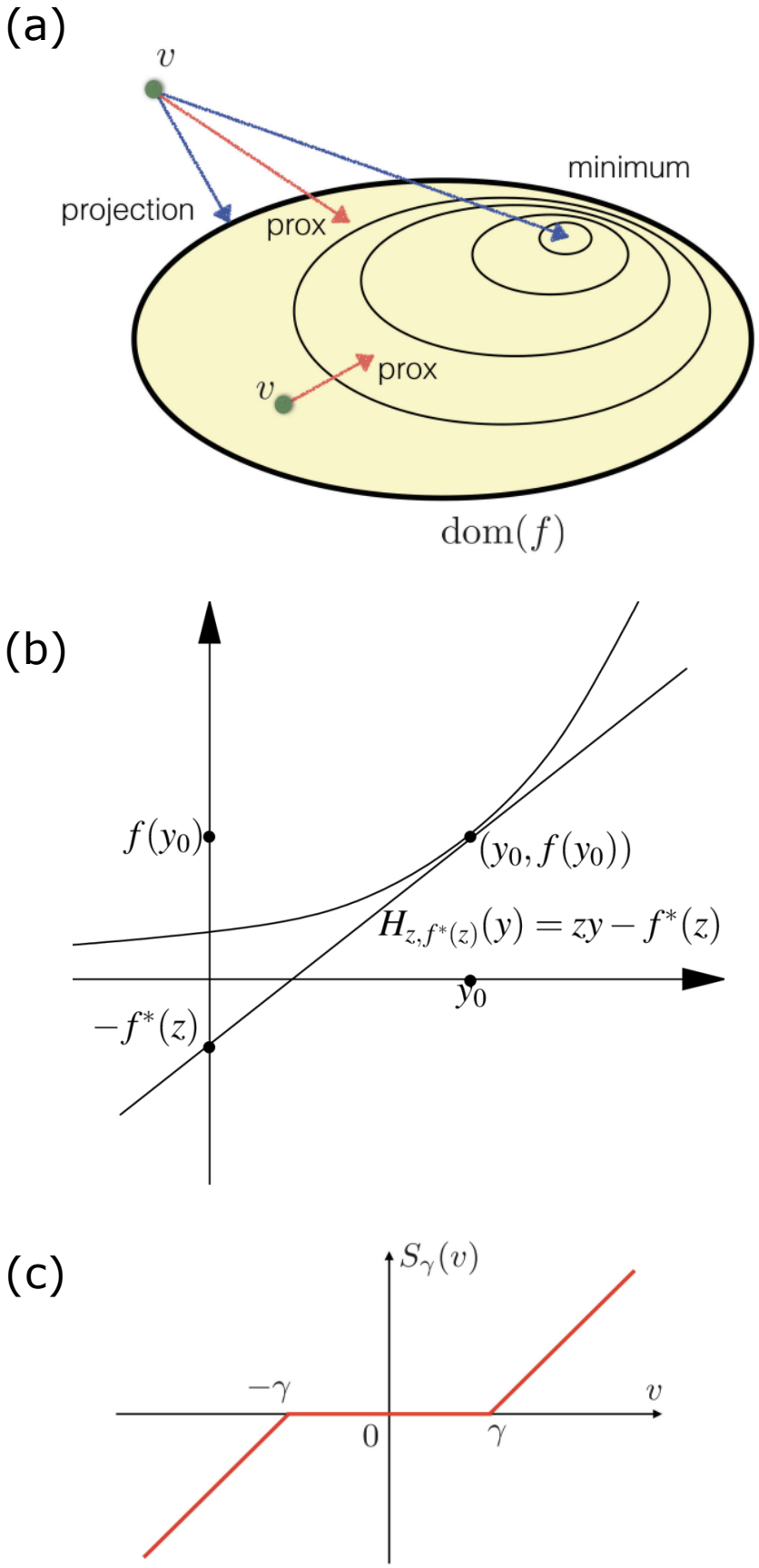

Figure III.5: Proximal operator, Legendre-Fenchel conjugate, Soft-thresholding. (a) Action of the proximal operator on vectors v. If the vector belongs outside the domain of f, it is directly projected onto it, but if it's already within, it approaches the minimum of f, with a Tikhonov trade-off to its original location ; (b) Legendre-Fenchel conjugate of a convex real function f. A convex function is best described by its epigraph, which is locally described by its tangential hyperplane, of which the intersecting point to the ordinary axis defined the conjugate ; (c) soft-thresholding of a single scalar.

be easily computed as the reunion of the separate proximals of its decomposition. Given a function f defined by:

$$f(\mathbf{u}) = \sum_{i=1}^{3} f_i(u_i),$$

for every $\mathbf{u} \in \mathbb{R}^3$, the proximal of f is given for any $\lambda \in \mathbb{R}^3$ by:

$$\text{prox}_{\lambda f}(\mathbf{u}) = (\text{prox}_{\lambda_i} f_i(u_i))_{i=1,\dots,3}$$

The proximal operator of a given function is not always easy to compute. Sometimes, as in the case of TV, it is more convenient to find the explicit formulation of its Legendre-Fenchel conjugate [220] (see Figure III.5.b.).

Definition III.1.3 (Legendre-Fenchel conjugate)**.** *Given a real-valued function f defined on $\mathbb{R}^3$, its Legendre-Fenchel conjugate f^* is defined for every $\mathbf{v} \in \mathbb{R}^3$ by:*

$$f^*(\mathbf{v}) = \sup \left\{ \langle \mathbf{u}, \mathbf{v} \rangle - f(\mathbf{v}) \ : \ \mathbf{u} \in \mathbb{R}^3 \right\}, \tag{III.25}$$

The proximal operators of a function and of its Legendre-Fenchel conjugate are tightly linked through the Moreau identity.

Definition III.1.4 (Moreau identity)**.** *Given $f : \mathbb{R}^3 \to \mathbb{R}$ and f^* its Legendre-Fenchel conjugate, $\lambda \in \mathbb{R}$ a constant, the following relation holds for any $\mathbf{u} \in \mathbb{R}^3$:*

$$\mathbf{u} = \text{prox}_{\lambda f}(\mathbf{u}) + \lambda \text{prox}_{f/\lambda}(\frac{\mathbf{u}}{\lambda}). \tag{III.26}$$

Using these handful properties, we may compute the proximal operators of the data term appearing in the above saddle-point problem (see Figure III.5.c.)).

Theorem III.1.1 (Soft-thresholding)**.** *Let $\alpha > 0$, $t_2 > t_1 > 0$, $\mathbf{u}^* \in \mathcal{F}(\mathbb{R}^3, \mathbb{R}^{\nvDash})$ and $\rho : \mathcal{F}(\mathbb{R}^3, \mathbb{R}^{\nvDash}) \to \mathbb{R}$ defined for every $\mathbf{u} \in \mathcal{F}(\mathbb{R}^3, \mathbb{R}^2)$ close to $\mathbf{u}^*$ by:*

$$\rho(\mathbf{u}) = \frac{1}{\alpha} \int_{\Omega_I} |I(\mathbf{x}, t_1) - I(\mathbf{x} + \mathbf{u}^*, t_2) \cdot (\mathbf{u} - \mathbf{u}^*) - \nabla I(\mathbf{x} + \mathbf{u}^*, t_2)(\mathbf{u} - \mathbf{u}^*)| dx.$$

Then we have for any $\lambda > 0$:

$$\text{prox}_{\lambda\rho}(\mathbf{u}) = \mathbf{u} + \begin{cases} \lambda\alpha\nabla I(\mathbf{x}+\mathbf{u}), & \text{if } \rho(\mathbf{u}) < -\lambda\alpha|\nabla I(\mathbf{x}+\mathbf{u})|^2 \\ -\lambda\alpha\nabla I(\mathbf{x}+\mathbf{u}), & \text{if } \rho(\mathbf{u}) > \lambda\alpha|\nabla I(\mathbf{x}+\mathbf{u})|^2 \\ \rho(\mathbf{u})\dfrac{\nabla I(\mathbf{x}+\mathbf{u})}{|\nabla I(\mathbf{x}+\mathbf{u})|^2}, & \text{if } |\rho(\mathbf{u})| \leq -\lambda\alpha|\nabla I(\mathbf{x}+\mathbf{u})|^2 \end{cases} \tag{III.27}$$

We call this function soft thresholding.

To compute the displacement field at a scale s, we may just apply Algorithm 1 with the previous proximal operators. One can see in figure III.4 that the TV-L1 optical flow indeed preserves sharper boundary in its reconstruction.

Algorithm 1 First order primal-dual gradient descent [218]

Input: $\tau, \sigma > 0, \theta \in [0,1]$, $(x^0, y^0) \in \mathcal{X} \times \mathcal{Y}$, $\overline{x}_0 = x_0$, N_{iter}

$k \leftarrow 0$
while $k < N_{\text{iter}}$ **do**
  $y^{n+1} \leftarrow \text{prox}_{\sigma F^*}(y^n + \sigma K \overline{x}^n)$
  $x^{n+1} \leftarrow \text{prox}_{\tau G}(x^n - \tau K^* y^{n+1})$
  $\overline{x}^{n+1} \leftarrow x^{n+1} + \theta(x^{n+1} - x^n)$
  $k \leftarrow k + 1$
end while

III.1.4 Large Displacement Optical Flow

LDOF tackles the problem of small objects movements. When confronted to large motions, we saw that a common technique is to use a coarse-to-fine pyramid to reduce the number of pixels within the image. Unfortunately small objects tend to be wiped off during the process, and utterly disappear at the coarsest scales. This optical flow method proposes to leverage descriptor matchings (which work for motions beyond a single pixel) in the optical flow computation. To capture smaller features, the authors proceed to a hierarchical clustering of the image, which has the advantage of strengthening the correspondence of the movement between similar regions. They rely on the boundary detector *gPb* [221], which returns a map of regions $\mathbf{x} \to g(\mathbf{x})$ within the images, with greater values of edges at the object's boundaries than between its different distinctive regions (see figure III.6). To avoid artefacts due to image intensity discrepancies, each region is included into a 32×32 sized patch, then normalized within it. To each region is also associated two descriptors, S and C. The first computes oriented histograms within the region (like in Histogram of Oriented Graph), the second their mean RGB color. The distance between patches is then computed through simple Eucledian distances, normalized over each patch distances, and the final distance is taken as the mean of the two:

$$\begin{aligned} d^2(S_i, S_j) &= \frac{||S_i - S_j||_2^2}{\frac{1}{N}|\sum_{k,l} ||S_k - S_l||_2^2} \\ d^2(C_i, C_j) &= \frac{||C_i - C_j||_2^2}{\frac{1}{N}|\sum_{k,l} ||C_k - C_l||_2^2} \\ d^2(i,j) &= \frac{1}{2}(d^2(S_i, S_j) + d^2(C_i, C_j)). \end{aligned} \tag{III.28}$$

These matching techniques are proven to perform badly in presence of deformation. This is why a corrective term to small shifts is required. This is provided again thanks to a Horn-Schunck like optimization problem. Denoting two patches P_1 and P_2, the shifting $\mathbf{u}$ is computed as the minimizer of the following functional:

$$E(\mathbf{u}) = \int (P_2(\mathbf{x} + \mathbf{u}) - P_1(\mathbf{x}))^2 d\mathbf{x} + \alpha \int |\nabla \mathbf{u}|_{\mathbb{S}_2}^2 \tag{III.29}$$

Unlike Horn-Schunck however, the regularisation parameter is set very high since it is very easy to match two patches. To limit computation time, the shifting is computed only for the 10 nearest neighbors as defined with distance d.

The motion is then derived as an approximation of the resulting shifts, along with the classical TV-L1 optical flow terms. To leverage easier optimization schemes, the L1 norm as well as the TV are replaced by a differentiable surrogate, namely: $s \to \Psi(s^2) = \sqrt{s^2 + \epsilon}$, where ϵ is taken close to zero. Likewise an image gradient similarity term, as well as a regularisation of the patches, are added:

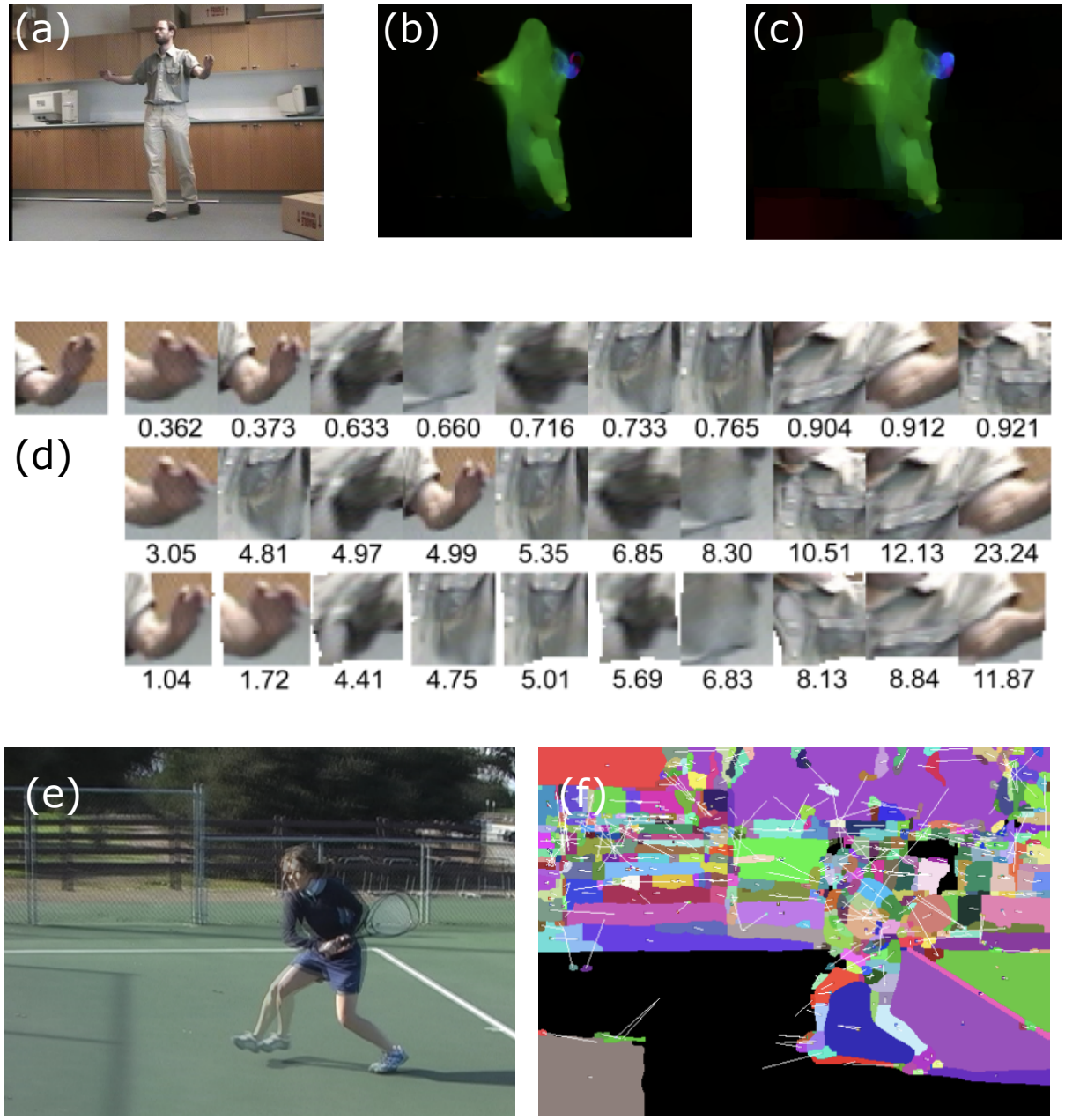

Figure III.6: Overview of Large Displacement Optical Flow (a) Image of a sequence where the person is stepping forward and moving his hands ; (b) the optical flow estimated with the method from [216] is quite accurate for the main body and the legs, but the hands are not accurately captured ; (c) LDOF on the other hand captures accurately the hand's movement ; (d) Nearest neighbors and their distances using different descriptors. Top: SIFT and color. Center: Patch within region. Bottom: Patch within region after distortion correction ; (e) Two overlaid images of a tennis player in action (f) Region correspondences (adapted from [222]).

$$\begin{aligned}\mathbf{w} = \underset{\mathbf{w}}{\operatorname{argmin}} \int & \Psi(|I(\mathbf{x}+\mathbf{w},t_2) - I(\mathbf{x},t_1)|^2 d\mathbf{x} \\ & + \gamma \int \Psi(|\nabla I(\mathbf{x}+\mathbf{w}(\mathbf{x}),t_2) - \nabla I(\mathbf{x},t_1)|^2) d\mathbf{x} \\ & + \beta \sum_{j=1}^{5} \int \rho_j(\mathbf{x}) \Psi\left(||\mathbf{u}(\mathbf{x}) - \mathbf{w}(\mathbf{x})||_2^2\right) d\mathbf{x} \\ & + \alpha \int \Psi\left(||(\nabla \mathbf{u}(\mathbf{x}), g(\mathbf{x})||_{\mathbb{S}_2}^2 d\mathbf{x}\right),\end{aligned} \tag{III.30}$$

where γ, β, α are regularisation constants and where:

$$\rho_j(\mathbf{x}) = \begin{cases} 0, & \text{if there is no correspondance} \\ \dfrac{\overline{d}^2(i) - d^2(i,j)}{d^2(i,j)}, & \text{else} \end{cases} \tag{III.31}$$

The terms are all differentiable, so one can resort to the same minimization strategy as laid out for Horn Schunck. We refer the reader to the reference ([216]) for an explicit formulation.

III.1.5 eFOLKI

eFOLKI [223] was not designed for accuracy, but for speed. It turned out that it has, in some respect, both. Real 3D motion is very different from elastic motion in microscopy. Some optical flow methods, which are foremost in standardized benchmarks – often with the view of improving robotic activities or self-driving cars –, perform actually very poorly in our context. eFOLKI is one of those methods that profit from this change, and we include it in our review as well as for future comparisons.

It relies on a dense estimation of flow field based on the Lucas-Kanade algorithm [224]. Unlike the previously mentioned algorithm, the Lucas-Kanade performs a local evaluation of the displacement field. Given a set of windows $\mathcal{S}$ of the images, it minimizes the following functional:

$$J(\mathbf{u},\mathbf{x}) = \sum_{\mathbf{x}' \in \mathcal{S}} w(\mathbf{x}' - \mathbf{x})(I(\mathbf{x}',t_1) - I(\mathbf{x}' + \mathbf{u}(\mathbf{x}),t_2))^2, \tag{III.32}$$

where w is a separable weighting function with compact support $\mathcal{W}$ centered around $\mathbf{x}$. Like for TV and HS, this functional is linearized around an estimated flow field $\mathbf{u}^*$ from a multiscale strategy:

$$J(\mathbf{u},\mathbf{x}) = \sum_{\mathbf{x}' \in \mathcal{S}} w(\mathbf{x}-\mathbf{x}')(I(\mathbf{x}',t_1) - I(\mathbf{x}'+\mathbf{u}^*(\mathbf{x}),t_2) - \nabla I(\mathbf{x}'+\mathbf{u}^*(\mathbf{x}),t_2)^T(\mathbf{u}(\mathbf{x}) - \mathbf{u}^*(\mathbf{x})))^2. \tag{III.33}$$

It is common to replace $\nabla I(\mathbf{x}' + \mathbf{u}^*(\mathbf{x}),t_2)^T$ by $\nabla I(\mathbf{x}')$ in order to delete the warping operation which adds a little bit of time. Solving either equation requires nonetheless several interpolations for each pixel, since they will inevitably be shared by several supports. The authors propose a method somewhat similar to Iterative Warping Schemes [225]. It consists of four steps, which we reproduce here:

$$\begin{aligned} I^*(\mathbf{x}) &= I_2(\mathbf{x} + \mathbf{u}^*(\mathbf{x})), \\ \delta I^k(\mathbf{x}) &= I^k(\mathbf{x},t_2) - I(\mathbf{x},t_1) - \nabla I(\mathbf{x},t_1) \otimes \mathbf{u}(\mathbf{x},t) \\ \mathbf{c}^k(\mathbf{x}) &= w(\mathbf{x}) * (\nabla I(\mathbf{x},t_1)\delta I^k(\mathbf{x}) \\ \mathbf{u}(\mathbf{x}) &= \mathbf{H}(\mathbf{x})\, \mathbf{c}^k(\mathbf{x}) \end{aligned} \tag{III.34}$$

where $\otimes$ is the Hadamard product and that matrix $\mathbf{H}$ is given by:

$$\mathbf{H} = w * (\nabla I(\cdot,t_1) \otimes \nabla I(\cdot,t_1)^T).$$

Note that unlike the preceding scheme, the update of the motion estimation depends on the coarse $\mathbf{u}^*$ evaluated both at the current evaluated pixel $\mathbf{x}$ and to its surrounding pixels $\mathbf{x}'$ as well. The iteration is done thanks to a Gauss-Newton strategy, which is proven to converge in fewer than 10 iterations.

III.1.6 Deep-Learning methods

Most deep-learning based methods are supervised, meaning they rely on a set of carefully annotated images with groundtruth displacement fields. Most of the currently developed deep learning optical flow methods follow a similar strategy, in great part for speed, with real-time applications in mind. It is because of this popularity that we wish to present them, but the reader must mark that their use in biological settings remains problematic. Indeed, like most deep-learning methods, they are very dependent on the data they are trained on [226], and it is noticed on multiple instances that many deep learning optical flow methods do not transfer well once the images they are inputted in are very different from those. Several benchmarks have been created in order to test these optical flow methods on a variety of configurations, but, unfortunately for us, no such bank of images exist for biological movement. The KITTI benchmark, for instance, geared a wagon with high resolution cameras for the obtention of images, and a Velodyne laser scanner tethered to a GPS localization system to deduce the displacement field [227]. But the challenges of the optical flow perceived by these cameras is very different than the ones from a fluorescence microscope: the objects' sizes can scale according to their distance to the camera, their illumination varies with shading, they may disappear from occlusions with another object, and they follow almost always rigid motions. Whereas in our case we do not have to worry about scaling, illumination variation or occlusion thanks to the good optical properties of fluorescence microscopy, while on the other hand we have to tackle with nonrigid motion. This inconsistency holds for the other classically used benchmarks, such as Middlebury [228] and MPI Sintel [229].

With this caveat in mind, supervised deep learning methods might be incorporated in various ways for motion estimation [231]. Some are pretty close to what we have presented, by just replacing the image intensities with features extracted through a convolutional neural network (CNN) architecture [232]. Others completely discard the idea of Tikhonov-like energy minimization methods, and compute the optical flow in an end-to-end manner [230] (see Figure III.7). Examples of the first include the application of a Siamese architecture to extract features in both images, paired with a joint architecture to measure the similarity with each features. Such as for instance PatchBatch [233], optical flow with hinge-embedding loss or DrLIM loss [234], or the one based on Markov random field by Güney and Geiger [235]. The end-to-end methods are faster, but require a larger training dataset which, even with the several benchmarks available today, is lacking. Many rely on synthetically produced optical flow images, for instance the FlyingChairs benchmark [236]. This is the strategy employed by FlowNet [237], SPyNet [238] and FlowNet2 [239], all methods that differ between themselves mainly by the use of coarse-to-fine strategies or the number of layers in their network. These two ideas were merged in a third, namely to incorporate cost volume in the architecture, in a famous architecture called PWC-Net [240] that proved not only significantly lighter than previous architectures but more accurate as well. Subsequent architectures, such as LiteFlowNet [232], iterative residual refinement (IRR) [241], Volumetric Correspondence Networks (VCN) [242], perfected it.

Since supervised learning largely depends on the training dataset, and since these are relatively scarce compared to the variety of motion we wish to estimate, some tried to implement self-supervised learning methods in their optical flow estimation scheme, i.e. methods that learn their motion solely from the pair of inputted images [243]. While less competitive for a long time against their variational based or supervised counterparts, we nowadays witness the appearance of many sturdy methods of this kind. These generally admit the brightness constancy assumption, or an equivalent of, for instance an MRF formulation [244], and use it as a loss to which their network must be trained [245]. Such are also [246] and [247], although their use of Generative Adversarial Networks more rightly classifies them in

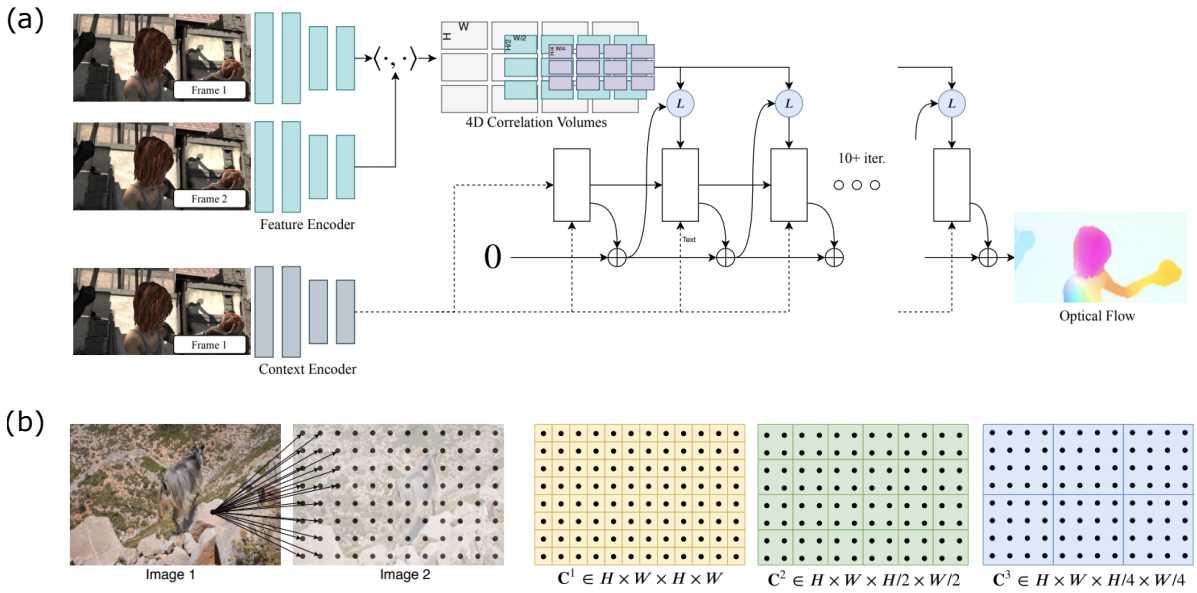

Figure III.7: An example of deep-learning based optical flow method: recurrent all-pairs field transform. RAFT is an end-to-end trained optical flow method. (a) It consists of 3 main components: (1) A feature encoder that extracts per-pixel features from both input images, along with a context encoder that extracts features from only I1. (2) A correlation layer which constructs a 4D $W \times H \times W \times H$ correlation volume by taking the inner product of all pairs of feature vectors. The last 2-dimensions of the 4D volume are pooled at multiple scales to construct a set of multi-scale volumes. (3) An update operator which recurrently updates optical flow by using the current estimate to look up values. (b) Building correlation volumes. Here we depict 2D slices of a full 4D volume. For a feature vector in I1, we take take the inner product with all pairs in I2, generating a 4D W ×H ×W ×H volume (each pixel in I2 produces a 2D response map). The volume is pooled using average pooling with kernel sizes 1, 2, 4, 8 from the set of correlation volumes (from [230]).

the category of "semi-supervised learning". The efficiency of unsupervised learning methods is very much determined by the proxy loss function, and most improvements on them are obtained by changing the data or regularisation term to obtain better accuracy against occlusion or illumination change. In this regard, unsupervised optical flow resembles in some way the variational method. The optical flow method we are to present in the last section of this chapter, in that respect, may very well be paired with an unsupervised minimization procedure. We leave this idea to an eventual interested and willing reader.

III.1.7 Some remarks on the staircasing effect

The convexity and the lower semi-continuity of the presented minimized energy functionals impose the solution to belong to a Sobolev space $W^{1,p}(\Omega, \mathbb{R}^2)$, where $p \in \{1, 2\}$ depends on the proposed method. We saw that the solution to the linear elasticity equations in the context of nuclear deformation must inevitably belong to $H^2(\Omega, \mathbb{R}^2)$. Is this troublesome? We pretend that it is, and that it corrupts the good estimation of mechanical quantities of interest. We will present at the end of this chapter a novel optical flow method the solution of which belongs to $W^{2,1}(\Omega, \mathbb{R})$. But the regularity properties are not the only trouble inflicting the presented optical flow methods. Another one lies in what is called the *staircasing effect*.

The *staircasing* effect is an artefact that makes the solutions of image processing problems look piecewise constant. It seems that it afflicts mostly variational problems with first order regularisations, however the best proofs we have found on the phenomenon regards the Rudin Osher Fatemi problem,

which extracts a denoised image u from a noisy image v by solving :

$$\min_{u \in BV(\Omega,\mathbb{R})} \mathrm{TV}(u) + \lambda \int_\Omega (u-v)^2 dx \tag{III.35}$$

where $BV(\Omega, \mathbb{R})$ is the space of bounded variations, and λ a regularisation parameter. We refer to Appendix B to read our claims about this phenomenon regarding optical flow. Our discussion is inspired by the work of [248].

As we will see next, the staircasing effect is a damning drawback in the estimation of strain and the Lamé parameters. Simply put, in simplistic axial deformation, the elasticity displacement is piecewise linear, with slopes changing each time with the Young's modulus. When the returned displacement field is piecewise constant, it is impossible to derive the right value of the Lamé parameters. Only the strain might be (more or less) correctly estimated in the sole case of the Horn Schunck method – a good example of how changing the application domain of a technique may reinstate older methods in favour of newer ones. We will see that the proposed optical flow in the next section overcomes this issue as well.

III.2 Proposed optical flow method

We see, in light of the previous sections, that our optical flow problem has to counteract two pitfalls in which current registration techniques fall into:

- The computed displacement field shall belong to $H^2(\Omega, \mathbb{R}^3)$,
- The overall displacement field shall not display any staircasing phenomenon.

We argue that both these issues can be counteracted with the choice of the proper regularization term. The data term will be kept similar to those aforementioned method, as it appears that the brightness constancy assumption holds very well for fluorescence images. More specifically, the data term shall not penalize the magnitude of the Jacobian of the displacement field, but its Hessian. It is based on the nuclear norm of third order tensors. We present it in the next section, and explain why it can fit our scheme. We also remind that, thanks to a recent result due to Friedland in [249], computing the nuclear norm for third order tensors is an NP-hard problem. So, although theoretically appealing, the computation of the nuclear norm of the Hessian of the displacement field is non practical. However, we show in the following section that it can be approximated by a polynomial-time approximation as introduced in [250]. Finally, the next section states clearly which optimization problem we have to solve, and offers a fast algorithm for this purpose.

III.2.1 Higher order regularization

We heretofore denote $\mathbf{u} \in H^2(\Omega, \mathbb{R}^3)$ a displacement field admitting second-order derivatives in the sense of distribution. Recall that its Jacobian $\nabla \mathbf{u} \in H^1(\Omega, \mathbb{R}^{3\times 3})$ is the second-order tensor field regrouping all its first-order derivatives, and that its Hessian $\mathcal{H}\mathbf{u} \in L^1(\Omega, \mathbb{R}^{3\times 3\times 3})$ is the third-order tensor field that regroups all its second-order derivatives. At each point $x \in \Omega$, we show that the size of the Hessian $\mathcal{H}\mathbf{u}(x)$ can be accurately quantified thanks to a norm defined first by Alexander Grothendieck and Robert Schatten [251]. It relies on the intuitive Hilbert-Schmidt inner product.

Definition III.2.1 (Hilbert-Schmidt inner product and norm)**.** *Let* $\mathcal{T} = (t_{i,j,k})_{1\leq i,j,k\leq 3}, \mathcal{T}' = (t'_{i,j,k})_{1\leq i,j,k\leq 3} \in \mathbb{R}^{3\times 3\times 3}$ *be two real third order tensors. The Hilbert-Schmidt inner product is defined by:*

$$\langle \mathcal{T}, \mathcal{T}' \rangle = \sum_{i,j,k}^{3,3,3} t_{i,j,k} t'_{i,j,k} \tag{III.36}$$

Its associated norm is the Hilbert Schmidt norm:

$$||\mathcal{T}||_2 = \sqrt{\langle \mathcal{T}, \mathcal{T} \rangle} \tag{III.37}$$

This definition, of course, remains valid for higher and lower order tensors. For first-order tensors, this becomes the Eucledian inner product. For second-order tensor, the Frobenius inner product.

Definition III.2.2 (Nuclear norm of a third-order tensor)**.** *Let* $\mathcal{T} \in \mathbb{R}^{3\times 3\times 3}$ *be a real third-order tensor. Its nuclear norm is defined by:*

$$||\mathcal{T}||_* = \inf \left\{ \sum_{i=1}^{r} |\lambda_i| \mid \mathcal{T} = \sum_{i=1}^{r} \lambda_i u_{1,i} \otimes u_{2,i} \otimes u_{3,i},\ ||u_{k,i}||_2 = 1,\ r \in \mathbb{N} \right\}. \tag{III.38}$$

Alternatively, one can show that the nuclear norm is equivalently defined as:

$$||\mathcal{T}||_* = \inf \left\{ \sum_{i}^{r} ||x_{1,i}||_2 \cdot ||x_{2,i}||_2 \cdot ||x_{3,i}||_2,\ \mid \mathcal{T} = \sum_{i=1}^{r} \lambda_i u_{1,i} \otimes u_{2,i} \otimes u_{3,i}\ x_{k,i} \in \mathbb{R}^3,\ r \in \mathbb{N} \right\} \tag{III.39}$$

Of course, this definition holds for tensors of higher or lower orders, as well as complex valued tensors. One can show that the infimum is attained, and so that the "inf" in the previous definition might be exchanged for "min". This rises from the convexity of the Hilbert-Schmidt norm from which the nuclear norm is defined (again, see [249] for further details). The nuclear norm has been studied as an interesting convex relaxation of the classical rank decomposition of high order tensors [252]. The same terminology for rank applies here.

Definition III.2.3 (Nuclear decomposition, rank decomposition)**.** *Let* $\mathcal{T} \in \mathbb{R}^{3\times 3\times 3}$ *be a real third-order tensor admitting the following decomposition:*

$$\mathcal{T} = \sum_{i=1}^{r} x_{1,i} \otimes x_{2,i} \otimes x_{3,i} \tag{III.40}$$

where $r \in \mathbb{N}$*. We say this decomposition is a nuclear decomposition if and only if:*

$$||\mathcal{T}||_* = \sum_{i=1}^{r} ||x_{1,i}||_2 \cdot ||x_{2,i}||_2 \cdot ||x_{3,i}||_2 \tag{III.41}$$

The rank is the minimal value of r *for such as decomposition.*

We see that these decompositions are actually the tensor equivalent of the singular values decompositions for matrices. Unlike their second-order derivative counterparts, they are unfortunately much harder to compute. It is long known that the rank decomposition is an NP-hard problem. While for a long time some harboured the hope that its convex sibling may prove easier to compute, these hopes were dashed in 2014 with the aforementioned study by Friedland. Often the nuclear norm is presented with another one, the spectral norm, which is equally used in the literature.

Definition III.2.4 (Spectral norm of a third-order tensor)**.** *Let $\mathcal{T} \in \mathbb{R}^{3\times3\times3}$ be a third-order tensor. Its spectral norm is defined as:*

$$||\mathcal{T}||_\sigma = \sup\left\{\frac{|\langle \mathcal{T}, x_1 \otimes x_2 \otimes x_3\rangle|}{||x_1||_2 \cdot ||x_2||_2 \cdot ||x_3||_2} \mid x_k \neq 0\right\} \tag{III.42}$$

An equivalent definition holds as well:

$$||\mathcal{T}||_\sigma = \sup\{|\langle \mathcal{T}, u_1 \otimes u_2 \otimes u_3\rangle,\ ||u_k||_2 = 1\} \tag{III.43}$$

Actually, both are the dual norm of one another, since we have, for every real third-order tensor $\mathcal{T} \in \mathbb{R}^{3\times3\times3}$:

$$||\mathcal{T}||_*^* = \sup_{||\mathcal{T}'||_*\leq1} |\langle \mathcal{T}, \mathcal{T}'\rangle| \leq \sup_{||\mathcal{T}||_*\leq1} ||\mathcal{T}||_\sigma ||\mathcal{T}'||_* = ||\mathcal{T}||_\sigma \tag{III.44}$$

and, since we have $|\langle \mathcal{T}, \mathcal{T}'\rangle| \leq ||\mathcal{T}||_* ||\mathcal{T}'||_\sigma$:

$$||\mathcal{T}||_\sigma \leq \sup_{||x_k||_2=1} |\langle \mathcal{T}, x_1 \otimes x_2 \otimes x_3\rangle| \ \leq \ \sup_{||x_k||_2=1} ||\mathcal{T}||_*^* ||x_1 \otimes x_2 \otimes x_3||_* = ||\mathcal{T}||_*^* \tag{III.45}$$

Therefore, it is well possible that using the spectral norm may lead to interesting results as well. We will circumscribe our presentation to the nuclear norm alone, as it is what seems to best preserve the sparsity of the Hessian of the displacement field. Indeed, while these definitions may appear abstract, they are perhaps easier to relate to the notion of singular value decomposition. The following theorem, which derives from Bessel's inequality, may prove handy in that respect.

Theorem III.2.1 (Tensors' norms and their singular values)**.** *Let $\mathcal{T} \in \mathbb{R}^{3\times3\times3}$ be a real third order tensor which admits the following orthogonal decomposition:*

$$\mathcal{T} = \sum_{i=1}^{r} \lambda_i u_{1,i} \otimes u_{2,i} \otimes u_{3,i} \tag{III.46}$$

Then the Hilbert-Schmidt norm, the spectral norm and the nuclear norm may be computed through the singular values as:

$$\begin{aligned} ||\mathcal{T}||_2 &= \left(\sum_{i=1}^{r} |\lambda_i|^2\right)^{1/2} \\ ||\mathcal{T}||_\sigma &= \max_{i=1,\dots,r} |\lambda_i| \\ ||\mathcal{T}||_* &= |\lambda_1| + \dots + |\lambda_r| \end{aligned} \tag{III.47}$$

In a geometrical point of view, the Hessian of the displacement field relates to its curvature. It appears clearly from the last equality that the nuclear norm of the Hessian of the displacement field will impose sparsity of it. Now, the nuclear norm applies for all tensor, and the Hessian is, according to Schwarz's theorem, a symmetric third-order tensor. Does this symmetry affect the value of the nuclear norm? Interestingly, no. Friedland offers an extension of Comon's theorem for this case. What is more bothersome, however, is that the nuclear norm depends on the base field. Take the following example.

Theorem III.2.2 (Base field dependence)**.** *Let $e_1, e_2 \in \mathbb{R}^2$ be two basis vectors of $\mathbb{R}^2$. Consider the following tensor:*

$$\mathcal{T} = \frac{1}{\sqrt{3}}(e_1 \otimes e_1 \otimes e_2 + e_1 \otimes e_2 \otimes e_1 + e_2 \otimes e_1 \otimes e_1) \tag{III.48}$$

$\mathcal{T}$ is a nuclear decomposition over $\mathbb{R}$, and we have:

$$\begin{aligned} ||\mathcal{T}||_{\sigma,\mathbb{R}} &= \frac{2}{3} \\ ||\mathcal{T}||_{\sigma,\mathbb{C}} &= \frac{2}{3} \\ ||\mathcal{T}||_{*,\mathbb{R}} &= \sqrt{3} \\ ||\mathcal{T}||_{\sigma,\mathbb{C}} &= \frac{3}{2} \end{aligned} \tag{III.49}$$

Other decompositions may be put forth to show that the spectral norm is base-field dependent as well. First, this forces us to a confession: we have omitted the subscript $\mathbb{R}$ for each norm, and which base field it was computed on, which is improper. Second, and more importantly, this means that the nuclear norm is not rotationally invariant. As such, it cannot be applied to physically describe the curvature of the displacement field – recall that image processing techniques require the optimization problems to be homogeneous and rotation independent. An even more vexing problem, perhaps, is the following one:

Theorem III.2.3 (NP-hardness)**.** *The spectral and nuclear norms of third-order tensors over $\mathbb{R}$ are NP-hard.*

This theorem leverages graph theory to be proven. Unfortunately, the symmetry of the tensor does not make the problem more tractable, as testified by Comon's conjecture. The theorem holds for higher order tensors. It holds *not* for second-order ones, as can be easily understood from the previous theorem. We show now in the next section a close-enough approximation of the nuclear norm that:

- is base-field, and henceforth rotation invariant,
- is polynomial-time computable.

III.2.2 Polynomial-time approximation

The approximation we will use is taken from Li in [250]. We put forth the main results that interest us here. We owe them notably the following notion.

Definition III.2.5 (Tensor partition)**.** *Let $\mathcal{T} \in \mathbb{R}^{3\times3\times3}$ be a real-valued third-order tensor. A set of tensors $\mathcal{T}_1, ..., \mathcal{T}_m$ is called a tensor partition of $\mathcal{T}$ if and only if:*

- *For every $j = 1, ..., m$, $\mathcal{T}_j$ is a subtensor of $\mathcal{T}$,*
- *For $1 \leq i, j \leq m$ such that $i \neq j$, the subtensors $\mathcal{T}_i$ and $\mathcal{T}_j$ have no common entry of $\mathcal{T}$,*
- *Every entry of $\mathcal{T}$ belongs to one of the subtensors T_i, $1 \leq i \leq m$.*

Definition III.2.6 (Tensor cut)**.** *Let $\mathcal{T} \in \mathbb{R}^{n_1\times...\times n_d}$ be a real-valued d-order tensor, $d \in \mathbb{N}^*$. A mode k tensor cut, with $1 \leq k \leq d$, is a partition into two tensors $\mathcal{T} = \mathcal{T}_1 \vee_k \mathcal{T}_2$ such that:*

$$\begin{aligned} &\mathcal{T}_1 \in \mathbb{R}^{n_1\times...\times n_{k-1}\times k_1\times n_{k+1}\times...\times n_d} \\ &\mathcal{T}_2 \in \mathbb{R}^{n_1\times...\times n_{k-1}\times k_2\times n_{k+1}\times...\times n_d} \\ &k_1 + k_2 = n_k \end{aligned} \tag{III.50}$$

Definition III.2.7 (m-regular partitions)**.** *We say that a real-valued d-order tensor $\mathcal{T} \in \mathbb{R}^{n_1 \times \ldots \times n_d}$ admits an m-regular partition, with $2 \leq m \leq d$ if and only if it admits a partition with successive $m-1$ cuts.*

For a given optical flow field $\mathbf{u} \in H^2(\Omega, \mathbb{R}^3)$, decomposed into its individual components function $\mathbf{u} = (u, v, w)$, a possible 3-regular partition of its Hessian field $\mathcal{H}\mathbf{u} \in L^1(\Omega, \mathbb{R}^{3\times3\times3})$ is the following:

$$\mathcal{H}\mathbf{u} = \{\mathcal{H}u, \mathcal{H}v, \mathcal{H}w\}$$

where $\mathcal{H}u, \mathcal{H}v, \mathcal{H}w \in L^1(\Omega, \mathbb{R}^{3\times3})$ are 2-order tensor fields, i.e. matrix fields. As underlined in the previous section, the nuclear norms of matrices are much easier to compute than those of their third order counterparts. But given the previous decomposition, how close is the nuclear norm of each Hessian of the components, to the nuclear norm of the full third-order tensor? This tricky question is partly elucidated by the following theorem.

Theorem III.2.4 (Bounds of third order tensor norms)**.** *Let $\mathcal{T} \in \mathbb{R}^{3\times3\times3}$ a real-valued third-order tensor. Suppose it admits a 3-regular decomposition $\mathcal{T} = \{\mathcal{T}_1, \mathcal{T}_2, \mathcal{T}_3\}$. Then the nuclear norm of $\mathcal{T}$ is both bounded from below and above:*

$$||(||\mathcal{T}_1||_*, ||\mathcal{T}_2||_*, ||\mathcal{T}_3||_*)||_2 \leq ||\mathcal{T}||_* \leq ||(||\mathcal{T}_1||, ||\mathcal{T}_2||_*, ||\mathcal{T}_3||_*)||_1 \tag{III.51}$$

Now, how tight is this approximation? Remember that the Cauchy-Schwarz inequality dictates the following bound between the L2 and L1 norm of a real vector $x \in \mathbb{R}^n$:

$$||x||_1 = \sum_{i=1}^{n} x_i \cdot 1 \leq \sqrt{n}||x||_2 \tag{III.52}$$

Therefore, the nuclear norm of the Hessian of the displacement field $\mathcal{H}\mathbf{u}$ admits a polynomial-time approximation with the following bounds:

$$\frac{1}{\sqrt{3}}(||\mathcal{H}u||_* + ||\mathcal{H}v||_* + ||\mathcal{H}w||_*) \leq ||\mathcal{H}\mathbf{u}||_* \leq ||\mathcal{H}u||_* + ||\mathcal{H}v||_* + ||\mathcal{H}w||_*$$

This is a tight approximation. Since $\mathcal{H}u, \mathcal{H}v, \mathcal{H}w$ are matrices, their nuclear norm is the 1-Schatten norm, as testified by equation (III.47).

Definition III.2.8 (Schatten norms)**.** *Let $p \in \mathbb{N}$, and $A \in \mathcal{M}_{n,m}$ be a real matrix. Given its singular values λ_k, $1 \leq k \leq \min(n, m)$, the Schatten norm of order p $||\cdot||_{\mathcal{S}}$ is defined as:*

$$||A||_{\mathcal{S}_p} = \left(\sum_{k=1}^{\min(n,m)} \sigma_k^p \right)^{\frac{1}{p}}$$

Theorem III.2.5 (Nuclear norm and Schatten norm)**.** *We have the followign equivalence for any matrix $A \in \mathcal{M}_{n,m}$:*

$$\begin{aligned} ||A||_* &= ||A||_{\mathcal{S}_1} \\ ||A||_\sigma &= ||A||_{\mathcal{S}_\infty} \end{aligned} \tag{III.53}$$

There are nowadays very efficient techniques to compute the singular values of any given matrix. In our case, the matrix in question is simple (3×3 at most), so the singular values can even be computed explicitly. In other words, we put forth a tight approximation of the nuclear norm at each point of the Hessian of the displacement field. We now define our new optical flow problem.

III.2.3 Proposed optical flow problem, minimization procedure

We propose the following variational problem as our new optical flow method:

$$\underset{\mathbf{u}=(u,v,w)}{\text{argmin}} ||\frac{\partial I}{\partial t} + \nabla I \cdot \mathbf{u}||^{\#} + \int_{\Omega} (\alpha_u ||\mathcal{H}u||_{S_1} + \alpha_v ||\mathcal{H}v||_{S_1} + \alpha_w ||\mathcal{H}w||_{S_1}) , \tag{III.54}$$

where, as previously said, $\mathcal{H}u, \mathcal{H}v, \mathcal{H}w$ are the respective Hessian of the components u, v, w of the displacement field (second-order tensors), $\alpha_u, \alpha_v, \alpha_w$ are regularisation constants, $|| \cdot ||_{S_1}$ is the 1-Schatten norm and $|| \cdot ||^{\#}$ is either the L1 norm or the L2 norm of scalar functions. We will see that using the L1 norm is advantageous in many instances. Depending on our choice, we should opt for either of two optimization procedures. Using the L2 norm, the optimized functional presents itself as the sum of two convex lower-semi continuous functionals, the first being differentiable with Lipschitz continuous gradient, and the second non-differentiable. Using the L1 norm, the first term becomes non-differentiable as well. In both cases, a splitting strategy is employed, meaning that we will alternatively reduce, in a gradient-descent-like way, the data terms and the regularisation terms. We know, from studying TV-L1 optical flow, that a data term does not need to be differentiable to be minimized, provided it possesses a known proximal operator. In fact, we will use the same proximal operator for the data term when we will chose $|| \cdot ||^{\#} = || \cdot ||_1$. Unfortunately, our regularisation term does not admit an explicit proximal operator. However Lefkimmiatis proposed a convenient way to approximate it through a fast optimization procedure in [253]. We adapt it here to the case of optical flow. But first, we discuss the regularity properties of the solution.

III.2.3.1 Regularity properties of the solution.

Our regularisation term applies for twice differentiable functions. It has recently been extended to any function in $L^1_{loc}(\Omega)$ [254]. The resulting semi-norm is the Hessian Total Variation defined for every $f \in L^1_{\text{loc}}$ and every open subset $A \subset \Omega$ as:

$$|D^2_1 f|(A) := \sup_F \int_A \sum_{i,j=1,\dots,n} f \partial_i \partial_j F_{i,j} d\mathcal{L}^n, \tag{III.55}$$

where $F \in \mathcal{C}^{\infty}_c(A)^{n\times n}$ with $||F||_{\infty,\infty} \leq 1$. It remains lower semi-continuous for the L^1_{loc} norm.

Any function $f \in L^1(\Omega)$ with bounded Hessian Total Variation is shown to belong to the space BV^2, meaning $f \in W^{1,1}(\Omega)$ and $\nabla f \in \text{BV}(\Omega)$ [255]. Interestingly, in dimension $n = 2$, the class of continuous and piecewise linear functions (CPWL) are dense in the unit ball of functions with bounded Hessian TV. These results, paired with the lower semicontinuity of this semi-norm, and the fact that $\text{BV}^2(\Omega)$ is compactly embedded in $W^{1,1}(\Omega)$ [256], show us two things. First, that the solution of our problem should at least be $\text{BV}^2(\Omega, \mathbb{R}^3)$. Second, that in the case where the underlying displacement field is continuous and piecewise linear, then the reconstructed signal should be as well. This last property would be of help for our elastography method in chapter IV.

In the special instance where the displacement field is twice-differentiable, we believe that the properties of the reconstructed signal can be slightly improved, namely that $\mathbf{u} \in W^{2,1}(\Omega, \mathbb{R}^3)$. We first show that the defined minimization problem admits a solution.

Let J be the minimized functional defined on $W^{2,1}(\Omega, \mathbb{R}^3)$ by:

$$J(\mathbf{u}) := ||\frac{\partial I}{\partial t} + \nabla I \cdot \mathbf{u}||^{\#} + \int_{\Omega} (\alpha_u ||\mathcal{H}u||_{S_1} + \alpha_v ||\mathcal{H}v||_{S_1} + \alpha_w ||\mathcal{H}w||_{S_1}) . \tag{III.56}$$

We prove the existence of a solution to the following optimization problem:

$$\inf \{J(\mathbf{u}) \mid \mathbf{u} \in W^{2,1}(\Omega, \mathbb{R}^d)\} \tag{III.57}$$

We use the *direct method in the calculus of variations*. J is bounded from below. Consider a minimizing sequence $(\mathbf{u}_n)_{n\in\mathbb{N}} \subset W^{2,1}(\Omega, \mathbb{R}^d)$, i.e. one that satisfies:

$$\lim_{n\to+\infty} J(\mathbf{u}_n) = \inf \{J(\mathbf{u}) \mid \mathbf{u} \in W^{2,1}(\Omega, \mathbb{R}^d)\} < +\infty. \tag{III.58}$$

J is coercive, so this sequence is bounded in $W^{2,1}(\Omega, \mathbb{R}^d)$. By Kondrachov's embedding theorem (II.1.10), $W^{2,1}(\Omega, \mathbb{R}^d)$ is compact for the $W^{1,1}(\Omega, \mathbb{R}^d)$ topology. Therefore $(\mathbf{u}_n)_{n\in\mathbb{N}}$ strongly converges in $W^{1,1}(\Omega, \mathbb{R}^d)$, up to a subsequence, to $\mathbf{u}^* \in W^{2,1}(\Omega, \mathbb{R}^d)$. Define $I(x, u, v, w, \mathcal{H}u, \mathcal{H}v, \mathcal{H}w)$ as the integrand of J. It is continuous with respect to each of its variables. It is convex with respect to each of its last three variables. By [257] it is weakly lower-semicontinuous with respect to the $W^{2,1}(\Omega, \mathbb{R}^d)$ topology. Therefore:

$$J(\mathbf{u}^*) \leq \liminf_{n\to+\infty} J(\mathbf{u}_n) = \min_{\mathbf{u}\in W^{2,1}(\Omega,\mathbb{R}^d)} J(\mathbf{u}) \tag{III.59}$$

Therefore $\mathbf{u}^*$ is a minimiser of J.

We furthermore show that any twice differentiable function $\mathbf{u}$ such that $J(\mathbf{u}) < +\infty$ belongs necessarily to $W^{2,1}(\Omega, \mathbb{R}^3)$.

Because the domain Ω is compact, it suffices to show that $\mathcal{H}\mathbf{u} \in L^1(\Omega)$. The boundedness of the regularisation parameter imposes that:

$$\int_\Omega \sum_{i=1}^{3} ||\mathcal{H}u_i||_* dx < +\infty. \tag{III.60}$$

Applying tensor cuts on the first dimension of $\mathcal{H}\mathbf{u}(x)$, $x \in \Omega$, the right part of inequality (III.2.4) assures that:

$$||\mathcal{H}\mathbf{u}(x)||_* \leq \sum_{i=1}^{3} ||\mathcal{H}u_i(x)||_*, \quad \forall x \in \Omega. \tag{III.61}$$

Furthermore, if $\mathcal{H}\mathbf{u}(x)$ is partitioned entrywise into $3 \times 3 \times 3$ elements, the left-hand part of inequalities (III.2.4) implies:

$$||\mathcal{H}\mathbf{u}(x)||_{\mathcal{S}_2} \leq ||\mathcal{H}\mathbf{u}(x)||_*, \quad \forall x \in \Omega. \tag{III.62}$$

Combining the last two inequalities, integrating over Ω, and bounding with (III.60), we get:

$$\int_\Omega ||\mathcal{H}\mathbf{u}(x)||_{\mathcal{S}_2} dx \leq \int_\Omega ||\mathcal{H}\mathbf{u}||_* dx \leq \int_\Omega \sum_{i=1}^{3} ||\mathcal{H}u_i(x)||_* dx < +\infty \tag{III.63}$$

On the other hand, for each multi-index α such that $|\alpha| = 2$, we have that:

$$|\partial^{|\alpha|} u_i| \leq \sqrt{\sum_{i=1}^{3} \sum_{|\beta|=2} (\partial^{|\beta|} u_i)^2} \leq ||\mathcal{H}\mathbf{u}||_{\mathcal{S}_2} \tag{III.64}$$

Therefore, integrating over Ω, we get that $\partial^{|\alpha|} u_i \in L^1(\Omega, \mathbb{R})$ for every $i \in \{1, 2, 3\}$.

III.2.3.2 Numerical resolution.

From now on, we refer to the discretized version of problem (III.54). We denote $\Omega_h = \mathbb{R}^{N_x \times N_y \times N_z}$ the discretized image space, where h is indicative of the regular spacing between pixels, and $\mathcal{X} =$

$\Omega_h \times \mathbb{R}^{2\times 2}$ the discretized space of second order tensor fields. This space is naturally endowed with the discrete Frobenius norm $||\cdot||_{\mathcal{X}}$, from which we can define the following scalar product $\langle\cdot,\cdot\rangle_{\mathcal{X}}$:

$$\begin{aligned}\langle \mathcal{A},\mathcal{B}\rangle_{\mathcal{X}} &= \sum_{i=1}^{N_x}\sum_{j=1}^{N_y}\sum_{k=1}^{N_z} \mathrm{tr}(\mathcal{B}(i,j,k)^T\mathcal{A}(i,j,k)) \\ ||\mathcal{A}||_{\mathcal{X}} &= \sqrt{\langle \mathcal{A},\mathcal{A}\rangle_{\mathcal{X}}}\end{aligned} \tag{III.65}$$

For ease of representation, we keep the same denomination of our previously mentioned scalars, vectors and tensors. The Hessian is computed through first-order finite difference schemes, and Neumann boundary condition. Taking a component u of the displacement field, this gives:

$$\begin{aligned}
(\mathcal{H}u)_{xx}(i,j,k) &= \begin{cases} u(i+2,j,k)-2u(i+1,j,k)+u(i,j,k) & \text{if } 1\le i\le N_x-2,\\ u(N_x-1,j,k)-u(N_x,j,k) & \text{if } i\ge N_x-1,\end{cases}\\
(\mathcal{H}u)_{yy}(i,j,k) &= \begin{cases} u(i,j+2,k)-2u(i,j+1,k)+u(i,j,k) & \text{if } 1\le j\le N_y-2,\\ u(i,N_y-1,k)-u(i,N_y,k) & \text{if } j\ge N_y-1,\end{cases}\\
(\mathcal{H}u)_{zz}(i,j,k) &= \begin{cases} u(i,j,k+2)-2u(i,j,k+1)+u(i,j,k) & \text{if } 1\le k\le N_z-2,\\ u(i,j,N_z-1)-u(i,j,N_z) & \text{if } k\ge N_z-1,\end{cases}\\
(\mathcal{H}u)_{xy}(i,j,k) &= \begin{cases} u(i+1,j+1,k)-u(i+1,j,k)-u(i,j+1,k)+u(i,j,k) & \text{if } 1\le i\le N_x-1,\\ & 1\le j\le N_y-1,\\ 0 & \text{otherwise},\end{cases}\\
(\mathcal{H}u)_{xz}(i,j,k) &= \begin{cases} u(i+1,j,k+1)-u(i+1,j,k)-u(i,j,k+1)+u(i,j,k) & \text{if } 1\le i\le N_x-1,\\ & 1\le k\le N_z-1,\\ 0 & \text{otherwise},\end{cases}\\
(\mathcal{H}u)_{yz}(i,j,k) &= \begin{cases} u(i,j+1,k+1)-u(i,j+1,k)-u(i,j,k+1)+u(i,j,k) & \text{if } 1\le i\le N_x-1,\\ & 1\le k\le N_z-1,\\ 0 & \text{otherwise},\end{cases}
\end{aligned} \tag{III.66}$$

The Hessian may be computed on the discrete nuclear domain alone, provided the Neumann boundary conditions are rightly adapted. This choice will be systematically made in the next chapter. The Hessian is an operator defined on Ω_h and taking its values on $\mathcal{X}$. Its adjoint operator, $\mathcal{H}^* : \mathcal{X} \to \Omega_h$, can be explicitly determined with backward differences and Neumann boundary conditions. Recall that for every $\mathbf{x} \in \Omega_h$ and $\mathcal{Y} \in \mathcal{X}$, we have:

$$\langle \mathcal{Y}, \mathcal{H}\mathbf{x}\rangle_{\mathcal{X}} = \langle \mathcal{H}^*\mathcal{Y}, \mathbf{x}\rangle \tag{III.67}$$

which, when inverted, gives us a direct characterization of the dual of the Hessian operator with respect to the Frobenius inner product:

$$\begin{aligned}
\mathcal{H}^*\mathcal{Y}(i,j,k) &= \mathcal{Y}_{xx}(i,j,k)-2\mathcal{Y}_{xx}(i-1,j,k)+\mathcal{Y}_{xx}(i-2,j,k)\\
&+\mathcal{Y}_{yy}(i,j,k)-2\mathcal{Y}_{yy}(i-1,j,k)+\mathcal{Y}_{yy}(i-2,j,k)\\
&+\mathcal{Y}_{zz}(i,j,k)-2\mathcal{Y}_{zz}(i-1,j,k)+\mathcal{Y}_{zz}(i-2,j,k)\\
&+\mathcal{Y}_{xy}(i-1,j-1,k)-\mathcal{Y}_{xy}(i-1,j,k)-\mathcal{Y}_{xy}(i,j-1,k)+\mathcal{Y}_{xy}(i,j,k)\\
&+\mathcal{Y}_{xz}(i-1,j,k-1)-\mathcal{Y}_{xz}(i-1,j,k)-\mathcal{Y}_{xz}(i,j,k-1)+\mathcal{Y}_{xz}(i,j,k)\\
&+\mathcal{Y}_{yz}(i,j-1,k-1)-\mathcal{Y}_{yz}(i,j,k-1)-\mathcal{Y}_{yz}(i,j-1,k)+\mathcal{Y}_{yz}(i,j,k)
\end{aligned} \tag{III.68}$$

Finally, we denote $||\cdot||_{1,1}$ the mixed $l_1 - \mathcal{S}_1$ Schatten norm, defined for every $\mathcal{Y} \in \mathcal{X}$ by:

$$||\mathcal{Y}||_{1,1} = \sum_{i=1}^{N_x}\sum_{j=1}^{N_y}\sum_{k=1}^{N_z} ||\mathcal{Y}(i,j,k)||_{\mathcal{S}_1} \tag{III.69}$$

We can show, thanks to Hölder's inequalities, that this norm admits a dual norm $||\cdot||_{\infty,\infty}$ defined for every $\mathcal{Y} \in \mathcal{X}$ by:

$$||\mathcal{Y}||_{1,1}^* = ||\mathcal{Y}||_{\infty,\infty} = \max_{(x,y,z)\in[\![1,N_x]\!]\times[\![1,N_y]\!]\times[\![1,N_z]\!]} ||\mathcal{Y}||_{\mathcal{S}_\infty} \tag{III.70}$$

In the discrete setting, the optical flow we wish to solve takes the following form:

$$\underset{\mathbf{u}}{\text{argmin}}\, ||\frac{\partial I}{\partial t} + \nabla I \cdot \mathbf{u}||^{\#} + \alpha_u||\mathcal{H}u||_{1,1} + \alpha_v||\mathcal{H}v||_{1,1} + \alpha_w||\mathcal{H}w||_{1,1} \tag{III.71}$$

where this time $||\cdot||^{\#}$ refers to either of the l1 or l2 norm defined for finite-dimensional vectors. We wish to approximate the proximal of $u \to ||\mathcal{H}u||_{1,1}$, defined for every $v \in \Omega_h$ and $\lambda \in \mathbb{R}$ by:

$$\text{prox}_{\lambda||\mathcal{H}\cdot||_{1,1}}(v) = \underset{u\in\Omega_h}{\text{argmin}} \frac{1}{2}||u-v||_2^2 + \lambda||\mathcal{H}u||_{1,1}. \tag{III.72}$$

Given the dual of the $l_1 - \mathcal{S}_1$ norm, this optimization problem might be cast into the following saddle point formulation:

$$\underset{u\in\Omega_h}{\text{argmin}} \max_{\Psi\in\mathcal{B}_{\infty,\infty}} \frac{1}{2}||u-v||_2^2 + \lambda\langle\Psi, \mathcal{H}x\rangle_{\mathcal{X}}, \tag{III.73}$$

where $\mathcal{B}_{\infty,\infty}$ denotes the $l_\infty - \mathcal{S}_\infty$ unit ball defined by:

$$\mathcal{B}_{\infty,\infty} = \left\{\Psi = [\Psi_1^T, ..., \Psi_{N_xN_yN_z}^T]^T \in \mathcal{X} \mid ||\Psi(i,j,k)||_{\mathcal{S}_\infty} \leq 1,\ 1 \leq i,j,k \leq N_x, N_y, N_z\right\} \tag{III.74}$$

Denote $(u,\Psi) \to \mathcal{L}_v(u,\Psi)$ the functional defined for every $u \in \Omega_h$, $\Psi \in \mathcal{B}_{\infty,\infty}$ by:

$$\mathcal{L}_v(u,\Psi) = \frac{1}{2}||u-v||_2^2 + \lambda\langle\mathcal{H}^*\Psi, u\rangle \tag{III.75}$$

The functional $\mathcal{L}_v$ is convex in its first variable and concave in its second. Therefore, there exists a unique saddle point $(\hat{u}, \hat{\Psi})$ that is solution of the minimax problem (III.73). Now consider the primal function $u \to p(u)$, defined for every $u \in \Omega_h$ by:

$$p(u) = \max_{\Psi\in\mathcal{B}_{\infty,\infty}} \frac{1}{2}||u-v||_2^2 + \lambda\langle\mathcal{H}^*\Psi, u\rangle = \frac{1}{2}||u-v||_2^2 + \lambda||\mathcal{H}u||_{1,1} \tag{III.76}$$

And the dual function $\Psi \to s(\Psi)$, defined for every $\Psi \in \mathcal{B}_{\infty,\infty}$ by:

$$s(\Psi) = \min_{u\in\Omega_h} \frac{1}{2}||u-v||_2^2 + \lambda\langle\mathcal{H}^*\Psi, u\rangle \tag{III.77}$$

We see that the dual function is expressed as the minimum of a differentiable and convex function. Its minimum is therefore attained where its gradient vanishes. The minimizer $\tilde{u}$ for a given $\Psi \in \mathcal{B}_{\infty,\infty}$ is then given by:

$$\tilde{u} = v - \lambda\mathcal{H}^*\Psi \tag{III.78}$$

and function s admits the following explicit expression:

$$\begin{aligned} s(\Psi) &= \frac{1}{2}||\lambda\mathcal{H}^*\Psi||_2^2 - \lambda\langle\mathcal{H}^*\Psi, v\rangle - ||\lambda\mathcal{H}^*\Psi||_2^2 \\ &= \frac{1}{2}||v||_2^2 - \frac{1}{2}||v - \lambda\mathcal{H}^*\Psi||_2^2. \end{aligned} \tag{III.79}$$

Because of the unicity of the minimizer $(\hat{u}, \hat{\Psi})$, equation III.78 allows us to retrieve the primal solution directly from the dual one. This is a peculiar instance of a broader family of primal-dual relations, best

embodied with the Fenchel-Duality formula. This is an interesting property, as the dual function, unlike its primal counterpart, is convex and differentiable, and admits the following gradient:

$$\nabla s(\Psi) = \lambda \mathcal{H}(v - \lambda \mathcal{H}^*(\Psi)) \tag{III.80}$$

for $\Psi \in \mathcal{B}_{\infty,\infty}$. Its minimizer is therefore readily accessible through gradient-descent-like methods. To determine the appropriate step-size, Lefkimmiatis offers a satisfying upper bound for the Lipschitz constant of ∇s. Take two variables $\Psi_1, \Psi_2 \in \mathcal{B}_{\infty,\infty}$ and denote $||\mathcal{A}||_{\text{op}} = \inf\{\beta \geq 0 \mid ||\mathcal{A}u|| \leq \beta||u||, \quad \forall u \in V\}$ for $\mathcal{A} \in V^*$, where V is any normed vector space and V^* its dual space. Then:

$$\begin{aligned} ||\nabla s(\Psi_1) - \nabla s(\Psi_2)||_{\mathcal{X}} &= ||\lambda^2 \mathcal{H}(\mathcal{H}^*(\Psi_1) - \mathcal{H}^*(\Psi_2))||_{\mathcal{X}} \\ &\leq \lambda^2 ||\mathcal{H}||_{\text{op}} ||\mathcal{H}^*(\Psi_1) - \mathcal{H}^*(\Psi_2)||_2 \\ &\leq \lambda^2 ||\mathcal{H}||_{\text{op}} ||\mathcal{H}^*||_{\text{op}} ||\Psi_1 - \Psi_2||_{\mathcal{X}} \\ &= \lambda^2 ||\mathcal{H}||_{\text{op}}^2 ||\Psi_1 - \Psi_2||_{\mathcal{X}}. \end{aligned} \tag{III.81}$$

Bounded linear operators respect the following relation:

$$||\mathcal{H}||^2 = ||\mathcal{H}^* \mathcal{H}||$$

Given that the norms of both forward and backward second-order differential operators are bounded by 4, we may deduce that $||\mathcal{H}|| \leq 8$. Combined with inequality (III.81), this gives us the following upper bound of the Lipschitz constant of the gradient of the dual function.

Theorem III.2.6 (Upper bound of the Lipschitz constant of the gradient of the dual function)**.** *Let L be the Lipschitz constant of ∇s. Then:*

$$L(s) \leq 64\lambda^2$$

We remind the FISTA algorithm in (2) (see also Figure III.8.a.), which minimizes convex functionals of the form:

$$\min_{x \in X} f(x) + g(x) \tag{III.82}$$

where X is a real Hilbert space, f a convex differentiable function the gradient of which has a known lipschitz constant L and g is convex and admits a known proximity operator. In our case, the dual problem we would like to solve is the following:

$$\underset{\Psi \in \mathcal{B}_{\infty,\infty}}{\text{argmax}} \; -\frac{1}{2}||v - \lambda \mathcal{H}^* \Psi||_2^2 = \underset{\Psi}{\text{argmin}} \; \frac{1}{2}||v - \lambda \mathcal{H}^* \Psi||_2^2 + \chi_{\mathcal{B}_{\infty,\infty}}(\Psi). \tag{III.83}$$

Algorithm 2 FISTA [259]

Input: $x^0 \in X$, $y_1 = x_0$, $t_1 = 1$, L, N_{iter}

$k \leftarrow 0$
while $k < N_{\text{iter}}$ **do**
  $x^{n+1} \leftarrow \text{prox}_{(1/L)F^*}(y^n - \frac{1}{L}\nabla F(y^n))$
  $t^{n+1} \leftarrow \frac{1+\sqrt{1+4(t^n)^2}}{2}$
  $y^{n+1} = x^n + \frac{t^n - 1}{t^{n+1}}(x^n - x^{n-1})$
  $k \leftarrow k + 1$
end while

Here, the first term is differentiable with Lipschitz-continuous gradient, and the proximal of the second term is the orthogonal projection onto the set $\mathcal{B}_{\infty,\infty}$. This projection can be computed using the following theorem.

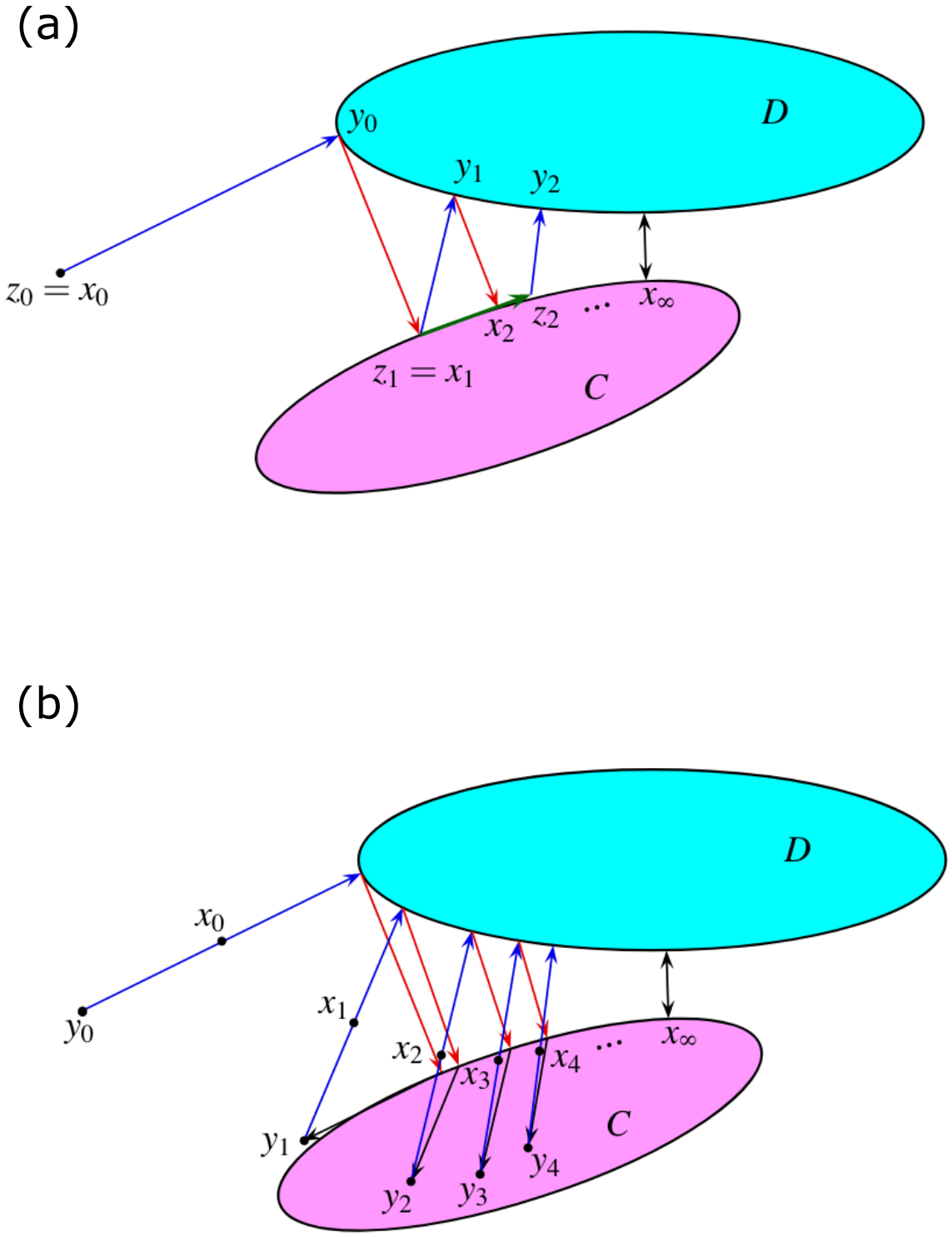

Figure III.8: FISTA and ADMM. Let C and D be two closed convex sets and consider the problem of finding a point $x_\infty \in C$ at minimum distance from D. Setting $f_1 = \chi_D$ and $f_2 = d_D^2/2$ gives (a) the FISTA iterations at the top and (b) the ADMM iterations at the bottom (from [258]).

Theorem III.2.7 (Schatten Norm Projections)**.** *Let $X \in \mathbb{R}^{d_1 \times d_2}$ be a real matrix admitting the singular value decomposition:*

$$X = U\Sigma V,$$

where U and V are unitary matrices of dimensions $d_1 \times d_1$ and $d_2 \times d_2$ respectively. The orthogonal projection of X onto the set $\mathcal{B}_{\mathcal{S}_p} = \left\{ Y \in \mathbb{R}^{d_1 \times d_2} \mid ||Y||_{\mathcal{S}_q} \leq \rho \right\}$ is given by:

$$\mathcal{P}_{\mathcal{B}_{\mathcal{S}_q}}(X) = U \text{diag}\left(\mathcal{P}_{\mathcal{B}_q}(\sigma(X))\right) V,$$

where $\text{diag}(\sigma(X))$ *is the diagonal matrix comprising the singular values of Σ. and $\mathcal{P}_{\mathcal{B}_q}$ is the orthogonal projection onto the l_q norm of radius ρ.*

Therefore the orthogonal projection operation can be done in three steps:

1. Compute the singular value decomposition of Ψ.
2. Project each component Ψ_i unto the set $\mathcal{B}_{\mathcal{S}_q}$.
3. Reconstruct the projected matrix via the singular value reconstruction.

The first step is efficiently done since the singular values are explicitly given both in the 2×2 and the 3×3 dimensions cases. The same can be said as for the third step. Only the second step seems intricate in a first glance. Lefkimmiatis here relies on the l_q projection algorithm developed by [260]. However, there are closed-form solutions for three cases of interest. Indeed, in case $q = 2$, the projection is readily given by the following expression:

$$\mathcal{P}_{\mathcal{S}_2}(\Psi_i) = \begin{cases} \dfrac{\Psi_i}{||\Psi_i||} & \text{if } ||\Psi_i|| > 1, \\ \Psi_i & \text{if } ||\Psi_i|| \leq 1, \end{cases} \tag{III.84}$$

If $q = \infty$, we have that:

$$\mathcal{P}_{\mathcal{S}_\infty}(\Psi_i) = U \text{diag}(\min(\sigma(\Psi_i), \mathbf{1}))V, \tag{III.85}$$

where $\mathbf{1}$ is a vector with all elements set to one and the min operator is applied component-wise. Finally, for the last case that interests us here, where $q = 1$, the projection is readily retrieved with a soft-thresholding operation:

$$\mathcal{P}_{\mathcal{B}_{\mathcal{S}_1}}(\Psi_i) = U \text{diag}(S_\gamma(\sigma(\Psi_i)))V, \tag{III.86}$$

where γ is given by:

$$\gamma = \begin{cases} 0 & \text{if } \sigma_1(\Psi_i) \leq 1 - \sigma_2(\Psi_i), \\ \dfrac{\sigma_1(\Psi_i) + \sigma_{\mathbf{2}}(\Psi_i) - 1}{2} & \text{if } 1 - \sigma_2(\Psi_i) < \sigma_1(\Psi_i) \leq 1 + \sigma_2(\Psi_i), \\ \sigma_1(\Psi_i) - 1, & \text{if} \sigma_1(\Psi_i) > 1 + \sigma_2(\Psi_i) \end{cases} \tag{III.87}$$

where the singular values are sorted in a decreasing order. Overall, we sum up the algorithm to compute the proximal operator of the intrdocued mixed norm in (4). We then solve the discrete version of ((III.54)) numerically with either of two first order splitting optimization algorithms. When $|| \cdot ||^{\#} = || \cdot ||_{\Omega,2}$, the data term is differentiable with Lipschitz-continuous gradient. Denote F

the ensuing differentiable data term. Let $\mathbf{u}, \mathbf{v}$ be two displacement fields, $\mathbf{J}_1 = \left(\nabla_x I^2, \nabla_x I \nabla_y I\right)^T$, $\mathbf{J}_2 = \left(\nabla_x I \nabla_y I, \nabla_y I^2\right)^T$, and $||\cdot||_{S_2}$ the Frobenius norm. The Cauchy-Schwarz inequality gives:

$$||\nabla F(\mathbf{u}) - \nabla F(\mathbf{v})||_{S_2} \leq 2\sqrt{||\mathbf{J}_1||^2 + ||\mathbf{J}_2||^2}||\mathbf{u} - \mathbf{v}||_2. \tag{III.88}$$

We can again use the FISTA algorithm with the inverse of the upper bound of this Lipschitz constant as a constant step size. When $||\cdot||^{\#} = ||\cdot||_{\Omega,1}$, the data term's proximal operator reduces to a soft-thresholding, as seen in the section introducing TV-L1 optical flow. Here we resort to an alternating direction of multiplier with constant penalty parameter, reminded in algorithm 3 (see also Figure III.8.b.).

Algorithm 3 Alternative Direction method of multipliers [259]

Input: $x^0 \in \Omega_h$, $y^0 = u^0 = x^0$, N_{iter}

$k \leftarrow 0$
while $k < N_{\text{iter}}$ **do**
  $x^{n+1} \leftarrow \text{prox}_{\lambda f}(z^n - y^n)$
  $z^{n+1} \leftarrow \text{prox}_{\lambda g}(x^{n+1} + u^n)$
  $u^{n+1} = u^n + \left(x^{n+1} - z^{n+1}\right)$
  $k \leftarrow k + 1$
end while

Algorithm 4 Proximal operator of the mixed Hessian schatten norm

Input: $\mathbf{v}$, $\Psi^0 = \Phi^1 = \mathbf{0} \in \mathcal{X}$, $\tau > 0$, $p \geq 1$, N_{iter}

$k \leftarrow 0$
while $k < N_{\text{iter}}$ **do**
  $\Psi^{n+1} \leftarrow \mathcal{P}_{\mathcal{B}_\infty}(\Phi^n + \frac{1}{64\tau}\mathcal{H}(\mathbf{v} - \lambda\mathcal{H}^*\Phi^n))$
  $t^{n+1} \leftarrow \frac{1+\sqrt{1+4(t^n)^2}}{2}$
  $\Phi^{n+1} = \Psi^n + \frac{t^n - 1}{t^{n+1}}(\Psi^n - \Psi^{n-1})$
  $k \leftarrow k + 1$
end while

III.2.4 Numerical evaluation

We believe this part to be applicable for medical imaging as well. There the tissue fills the entirety of the image domain. We therefore propose two distinct evaluations of our optical flow method. One, where the elastic domain corresponds to the image domain, and the second, where the elastic domain is strictly included in the image domain.

Denote s an estimated signal – potentially vector or tensor valued – defined over a rasterized domain R^N, s_t its ideal simulated counterpart, s^h and s^e the restrictions to two subdomains of interest (for instance, on stiff inclusions or the background), $\overline{s}$ its mean value, and σ_s its standard variation. We will use:

- the root mean square error RMSE $= \sqrt{\text{MSE}} = \sqrt{\frac{1}{N}\sum_{i=1}^{N}||s - s_t||_{S_2}^2}$,
- the signal ratio SR $= \frac{\overline{s^h}}{\overline{s^e}}$,
- the contrast-to-noise ratio CNR $= \sqrt{2(\overline{s^{\text{h}}} - \overline{s^{\text{e}}})^2/(\sigma_{s^{\text{h}}}^2 + \sigma_{s^{\text{e}}}^2)}$

We introduce the following abbreviations: Horn and Schunck (HS) [203], TV-L_1 [261], large-displacement optical flow (LDOF) [222], and iterative Lukas-Kanade (ILK) [223]. We denote ours by Hessian.

The material fills the whole image. We represent the material as a linear elastic square of dimensions 100×100. Its Young's modulus is fixed to $E_0 = 1$, except at $N = 1, 2, 3$ inclusions where it may take, depending on the number of inclusions, the finite values E_1, E_2, E_3. We suppose the upper and lower parts of the domain are clamped. We apply a known constant traction force T at the left and right parts of the domain. Given a Poisson's ratio ν, we may create two images, one before deformation, one after, according to the framework laid down before. We consider four experiments, in which several pairs of such images will be generated, and used to evaluate the effectiveness of our optical flow technique. In the first one, we set the number of inclusions to 2, with $E_1 = 3$ and $E_2 = 5$. Poisson's ratio is fixed at $\nu = 0.33$ to model the compressibility of the tissue. Then, we suppose the boundary tractions to take varying values $\mathbf{T} \in \{0.01, 0.12, ...0.03\}$. In the second experiment, we set the same number of inclusions, and fix the boundary tractions to be at $\mathbf{T} = 0.02$. This time, however, we evaluate the stability of optical flow techniques against varying Poisson's ratio $\nu \in \{0.3, 0.33, ...0.49\}$. The closer ν gets to 0.5, the less compressible the material becomes. In the third experiment, the traction force is again fixed at $\mathbf{T} = 0.02$, and the Poisson's ratio at $\nu = 0.33$. This time, we evaluate the stability of optical flow methods against varying values of Young's moduli in the inclusions $E_1, E_2 \in \{(3, 3), (3, 4), ..., (8, 8)\}$. And finally, in the fourth experiment, we evaluate the stability of our method for varying number of inclusions, fron none to 3, where $E_1 = 3, E_2 = 5, E_3 = 7$.

The lateral and axial displacements for a given compressible material with two stiff inclusions are consigned in Figure III.9. We see our optical flow retrieves much more faithfully the true displacement field. While the other methods retrieve acceptable axial displacements, their lateral displacement is very noisy; while ours remains very accurate even in this specific instance. This is especially evident when comparing the level lines in black, which capture the regularity of the flows. Compared to other state-of-the-art optical flow methods, ours presents no staircasing. Figure III.11 plots the axial displacement field profile at $Y = 50$. As announced in the first section, the axial displacements of a linear elasticity body under constant axial traction is piecewise linear, with the slopes being inversely proportional to the value of the Young's modulus. We see here that the slope of the true displacement dampens each time it meets a stiff inclusion. We also note that our method almost exactly captures the right slope of the true displacement field. This property will be useful in the following chapter, where the regularity of the displacement field, or in this case the value of the slopes, will be used to detect stiff inclusions and their Young's moduli. Other state-of-the-art optical flows, although accurate in magnitude, presents too many local irregularities because of the staircasing effect: we will see that this will be considerably detrimental for elastography methods.

This is even more evident with the derived strain. Because the differentiation tends to amplify the noise in the images, the staircasing effect becomes considerably detrimental. One may see it in Figure III.10, which plots the axial component of the strain ε_{xx}. Again, the two dips in the strain happen at the place where the inclusions lie. Remark that it is lower in the right (stiffer) inclusion than in the left (softer) one. We see the derived axial strain from all optical flow methods are extremely noisy. Interestingly, Horn-Schunck's method, the oldest of all, fares quite decently compared to its more sophisticated counterparts. This is because it incorporates some smoothing over time in its derivatives, as laid down at the beginning of this chapter. But ours remain far more accurate. The difference in axial stiffness within the two inclusions are very faithfully computed. This is even more evident in the axial strain profile at $Y = 50$ (figure III.11).

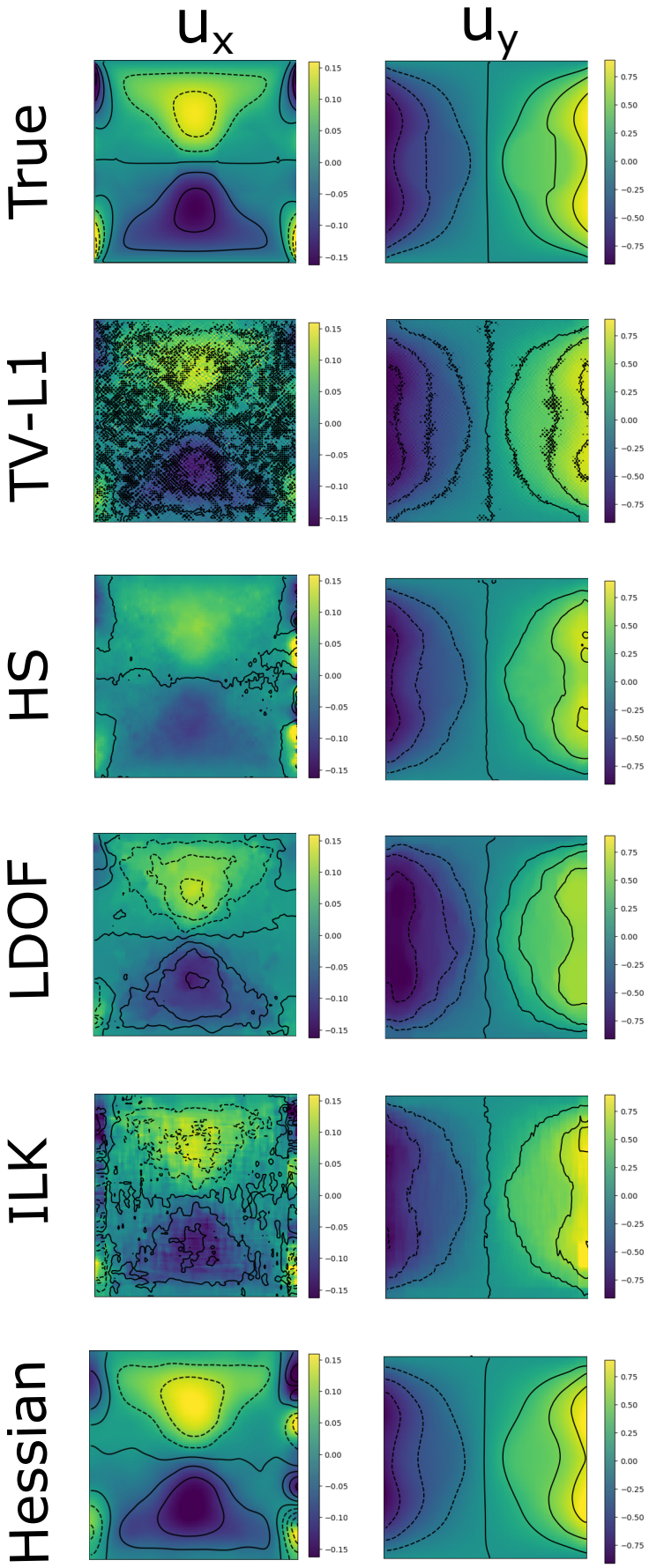

Figure III.9: Axial and lateral displacements of optical flow methods and ours for a linear elastic material with two stiff inclusions.

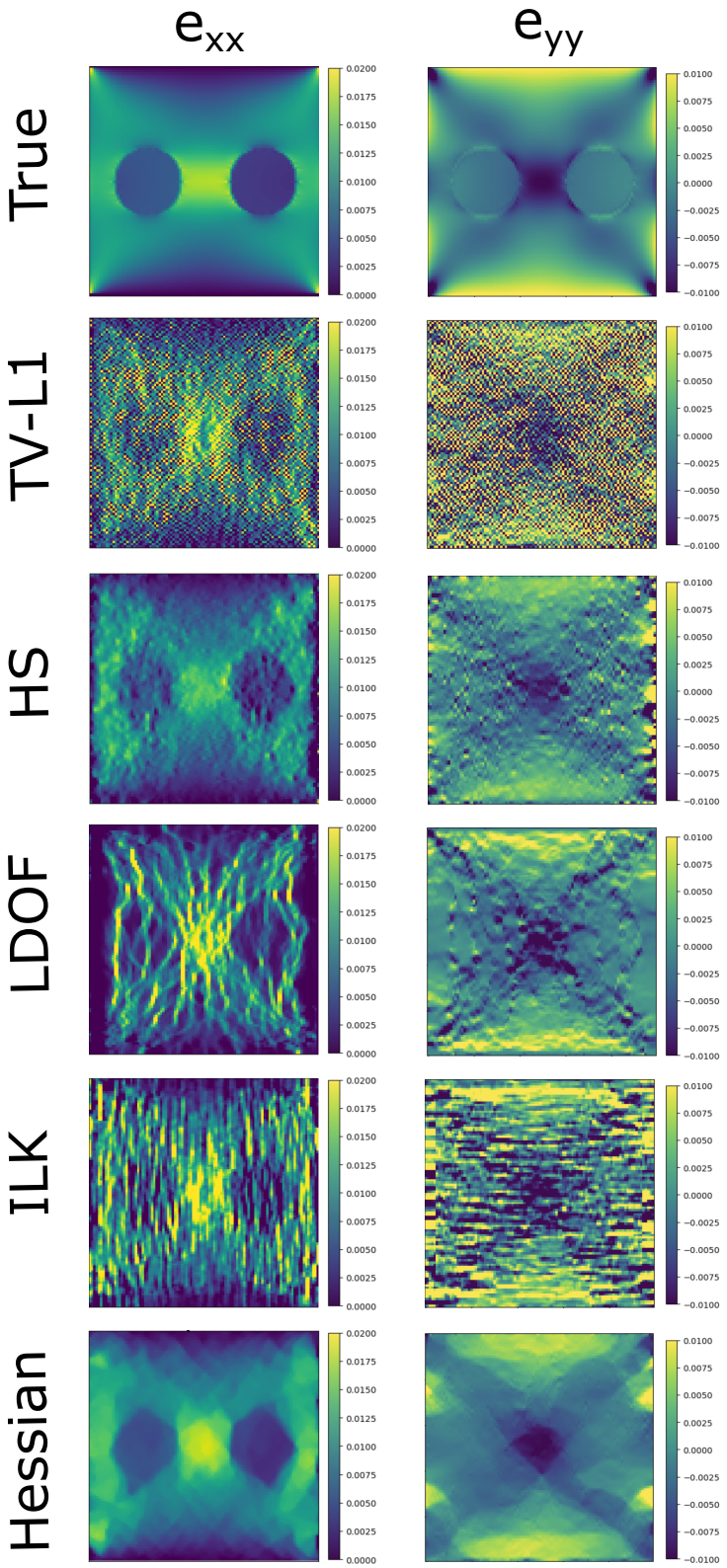

Figure III.10: Axial and lateral strain components of the strain of optical flow methods and ours for a linear elastic material with two stiff inclusions.

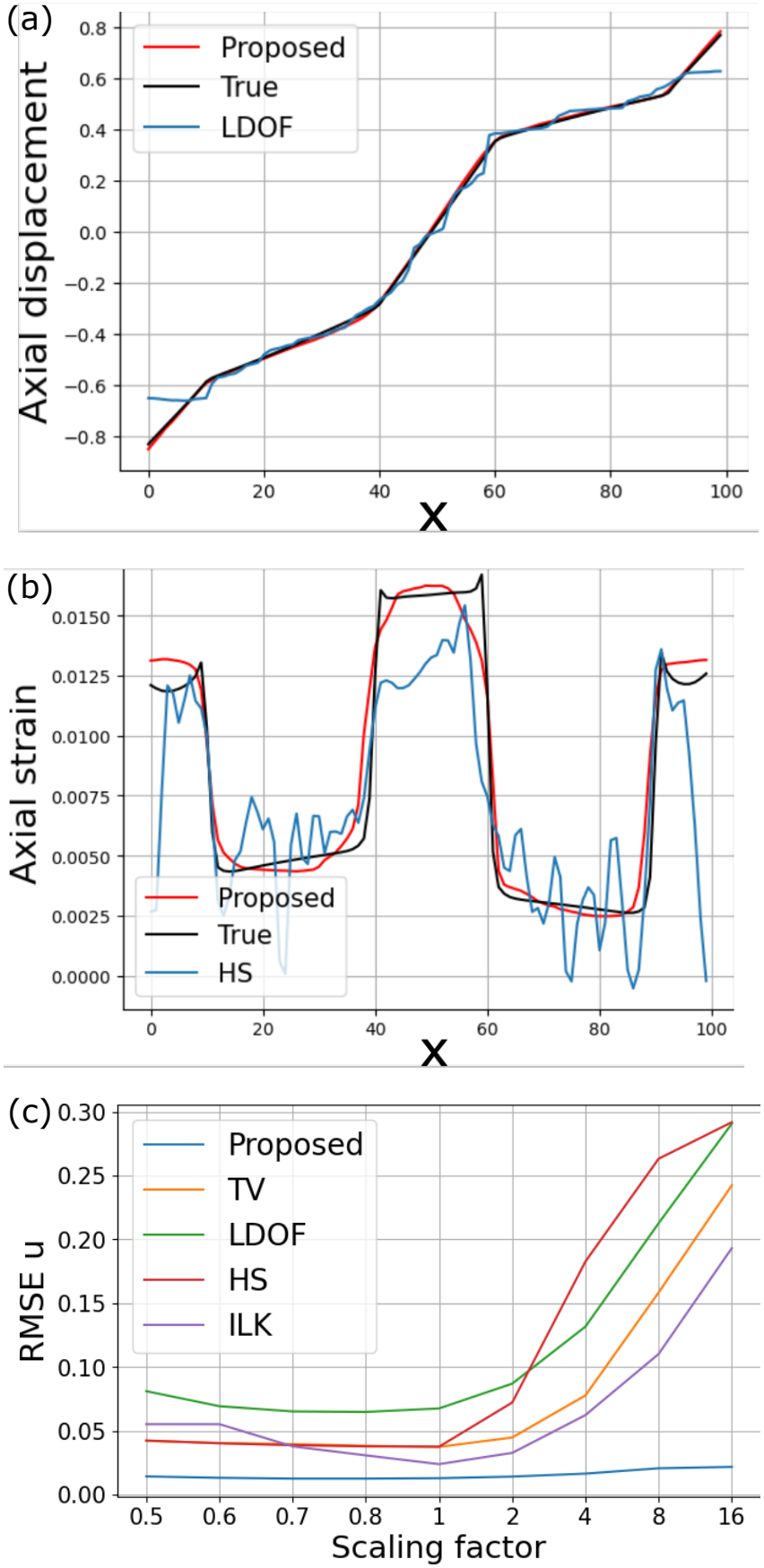

Figure III.11: Displacement and strain profiles. Stability against regularisation parameters. (a) Axial displacement along Y = 50; (b) axial strain profile along Y = 50 ; (c) RMSE of the displacement field against varying scaling of the regularisation parameter.

All these qualitative observations are confirmed quantitatively in Table III.1. In it, we see the RMSE of our optical flow method consistently, and by far, surpasses those of its counterparts. This is true as well for the derived strain, for the reasons we just outlined.

	RMSE $\mathbf{u}$ $(\cdot 10^{-2})$					RMSE ε $(\cdot 10^{-2})$				
Experiments	TV-L1	HS	LDOF	ILK	Hessian	TV-L1	HS	LDOF	ILK	Hessian
T	18.24	11.09	9.04	10.33	**5.58**	7.44	1.24	1.27	2.14	**0.60**
ν	29.51	28.04	31.88	18.95	**9.76**	11.15	6.75	4.60	5.91	**1.91**
E	25.77	35.70	36.40	42.36	**13.03**	12.83	9.93	6.44	8.16	**2.80**
Nb. inc.	36.00	34.92	47.12	25.82	**13.33**	12.84	9.03	6.68	7.94	**2.86**

Table III.1: RMSE of the reconstructions of the displacement field and strain field for experiments with varying stretching conditions.

The evaluations were done with the optimal regularisation parameters for optical flow. In practice, these are not known, but guessed. For different scalings $a \in \{0.5, 0.75, ..., 16\}$ of these parameters, we may see that the accuracies of the optical flow methods drift considerably, both in displacement and strain reconstruction (figure III.11). On the other hand, ours remains remarkably stable.

The material fills a compact subspace of the image. This is the case that interests us here the most. Here we modeled a round nucleus of radius 45 with a heterochromatin gathering around nuclear pore complexes at the nuclear periphery. The boundary and its neighborhood is stiffer than the interior. The nucleus is supposed circular, as is the case for white blood cells for instance. Unlike with the other one, we implemented our optical flow method solely on the boundary of the nuclear domain. This is a hypothesis we can admit here easily, because of the compactness of the genetic material and the easiness in the segmentation procedure. It allows for sharper boundaries that we would have missed otherwise. More specifically, our method is run on the whole image, and at each step of the iteration process, the flow field is extended at the boundary of the nucleus before being differentiated for computing the strain. Again, given a Poisson's ratio ν, we create two images, one before deformation, the other after, thanks to the same framework. We consider three experiments. In the first one, the boundary has a Young's modulus of 1, and the inside of 0.2, and Poisson's ratio is set to 0.33. Then we apply a constant traction force $||\mathbf{T}|| \in \{0.004, ..., 0.008\}$ at the right half of the nucleus and simulate our deformations. In the second one, the boundary the traction is fixed at $||\mathbf{T}|| = 0.006$, and Poisson's ratio is varying $\nu \in \{0.33, ..., 0.49\}$. In the third one, the traction and Poisson's ratio are fixed, and the interior Young's modulus is taken varying $E \in \{0.2, ..., 1\}$.

The axial and lateral displacements are consigned in Figure III.12. The same conclusions for the whole image simulation apply here. Our flow field is much more faithful than the ones of the counterpart optical flow methods. Again, this is especially evident when comparing the lateral component u_u, which is well known to be harder to retrieve. And unlike for other optical flow methods, the errors are not amplified when computing the strains by differentiation (see Figure III.13). Though the axial strain, which is very low, is a bit erroneous, it is yet considerably better than the other ones. Again, we see that Horn-Schunck optical flow is the second-best contender in here.

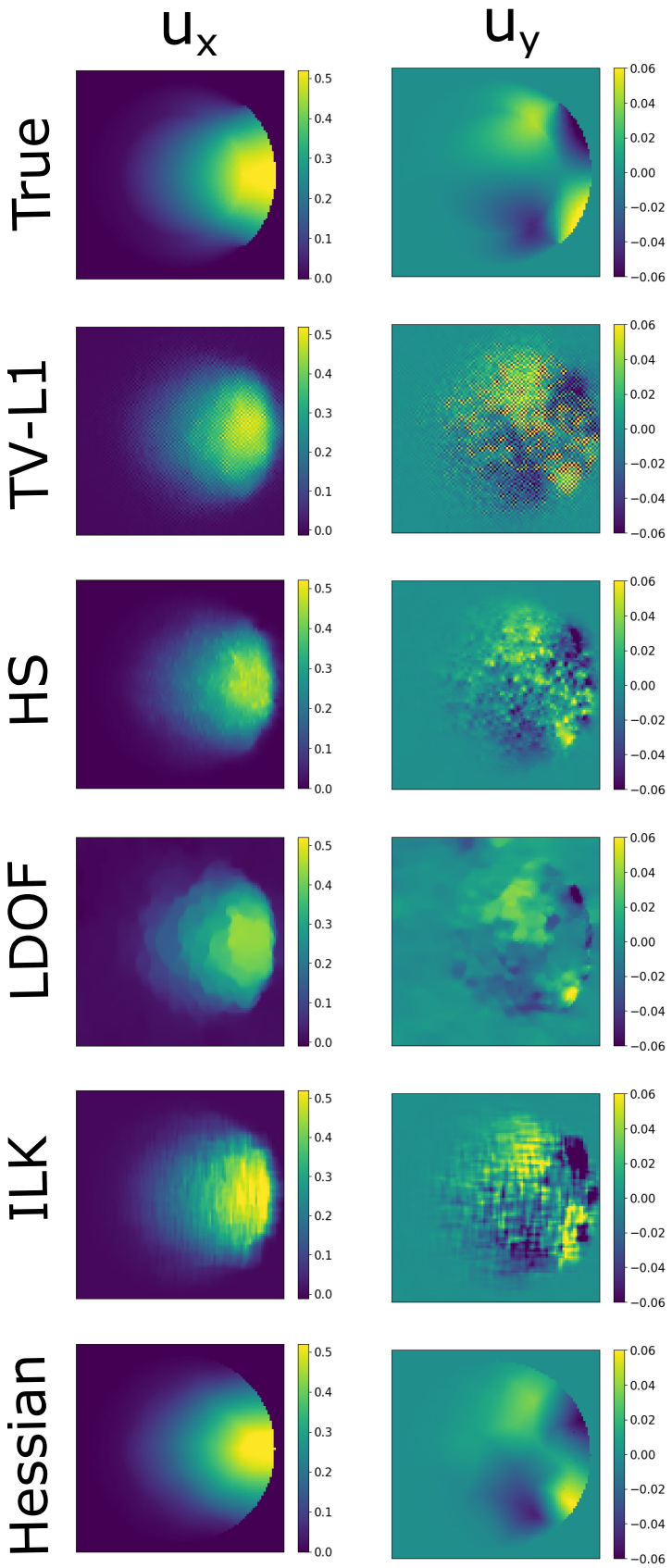

Figure III.12: Axial and lateral displacements of optical flow methods and ours for a linear elastic nucleus.

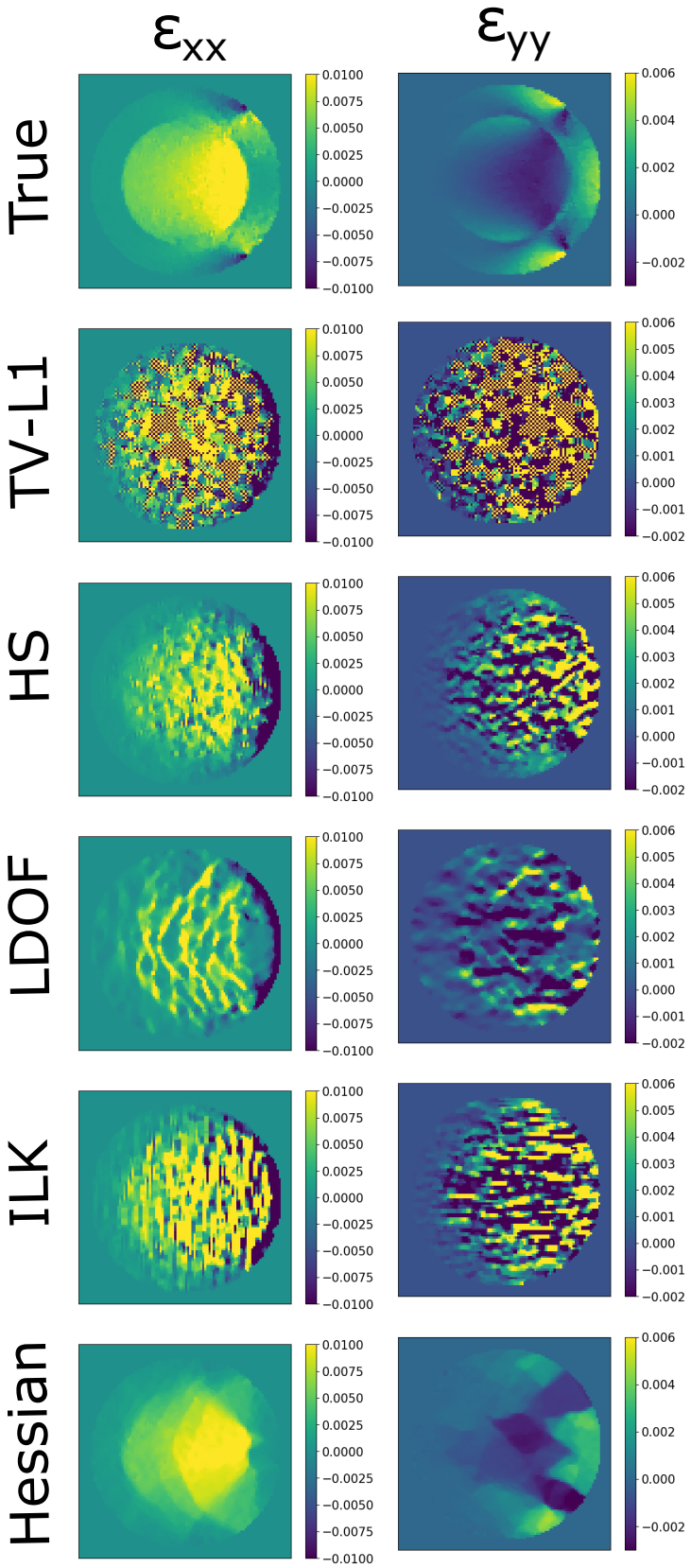

Figure III.13: Axial and lateral strain components of the strain of optical flow methods and ours for a linear elastic nucleus.

III.3 Application 1: influence of vimentin intermediate filaments on the deformations of glioblastoma nuclei during invasion

This part of the work was done in collaboration with Emma J. van Bodegraven, Elvira Infante and Sandrine Étienne-Manneville from the Cell Polarity, Migration and Cancer Unit of Institut Pasteur. We here deal with the subject of cancer invasion, specifically glioblastoma cells. We already explained in the first chapter of this thesis how the invasive capabilities of cancer cells were directly linked to the physical properties of the nucleus. We also reminded the reader that invasion, especially through metastasis, turns a locally growing tumor into a live-threatening disease. Therefore, any biological intelligence on the process of invasion may be vital for future treatment. Here, our collaborators focused on glioblastoma cells (GBM), which originate from glial cells glia precursors or neural stem cells [262]. They are the most common malignant primary brain tumours and, unfortunately, no cure is known to fight it, specifically because of the agressive invasive capabilities of these cells. Our goal is to determine whether the knocking out of vimentin intermediate filaments in the nucleus alter the invading capabilities of the invading cells. Prior *in vitro* experiments seem to indicate it does first and foremost for "leader" cells, and for "follower" cells to a lesser degree. We here confirm this hypothesis for *in vivo* experimentation.

GBM spheroids were embedded in 75% Matrigel and 20 μl hydrogel drops were placed on glass-bottom dishes. Hydrogels were polymerized at 37 °C for 45 min. Spheroids were labelled with SiR-DNA (1:1,000, Tebu-Bio, Spirochrome AG, SC007 SiR-DNA kit) and CellTracker Red CMTPX (1:10,000, Invitrogen C34552) in medium for 16 h. Live imaging was started at 24 h after cell embedding in hydrogel. Labelled cells were imaged for 5 min with a Nikon Ti2E spinning-disk confocal microscope equipped with an sCMOS camera (pixel size 6.5 μm, 2048 x 2044 pixels), long working distance x40 water immersion objective, and temperature-controlled environment. Images were taken at a 1 μm z-resolution and maximum speed. The nuclei of migrating cells are first tracked and segmented. The segmentation process is assured through a combination of HK-means [263] and Active Contours [264]. The HK-means is only applied on the first frame as an initialization. It performs an N-class thresholding through K-means classification. This initial mask is then inputted in the Active Contours algorithm (see Figure III.14). We explain why we believe this combination to be better than classical thresholding algorithms. These generally decompose the image into histograms, that they cut according to some criterion. A lot of refinement can be devised from this initial strategy. For instance, the histograms can be clustered into separate classes to account for the various spikes of intensity pixels within it. It may also include some other features, related to texture, for instance, to hone the accuracy of their distance measure. Also, several post-processing techniques, including simple ones such as denoising, allow the filtering of degenerate segmentation from this rudimentary approach. Nevertheless these methods apply best when the cell is highly homogeneous. On the other hand, we desire to have the most varied texture within the nucleus, as to allow the best optical flow tracking of each pixel intensity. This incompatibility of goals leads us to edge contour-oriented segmentations. The most rudimentary examples of such methods are simple edge detectors based on the gradient of the image: because the intensity sharply fluctuates at objects' boundaries, they must appear clearly when taking the finite differences of the image. Active-Contours methods allow the combination of region-based parameters with edge-based ones. They may be written as the solution of the following minimization problem:

$$\underset{K, I_K, I_{K^c}}{\operatorname{argmin}} ||I - I_K^C||^2_{I_K^C} + \lambda ||I - I_K||^2_{I_K} + \nu \int_{\partial K} g_I, \tag{III.89}$$

where the superscript designates the complementary, λ and ν are positive constants, I_K the mean intensity of the domain K of the image, and g_I an edge-detection function defined as $g_I = 1/(1+\rho|G*\nabla I|)$, with $\rho > 0$. The surface K may be represented implicitly as the null isosurface of a higher dimensional function, but for faster implementation we chose instead to define the contour as a set of ordered point and the surface as a set of triangulated mesh.

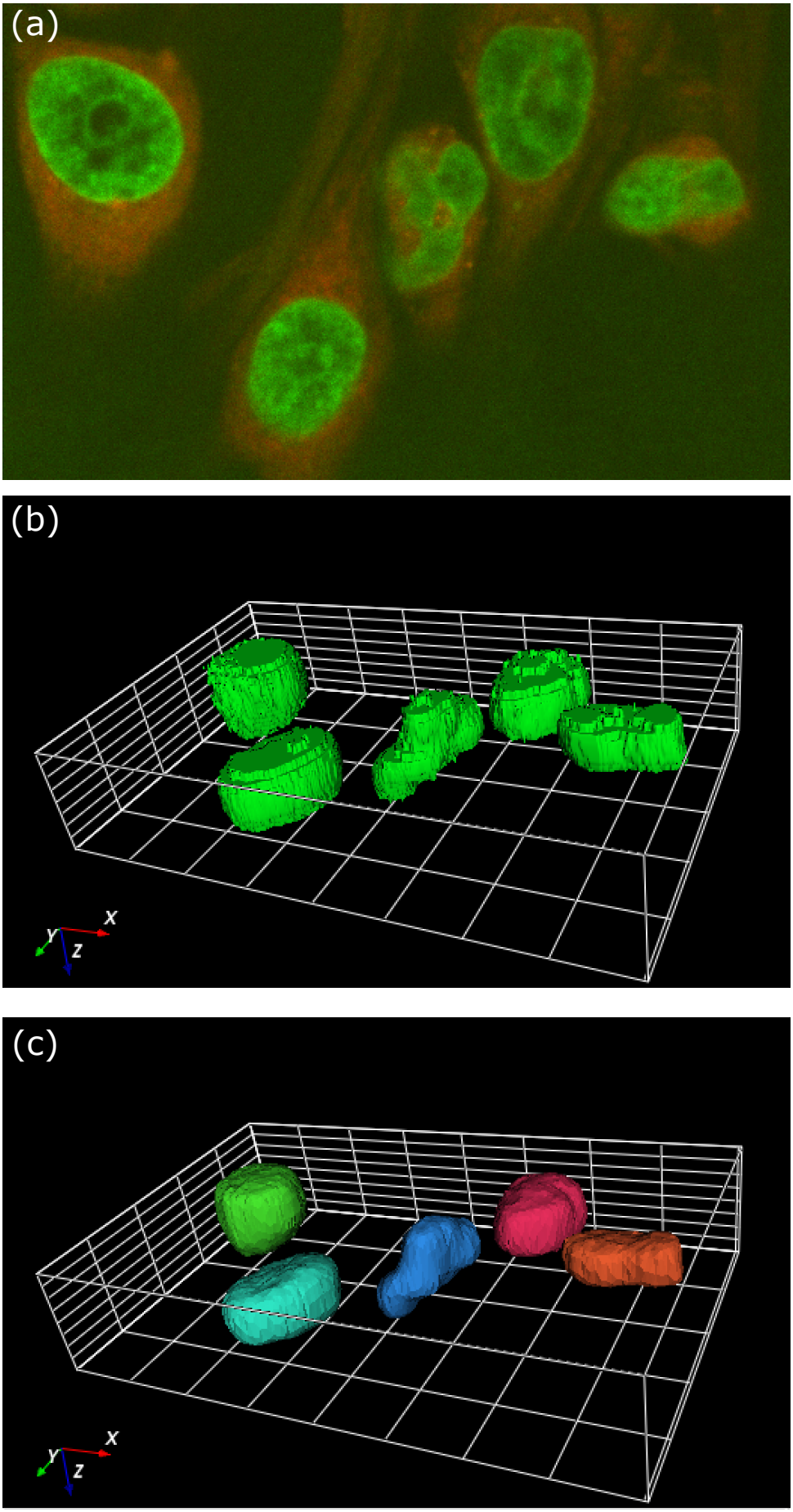

Figure III.14: Segmentation of invading glioblastoma cells' nuclei. (a) z-stack of a 3D image obtained by fluorescence microscopy of immunoglioblastoma nuclei in green ; (b) 3D segmentations results using HK-means, we may see the boundary is not smooth ; (c) refinement of the HK-means segmentation with active contours, we may see the boundary has better regularity.

The movement within each nucleus is then extracted at the "voxel" level with the Horn Schunck optical flow method (at the time of this analysis, we didn't fully elaborate our novel optical flow method with the Hessian Schatten norm of the displacement field; should we further this work, we would certainly use it instead), resulting in a vector field of displacements per time frame. However, so-called "rigid" displacements such as translations and rotations do not induce nuclear strain nor deformation. To instead assess the part of the displacements involving deformation, we compute the second order strain tensor from the relative motion of neighboring pixels. The tensor is computed by taking the symmetric part of the spatial derivatives of the displacement. In this way, it reflects whether the different parts of the nucleus move closer together or farther apart at a local level, thereby reflecting compression and extension. While expressive, the result is a high-dimensional tensor at each point in the nucleus and at each time frame. To derive a single measure of deformation for comparison between populations, we first derive a single value per point by computing the Frobenius norm of the tensor, which weighs shear and hydrostatic movements equally. The global deformation measure of each nucleus is then derived by computing the mean value of this local deformation through space and time. We now detail the numerical computation leading to this analysis.

Given the micrometer-scale resolution of the images, we consider each nucleus $k \in \{1, ..., K\}$ under study as a continuous media in a compact domain $\Omega_{k,t}$ that deforms over time, $t \in [0, T]$. After tracking and segmenting the nucleus, we extract the displacement fields between successive time frames (see Figure III.15). We then use the resulting data to measure the deformation of each nucleus at each point $\mathbf{x}$ of their domain and each time t of the invasion. To this end, we compute the time-dependent second order strain tensor, defined as the symmetric part of the Jacobian of the displacement field u:

$$\forall(\mathbf{x}, t) \in \Omega_{k,t} \times [0, T],\ \varepsilon(\mathbf{x}, t) := \frac{1}{2}(\nabla \mathbf{u}(x, t) + \nabla \mathbf{u}^T(x, t)) \tag{III.90}$$

Other higher order definitions of the strain such as Green's tensor are too sensitive to noise in our setting. The resulting strain tensor can be in turn used to compute strain invariants that characterize the mechanical behavior of the deforming domain quantitatively. In particular, we chose the Frobenius norm of the strain tensor as a measure of local deformation because it accounts for both hydrostatic and shear distortions:

$$\forall(\mathbf{x}, t) \in \Omega_{k,t} \times [0, T], d_k(\mathbf{x}, t) = \sqrt{\sum_{i,j} \varepsilon_{ij}(\mathbf{x}, t)^2} \tag{III.91}$$

At last, we compute the mean value of this locally defined deformation measure over the spatial domain and over the invasion time to characterize the global deformation of one labeled nucleus:

$$D_k = \int_{t \in [0,T]} \int_{\mathbf{x} \in \Omega_{k,t}} \frac{d_k(\mathbf{x}, t)}{V_k T}, \tag{III.92}$$

where $V_k(t)$ is the volume of the nucleus at time t.

We take $N_{voxels} n_x n_y n_z$ to be the volume $V_k(t)$ of the segmented nucleus at time t, where n_x, n_y, n_z are the respective dimensions in micrometers of the voxels and N_{voxels} is the number of voxels belonging to the segmented domain. We use the minimization scheme of the Horn-Schunck optical flow as laid out in the beginning of the third chapter. Because the displacements are at sub-pixel resolution, we need not to employ a coarse-to-fine strategy. We post-process the derived displacements with a median filter to remove noise before differentation. The corresponding strain tensor is calculated by convolution with a Sobel filter, and the mean deformation of each nucleus by averaging these computations over the segmentation masks. In this way, each nucleus, be it control or IF-depleted, leader or follower, is thus assigned a deformation value. We compare the resulting values through Student's t-tests.

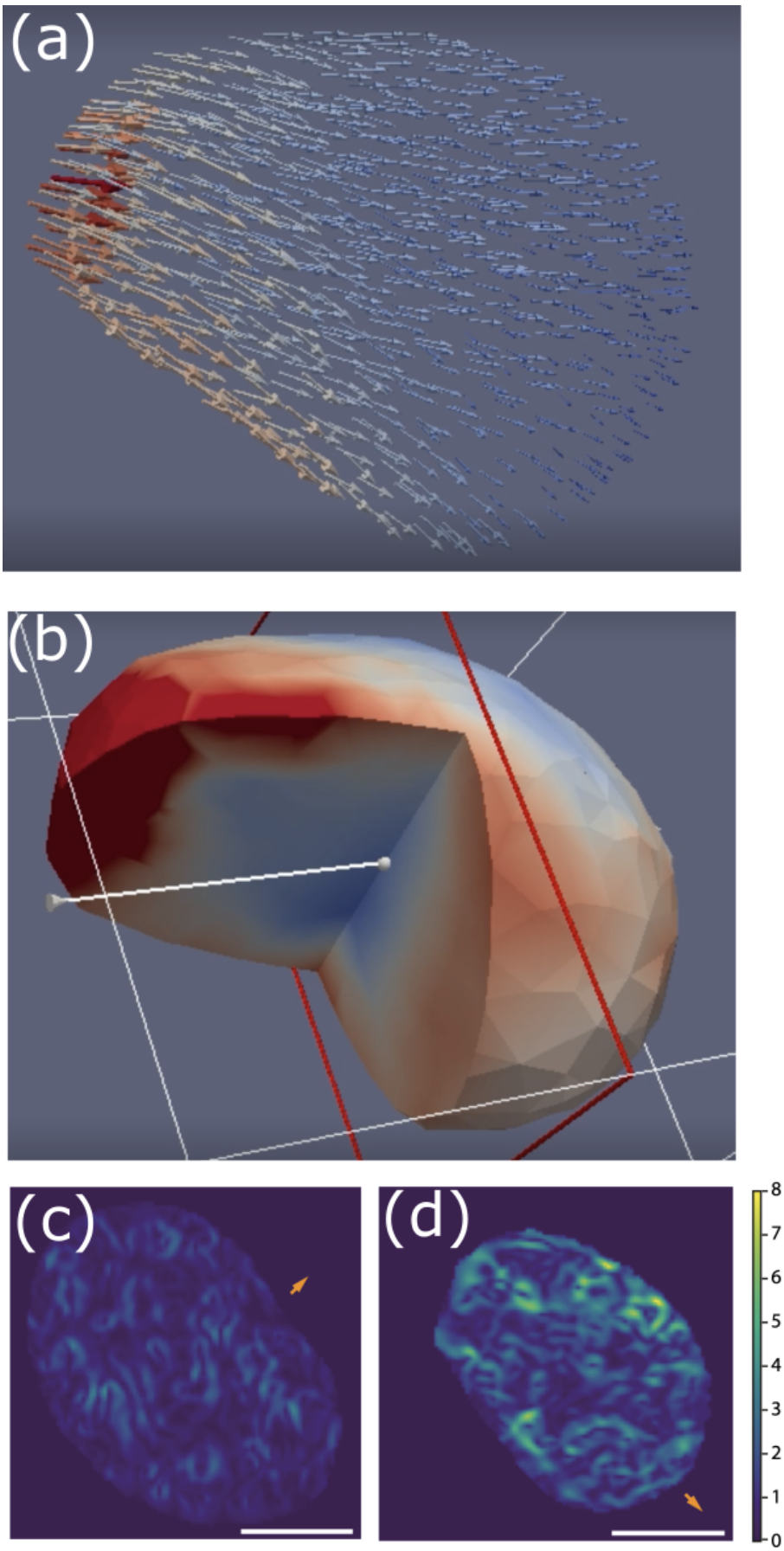

Figure III.15: Displacement and strain of an glioblastoma nucleus. (a) 3D displacement field of a deforming nucleus ; (b) 3D Frobenius norm of the strain field of the same nucleus ; (c) z-stack of the Frobenius norm of the strain field a CTL nucleus ; (d) z-stack of the Frobenius of the strain field of a KO nucleus, we may notice the much higher deformations.

Figure III.16 shows the results of this comparison. In it, it clearly transpires that the leading IF-depleted nuclei deform significantly more than the control ones. There are no differences spotted between following nuclei. This seems to indicate that cytoplasmic IFs play a predominant role in protecting the nucleus from the compressive forces exerted on leader cells.

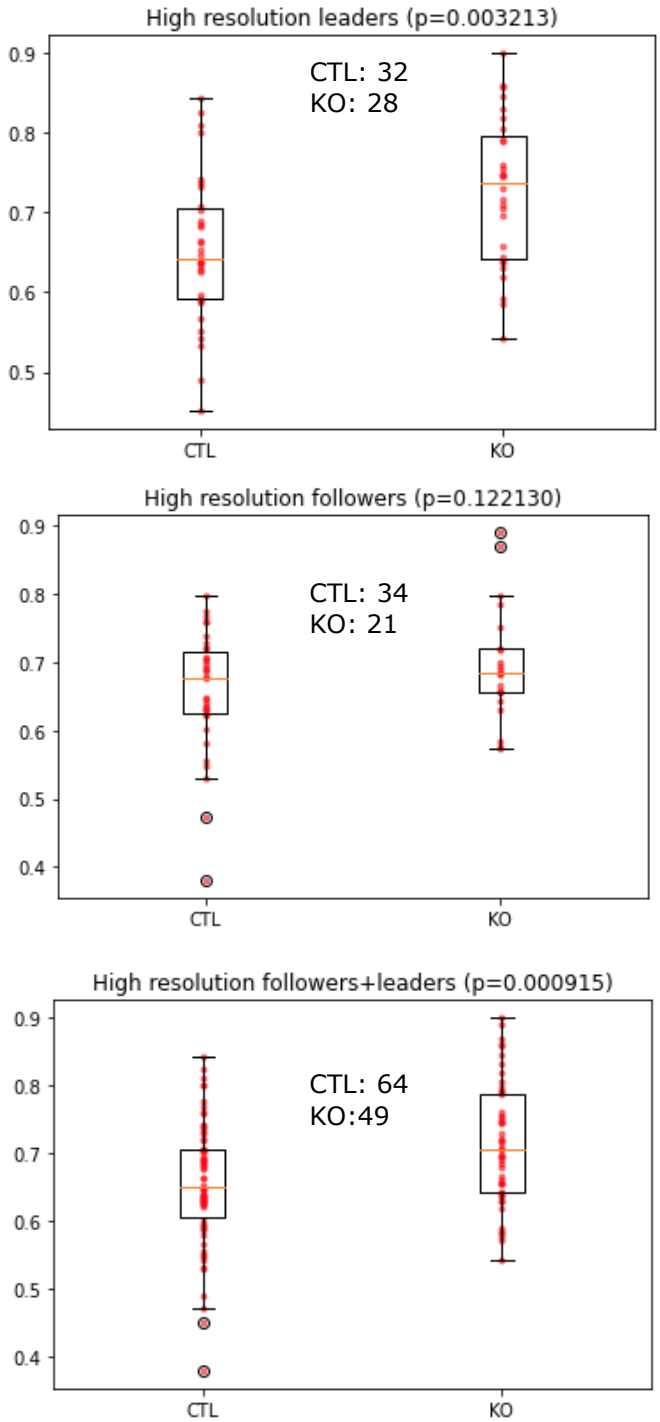

Figure III.16: Statistical comparison of the mean of the Frobenius norm of the strain tensor of glioblastoma nuclei with or without knocked out intermediate filaments.

Chapter IV

Estimation of physical quantities from displacements

This final chapter shows how we process the displacement fields computed by our optical flow technique in chapter 3 to derive physical quantities of interest. It answers the challenges of problems 2 and 3. We propose two methods to estimate heterogeneous stiffness maps from displacement fields. The first assumes known boundary traction forces and retrieves absolute values of the stiffness. The paper regarding this method has been published in [265]. The second assumes that we do not know the boundary traction forces and retrieves relative values of the stiffness. This part of our work is under review. We apply this second framework to compute the relative stiffness of two types of deforming nuclei, namely those of SKOV3 cells and cardiomyocytes. We then propose a PDE-constrained optimization framework to measure the stress and the boundary traction forces within a deforming nuclei. This framework is published in [266]. After a numerical evaluation, we apply it to study the stress and boundary forces applied on the nucleus of an invading Toxoplasma gondii.

IV.1 State of the art

We first review the state of the art on elastography methods, then on the estimation of boundary forces around the nucleus.

Elastography. We showed in Chapter I that the stiffness of the cell nucleus is an important marker for diseases as diverse as Emery-Dreifuss muscular dystrophy, Hutchinson-Gilford progeria syndrome, or cancer [9]. To measure stiffness, biologists perform a simple tensile test [267], [268]. They apply a known force on the nuclear surface, for example with an atomic-force microscope, and measure how much the length or perimeter of the nucleus changes. A single figure of merit—a constant Young's modulus E—is then derived from the shape measurement using analytical versions of Hooke's law in some characteristic dimension [159]. While the experimental setup and the measurements themselves are convenient, these methods oversimplify the composition and geometry of the nucleus and the physical relationship with the elasticity modulus, reducing the description of the process to a single number and also ignoring any cellular material between the probe and the nucleus. In order to deform the nucleus enough, the practitioner has to significantly squeeze the cytoskeleton at the risk of compromising the cell's integrity. Such an extreme handling is required to overcome the limitations in the imaging process.

By contrast, medical elastography has long relied on ultrasound imaging to detect stiff inclusions in the body—tumors for example—with its resolution being better matched to the human scale [269]. To this end, a light mechanical stress is applied on the tissue, either as a static compression or dynamically

in the form of pressure waves. In the former case, one then applies registration techniques to estimate the deformation fields. These have enough resolution to drive a reconstruction algorithm that ultimately yields a map of Young's modulus.

Only recently has microscopy improved enough to allow the use of similar techniques in biological settings. For example, [270] applies a dynamical tension on cells to measure their elasticity at the cost of a complex setup, whereas [271] leverages the natural compressions of the cell. The latter, however, can only extract dimensionless maps and at limited speed. Interestingly, imaging resolution has also increased in the traditional setting of nuclear probing described above [272, 273]. The result are fluorescent images with rich texture. To this end, we first need to estimate the deformation from the images.

Optical flow has been used to compute tissue strain in multiple medical imaging applications [274]. The most popular among such OF methods is based on vectorial total variation (TV-L_1) [261]. However OF by itself is not accurate enough to estimate the fine lateral displacements required to reconstruct sensitive stiffness maps under small compressions. To overcome this limitation, most elastography methods preprocess the displacement field "before inverting" for Young's modulus, for example by assuming incompressibility of the tissue [275]. Unfortunately, these approaches are not applicable in biology because cells and their nuclei are highly compressible. Instead of preprocessing, other methods resort to complex optimization schemes to stabilise the elasticity map [276], but their computational complexity is unfit for the long acquisitions required to study cell migration [277] and do not scale well to 3D. Both do so via elasticity models like (II.16) and can be adapted to quasi-static regimes of deformation. We will refer to them using two commonly admitted term in the literature as: direct reconstruction methods, and indirect reconstruction methods [278, 273]. In either case, the algorithms require knowledge of the traction forces $\mathbf{T}$. If the stiffness is assumed homogeneous at the boundary, one can recover $\mathbf{T}$ from the displacements $\mathbf{u}_{|\partial\Omega}$ at the boundary, but at the price of differentiation.

Direct reconstruction methods are fast but vulnerable to noise because they invert the matrix of the system directly. Let $\hat{\mathbf{u}}$ be the discrete coefficients of $\mathbf{u}$ in some basis, for example of finite elements [279]. Then (II.16) can be discretized into the sparse linear system of equations $K\hat{\mathbf{u}} = \mathbf{t}$ with K the stiffness matrix—which depends on the basis used for discretization (e.g., finite elements) and on E—and $\mathbf{t}$ the discretization of $\mathbf{T}$. This system can be rearranged into the alternative system $B\hat{\mathbf{e}} = \mathbf{t}$ to instead bring out the coefficients $\hat{\mathbf{e}}$ of the stiffness E. Here B is a matrix that depends on the basis and on $\hat{\mathbf{u}}$.

Thanks to the sparsity of B, a direct inversion scheme can recover the stiffness $\hat{\mathbf{e}}$ in a computationally efficient way. Direct methods are almost exact in the axial direction of the deformation. However they are very sensitive to noise, and fail entirely when the traction at the boundary is unknown. These limitations have only been overcome for incompressible materials [275]. This is because the lateral displacements, which are the most sensitive to noise, are informed by the axial displacements due to the field being divergence-free. Unfortunately, biological material is compressible.

On the other hand, *indirect reconstruction* methods use the computed displacement field $\tilde{\mathbf{u}}_{|\Omega}$ to feed a PDE-constrained optimization framework of the form

$$\begin{aligned} \arg\min_{\mathbf{u},E} \quad & J(\mathbf{u},E) = ||\mathbf{u} - \tilde{\mathbf{u}}_{|\Omega}||^2_{\Omega,2} + \beta G(E) \\ & \text{subject to Eq. } (II.16), \end{aligned} \tag{IV.1}$$

where $\beta \in \mathbb{R}_{>0}$ is the weighting parameter, and $G(E)$ regularizes the stiffness E; for example, $G(E) = ||E||^2_{\Omega,2}$ in [276]. In other works, the data term of the optical flow is included directly into the PDE-constrained framework [280, 281].

In practice, indirect methods are robust to noise due to the regularization term. It is unclear how exactly the space where the displacements belong affects the accuracy of the reconstruction, but—at least—one expects that more accurate displacements should bear better reconstructions. In general, problem (C.13) admits an unconstrained formulation that can be solved with a quasi-Newton gradient-descent algorithm [276]. However, even if the gradient can be computed with an adjoint-based approach [282], indirect methods are usually too slow for application to large biological datasets. We nevertheless expose how the adjoint method works since we are to use it in two of the following proposed frameworks.

Using the finite element method, we compute for each Young's modulus E the solution $\mathbf{u}$ of the equations. The implicit function theorem allows us to consider $\mathbf{u}$ as a function of E, and therefore the functional J as a function of E alone. This means that we can formulate our constrained problem into an unconstrained one. It is then solved through the use of a quasi-Newton gradient descent algorithm that seeks to find the boundary condition E that minimizes the prescribed functional. We recall the L-BFGS algorithm, which we will use, in Algorithm (5).In order to avoid large computations, we compute the gradient using the adjoint method. We refer to Appendix C for an intuition of how it works.

Algorithm 5 L-BFGS algorithm to minimize a twice differentiable function $x \to F(x)$[283]

Input: $x^0 \in \Omega$, $\mathcal{H}^0$, N_{iter}

$k \leftarrow 0$
while $k < N_{\text{iter}}$ **do**
  $p^{n+1} \leftarrow -\mathcal{H}^n \nabla f^n$
  Chose α^n satisfying Wolfe's conditions
  $x^{n+1} = x^n + \alpha^n p^n$
  $k \leftarrow k + 1$
end while

Stress and traction forces estimation. Except for [284], there have been no unifying frameworks to compute the stress and boundary traction forces of deforming cells. Most methods, as said in chapter 1, are only applicable to specific experimental settings. These methods, though effective to verify specific hypothesis, are hardly generalizable, especially to the *in vivo* case.

For instance, the stresses within growing embryonic tissues have been successfully computed in the past using microdroplets [285]. These are stabilized fluorocarbon oil component with a known initial shape (spherical for instance). When coated with integrin or cadherin receptor ligands, and inputted in the vicinity of cells, they undergo tensions from them. Their shapes change, and this change can be effectively monitored through fluorescence microscopy. Because the droplets have known mechanical properties, this shape can be related to the surrounding stress through a simple formula, for instance Laplace's law. This process is repeated for all the aggregates of droplets within the tissue, and summarized statistically to have a general appreciation of the amount of forces at play.

Unfortunately this kind of methods does not yield spatially resolved values of the stress and traction forces. Traction Force Microscopy aims at doing specially that [286]. Instead of studying the shape of droplets, it computes the interfacial forces between a cell and an elastic substrate. This elastic substrate can surround the cell, or the cell can adhere on top of it. Again, its mechanical properties are precisely known. It is generally a soft substrate, such as a polyacrylamide, that remains in the linear regime at the cellular-force scale. This time, the microscope does not track the shape of the substrate, but the movement of fluorescent beads that stud it. The methods that reconstruct this movement depend on the density of the beads: should there be a lot of them, correlation based PIV techniques are preferred ; should there be a few, then multiple particles tracking methods are best. The discrete map of movement obtained from these videos are then inverted using the linear elasticity equations of the substrate to yield a 2D (or

3D) map of stress. Again, multiple solutions may apply here. If the substrate is linear, homogeneous, isotropic, and the deformations small and planar, then one may seek to invert the convolution of the Green function with the traction forces to obtain them. This is done either with the Boundary Element Method or Fourier Transform Traction Cytometry (FTTC). Some versions of this method resort to PDE-constrained optimization, a bit like the indirect elastography framework we just introduced [287], but these generally applied on derived stress from the computed displacement field. Historically, TFM has mostly been applied to single cells. But recent advances allow an extension to multicellular processes. These are harder to study, as the reconstructed forces do not take into account the intracellular adhesion processes.

A last set of methods rely on the effective leverage of finite element methods [288]. Using fluorescence images of the deformation of a cell, or tissue, a correlative-based PIV technique compute the displacement field between each frames. From this displacement map, only the boundary is kept. The domain of the cell is then tessellated according to an algorithm akin to the one we laid out in chapter II. The boundary displacement map are then interpolated to the boundary nodes of the resulting mesh, and the partial differential equations ruling the cellular domain (for instance a Stokes' model) are solved using the finite element method. This gives a high resolution map of the displacement map within the cell, and of all the resulting forces thereon. Unfortunately, the accuracy of this method relies too much on the initial estimation of the boundary displacement field. PIV techniques are known to perform less well than optical flow. Furthermore, as for optical flow, they are especially erroneous at objects' boundaries. Also, the process of estimating the displacement field is completely separated from the mechanical properties of the domain.

We believe indeed that it is benefic to separate the displacement estimation process from the physical quantities estimation process, because these leverage significantly different methods for their purpose. Also, a separation also opens up to the developments of two flourishing fields: computational imaging, and computational physics. Nevertheless, we will only use the obtained displacement field as an initialization: in the end, the one that will be used should be the projection of this displacement field to the spcae of the solutions of the linear elasticity equations ruling the nuclear domain.

IV.2 Proposed elastography methods

We offer two elastography frameworks, one for when the boundary traction forces is known, the second when it is not known. In the first one, we resort to known elastography methods in the medical imaging community. We will see that, thanks to the regularity property of the developed optical flow in the previous chapter, these elastography methods can be adapted to the case of biological material. As we will see, this feat was not possible with other optical flow techniques.

IV.2.1 Computation of the absolute values of the Young's modulus

Here we suppose ourselves in possession of a widely accessible setup consisting of a plate compression imaged with fluorescence microscopy (see Figure IV.1). Other compression devices can likewise be adapted to our framework. The advantage of using this specific setting is that the force is homogeneous and applied to a large portion of the nucleus. Should it be local, for instance with an atomic force microscope, our framework should work equally well, but in the additional condition that the applied deformation "ripples" over the entirety of the domain. Indeed, the displacement field acts as a propagating wave, the variation of which indicates the presence of stiff lump. Here we will leverage the fact that our own optical flow method reconstitutes very well piecewise linear displacement fields, unlike other optical flow methods which suffer from from the staircasing effect. This case happens for experimental settings applying axial deformations, and when the stiffness of the cell can be modeled as a piecewise constant function. Our computational approach is fast enough for long time-lapse acquisitions and 3D

imaging. It is able to cope with two common pitfalls of biological elastography: high compressibility and small compressions to avoid damage. We show our method is faster and more accurate than the state-of-the-art.

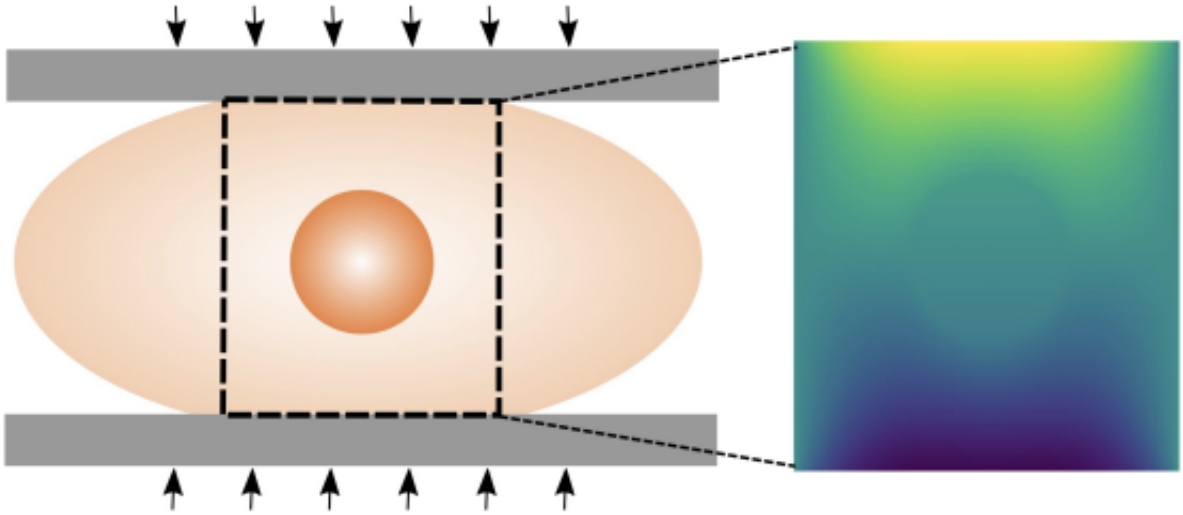

Figure IV.1: General experimental setting for elastography techniques. We follow with fluorescence microscopy the compression of a marked cell and its nucleus under a probing tool of which we know the exact applied forces. Using the images to compute the displacement field (axial component on the right), we invert this displacement field to obtain the Young's modulus map. Here we see that the axial displacement already delineates a stiff circle in the middle corresponding to the nucleus.

To see the importance of what we just set forth, consider the simple example of uniaxial deformation. Suppose $d = 1$ and recall that the divergence of the stress should be zero because there is not external forces, $\nabla \cdot \varsigma = 0$. This means $\partial_x (p + 2\mu\varepsilon_{1,1}) = 0$, and thus $\varepsilon_{1,1}\partial_x E = -E\partial_x\varepsilon_{1,1}$ because $p = \mu\varepsilon_{1,1}$. If E is piecewise constant, then we can consider its derivative a Dirac comb with Diracs at the change of stiffness. This means that a piecewise constant strain $\varepsilon_{1,1}(\mathbf{u})$ works as a solution. Therefore, a piecewise linear $\mathbf{u}$ is a solution of $\nabla\cdot\varsigma = 0$ as we wanted to show. This is a conceptual example to justify the framework, but axial displacements in the stiffness inclusions are also piecewise linear in 2D. This can be interpreted more intuitively by thinking about a series of springs (see Figure IV.2). Consider N springs with constant stiffness $(E_i)_{i\in\{1,\dots,N\}}$, strung in series at positions $(x_i)_{i\in\{1,\dots,N\}}$. The first end is fixed, and the last one is tethered to a constant traction force T. A simple integration of equations (II.16) yields a piecewise linear solution $u(x) = \sum_{i=1}^{N}\left[\frac{T}{E_iK}x + \sum_{k=1}^{i}\left(\frac{1}{E_kK} - \frac{1}{E_{k+1}K}\right)x_k\right]\chi_{[x_i,x_{i+1}]}(x)$, where $K = \frac{1-\nu}{(1+\nu)(1-2\nu)}$ is constant, and $\chi_{[x_i,x_{i+1}]}$ are indicator functions. We see that the slope of the displacement field is inversely proportional to the stiffness of the material.

We consider the cell and the nucleus as continuous media in a compact domain Ω. We consider that the applied forces are small, which is compatible with the protection of the cellular integrity. Further we assume that these forces are applied slowly enough to avoid triggering the viscous properties of the cell. Under these conditions, the cell and the nucleus can be represented as a linearly isotropic elastic material.

We saw that traditional optical flow methods use a first-order regularization term that causes staircasing. It also constricts the solution to the Sobolev space $W^{1,s}(\Omega, \mathbb{R}^d)$, $d \in \{2, 3\}$, where s depends on the L^s norm that is used to penalize the Jacobian. Due to the differentiation step in the reconstruction procedure, the displacements resulting from these optical flow techniques yield highly oscillatory strain components, in contradiction with the expectation that the constant traction on the boundaries ought to produce a smooth stress over the domain (II.16), while being at the same time linearly dependent on

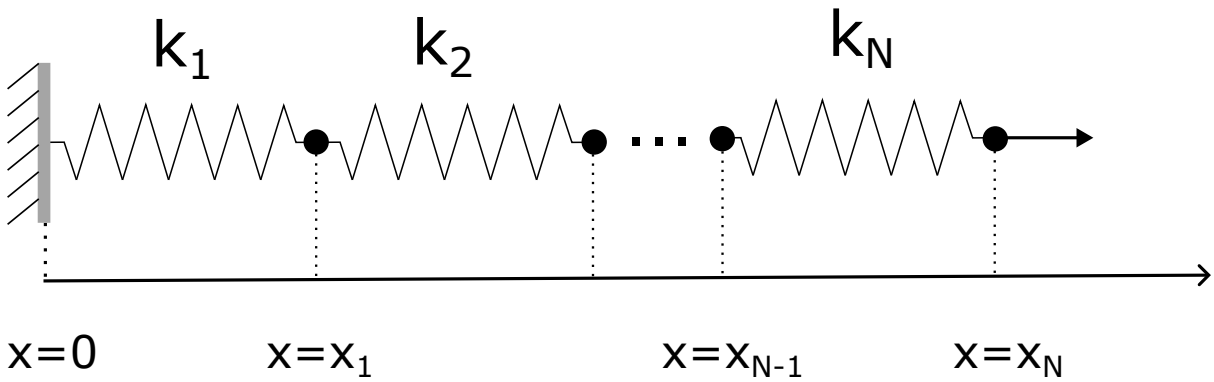

Figure IV.2: Symmetric axial deformation reduces to 1D deformations. This can in turn be represented by N springs strung in series.

ϵ and E. The optical flow framework we presented, on the other hand, creates piecewise linear displacement fields for axial deformation and generally displacement fields that are in $W^{2,1}(\Omega, \mathbb{R}^d)$. This property is vital for the elastography reconstruction frameworks that follow.

We consider two reconstruction methods of Young's modulus from a displacement field: direct, and indirect.

The direct reconstruction framework is inspired by Zhu in [279]. It supposes a simple rearrangement of the linear elasticity equation in a square domain. We mesh the image domain into N_e rectangular elements with the $(N_\text{x} \times N_\text{y})$ pixels as nodes. By discretizing the problem in a finite-elements basis, it can be shown that (II.16) can be formulated as the linear system $\mathbf{De} = \mathbf{t}$. Here, $\mathbf{e}$ is the vector containing the Young's modulus of each element, $\mathbf{t}$ is the vector corresponding to the traction, and $\mathbf{D}$ is a $(2N_\text{x}N_\text{y} \times N_\text{e})$ sparse matrix that depends on the estimated displacements $\mathbf{u}_\text{OF}$, on Poisson's ratio ν, and on the dimensions (a, b) of each element rectangular element.

The indirect method we will use is inspired by Oberai in [276]. It specifically penalize a quadratic term of the Young's modulus:

$$\begin{aligned} \text{argmin}_E \quad & J(\mathbf{u}, E) = \int \left(||\mathbf{u} - \mathbf{u}_\text{OF}||^2 + \beta ||E||^2 \right) d\Omega, \\ \text{s.t.} \quad & \text{Eq. } (II.16), \end{aligned} \tag{IV.2}$$

where $\beta \in \mathbb{R}_{>0}$ is a regularization parameter. These methods can also include the OF term directly in the variational form [280, 281]. Given a stiffness map $E(\mathbf{r})$, the finite-elements method then yields a variational form of (II.16) for $\mathbf{u}$.

Our claim is that OF regularized with the Hessian-Schatten norm is accurate enough to feed into a direct method. Hereafter, we refer to the combination of the two as *Proposed*. Combinations of other OF methods with indirect approaches are used for comparison. We did not include combinations of these OF methods with direct inversion approaches, since they systematically collapse.

Data Generation. We simulate a cell under plate compression (Figure IV.1). We consider (100×100) images of the cellular domain. Poisson's ratio ν is set to 0.33, indicating that we take the material to be compressible. We model the nucleus as a disk that accounts for 10% to 30% of the surface of the cell [289]. We ascribe a dimensionless stiffness of 1 to the cytoplasm and a stiffness of 5 to the nucleus (Figure IV.3) [289]. This could also represent any potential granularity inside the nucleus if the whole image was considered as the nucleus. Constant and uniform traction is applied on the upper and lower part of the image (Figure IV.1). For each boundary-traction value and each radius of the nucleus,

Experiment 1	NRMSE	SR	CNR	Runtime (s)	**Experiment 2**	NRMSE	SR	CNR	Runtime (s)
Proposed	**19.12 ± 0.65**	**7.77 ± 0.22**	5.86± 1.46	**5.62± 0.27**	**Proposed**	**22.27 ± 3.67**	**7.80 ± 0.74**	6.68 ± 1.75	**5.61 ± 0.20**
TV-L_1 + Indirect	25.92 ± 1.74	1.71 ± 0.35	3.44± 1.54	301± 181	TV-L_1 + Indirect	31.50 ± 3.68	1.62 ± 0.30	4.05 ± 1.49	243 ± 176
ILK + Indirect	29.22 ± 5.46	1.63 ± 0.27	5.87 ± 1.29	201 ± 110	ILK + Indirect	32.99 ± 10.69	1.58 ± 0.17	6.16 ± 1.28	144 ± 35
LDOF + Indirect	22.51 ± 1.97	1.60 ± 0.24	9.17± 3.59	151± 73	LDOF+ Indirect	27.82 ± 3.25	1.52 ± 0.26	5.58 ± 3.59	146± 100
HS + Indirect	21.10 ± 0.57	2.15 ± 0.19	**13.26 ± 1.41**	146 ± 57	HS+ Indirect	23.29 ± 3.04	2.27 ± 0.11	**12.88 ± 2.04**	263 ± 222

Table IV.1: Mean and standard deviation of the accuracy of the reconstruction for each evaluation metric.

a variational formulation of (II.16) is solved for the displacements using the finite-elements method. The resulting displacements are used to create a deformed image by warping the initial one with bicubic interpolation. These two images, along with the traction on the boundaries, are used to reconstruct Young's modulus and evaluate our method.

Evaluation Method. We denote E_{c} and E_{n} the evaluated stiffness over the cytoskeletal and nuclear domains, respectively, $\overline{E_{\mathrm{c}}}, \overline{E_{\mathrm{n}}}$ their mean value, and σ_{c}, σ_{n} their standard deviation. We evaluate the performance of our method with four metrics: the root-mean-square error normalized over the maximum of the true stiffness (NRMSE), the contrast-to-noise ratio CNR $= \sqrt{2(\overline{E_{\mathrm{c}}} - \overline{E_{\mathrm{n}}})^2/(\sigma_{\mathrm{c}}^2 + \sigma_{\mathrm{n}}^2)}$, the signal ratio SR $= \frac{\overline{E_{\mathrm{n}}}}{\overline{E_{\mathrm{c}}}}$, and the runtime of the reconstruction. Regarding the estimation of displacements, we again challenge our method with the most popular OF methods: Horn and Schunck (HS) [203], TV-L_1 [261], large-displacement optical flow (LDOF) [222], and iterative Lukas-Kanade (ILK) [223]. Since the direct-reconstruction method collapses entirely when paired with any of these (data not shown), we only pair them with the indirect-reconstruction method. We implement it with the dolfin-adjoint library [201].

Experiment 1. We compare accuracy versus the boundary traction $||\mathbf{T}|| \in \{0.03, 0.0325, ..., 0.0375\}$ with a fixed nuclear radius of 20 (Table IV.1). Our method runs faster than the others by two orders of magnitude. Note that this is mainly because the quality of the proposed OF enables the use of the direct method. Its computation time (2.42 ± 0.13s) is comparable to that of the other OF methods (e.g., 2.07 ± 0.11s for TV-L_1). However, this is mainly due to the fact that we deliberately chose a low number of iterations of the proximal estimation step. Should we increase it, for further regularity properties, this would increase the runtime. Our proposed method is also more accurate both in NRMSE and SR, and achieves great contrast (Figure IV.3). However, its CNR is poorer than that of some of the competing methods because the regularization of E in the indirect method imposes a low variance on the reconstruction. In return, the results of the other methods greatly underestimate the magnitude of the modulus. One can also see that the accuracy of the reconstructions with indirect is very shabby at the boundary of the left and right part of the domain. This is due to the low amount of traction applied there, and also because of the great inaccuracies in the lateral component of the displacement field, as testified in the previous chapter. As expected, TV-L_1 does a better job at preserving the edges of the displacement than the L_2 norm in HS (Figure IV.3).

Experiment 2. We set the traction to $||\mathbf{T}|| = 0.0375$, and simulate compression with the radius $R \in \{20, 22.5, ..., 30\}$. The conclusions are the same in terms of accuracy and performance as in Experiment 1 (Table IV.1). We see, however, that the TV-L_1, ILK, and LDOF methods paired with an indirect-reconstruction method are much more sensitive to the size of the nucleus, while the accuracy of our method does not vary significantly. This accuracy is maintained for smaller nuclei too (Figure IV.3). Should we want to improve the reconstruction for small objects, one would have to revisit the coarse-to-fine strategy defined in the previous chapter. Like we mentioned with LDOF, this tends to wipe off movements of small objects at the coarsest scales. To counteract it, we may try to incorporate some additional features penalization in the variational framework.

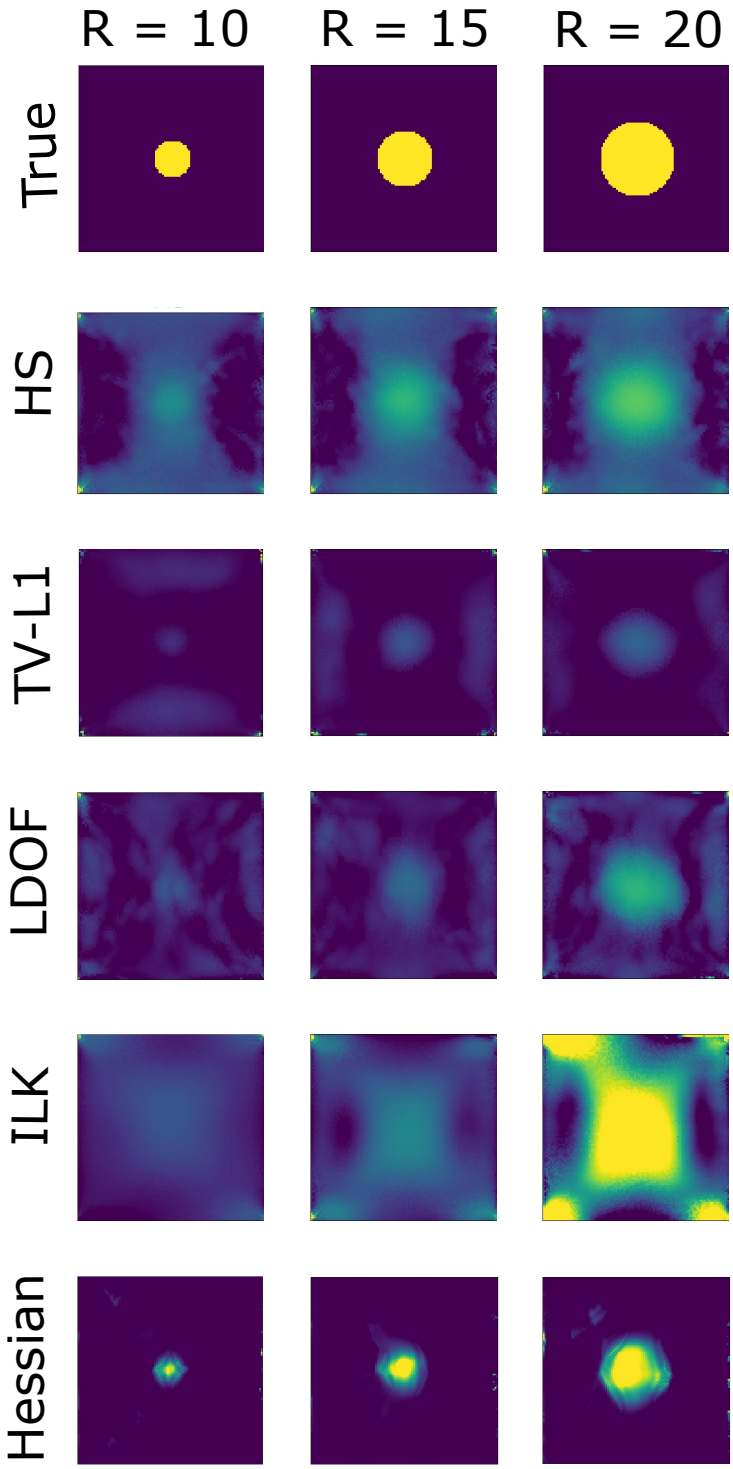

Figure IV.3: Reconstructed Young's modulus of the cell and its nucleus. We see that our method is considerably more accurate than any other optical flow method. Its resolution is also very high, as it even detects very tight stiff circles. Mark that ours was paired with a direct reconstruction method, and hence is much faster.

IV.2.2 A mixed PDE framework for the computation of relative Young's modulus

The previous framework can be aptly paired with any of the compression method we presented in Chapter 1. Unfortunately, for most, it is very difficult to know accurately the amount of force that is applied and, even more cumbersomely, the exact region to which it is applied. For *in vivo* setting for instance, the computation is outright impossible. However, in this section, we show that it is possible to retrieve the map of the relative Young's modulus. Meaning, ascribing a reference region with a reference value (most often the boundary, because it contains the lamina meshwork), we can compute the stiffness ratio between each point of the nuclear domain compared to this reference value. One would argue that it is possible to adapt the previously established methods to this setting. Indeed, we would only need to set $E = 1$ to the boundary of the domain, use the boundary displacement field to compute the traction $\mathbf{T}$. This configuration will be taken into account, but as we will see, the achieved results are very erroneous. Mostly, we have to blame the noise afflicting optical flow techniques at the nucleus' boundary. Indirect reconstruction methods are more stable to do decent reconstructions in some cases, but as laid out before, they are too slow in practice to be run for large dataset. Instead, we propose a new elastography method to invert the displacements for the stiffness map in a way that is robust and efficient. It is based on a modified system of elliptic partial differential equations of the relative stiffness. It accounts for the compressibiltiy of the nucleus and does not require knowledge of the traction boundary conditions.

Our work extends that of [290] for incompressible tissues. We suppose that the Young modulus takes known reference values E_r at certain part of the domain. This includes the nuclear boundary, as we have stated earlier, but may also comprise some specifically marked segmented regions as in [271]. Here we suppose that E is twice differentiable in the distributional sense. Although inaccurate in some cases, we nevertheless know this is a good approximation. The mean normal stress is:

$$p = \frac{\varsigma_{xx} + \varsigma_{yy}}{3} = 2\mu(\varepsilon_{xx} + \varepsilon_{yy}) \tag{IV.3}$$

where μ is the second Lamé parameter. This equation can be written also in the following way:

$$\varsigma_{ij} = p\delta_{ij} + b_{ij} \tag{IV.4}$$

where b is the stress deviation tensor. The constitutive equations of the stresses $\varsigma_{xx}, \varsigma_{yy}$ and ς_{yy} can be therefore recasted as:

$$\begin{aligned} \varsigma_{xx} &= p + 2\mu\varepsilon_{xx} \\ &= 2\mu(2\varepsilon_{xx} + \varepsilon_{yy}), \\ \varsigma_{yy} &= p + 2\mu(\varepsilon_{yy}) \\ &= 2\mu(\varepsilon_{xx} + 2\varepsilon_{yy}), \\ \varsigma_{xy} &= 2\mu\varepsilon_{xy} \end{aligned} \tag{IV.5}$$

Inputting the constitutive equation in (II.16) into the momentum equation, this allows us to express the following first order system of equations for E, valid at each point:

$$\begin{bmatrix} a_{11}\varepsilon_{11} + a_{22}\varepsilon_{22} & a_{12}\varepsilon_{12} \\ a_{21}\varepsilon_{21} & a_{22}\varepsilon_{11} + a_{11}\varepsilon_{22} \end{bmatrix} \begin{bmatrix} \partial_x \ln(E) \\ \partial_y \ln(E) \end{bmatrix}$$

$$= - \begin{bmatrix} \partial_x(a_{11}\varepsilon_{11} + a_{22}\varepsilon_{22}) & + & \partial_y(a_{12}\varepsilon_{12}) \\ \partial_x(a_{21}\varepsilon_{21}) & + & \partial_y(a_{22}\varepsilon_{11} + a_{11}\varepsilon_{22}) \end{bmatrix} \tag{IV.6}$$

where:

$$\begin{aligned} a_{11} &= \frac{(1-\nu)}{(1+\nu)(1-2\nu)} \\ a_{22} &= \frac{\nu}{(1+\nu)(1-2\nu)} \\ a_{12} = a_{21} &= \frac{1}{1+\nu} \end{aligned} \tag{IV.7}$$

We introduce the matrix fields $\mathcal{A}$ and $\mathcal{F}$ such that:

$$\mathcal{A}\nabla \ln(E) = \mathcal{F} \tag{IV.8}$$

Remark that $\mathcal{F}$ is ill-defined if we do not assume $\mathbf{u} \in W^{2,1}(\Omega, \mathbb{R}^2)$ for mixed boundary conditions.

Second order partial differential equations of the relative Young's modulus have also been considered in the past [291], [292]. Despite their apparent differences, these equations all have in common to be hyperbolic. The method of characteristics is therefore a method of choice to both directly solve them or to derive some of their analytical properties. It generally turns out from this analysis that characteristic curves are parallel to the principal axes of the strain, and that knowing a point-wise value of two intersecting characteristic curves are enough to reconstruct the Young's modulus within the whole region these curves encompass [292]. As a rule of thumb, it is in theory sufficient to know the value of E across all the boundary to solve equation (IV.6) over the whole domain [278]. This means that the equation we established is well-posed in our case, and should admit a unique stable solution. However we see in practice that it does not. The reason is that noise invariably corrupts the computation of the strain, and in "wave-propagation" like equations as the one we study, the accumulation of local errors tend to globally accumulate in a general reconstruction collapse. A Tikhonov-like penalization of the global reconstruction was proposed with a finite-difference scheme [293], but this framework is delicate to adapt to domains with non simplistic geometries and requires heavier computations. Instead, we deliberately add a second-order term to our system of equations in order to render it elliptic:

$$\mathcal{A}\nabla \ln(E) + \mathcal{B} = \mathcal{F} \tag{IV.9}$$

where $\mathcal{B} = (\gamma_1 \Delta \ln(E), \gamma_2 \Delta \ln(E))^T$, and γ_1 and γ_2 are two (small) regularization constants. From a physical point of view, hyperbolic and parabolic equations are generally associated with dynamic behaviors that transport initial values at the boundary to the whole domain. Whereas elliptic equations as (IV.9) are rather representative of static behaviors, which better describe the physics behind stiffness distribution.

We introduce the new variable $\sigma = \nabla \ln(E)$. We multiply this system with $\tau = (\tau_1, \tau_2) \in H(\text{div}, \Omega)^2$ and $v \in H(\text{div}, \Omega)^2$. By integrating over Ω and applying the Green identity, we get the following weak formulation:

$$\begin{cases} \int_\Omega \mathcal{A}\sigma \cdot \tau + (\gamma_1 + \gamma_2) \int_\Omega \sigma \cdot \nabla(\tau_1 + \tau_2) = \int_\Omega \mathcal{F} \cdot \tau \\ \int_\Omega \sigma \cdot v = \int_\Omega \nabla \ln(E) \cdot v \end{cases} \tag{IV.10}$$

which admits a unique solution for every $\mathcal{F}$ thanks to the validity of the inf-sup condition and the Babuska-Brezzi theorem. We solve (IV.10) numerically with the finite element method. The relative Young's modulus is recovered through exponentiation of the solution. After proper meshing of the nuclear domain, we discretize the values of interest with second order continuous galerkin interpolators, and assemble the whole system. Matrix $\mathcal{A}$ is sparse, but indefinite and non symmetric, therefore we resort to a generalization of symmetric Krylov methods, namely the minimal residual method (GMRES) preconditioned with incomplete LU factorization. The framework scales linearly with the dimension of the discretization, allowing very fast inversion, as the next section will testify.

We proceed to two distinct evaluations of our framework. First, given true displacements, we compare our stiffness reconstruction algorithm to direct and indirect reconstruction methods. Second, we measure the accuracy of our full pipeline and its effectiveness in detecting abnormal stiffness heterogeneities in cells' nuclei. The first part is equally useful for medical imaging as well, so we will not constrain its experiments to biological settings.

The employed metrics are the following. Denote s an estimated signal – potentially vector or tensor valued – defined over a rasterized domain R^N, s_t its ideal simulated counterpart, s^h and s^e the restrictions to the heterochromatin and euchromatin domains respectively, $\overline{s}$ its mean value, and σ_s its standard variation. We will use:

- the root mean square error RMSE $= \sqrt{\text{MSE}} = \sqrt{\frac{1}{N}\sum_{i=1}^{N}||s - s_t||^2_{S_2}}$,
- the signal ratio SR $= \frac{\overline{s^h}}{\overline{s^e}}$,
- and the contrast-to-noise ratio CNR $= \sqrt{2(\overline{s^{\text{h}}} - \overline{s^{\text{e}}})^2/(\sigma^2_{s^{\text{h}}} + \sigma^2_{s^{\text{e}}})}$.

The RMSE is a general indicator of overall accuracy of the stiffness. It nevertheless does not suffice on its own here. For instance, suppose that one elastography method computes accurately a stiff inclusion within the elastic domain, but it finds it rather smaller than it should, the RMSE can suffer quite substantially. On the other hand, if the shape of the reconstruction is right, but the values of the inclusion is wrong, by say a tenth of what it should be, the RMSE would not be so much changed. Whereas in our case, it can be more interesting to have better inclusion values, regardless of the shape. This is why we supply this first error metric with the signal ratio. The contrast-to-noise ratio is more useful in medical imaging. In a nutshell, it evaluates how "visible" a stiff inclusion, like a tumor, is in the elastogram. It remains nevertheless helpful in our case, as it can indicate how much the heterochromatin domain (stiff) and the euchromatin (soft) are discernable to the human eye.

Our proposed optical flow method is designated by "Hessian". Our stiffness reconstruction framework is benchmarked against the performances of direct [279] and indirect elastography [276], both with known traction boundary forces and reconstructed boundary forces. It is named "Mixed PDE". We refer to "direct relative" and to "indirect relative" when the traction boundary forces are not given, but recovered from the displacement field. When they are, we will only say "direct" and "indirect". Although this advantageous configuration is impossible in biological imaging, it is in medical imaging. We show that our method compares nonetheless much better.

We suppose the elastic body to be a square that fills the entirety of a 100×100 image (see Figure IV.4.a). Its upper and lower parts are clamped; its left and right sides under constant traction forces. It assumes a constant Poisson's ratio $\nu = 0.33$. Its Young's modulus is equally constant to E_0, except for one to three inclusions, where it respectively equals, depending on the number of them, to E_1, E_2 and E_3. For these we will set values ranging from 3 to 7, encapsulating the correct range for both tissues in medical imaging and biological material.

Figure IV.5 displays the Young's modulus reconstructions for one to three inclusions with increasing stiffnesses. Although "direct relative" and "indirect relative" recovers the right position and shapes of the inclusions, the stiffnesses of the inclusions are underestimated. This is slightly corrected when the traction forces are inputted with "direct" and "indirect". But even then, our Mixed PDE framework is much more accurate and computes the almost exact value of the Young's modulus at each inclusion. Notice also how the values of direct and direct relative reconstructions tend to be lower in regions where

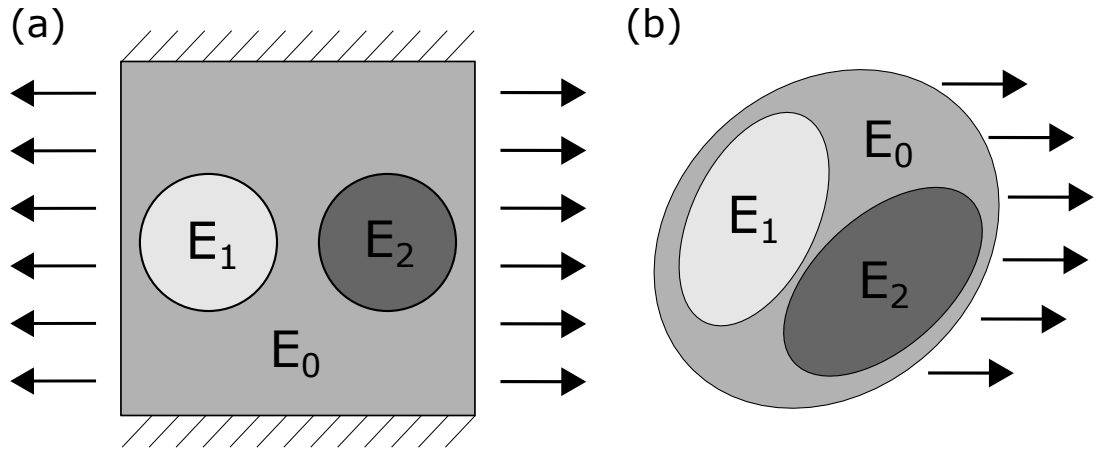

Figure IV.4: Examples of simulated experimental settings in elastography. The values E_0, E_1, E_2 denote the stiffness of the background and of the two inclusions, the arrows represent the applied traction on the boundary. We use (a) for the evaluation of the Mixed PDE because it is most general to elastography (e.g., medical), and we use (b) in our whole framework evaluation for an experiment that is closer to potential real conditions involving the nucleus.

the traction is not applied. This is mainly due because the deformation doesn't propagate easily in this region of the image. Whereas in our case, since we do not propagate the force, but the Young's modulus defined over the whole boundary, this problem does not occur. Unfortunately we cannot explain why this artifact does not appear for indirect reconstruction methods. We suppose that, because the null boundary traction forces are enforced at each step of the iterative process, they may be better recognized in this region. To further this line of enquiry, one may try to reformulate our method with free boundary conditions at the bottom and the top of the image. We did not investigate however this line of research, but it might be interesting for further adaptation for medical imaging. The superiority of our method testified in the diagonal profiles as plotted in Figure IV.6. In it we only kept the indirect reconstruction as comparison for better clarity. Again we see that the true values of the inclusions are much faithfully reconstructed with our method. This is especially evident for the three inclusions case, where indirect bungles the reconstruction for the third inclusion. We may further notice some artifact for our own method. For instance, at the right part of such inclusion, the value of the Young's modulus dips. Also, for three inclusions, the radii of the inclusions are smaller than they ought to be. In fact, in that respect, indirect reconstruction methods might do a slightly better job. This is can be seen in the reconstructions in Figure IV.5 as the "comet-tail" like figure behind some inclusions. We believe this can have two causes. First, since it is less present in the one inclusion case, this might indicate that this comes from the regularity assumption we set for E (remember we set it to be twice differentiable). This could be a way for the algorithm to smooth out the variations at the boundary of the inclusions. What conforts us in this hypothesis is that the tail-like artifact does not appear, or very dimly, for softer inclusions. On the other hand, there is no reason to see this asymmetry, so there should be another cause to this artifact. One line of enquiry might be the irregularity of the domain: since the image has 90 degrees corners, the smoothness assumption is actually violated in this case, and therefore the regularity of the displacement field called in question. We also noticed (data not shown) that this problem vanishes for smooth boundaries as in Figure IV.4.b.

All these "qualitative" discussions are further confirmed quantitatively. The RMSE of the elastography methods are consigned in Table IV.2. Again ours proves consistently superior regardless of the experimentation. We see that indirect reconstruction methods nevertheless do better than direct ones. Most of the gains are due at the part of the boundary where the traction is not applied, and around the inclusions, where direct reconstruction methods tend to reconstruct smaller radii as well. Also we may notice that "relative" methods are far less accurate than their counterparts. This might be because the

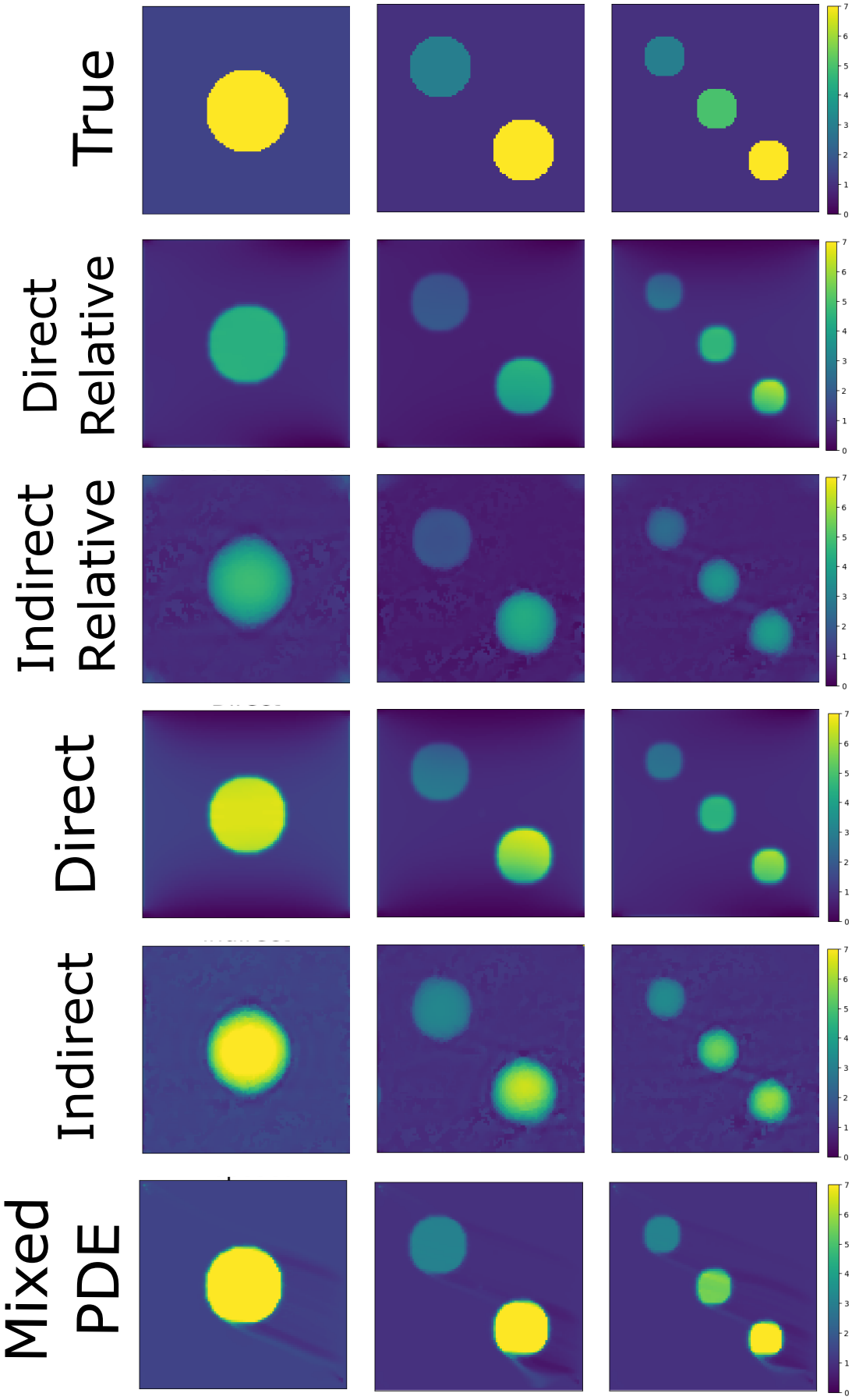

Figure IV.5: Classical elastography reconstruction methods against our Mixed PDE.

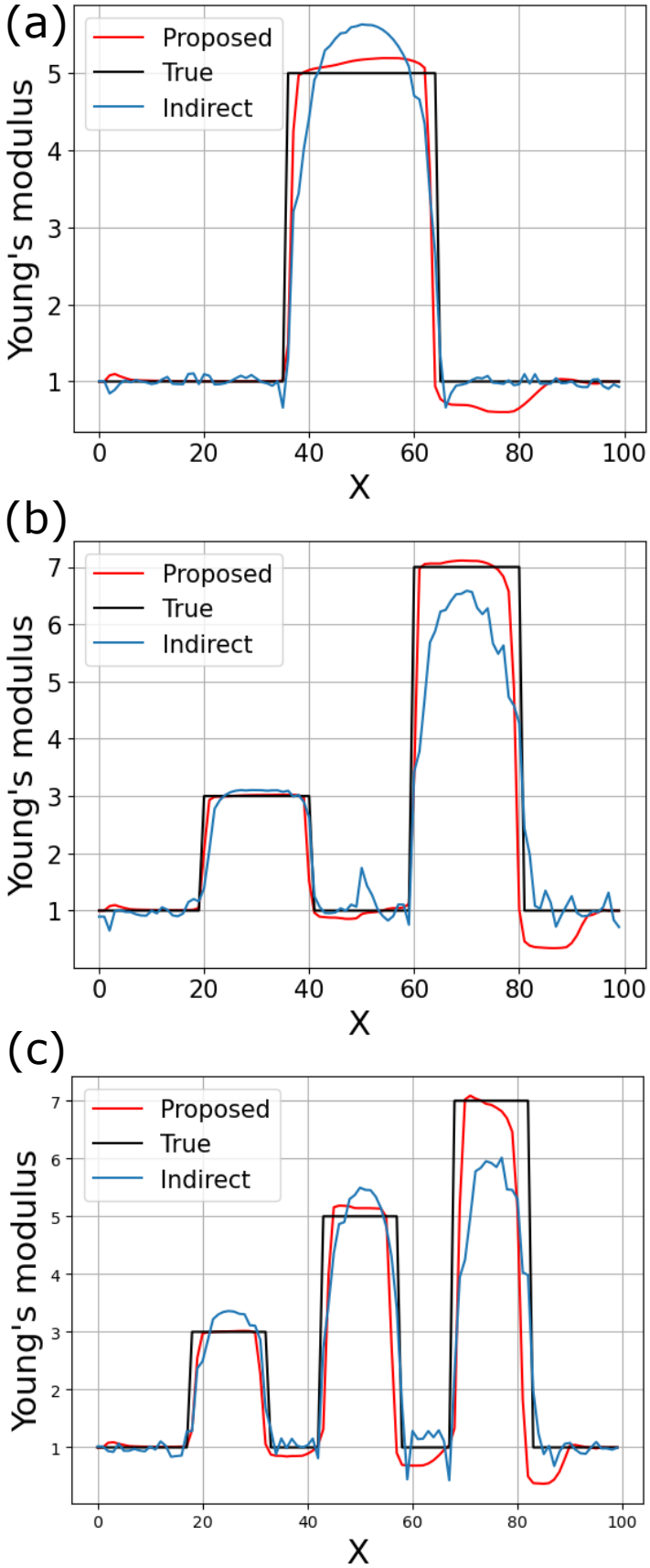

Figure IV.6: Profile of the elastography reconstruction methods for a varying number of inclusions. Reconstruction profile with: (a) one inclusion ; (b) two inclusions ; (c) three inclusions.

Experiments	Dir. r.	Ind. r.	Dir.	Ind.	Mixed PDE
T	0.25	0.19	0.12	0.10	**0.08**
ν	0.23	0.17	0.15	0.12	**0.09**
E	0.16	0.17	0.11	0.10	**0.09**
Nb. inc.	0.26	0.24	0.16	0.09	**0.05**

Table IV.2: RMSE of the elastography reconstruction methods for experiments with varying stretching conditions.

Number of Nodes	Indirect	Mixed PDE
100×100	9min 14s	2.7s
500×500	7h 19 min 59s	26s
1000×1000	1d 3h 58 min 42s	2min 37s

Table IV.3: Runtime of our Mixed-PDE method compared to indirect reconstruction.

differentiation at the boundary tends to be erroneous, even when true displacements are given: just think that one needs to wrap the image before doing that. We may perhaps further increase the accuracy of those, by chosing more carefully the differentiation schemes, but to search for gains at this level of accuracy only showcases the sensitivity of such methods to the choice of boundary conditions. The runtime of indirect reconstruction method versus ours is displayed in Table IV.3. A single CPU was used for each experiment. The direct reconstruction method is sensibly similar to ours, and the runtime does not change when we use known boundary tractions or reconstructed. We see that indirect elastography's runtime grows intractable with the number of nodes, whereas ours remains considerably fast. More precisely, we see that the runtime expands exponentially for the indirect reconstruction method, and linearly for ours. This confirms that our method can readily be applied for 3D reconstruction as well. Unfortunately, we could not yet apply it for this configuration yet. This is a data creation issue: our framework, though applicable in theory for creating 3D images as well, has additional inaccuracies in this setting that need to be dealt with. But the results found here are encouraging.

For the whole framework evaluation, we consider two configurations of interest. The first is termed "stiff lamina", the second "stiff heterochromatin". In "stiff lamina", the heterochromatin gathers around the nuclear pore complexes at the nuclear periphery. In this sense, the word lamina is misleading, as really it is a continuation of the lamina meshwork with the heterochromatin domain that is studied here. But since we refered up until here to the boundary part of the nucleus as the one dictated by the lamina, we feel it is fitting. The boundary and its neighborhood is 5 times stiffer than the interior. The nucleus is supposed circular, as is the case for white blood cells for instance. In "stiff heterochromatin", the heterochromatin gathers around a nucleolus, the euchromatin stays loose in a highly transcriptive domain, and the remaining of the nuclear interior is filled with nuclear bodies. The nucleus is modeled as an ellipsoid of stiffness 1, such as for cancer cells, with two ellipses with respective stiffnesses of 0.2 and 5 (see left column of Figure IV.7 and Figure IV.8).

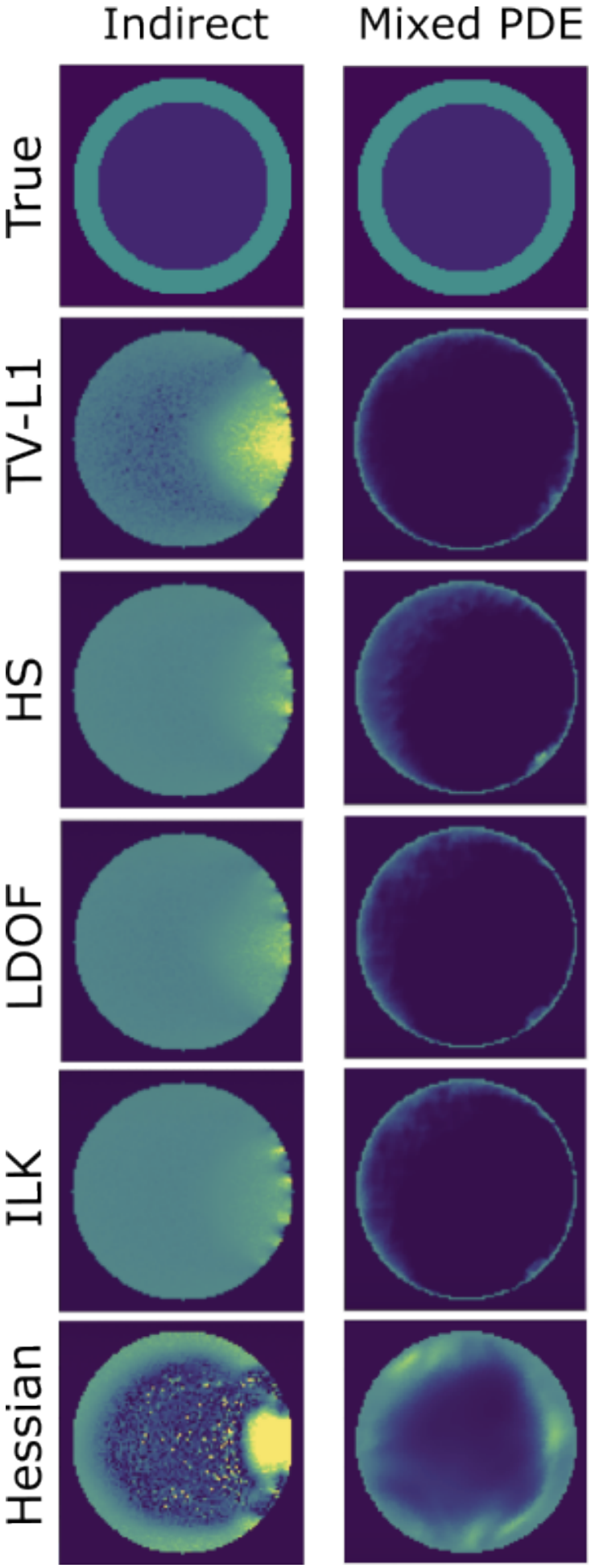

Figure IV.7: Whole pipeline evaluation with heterochromatin gathering at the nuclear pore complexes.

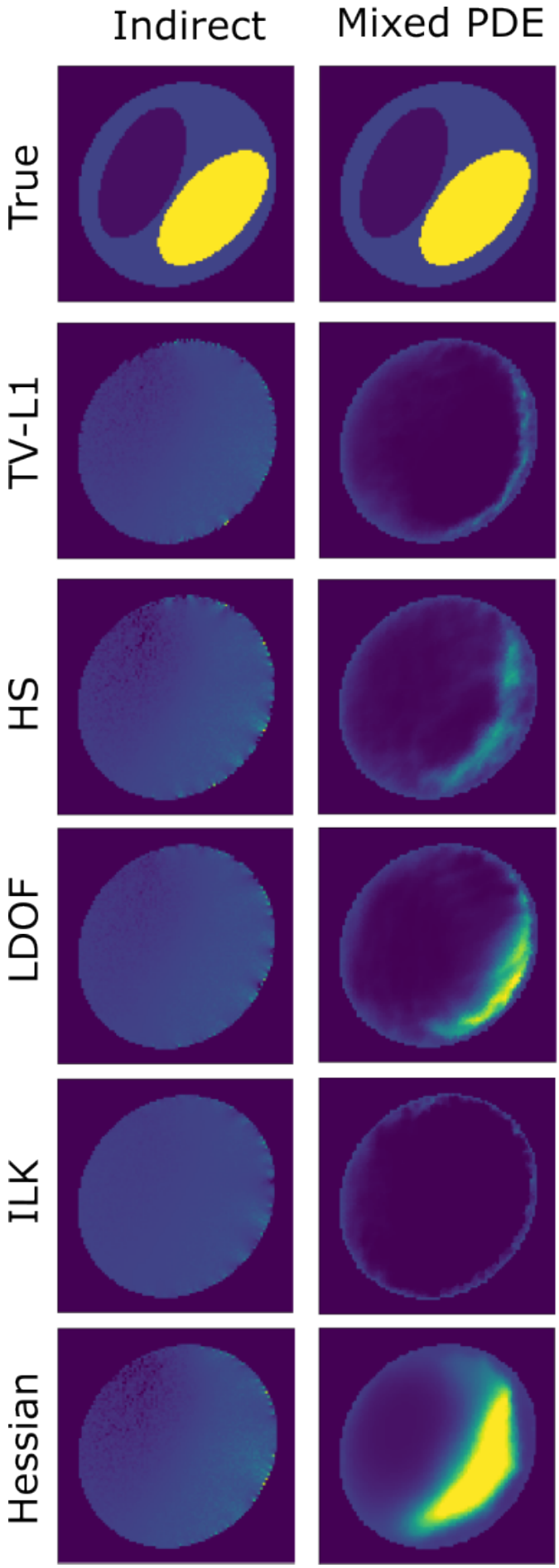

Figure IV.8: Whole pipeline evaluation with heterochromatin gathering at a nucleolus within the nuclear interior.

We pair each optical flow technique with indirect relative elastography and Mixed PDE elastography. Three experiments are undertaken: one with varying traction, one with varying Poisson's ratio, one with varying Dirichlet and Neumann boundary domains Γ_u and Γ_t. The tractions are applied on the right part of the nuclei in Figure IV.7 and Figure IV.8. For each configuration, a lower value of RMSE and a higher value of CNR are desired. The ideal SR is 0.2 for the "stiff lamina" configuration, and 20 for the "stiff heterochromatin" one. In that light, Table IV.4 shows that our proposed combination, Hessian + Mixed PDE, far surpasses any other with any metrics whatsoever. In particular, one may notice that our combination retrieves almost exactly the stiffness ratio in all cases, which makes our method a solid candidate for diagnosis and prognosis purposes.

Experiments			Indirect					Mixed PDE				
			TV-L1	HS	LDOF	ILK	Hessian	TV-L1	HS	LDOF	ILK	Hessian
Stiff lamina	T	RMSE	0.49	0.49	0.50	0.49	0.45	0.34	0.31	0.32	0.34	**0.25**
		SR (0.2)	0.97	0.95	0.85	0.93	0.70	0.01	0.07	0.04	0.03	**0.23**
		CNR	0.28	0.46	0.51	0.42	1.09	1.38	1.40	1.22	1.17	**1.87**
	ν	RMSE	0.49	0.50	0.49	0.53	0.51	0.36	0.32	0.35	0.34	**0.28**
		SR (0.2)	0.87	0.77	0.74	0.78	0.37	0.00	0.01	0.00	0.00	**0.21**
		CNR	0.46	0.71	0.81	0.58	1.98	1.39	1.40	0.95	1.25	**1.99**
	BC	RMSE	0.57	0.49	0.49	0.51	0.48	0.34	0.31	0.35	0.35	**0.23**
		SR (0.2)	0.86	0.95	0.85	0.90	0.52	0.00	0.02	0.00	0.00	**0.21**
		CNR	0.35	0.42	0.53	0.32	1.19	1.27	1.36	1.16	1.06	**1.41**
Stiff heterochromatin	T	RMSE	1.48	1.50	1.51	1.51	1.42	1.55	1.92	1.49	1.93	**0.96**
		SR (20)	1.34	1.36	1.37	1.37	1.30	31.82	0.09	57.39	0.00	**21.90**
		CNR	0.81	0.80	0.80	0.61	1.47	1.47	1.15	1.45	1.29	**4.68**
	ν	RMSE	1.52	1.55	1.54	1.53	1.54	1.91	1.93	1.39	1.93	**0.90**
		SR (20)	1.30	1.34	1.31	1.35	1.30	0.00	0.00	0.00	8.00	**18.43**
		CNR	0.33	1.01	1.20	0.99	1.52	0.20	1.34	1.90	1.03	**3.14**
	BC	RMSE	1.46	1.48	1.46	1.49	1.44	1.64	1.91	1.82	1.93	**1.00**
		SR (20)	1.30	1.34	1.31	1.35	1.30	11.22	0.31	124.39	0.00	**26.47**
		CNR	1.20	1.01	1.20	0.92	1.50	0.20	1.34	1.90	1.03	**3.16**

Table IV.4: Quantitative evaluation of the whole pipeline for the two real-like configurations. RMSE, SR (target value) and CNR of the reconstructed stiffness for all combinations of optical-flow methods (ours is Hessian) with the two most accurate elastography methods: relative indirect, and our Mixed PDE.

Actually, all other combinations collapse entirely. This is evident in figures IV.7 and IV.8. We believe this is a direct consequence of both the irregular geometry of the nucleus and the inevitable inaccuracy of the displacement field at the boundary, which corrupts the reconstructed traction forces. Because we supposed $E \in H^2(\Omega, \mathbb{R})$, our method smoothes the shape of the Young's modulus at the boundary of inclusions. Nevertheless the positions of the inclusions are well spotted, and the computed stiffnesses are correct. To further improve the shape of the reconstruction, one might think of using non-local definition of the Hessian operator during the optical flow computation. This would entangle the optimization procedure, and increases the computation time, but if the need be felt this line of enquiry is interesting.

IV.3 Application 2: estimation of the relative stiffness distribution of deforming cardiomyocytes and SKOV3 cells' nuclei

Our method is finally applied for real images of nuclear deformation. Again, two cases are considered: an *in vitro* one, and an *in vivo* one (see Figure IV.9). These images are owned by biologists with whom no collaborations are under way. Here we only apply our elastography method for further validation. Indeed, each of these images come from experiments of their own which establish their own values of the stiffness. Our aim here is to say that our results differ not much from theirs, only they act under either lower hypothesis or yield higher precision in its evaluation (for instance by giving a whole map of the Young's modulus instead of a single value of interest).

The *in vitro* case displays the local bending of an SKOV3 cell's nucleus to an AFM's probe [272]. The reconstructed Young's modulus shows a soft nuclear interior, except at the overall boundary, and especially at the bottom part of the nucleus. This is expected, since the nucleus preserves its shape, and since it is laid on a plate covered with fibronectin, to which it strongly bounds. We also thresholded the stiffness between the boundary and the interior, and computed a stiffness ratio of 1.33. This is close to the findings of [272], which established a ratio of 1.36 through approximate means involving the change in perimeter and volume. Note that here the deformations are localized, but sufficiently important. Should the applied stress be weak, the reconstruction of the overall stiffness might be called into question, as the deformation would have not "rippled" throughout the entirety of the nuclear domain. This is the reason why we utilized plate compression in our simulation before for the computation of absolute values of the Young's modulus. Note also that the details of our reconstruction cannot be trusted yet. For instsance, we see some speckles of high stiffness at the top and the right of the reconstruction: these are too small to be anything but some irregularity of the reconstruction. Further evaluations on the resolution of our method needs to be established. But the numerical evaluations undertaken so far can assure us of the faithfulness of the two regimes of stiffness (soft in the middle and stiff at the periphery) governing the nucleus.

The *in vivo* case displays the deformation of a myocardyocyte's nucleus between two peaks of heart contractions. We owe these images to [271], who proposed an elastography method of their own requiring a preliminary segmentation of the heterochromatin and euchromatin domains. Their segmentation relies on the correlation between image intensity and chromatin density in the image. Indeed, when the compaction is higher, the concentration of fluorophore in the domain is proven to be higher as well. But this does not take some dispersion effects that can violate this simple relationship. In some cases, it would be better to not trust any segmentation of the nuclear interior. This is why our method is interesting here. Likewise, we implemented a thresholding operation to show compute a stiffness ratio between the soft part of the domain and the stiff part. We find that it amounts to 9.41, against 10 in the case of [271], without the aid of preliminary segmentation. In their article, [271] showed that when the Klarsicht, ANC-1, Syne Homology domain of the Linker of Nucleoskeleton and Cytoskeleton complex are disrupted, then the intranuclear elasticity distribution results in similar heterochromatin and euchromatin stiffness. We believe our method could be easily implemented to show similar results for cases where the segmentation of the interior of the nucleus is not possible.

To conclude, we presented a fast and robust method for recovering the stiffness map of cells' nuclei based on images of their deformation. To the best of our knowledge, this is the first that doesn't require any prior intelligence on the nuclear stiffness. Our framework pairs a novel optical flow technique with a fast mixed PDE solve. It displays consistent accuracy in multiple numerical simulations. Its prognosis capabilities are established. Its speed makes it operative on 3D images as well. Applications on previously studied real images of deforming nuclei confirmed previously established biological functionalities.

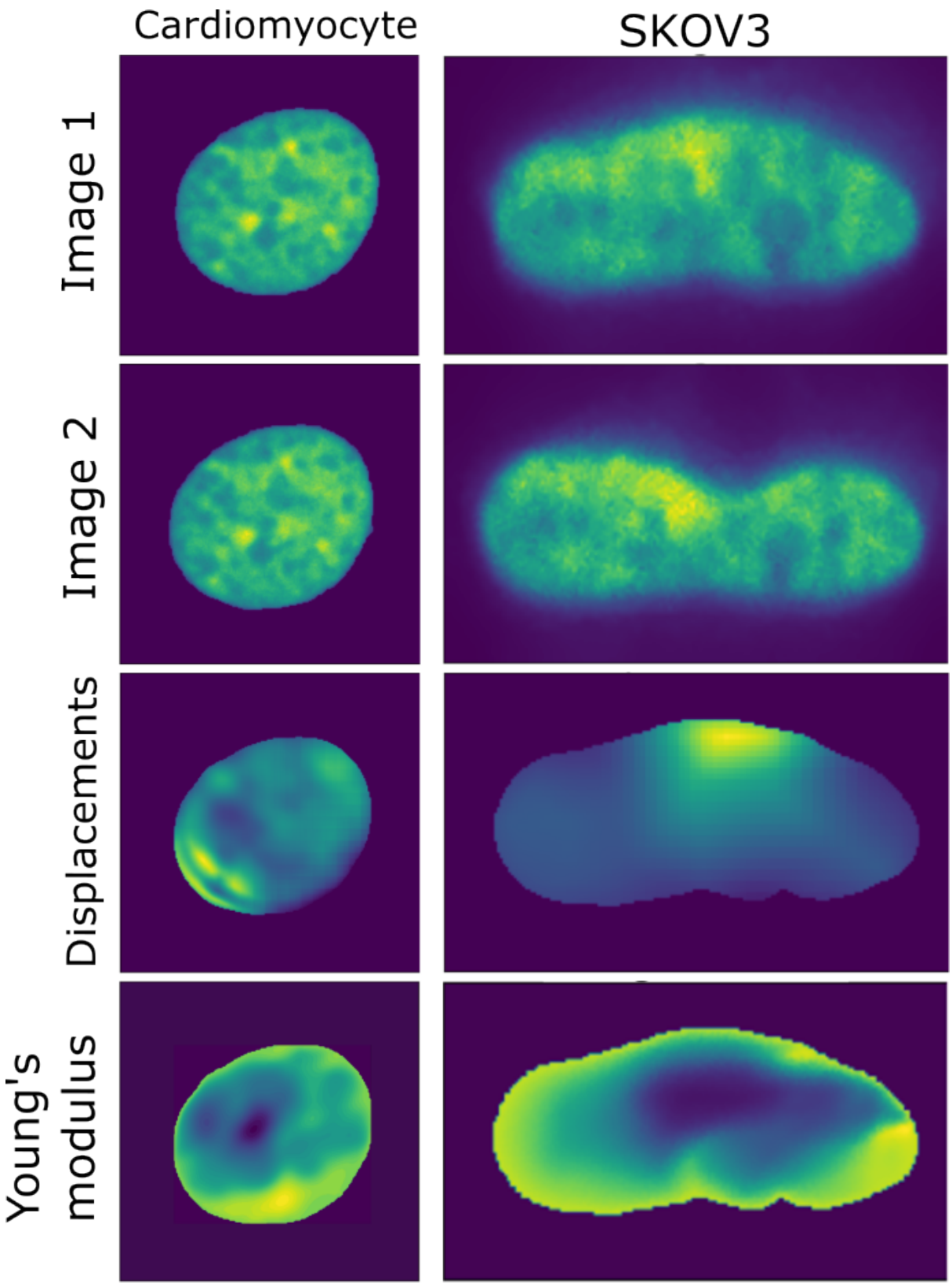

Figure IV.9: Application of our elastography method on real images of deforming nuclei.

IV.4 Proposed method for measuring stress and boundary traction forces

We now tackle the second problem stated in Chapter II. Given the Young's modulus distribution E of the nucleus, its Poisson's ratio ν, and images before and after deformation of the nucleus, compute the stress field ς and the boundary traction forces $\mathbf{T}$. Despite the recent advances in mechanobiology, there lacks yet a large bank of values of the Young's modulus and the Poisson's ratio of biological material. We nevertheless encounter some, and it has been the custom in the past that, in order to study the mechanical behavior of a given biological material, biologists use the available values of other nuclei that are known to respond similarly. Like in the previous section, we divide our presentation into two. First, we expose our novel image processing method to compute accurately the stress field and the boundary traction forces. We will see that it also bolsters the displacement and strain values that we computed in the previous section. As luck would have it (or, in this case, the absence thereof), we developed this part of the work before finishing our inquiry on optical flow with regularised Hessian Schatten norms. It remains to systematically evaluate its combination with this new optical flow method of ours. The results are nevertheless very satisfying with Horn-Schunck optical flow, as the reader will see. Then, in a second step, once validated numerically, we will apply this framework to videos of invading Toxoplasma gondii to describe the mechanics of its nucleus.

Our framework follows the one introduced in [284]. It's a PDE-constrained optimisation framework to compute all the mechanical quantities of interest in the study of nuclear deformation, namely: displacement, strain and stress at each of the pixels inside, and the traction forces on the boundary. First, a displacement field is derived using optical flow. Then an inverse optimization problem is formulated: it seeks to find those displacements that come closest to the computed field while also abiding by the dynamical model of the nucleus. Using finite differences, we retrieve from this solution the strain and stress fields, as well as the traction force on the boundary.

Simulating traction over the nuclear boundary, we warp a 2D image of a nucleus to create a second one after deformation, as laid out in chapter II. These two images are used to test the validity of our method: we show that our reconstruction not only faithfully reproduces the mechanical quantities guiding deformation, but that it distinctly surpasses the results we would get from optical flow techniques alone. Unlike previous simulations, we used this time images of a glioblastoma nucleus, as to better simulate the real texture of a fluorescence image.

We saw in the first chapter that building a comprehensive model that would account for all nuclear components and all protein interactions such as the LINC complex is still out of reach. Yet research over the last decades agrees its overall mechanical response relies mostly on the properties of two of its constituents: the nuclear lamina and the chromatin. The nuclear lamina is a 10 - 100 nm meshwork that underlies the nuclear envelope. The chromatin fills the nuclear interior, which is about 10 μm thick. Both domains are linked through molecular interactions. We therefore model them as a lamin shell wrapping the chromatin domain without sliding on it.

In the remaining of this section, we will assume that lamina and chromatin are both continuous media. This assumption holds true at the microscopic level, where most confocal microscopes operate, but would need to be reevaluated if one were to work with smaller scales, where the meshwork structure of the lamin and the fractal-like configuration of the chromatin might be more relevant. Suppose now the nucleus encompasses a domain $\Omega \subset \mathbb{R}^n$, where $n \in \{2, 3\}$. We define lamin as the boundary of this domain and chromatin as its complement, i.e. as the whole domain except the boundary. The literature concurs on assigning either of two main mechanical models to them: elastic or viscoelastic. We will assume both domains follow an isotropic linearly elastic model, albeit of different stiffness; this is a good approximation at large timescales and small deformations, two regimes that well fit our biological data.

We suppose here that nuclear deformation happens only from external mechanical constraints and not from volumic forces as to model mechanotransduction. The framework we propose applies nonetheless to any other kind of mechanical model. This settled, we can establish the equations ruling the nuclear domain Ω.

$$\begin{cases} \nabla \cdot \varsigma = 0 & \text{in } \Omega, \\ \varsigma(\mathbf{u}) := \lambda \text{tr}(\varepsilon(\mathbf{u}))I + 2\mu\varepsilon(\mathbf{u}) & \text{in } \Omega, \\ \varepsilon(\mathbf{u}) := \frac{1}{2}(\nabla\mathbf{u} + \nabla\mathbf{u}^T) & \text{in } \Omega, \\ \lambda = \lambda_l,\ \mu = \mu_l & \text{on } \Gamma, \\ \lambda = \lambda_c,\ \mu = \mu_c & \text{in } \Omega \setminus \Gamma \\ \mathbf{u} = \mathbf{g} & \text{on } \Gamma. \end{cases} \tag{IV.11}$$

Here, $\mathbf{g}$ is the displacement on the boundary, and we recall that λ and μ are the Lamé parameters given by:

$$\begin{aligned} \lambda &= \frac{E\nu}{(1+\nu)(1-2\nu)} \\ \mu &= \frac{E}{2(1+\nu)} \end{aligned} \tag{IV.12}$$

where subscripts should be added according to the domain on which they are evaluated. Note here that we only assumed Dirichlet boundary conditions, but Neumann could easily be included. We will see that, in a mathematical point of view, the optimization problems we will solve do not differ much by swapping one with the other.

Given images of the nucleus before and after deformations, we first compute the displacement field using the Horn-Schunck method by solving the following variational problem, as laid down in the beginning of Chapter 2:

$$\underset{\mathbf{u}}{\text{argmin}} \int_{\Omega_I} \left(\frac{\partial I}{\partial t} + \mathbf{u} \cdot \nabla I \right)^2 + \alpha ||\nabla \mathbf{u}||^2$$

where Ω_I is the domain of the image function I and α is a regularization constant. Of course, now we would apply the second order optical flow as proposed before.

Starting with the solutions computed with optical flow, one can differentiate the velocity to compute the strain, then the stress, and then the traction vector over the boundary. But we wouldn't profit from the information we might get from the mechanical knowledge we hold on the nucleus: there is a better strategy. One would like to choose, among all the displacement fields, the 'closest' to the one computed with optical flow that still obeys the dynamical equations stated in the previous paragraph. We thus propose an alternative problem. Noting $\hat{\mathbf{u}}$ the solution computed from optical flow:

$$\begin{aligned} \underset{\mathbf{u},\mathbf{g}}{\text{argmin}} \quad J(\mathbf{u},\mathbf{g}) := \int (\mathbf{u} - \hat{\mathbf{u}})^2 + \beta \left(\nabla \mathbf{g} \cdot n_\perp\right)^2 d\Omega, \\ \text{s.t.} \quad \nabla \cdot \varsigma = 0, \qquad & \text{in } \Omega, \\ \varsigma(\mathbf{u}) := \lambda \text{tr}(\varepsilon(\mathbf{u}))I + 2\mu\varepsilon(\mathbf{u}) \qquad & \text{in } \Omega, \\ \varepsilon(\mathbf{u}) := \frac{1}{2}(\nabla\mathbf{u} + \nabla\mathbf{u}^T) \qquad & \text{in } \Omega, \\ \lambda = \lambda_l,\ \mu = \mu_l \qquad & \text{on } \Gamma, \\ \lambda = \lambda_c,\ \mu = \mu_c \qquad & \text{in } \Omega \setminus \Gamma, \\ \mathbf{u} = \mathbf{g} \qquad & \text{on } \Gamma, \end{aligned} \tag{IV.13}$$

where $\mathbf{g}$ is the boundary displacement which, unlike in the equations of linear elasticity equations laid down before, here acts as a control variable, and $n_\perp$ the boundary's tangent. The gradient of the displacement is again penalized to ensure regular solutions, which otherwise would lead to spurious values

of the strain and the stress. Just like for indirect elastography, we use the L-BFGS descent method paired with the adjoint method laid out in Appendix C. Unlike this method, however, the control variable is not a scalar defined over the whole domain, but a vector-valued function restricted at the boundary.

Now that we are equipped with all the necessary ingredients for the computation of our strain, stress and traction forces fields, we evaluate the accuracy of our framework in a numerical way, as previously done for displacements and strain fields. We will in particular evaluate the accuracy of the hydrostatic strain ε_h and the von Mises stress ς_M, defined thus:

$$\begin{aligned} \varepsilon_h &= \mathrm{tr}(\varepsilon) \\ \varsigma_M &= \sqrt{\frac{3}{2} s : s} \\ s &= \varsigma - \frac{1}{3}\mathrm{tr}(\varsigma) I \end{aligned} \tag{IV.14}$$

where I is the identity matrix. The hydrostatic strain measures the volumetric part of the deformation. It is a strain invariant as introduced in chapter 2. When positive, it indicates that the material under study increases in volume, and shrinks when negative. The von Mises stress is the second invariant of the deviatoric stress. It is often used to determine when the yielding of a ductile material occurs. In other words, beyond some thresholding value of it, some materials are known to enter plastic deformations, from which they cannot resume their initial shape. One can show that the von Mises stress is related to the elastic strain energy of distortion. Although we do not study large deformations that can result to yielding, this value nevertheless nicely encapsulates the properties of the deviatoric response of the stress, and is even in some regard more used than the deviatoric stress response.

We measure the accuracy of our method with the root mean square error (RMSE) of the hydrostatic strain and of the von Mises stress, normalized over the range, along with the ratio of the norm of the computed boundary traction over the norm of the true traction. We suppose a Young modulus of 250 Pa and a Poisson ratio of 0.3 for the chromatin, and that the lamin is 5 times stiffer. This corresponds to the widest span that is found in the literature, and the most difficult one to deal with: this is the reason why we chose it here as a good challenge. To produce higher deformations, we extend the traction domain to the bottom of the nucleus. We compare the accuracy of our method against the other optical flow techniques alone, paired with differentiation scheme as advertised in the beginning of this section.

We choose the regularization parameters of all these methods according to the L-curve criterium [294]. This is a log-log plot of the norm of a regularized solution versus the norm of the corresponding residual norm. It is a trade-off curve that plots the amount of error one would get from each regularisation parameter. The name comes from the fact that it has a characteristic "L" shape. One can prove that, in most cases, it also displays a distinct corner that indicates a specific value of the regularisation parameter. This regularisation parameter is known to be optimal and is the one we choose here.

The overall results obtained with the warping of a real glioblastoma nucleus is laid out in Figure IV.10. We compare our framework to the use of optical flow technique alone. We note that that the stress and traction forces are better computed in our setting. We see that the von Mises stress is particularly erroneous for the Horn-Schunck optical flow method. This is again due to the staircasing effect, and the bad regularity property of its displacement field. Remarkably, even the displacement field is refined with our framework. This is due to the fact that the optical flow displacement field is projected on the space of solutions of the linear elasticity equations through our PDE-constrained optimization scheme. Nevertheless, we note that the Horn-Schunck method fares quite descently on its own: if the general shape of the distortions is not well plotted, and the smoothness of the displacement field wrong, the direction in the traction forces is at least correct, and the magnitude of the stress in the correct range.

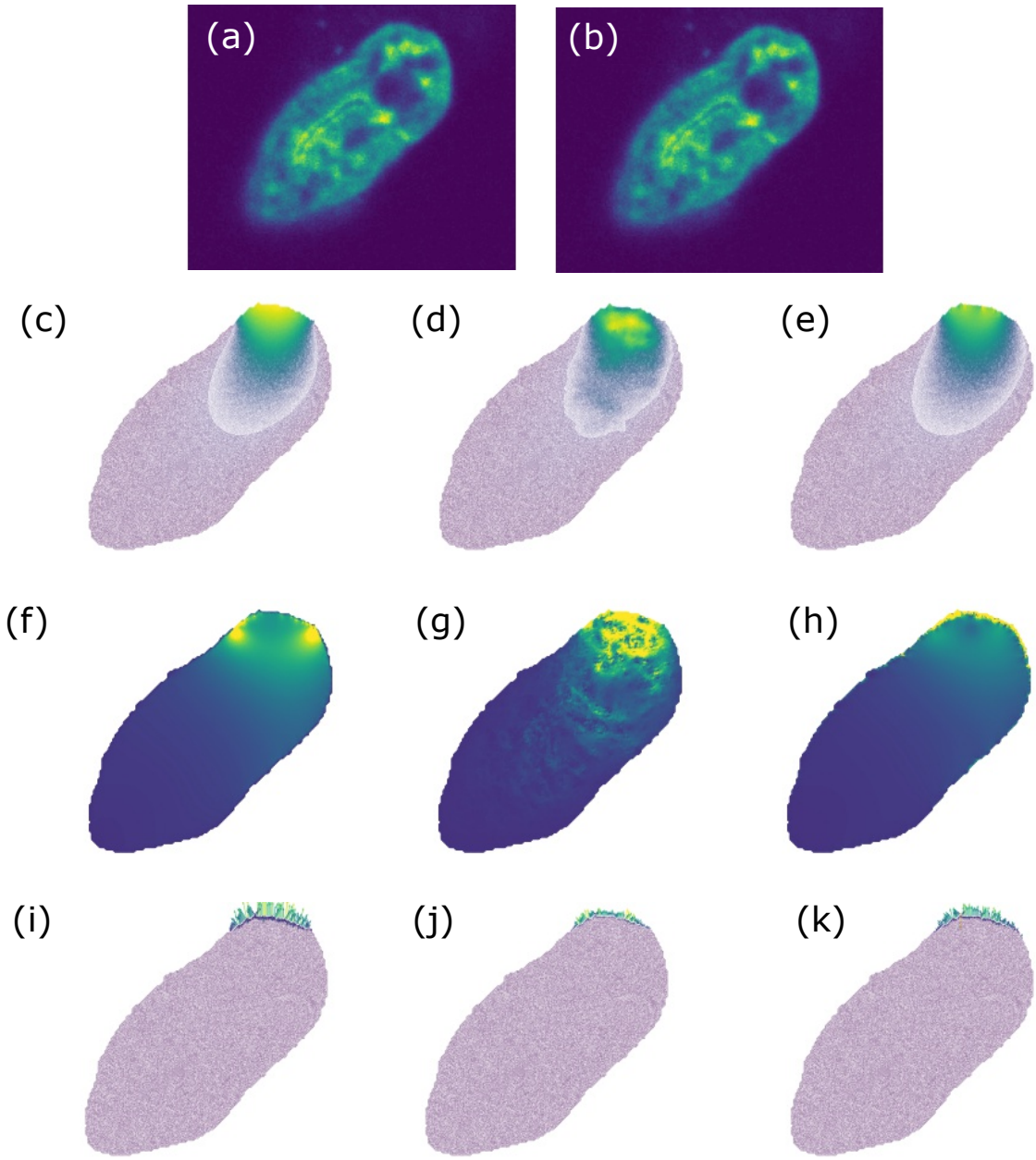

Figure IV.10: Simulation and computation of the displacement, stress and boundary traction. Comparison of the mechanical quantities of interest (displacement, stress, traction) obtained using HS and our method in regard of the ground truth quantities obtained from finite element analysis. Here $||T|| = 2.5$ Pa and lamin is 5 times stiffer than chromatin. (a) Image before deformation ; (b) Image after deformation ; (c) True displacement field ; (d) Displacement field obtained with Horn-Schunck ; (e) Proposed displacement field ; (f) True von Mises stress ; (g) von Mises stress with Horn-Schunck ; (h) von Mises stress with our method ; (i) True boundary traction forces ; (j) Boundary traction forces with Horn-Schunck ; (k) Boundary traction forces with our method.

First experiment. We compare the variation in accuracy for increasing values of the boundary traction $||\mathbf{T}|| \in \{0.25, 0.375, ..., 0.75\}$ Pa. While excellent at computing the strain and the stress, optical flow methods prove less accurate and less robust against varying deformations compared to our method (Figure IV.11). Furthermore they outright fail at retrieving the traction, despite good stress recovery. On the contrary, our method is relatively accurate, although it does suffer from deviations with increasing traction. We believe this can be overcome by using non-linear elasticity equations to account for larger deformations.

Second experiment. We fix the initial traction to 2 Pa and compute the accuracies for varying values of the Poisson ratio of the lamin $\nu_{\text{lamin}} \in \{0.30, 0.34, ..., 0.48\}$. Again, our method proves consistently more accurate and robust. This is especially true when the lamin becomes incompressible: while our method's stress accuracy remains stable, the accuracy of optical flow methods plunges.

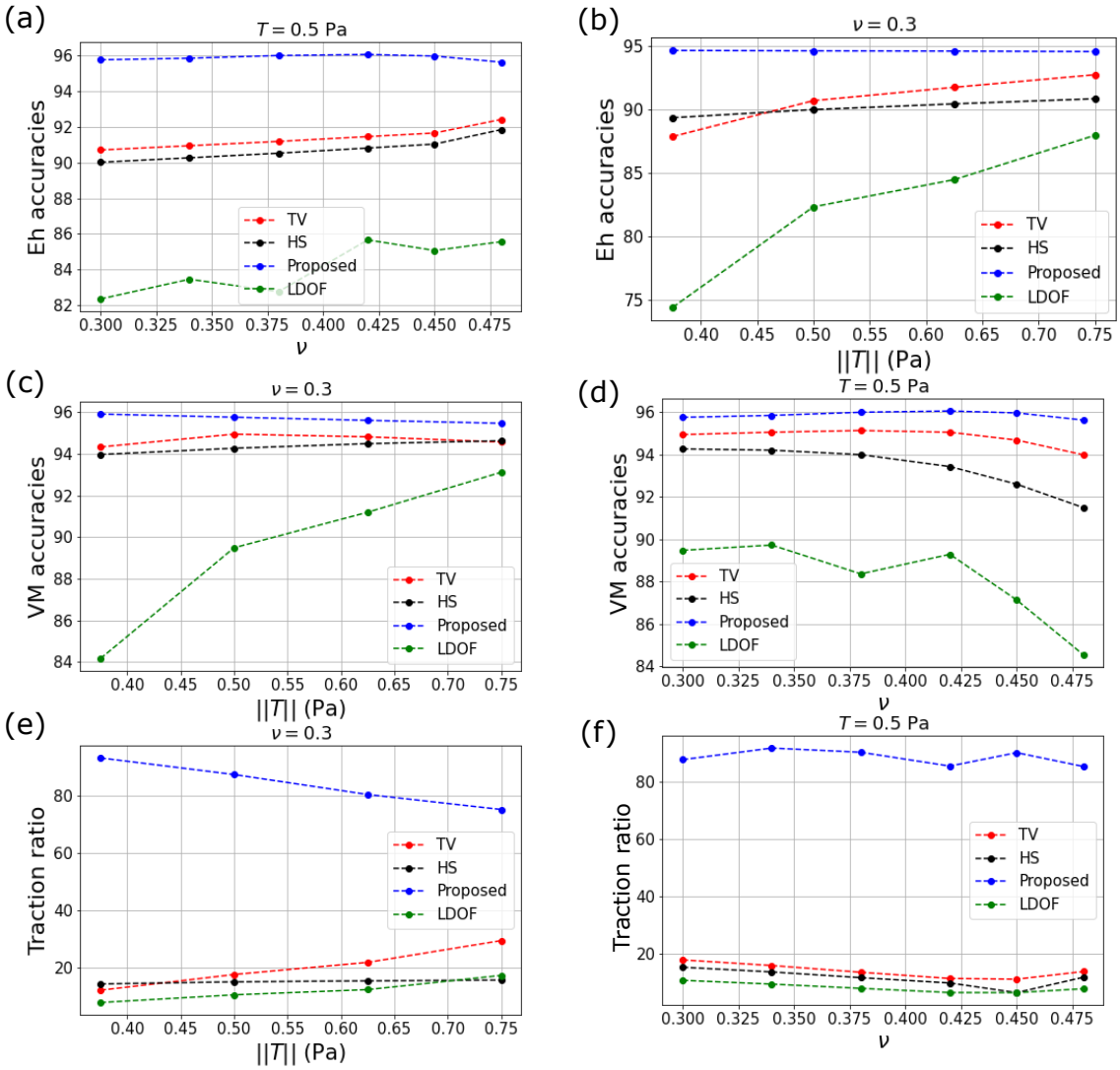

Figure IV.11: Accuracy of the retrieved quantities for each experiment. Evolution of the accuracies of the von Mises stress, the hydrostatic strain and the traction boundary of our method against the three top performing optical flow methods.

IV.5 Application 3: temporal evolution of the forces and stress within the nucleus of Toxoplasma gondii during invasion

This part of the work was done in collaboration with Luis Vigetti and Isabelle Tardieux from Université Grenoble Alpes. The goal of this collaboration is to study the mechanical properties of *Toxoplasma gondii* during invasion and migration. Unlike amoeba cells and many protozoans that swim in fluids, for which the deformation is mostly assumed by the cilia and flagella [295], the Apicomplexa phylum members seem to endure the mechanical constraints of their microenvironment without relying on neither cell protrusion nor these appendages. This is intriguing as these parasites require the good preservation of their genetic material to replicate within host cells (see Figure IV.12.b). *Toxoplasma gondii*, for instance, displays remarkable motility once in its tachyzoite developmental stage, navigating through tight spaces of extracellular matrices or physiological barriers [296]. How it does so without damaging its nucleus remains yet to be documented. Here we propose to monitor the evolution of strain, stress and boundary traction forces with the previously presented framework of an invading *Toxoplasma gondii*.

Let us first recall some key structural properties of this parasite once in the tachyzoite stage [297]. Figure IV.12.a. displays its general architecture. *Toxoplasma gondii* is approximately 7 μm long and 3 μm large, much smaller than the previously studied glioblastoma cells, and significantly faster. Notice also it takes an ellipsoid shape, with strong polarity and a left-handed spiral organization of 22 microtubules. Inside, the nucleus is approximately 1μm. The apical complex is made of secretary organelles named rhoptries and micronemes and a retractile conoid. This organization favors a chiral and directional type of movement called "gliding", powered by an actomyosin motor system, the speed of which may reach up to 2-5 μm/second. This mobility appartus allows it to perform a wide range of migration actions, such as navigating through the ECM, invading a host cell, and egressing from host cells (see Figure IV.12). Here we will only briefly mention the first two steps.

The migration capabilities of *Toxoplasma gondii* is secured through the good functioning of an actomyosin motor. This motor hosts frequent polymerisation and depolymerisation activities that produce the overall tensile capabilities of the cell. It is yet difficult to determine precisely which motor proteins are foremost in this process. It was for instance shown that the absence of MyoA, Mic2, AMA1 do not debase the motility of the parasite. Nevertheless we know that this motor lies between the plasma membrane and the inner membrane complex. This last component is a specificity of phylums of the Apicomplexa and is located right below the plasma membrane. Electron microscopy enabled biologists to describe it quite precisely, and we may say, in a word, that it is an intricate organization involving alveoli structures, a subpellicular network made of intermediate filaments, and of specific intramembrane particules. Some of these intramembrane particules have transmembrane domains, which allow the proper invasion of the parasite. The actin filaments, together with class XIV myosin, form what is known as the glideosome. This dynamic proteic complex motions the cell into three distinct behaviors. The first one is the counterclockwise helical movement, the second the clockwise circular motion, and the last one twirling. The first two are called productive migrations, since they move the cell forward. The last one is said to be nonproductive, as it pins the cell on the spot.

Toxoplasma gondii invades a host cell remarkably fast – as few as 20 to 30 seconds. This speed is mostly enabled through a very efficient proteic complex named the RhOpry Neck Protein. It regroups: the proteins RON2, which has the transmembrane domain and forms a co-structure with AMA1; RON4, which binds to ALIX, ESCRT, and CIN85; RON8, which binds to the F-actin cytoskeleton of the host cell, among others. In a nutshell, all of these proteins coordinate with one another to enable a solid "gripping" of the parasite to its host. They form a ring-like structure at the membrane of the host cell through which *Toxoplasma gondii* will have to squeeze in order to invade. We call this structure the Zoite-Cell Junction, or ZCJ. It is believed that it not only serves as an entry point, but also as an anchoring apparatus, through which lots of forces are produced.

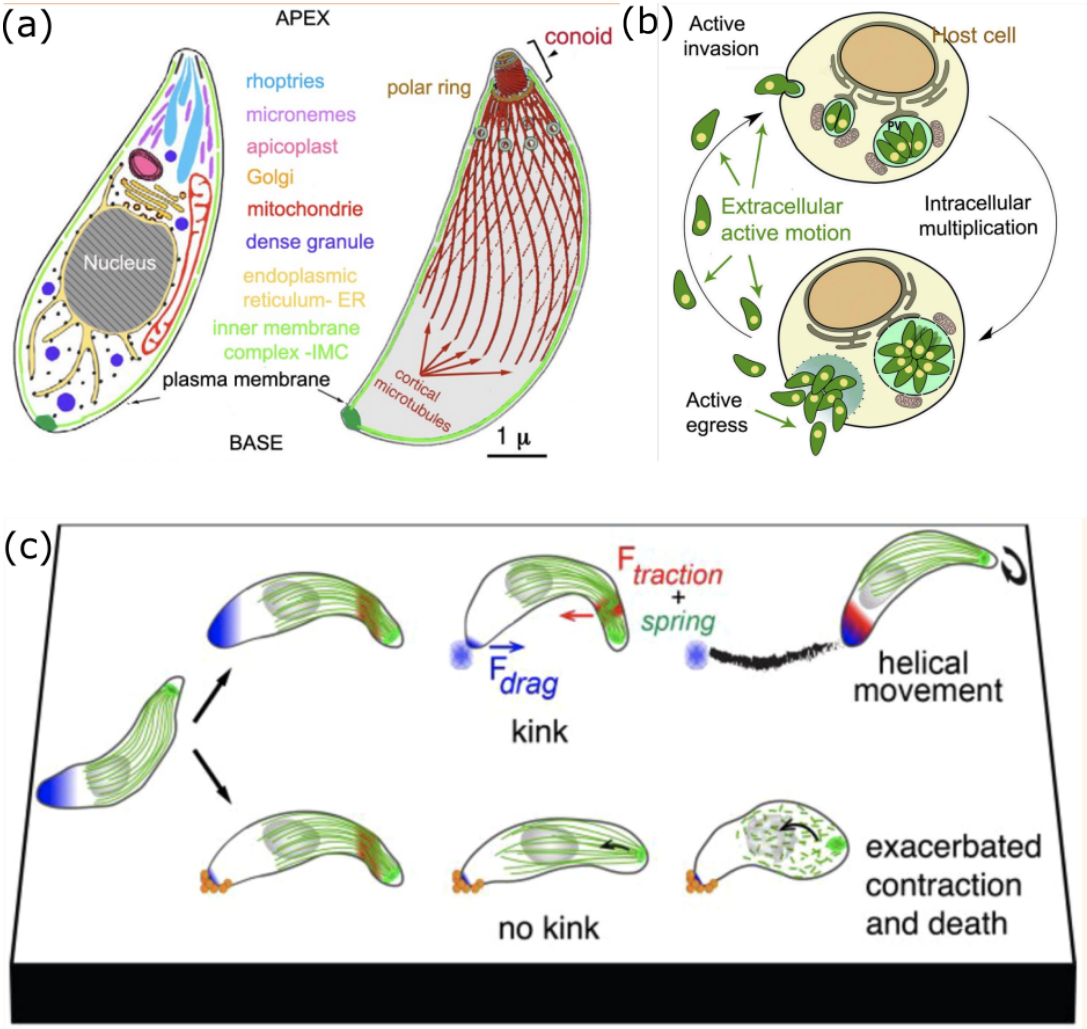

Figure IV.12: Presentation of Toxoplasma gondii. (a) Architecture of a Toxoplasma gondii cell ; (b) Life cycle of a Toxoplasma gondii cell ; (c) Gliding of Toxoplasma gondii with and without kink (from [298]).

We dispose of several videos of invading *Toxoplasma gondii*. The second line of these enjoys a higher magnification thanks to the use of superresolution techniques with a high resolution confocal microscope. These were paired with RH DKU80 NUP302 x3HA staining to mark the pores of the nucleus expressing cytosolic markers and fluorescent nucleoporins. This allows a convenient texture of the nucleus despite its small size. In the first video of invasion, we applied the optical flow method developed in the previous chapter to compute the displacement field of the nucleus at each frame of the invading *Toxoplasma gondii* (see Figure IV.13). The strain was derived by simple differentiation, and several simple shape descriptors, namely the perimeter, the surface, and the curvature, were computed as well along the way. The evolution in time of the mean value of each of these quantities is plotted in Figure IV.14 for three invasion videos. We may see that the deformation is higher on almost every measure when the nucleus invades, which is to be expected despite the high motility of the cell before and after, and is testimony of the computational faithfulness of our method. Secondly, 2D display of the deformation map in IV.13 shows that most of the deformation occurs at the apical complex of *Toxoplasma gondii*. This region is known to gather the densest amount of microtubules, which may indicate a protecting role during invasion. Only at the end, after the nucleus passed the "8-shape", does the back start to monitor some mild deformation, but to a lesser extent. After invasion, the nucleus still monitors a decent amount of deformation, despite its shape not varying, mostly because of repositioning purposes within the host.

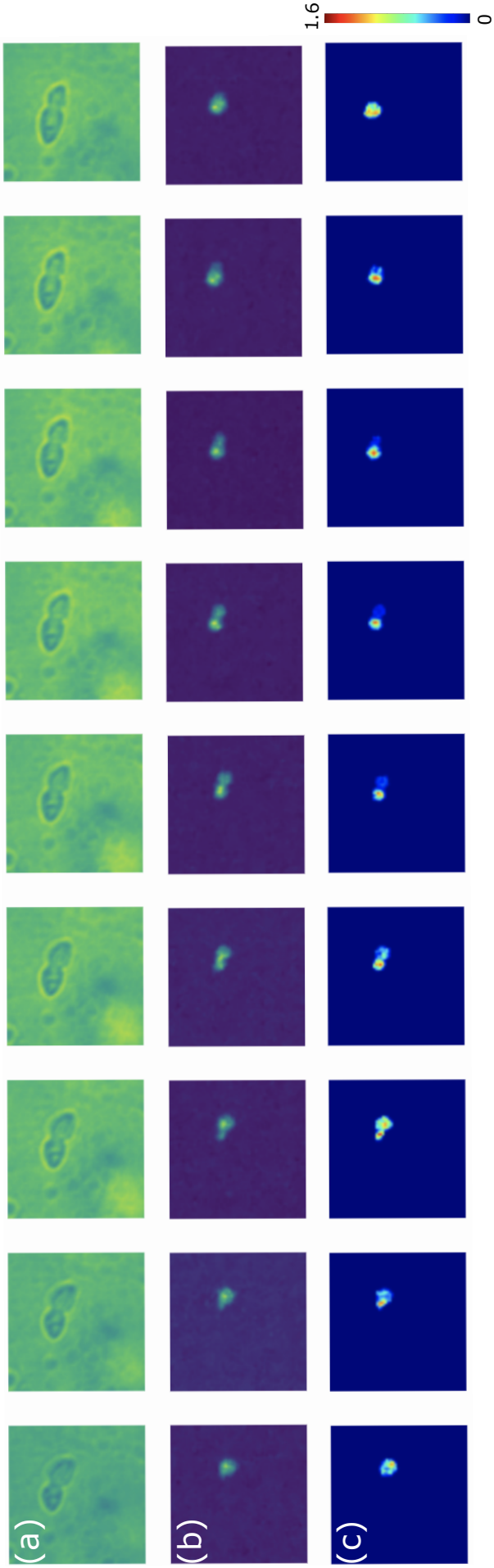

Figure IV.13: Time evolution of the deformation of *Toxoplasma gondii* (a) Invasion of *Toxoplasma gondii* into a host cell ; (b) fluorescence imaging of the nucleus ; (c) Frobenius norm of the strain that is induced by the above presented method

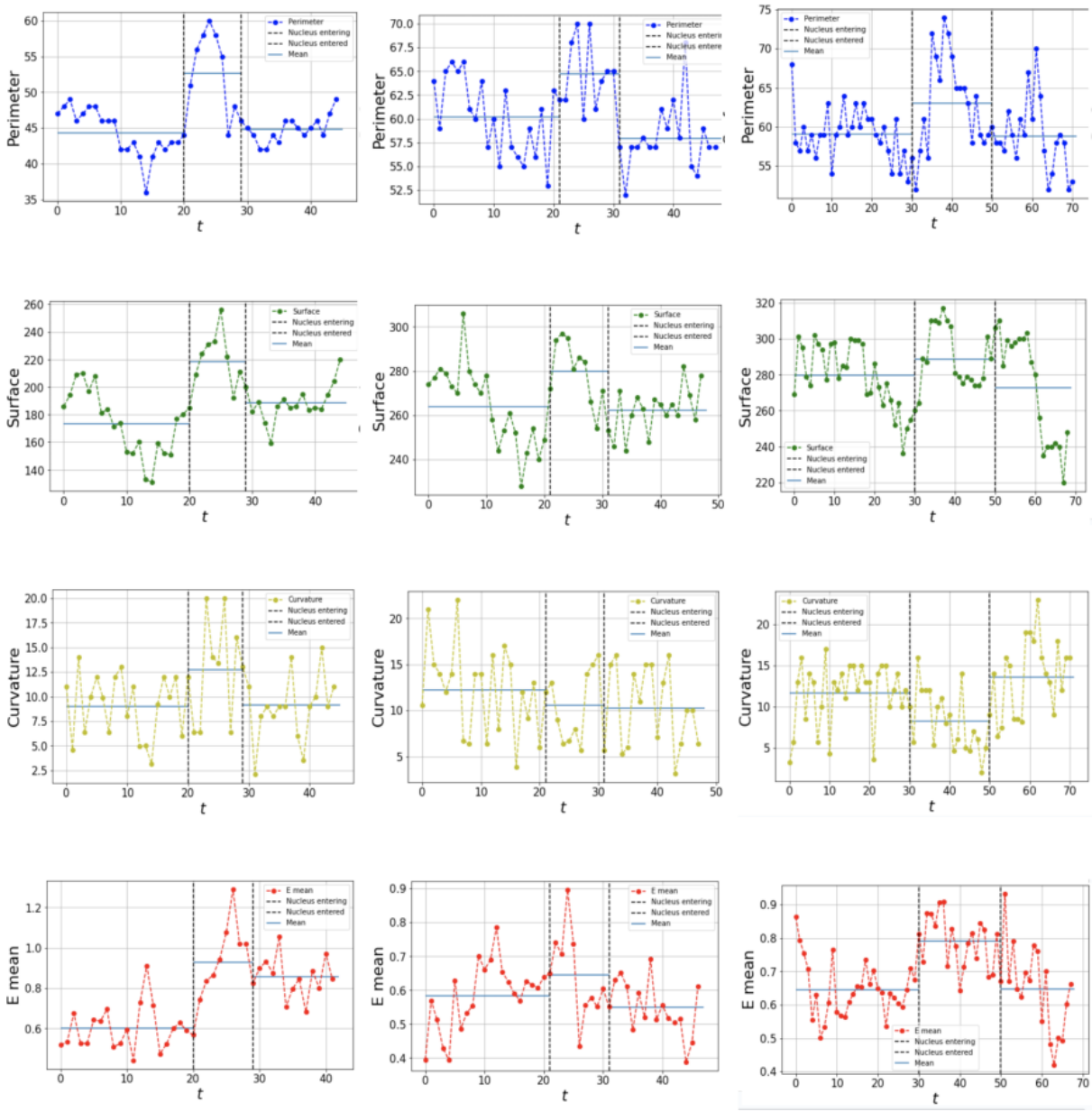

Figure IV.14: Time evolution of perimeter, surface, curvature, and of the mean of the Frobenius norm of the strain of three invading *Toxoplasma gondii* cells. We may notice that both shape descriptors and Frobenius norm computations indicate a larger deformation of the nucleus during invasion.

In the second line of video (see Figure IV.15), where the magnification is higher, we compute the deviatoric strain and the traction forces at the boundary. To do so, we need to know the Lamé parameters. Unfortunately, these are not known, but we can surmise them based on the available values of different similar nuclei that the Young's modulus ranges between 100 Pa to 200 Pa (here we chose 150Pa) and Poisson's ratio hovers around 0.3. Anyway, even if the absolute values of the computed stress and traction forces may be called in question, their general direction and relative values between each time frame is accurate, and not so bound to produce errors in our interpretation. Based on this hypothesis, we apply the previously developed framework to compute the stress map and the boundary traction forces to our images. The stress, in this particular case, is redundant to the traction forces and is mostly gathered around where the boundary is deformed, so we did not plot it here. We see however that the deviatoric strain is very expressive. We notice that the traction forces are mostly left-oriented, which is concurrent with the peculiar left-handed spiral architecture of *Toxoplasma gondii*. We also see that most of the traction occurs at the very beginning of the invasion process, where the nucleus is about to penetrate the host's material. We believe this indicates that the ring cannot be the only force inducing component during invasion. One idea to test would be to see if there are any further polymerisation activities at this very moment of the invasion capabilities. Also, because of the left-handed direction of the traction forces, this might also suggest that the forces are led somehow along the microtubules architecture.

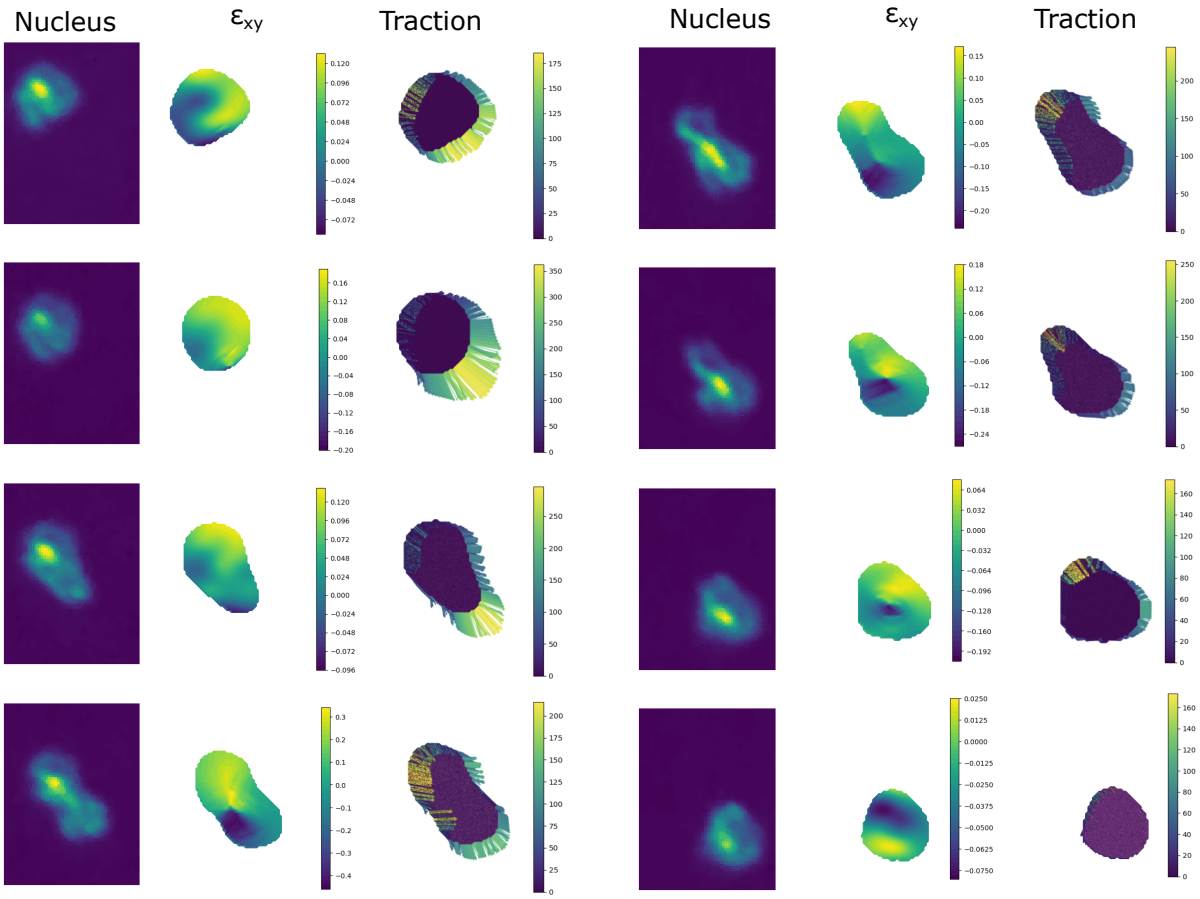

Figure IV.15: Super resolution of the time evolution of an invading Toxoplasma gondii cell along with its deviatoric strain and boundary traction. From top to bottom, left to right. First column: fluorescence image of the nucleus of an invading Toxoplasma gondii. Second column: deviatoric strain computed with the optical flow method. Third column: boundary traction forces computed with the PDE-constrained optimization framework.

Conclusion and perspectives

We modeled the nucleus as a continuum medium. In this setting, we revisited some of the key structural aspects ruling its mechanical properties, and came by degrees to a more abstract mathematical model of its behavior. We showed that in the resolution limit in which most confocal microscopes operate, the nucleus can be described as a visco-elastic material, with heterogeneous stiffness and viscosity inside its domain, according to theirs being evaluated at the lamin domain, the heterochromatin domain, the euchromatin domain, or in the interchromatic space. In the biological configurations that interest us the most, the deformations are low and quasistatic, and therefore this model can be simplified into an isotropic linear elastic model. Moreover, we showed that the specific geometry of the nucleus, which is itself governed by the peculiar organization of its components, allows us to assume further geometrical hypothesis, from which we derived additional regularity properties that the physical quantities of interest must observe. This modelization ended with the statement of three problems, stated in mathematical terms, that our computational tools would have to solve. Because the mechanical behavior of the nucleus is precisely determined by physical and mathematical models, we were able to devise a data creation framework, based on the finite element method, to create two images of a nucleus, one before deformation and one after, with known underlying physical quantities of interest. This framework was consistently used thereafter to evaluate numerically the accuracy of our proposed methods. We then offered a novel method to estimate the motion inside the deforming nucleus from images of its deformation. It revisits the well-known technique called optical flow. In its variational setting, optical flow states that the motion between two images can be accurately computed, provided we suppose that the brightness between them does not change, and that we assume some regularity properties. We showed that fluorescence microscopy settings were particularly adapted to fulfill the first of this hypothesis. The second hypothesis alleviates the ill-posedness of the problem, but endows at the same time the solution with specific regularity properties. We reviewed state-of-the-art optical flow techniques, and saw that the regularisation terms that were used were all inconsistent with the regularity prerequisites that emerged from our continuum mechanics analysis. Furthermore, we showed that they were all first-order regularisation methods, for which it is remarked in practice that the resulting flow suffers from what we call the staircasing effect, an image artifact that makes the reconstructed signal piecewise constant. These two drawbacks are incompatible with the good reconstruction of the flow field, and the physical quantities thereon. We devised our own optical flow method to circumvent these pitfalls. Its regulariser is based on the Schatten norm of the Hessian of the displacement field. After proving that the obtained regularity properties were superior to those of state-of-the-art optical flow methods, we offered an effective numerical scheme to compute it in the discrete setting. Numerical evaluations consistently showed the superiority of this method over standard optical flow methods in the context of elastic deformation. Because the regularity properties were more properly handled, the derived strain proved to be very accurate as well. In that context, we applied optical flow to compute the deformation of the nuclei of invading glioblastoma cells with knocked-out vimentin intermediate filaments, and showed that they were deforming significantly more than their wild type control counterparts. Finally, we explained how to process the displacements obtained with our new optical flow method to derive the relevant physical quantities pertaining elastic deformation. We presented the problem of elastography, or how to

determine the heterogeneous Young's modulus within the nucleus. We offered two frameworks, one yielding absolute values of the Young's modulus, the other relative values of it, depending on whether we possessed or not the values of the boundary traction forces deforming the nucleus, to evaluate it. Again, these frameworks were extensively evaluated numerically, and applied in a configuration of interest, namely the computation of the relative elasticity of an SKOV3 cell's nucleus and cardiomyocytes' nuclei. Given the Young's modulus and the Poisson's ratio, we also presented a PDE-constrained optimization framework to computing the stress and the boundary traction forces of the deforming nucleus. This framework was applied to study the invasion of Toxoplasma gondii in a host cell.

We believe these frameworks can yield further insights in the mechanical properties of deforming nuclei. However there remains a handful of open questions that we discuss here.

Discussion on the mechanical modelization. We saw that in many cases of interest the nucleus behaves as an isotropic linear elastic material. In fact, because of the high compressibility of the nucleus, the circumstances under which a nucleus exits this linear regime to enter a nonlinear one are not easily identified. Nevertheless we must consider this possibility in some cases of extreme deformations, even though these would come with additional mechanotransduction processes. In this case, one can show that the regularity properties of the displacement field will remain the same, provided the nucleus can be considered as a hyperelastic material. Therefore, the presented computational methods should apply to a large extent. On the other hand, in the case where the deformations cease to be quasistatic, but periodic, or time-dependent in general, we would have to consider viscous behavior as well. In this case, the spatial regularity of the nucleus holds as well, but we might consider the regularity properties related to time. Furthermore, while it is very easy (thanks to Newton's method) to adapt our data creation framework to the nonlinear case, it is more difficult to do so for the viscoelastic one. Here, we would need to warp an initial image several times, in order to display the dependence over time of the different physical quantities. The errors created in each warp would then magnify, and the faithfullness of the created data would be rightly called into question. One can consider a combination of simplistic modeling of a cloud of points, each strung to one another with dashpots and string, and the perturbation of which is analytically determined. In that sense, the warping would become unnecessary, and the image would be created at each frame by simple generation. However, since the mechanical properties would be defined locally, the global properties, such as the Poisson's ratio, would have to be checked carefully.

Discussion on the motion estimation. Because the spatial regularity properties would be conserved, changing the mechanical model of the nucleus would not require substantive modifications of the proposed optical flow method. Should the estimated deformation be viscoelastic, the regularity properties regarding time might be met with a simple fusion technique as is already proposed with several optical flow frameworks. There remain however some challenges that regard only our optical flow method. We saw that its variational minimization required the computation of the proximal operator of the mixed norm of the Hessian of the displacement field. This proximal operator is not explicitly determined, but approximated with a fast approximation scheme. However fast this framework be, the overall computation of the flow field might appear slow, especially when embedded in the coarse-to-fine large motion estimation strategy. Perhaps not as much as to invalidate its use for long-time 3D deformations, but enough to make it less ergonomic. One should keep in mind that these image analysis tools will be handled not by image analysts alone, but by biologists not necessarily endowed with the proper computational background to handle them. In that regard, our laboratory developed Icy, an imaging platform in which a large panel of image analysis tools can be used. In practice, we see that the most commonly used tools on this platform are the ones fulfilling two criteria: they require few parameters, and they are fast. Our optical flow method requires very few parameters, but it might need an acceleration for it to become popular amid biologists. In that respect, an initialization procedure might be used, for instance using a dense inverse search, where the magnitude of the flow field will be fastly estimated in a first

step, then refined with the actual framework, with a few iterations at the end only to enforce the right regularity properties. This would have the advantage of suppressing the coarse-to-fine strategy, and reducing the amount of times we need to estimate the proximal operators. Another subject of interest is the comparison of our optical flow method to higher order regularisation methods. Those include optical flow methods regularised with BV2 functionals, TV2, Hessian-TV, or Total-Generalized Variation. In the continuous setting, theory dictates us that ours should better represent the elastic properties of the displacement, but the story might be different in the discrete setting. Unfortunately, most of these regularisation functionals were not applied to optical flow. Moreover, their codes are scarcely freely available. An extensive comparison would require a significant implementation effort, but we believe that it is worth the search, even for image analysis in general. Finally, again because of the coarse-to-fine scheme, it is possible that high amounts of strain applied to a very small spot in the nucleus be wiped off. We could employ in that regard the same strategy as Large Dispalcement Optical flow and include some texture properties in the variational formulation of our framework. However, the matching criteria should be in par with the specific texture of fluorescence images, which as we saw is very different from the ones met in 3D every-day life motion.

Discussion on physical quantities estimation. The first challenge that crosses elastography is when it should be applied to the nonlinear setting. We saw that one could opt for an indirect strategy, where the Young's modulus is estimated iteratively through a PDE-constrained optimization framework. However, this comes at a high computational price, sometimes prohibitive for high resolution images. One idea would be to adapt a coarse-to-fine strategy, in which we linearize the linear elasticity equations at each scale, and solve at each the mixed PDE we proposed in the last chapter of this thesis. It remains however to be proven that this strategy might converge in practice. A second challenge for elastography is to know precisely when it is a well-posed problem. In other words: when are we sure that the applied forces are large enough so that the reconstructed Young's modulus map is faithful? One understands intuitively that when the applied force is local and small, the deformation does not "propagate" to the whole nuclear domain, therefore the stiffness map should be called in question. But to the best of our knowledge, there are yet no unified and systematic response to this question. Another problem regards the estimation of the Poisson's ratio. There, some direct and indirect methods propose their solutions. In our case, we could also formulate a novel mixed PDE framework, this time with two variables, and with two elliptic terms. Another strategy might be to estimate it in two steps: the mixed PDE framework to estimate fastly the Young's modulus, paired with an iterative reconstruction framework for the Poisson's ratio. The biggest challenge in the estimation of the stress tensor and the traction forces is the knowledge of the Lamé parameters. The solution to this problem remains in the hands of the biophysicists, who possess the experimental apparatus to create a bank of stiffness parameters for a large body of nuclei. It remains to be known whether someone will deem this objective worthy of the effort necessary to do it. A second challenge regards the estimation of these fields in 2D, when the deformation is in fact 3D. In that respect, BioFlow already proposed some mitigating parameters that estimate "out-of-flow" motion that we could incorporate.

We hope that the methods and results obtained during this thesis will help biologists tackle yet unanswered questions in nuclear mechanobiology, and open new avenues in computational imaging. To that end, the code will be made available on consecrated platforms.

Appendix A

Microscopy techniques

A.1 Fluorescence microscopy

In a nutshell, as its name implies, fluorescence microscopy sheds a light of known wavelength to a fluorophore attached to a protein of interest in the nucleus (see Figure A.1). A few nanoseconds after its absorption, the fluorophore emits light of another (usually shorter) wavelength that is detected by the microscope [299]. This discrepancy between the wavelengths of emitted and received light is named the Stokes shift, and is the reason why we may filter out the noisy emission to keep only those of the fluorophore [300]. This bolsters high contrast that makes fluorescence microscopy a very enticing alternative compared to brightfield microscopy, which receives equal amount of light both from the background and the material of interest [301]. The efficiency of the different fluorophores are studied down to their molecular level. Light emission occurs when certain electrons stray away to farther orbitals: we say that the molecule is in an «excited state», and that it «relaxes» when the said electrons move back [302]. This whole process of excitation is actioned through an electrical machinery initiated by the received photons that alter the vibrational and rotational states of the molecule. Nowadays, most of the employed fluorophores are engineered to allow a wide and accessible outer orbital area [303], often thanks to a ring structure studded with numerous pi bonds [304]. This can be seen for instance in the very popular GFP, which underwent post-translational alteration of three amino acids to allow large imidazolone ring structure [305]. Indeed, the required energy to shift the molecule to an excited state is desired to be as low as possible, to the point of enabling fluorescence under visible wavelength illumination – we recall that a photon's wavelength is directly related to the formula $E = h \times c/\lambda$, where h is Planck's constant and c and λ are the speed and wavelength of light in vacuum, respectively. And while it is possible for multiple photons of greater wavelength to combine their energy for the transition of a single electron to an excited state, the extreme rapidity of the process (in the order of femtoseconds) makes it rather unlikely that low energy illumination will suffice to trigger fluorescence, except under a damaging profusion of illumination – one will object the existence of two-photon microscopy, but this optical system generally requires a complex setup that is not universally met among laboratories. The low wavelength requirements of the fluorophores is the main physical property that explains why fluorescence microscopy is so universally employed among biologists. However this short depiction of the process of excitation and emission does not take into consideration several competing physical phenomena that may thwart our schemes.

There are actually many electronic orbitals staged at higher and higher lengths [306]. While a certain amount of photon energy shedding may suffice for a fluorophore to shift from its groundstate configuration S_0 to an excited state S_1, a greater provision of it may shift it to even greater excitations states, say S_2 [307]. The excitation spectrum of a fluorophore is consigned in what is termed a Jablonski diagram [308], [309], established after a systematic evaluation of its absorption and emission properties,

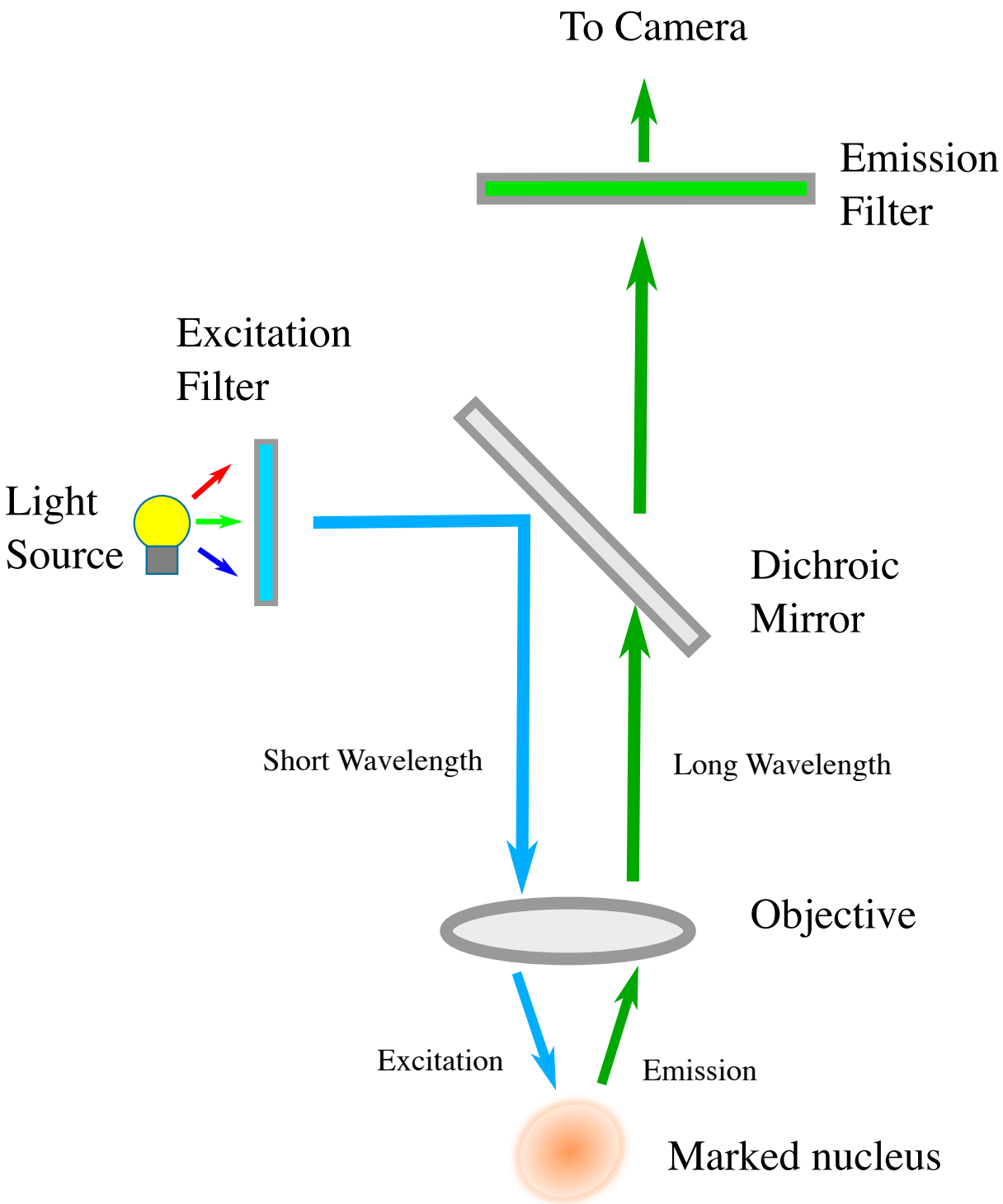

Figure A.1: General principles of fluorescence Microscopy.

and used thereafter to evaluate certain quantities of interest, for instance the molar extinction coefficient that quantifies the probability that a fluorophore will absorb a photon. What becomes clear from the look of several of these diagrams is that a higher excitation state does not necessarily yield higher emission, and that the received photon energy dissipates through other paths. Internal conversion of a molecule from an excited state to a lower excited state, for instance, is accompanied by vibrational relaxation that spends the energy surplus in nearby molecular interactions [310]. This is partly the reason why the Stokes shift showcases higher wavelength during emissions. When sufficiently big enough, this energy expenditure allows great separation of wavelengths between emission and excitation, which is leveraged in the microscope setting to obtain better contrast – and nowadays a lot of new fluorophores are engineered to enable larger and larger Stokes shift, especially in view of avoiding the very cumbersome *crosstalk* phenomenon [311]. However, one must be careful that this energy expenditure does not impede emission, but fortunately for us, it is experimentally shown that this dissipation can only, at the utmost, downgrade a fluorophore from a very excited state S_2 to a mildly excited state S_1, and is not enough to completely bring it back to a groundstate S_0 [312]. What is even more interesting in our case, the Jablonski diagrams show, for a very high number of occurrences, a symmetry between excitation and emission spectra, especially around peak wavelengths. In other words, the stochastic processes ruling the energy dissipation within the molecule are stable enough to get an almost deterministic return of emission: given a light of known wavelength, the fluorophore will certainly emit another light of known wavelength, independently of configuration. Now this would be enough to ensure us a trustworthy texture of the enlightened nucleus, if there were not two undesirable effects.

The first is phosphorescence [313]. An orbital normally harbours a pair of electrons with opposite spins. We name this configuration a *singlet state* [314]. Sometimes it happens that two bonding electrons with parallel spins are found in separate orbitals. While in the first configuration the magnetic moments of the electrons cancel off, in the second configuration they may be found in three forms, parallel, perpendicular or antiparallel to the direction of a magnetic field. This is called a *triplet state* and is known to be very stable. Most of the time, the energy level of a triplet state is lower than that of a singlet state. Because of their stability, triplet states tend to take a longer time to transition to a ground state, even more when photons are continually absorbed and move them to higher range of excitations. Eventually energy phases off through a light emitting process called phosphorescence, but this may come with high time delays, corrupting the accuracy of the signal. The second undesirable effect is *photobleaching*. This term designates the fading phenomenon that accompany the repeated switching between an excited state and a ground state (see Figure A.2). The best fluorophores are known to undergo up to 40,000 cycles of such changes, beyond that the emitting light waxes off. Bleaching is mostly ascribable to the presence of triplet states, because the non nullity of their magnetic moments offer more opportunities for their electrons to interact with other molecules, especially oxygen.

As we see, both of these unsettling problems surge from the existence of triplet states. Nowadays several companies offer dyes with great photostability, to the point of reducing several folds the amount of these. In practice, these dyes are found sufficient to counter any phosphorescence issues and photobleaching under low and short illumination. However longer acquisitions unfortunately occcasion photobleaching at the end of each registering. These happen most of the time for biological phenomenons that span more than 24 hours. Nevertheless, the stochastic processes of the molecule are again in our side, since it is shown that the photobleaching effect appear uniformly throughout the fluorophores. As we will see, in most cases it can be efficiently dealt with during preprocessing of the image, often through a simple normalization over time.

For further report, the interested reader may satisfy his curiosity by reading the extensive works of [316] and [317]. To conclude our short review, we may assume without prejudice that the texture of an image produced through fluorescence microscopy is trustworthy for our future optical flow method. As to the exact configuration of the microscope, whether it be widefield, confocal, light sheet, or else,

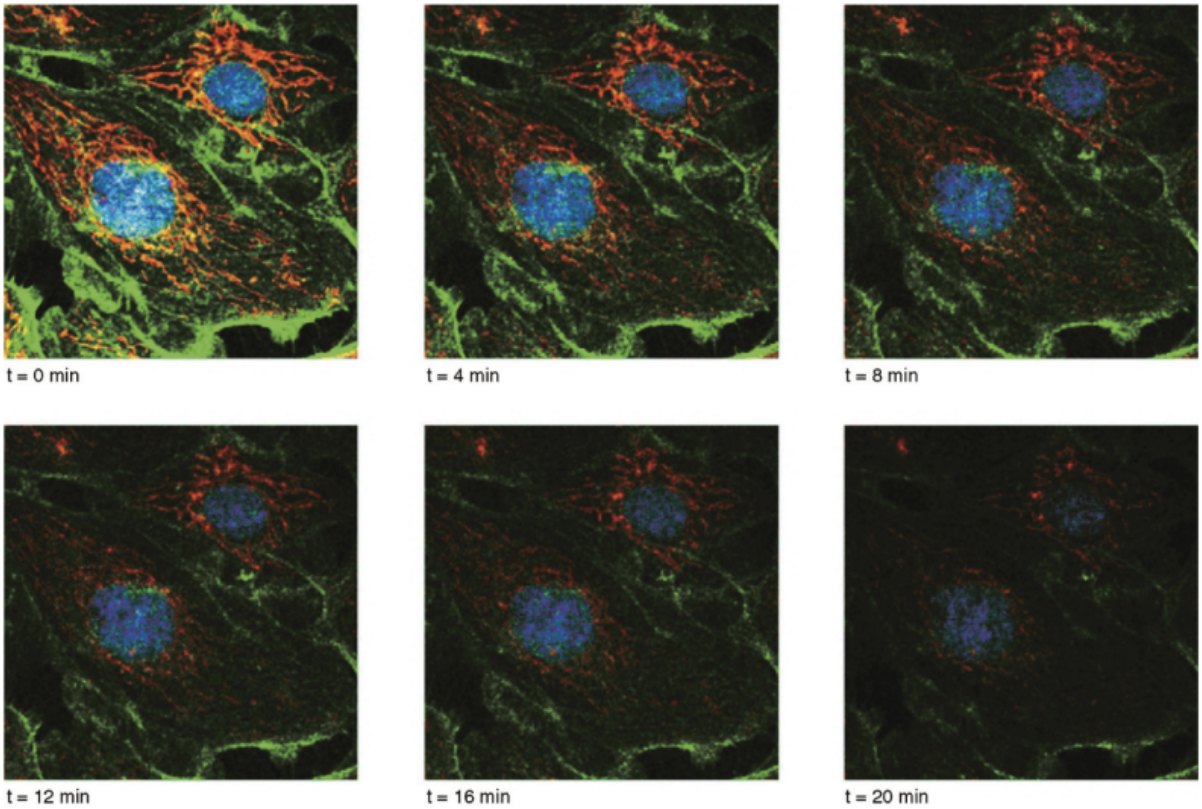

Figure A.2: Photobleaching . Photobleaching dampens the fluorophores' light emission in an homogeneous way that can be easily handled with proper image normalization techniques(from [315]).

they generally produce orthogonal projections of the sample plane on which most motion occurs for 2D images, and add a small lag between stacks for 3D images. In other words, regardless of the optical system, the geometric description of space is well respected, or can be properly mended with simple rescaling operations.

A.2 Brillouin microscopy

Brillouin microscopy relies on Brillouin light scattering to quantify the viscoelastic properties of the nucleus (see Figure A.3). This is an inelastic process occasioned by the interaction of light with density fluctuations in a macromolecular chain condensate material. The resulting mass oscillation within the medium can be modelized as the propagation of acoustic waves of quasi-particles named phonons. The photons undergo diffraction against these waves, but unlike Rayleigh scattering, the velocity of the grating shifts the light frequency through the Doppler effect. The two resulting opposing shifts are called Stokes Brillouin and Anti-Stokes Brillouin peaks. Since the viscoelastic properties determine, to some extent, the sound-wave properties of the phonons, a simple inversion of the complex longitudinal modulus $M(\nu) = M'(\nu) + iM''(\nu)$, where the real part relates to the elastic propertes and the imaginary part to the viscous properties, and where ν is the frequency of the scattering, might yield a complete viscoelastic characterisation of the medium. More precisely, the real part of M relates to the stored elastic energy inside a sample. Given that $\nu = Vq$, where V is the sound's velocity in the medium, and $q = \frac{2n}{\lambda_0}\sin(\theta/2)$, where n is the material refractive index, λ_0 the incident wavelength, θ the angle between the incident and scattered light, this energy may be readily retried through the relation $V = \sqrt{M'/\rho}$, where ρ is the mass density of the material. Likewise, denoting Δ_B the Brillouin side bands' line width, the exchanged wavevector q follows $\Delta_B = \Gamma q^2$, where Γ is the attenuation coefficient, related to the longitudinal viscosity η by $\eta = 2\Gamma\rho$. Note that ν and Γ scale inversely with the incident

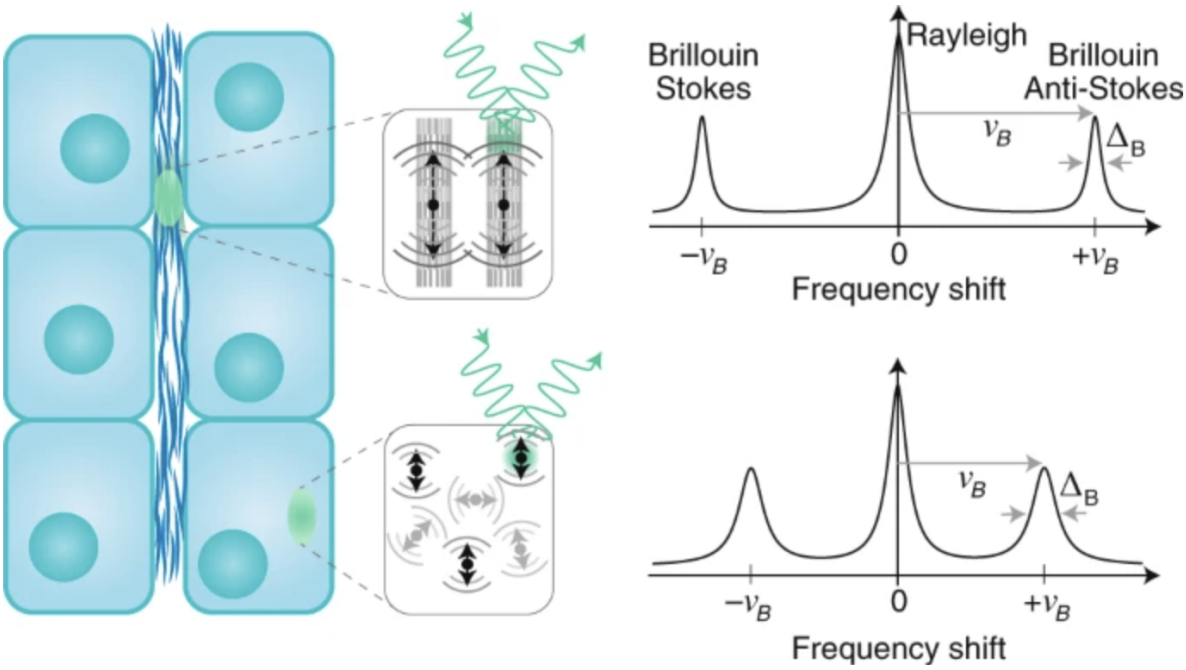

Figure A.3: General principles of Brillouin microscopy When light crosses density fluctuations in the biological material, the macromolecular chain condensante oscillates just as an acoustic wave (left). The Stokes Brillouin and Anti-Stokes Brillouin shift is produced by the Doppler effect and serves to recover the visco-elastic properties of the oscillating material. (from [153]).

laser wavelength, and it is sometimes preferred to study their dimensionless counterparts $\overline{\nu} = \nu/\nu^W - 1$ and $\overline{\Gamma} = \Gamma/\Gamma^W - 1$, where ν^W is the Brillouin frequency shift of distilled water and Γ^W is the attenuation coefficient in distilled water.

This microscopy technique was for a long time confined to the study of homogeneous, then heterogeneous, non-biological materials, for instance crystal-line polymer latex films, where long spectral time scan is tolerated. Back then, the main challenge was to find high numerical aperture broadening to allow large backscattering phenomena. A simple narrow-band frequency laser for emission along with a high-resolution spectrometer, incorporating for instance a Fabry-Perot interferometer, allowed proper quantification of the longitudinal elastic modulus. However, a hefty part of the scattering of this configuration proves to be elastic. In biological material, these are even more proficient, making the signal too dim to be correctly interpreted. We needed to wait up until 2008 to see the appearance of the first Brillouin microscope based on virtually imaged phased array, which, unlike the Fabry-Perot interferometer, does not require the scanning of the optical cavity to spatially disperse the received signal. This setting greatly improved the contrast between elastic and inelastic scattering, notably thanks to the additional use of beam apodization, Lyot filtering and diffraction masks, and was properly paired with Raman or fluorescence microscopy techniques to enable the input of shape descriptors as well. It can likewise be expected that it will soon allow several probing tools in his setting, as testified by the recent adaptation of this imaging technique with micropillar traction force microscopy. Note that these settings also apply in 3D imaging when paired with a confocal microscope, but one should be carefuly of the case where the axial extent of the scattering volume is shorter tham the phonon propagation length, in which case the imaginary part of the longitudinal modulus may be compromised.

Despite these encouraging breakthroughs, Brillouin microscopy remains less accessible to biological laboratories than classical fluorescence microscopy. Furtheremore its exacting technical requirements come with a handful of drawbacks. In a theoretical point of view, the inversion of the longitudinal modulus requires the exact knowledge of the refractive index of the biological material – an information

accessible through tomographic phase microscopy or digital holographic microscopy, for instance, but very demanding. Most often analysts rely on not-so-obvious conjectures – the Lorentz-Lorenz relation, for instance, states that the refractive index may be related to the more accessible mass density, which, when proven wrong, can compromise the faithfulness of the resulting properties. Often it is more prudent to rely on partial characterisation of the material, like restricting the analysis to the determination of the loss tangent $\tan(\phi)\frac{M''}{M'}$. Also, despite the aforementioned technological advances, Brillouin microscopy yields a very poor signal, and needs to be deployed at short time-scales, lest the biologist incurs the risk of damaging the material through phototoxicity: current lasers in this setting require to shed a light spanning from a few mW to hundreds of mW. The current solutions to this pitfall, such as non-linearly stimulated Brillouin microscopy, require substantially greater power inlet for the laser, which again restricts further the usage of this technique in labs of average income. Even once the theoretical and technical inconveniences have been overcome, the resulting spectra may not be blindly accepted as such. Recent studies point out the Brillouin shift depends not only on the stiffness and viscosity of the biological material, but may be in some cases extremely dependent on its water content. While very appealing to the eye, the resulting spatial resolution in Brillouin microscopy should be debated as well. There is no straightforward definition of the diffraction limit of a Brillouin microscope, since this depends as much of the spatial diffraction limit as of the phonon propagation length and the homogeneity of the sample. Furthermore, the real part of the longitudinal modulus M is harder to interpret than the Young's modulus E. We will give a precise definition of the latter in the last section of this chapter. In the meanwhile, bear in mind that the former relates to precise phase-shifting properties of a physically convenient proxy names phonons, while the other directly relates (often linearly) the precise microscopic deformation properties to the applied stress: while the first might still find its way into the biological investigation of the material, the second is much more easily interpreted. While promising in many respect, Brillouin microscopy requires yet several improvements, both in its accuracy in the description, and its availability in the use, to make it a universally acknowledged imaging tool.

Appendix B

Staircasing effect

B.1 Perimeter, jump sets, co-area formula

We here revisit the notions of bounded variations under a new light. We will see that many image processing problems including the total variation as a regularisation term might be reformulated in terms of sets and perimeters. This is thanks to the *co-area formula*. We first introduce some basic definitions which are all further reviewed in [220] or [318]. This appendix is strongly inspired by the reading of these two references, and the reader shall report to those two for additional information.

Definition B.1.1. *A measurable set $E \subset \Omega$ is said to have a finite perimeter if its indicator function $\chi_E \in BV(\Omega, \mathbb{R})$. In this case, the perimeter is the total variation of χ_E and we denote it* Per(E).

One can show that this definition is valid "geometrically'. Indeed, using Meyers-Serrin's approximation theorem, we have that:

$$\text{Per}(A \cup B) + \text{Per}(A \cap B) \leq \text{Per}(A) + \text{Per}(B), \tag{B.1}$$

for all sets $A, B \subset \Omega$ of finite perimeters. Likewise, the notion of a boundary naturally arises from the definition of the distributional derivative of the characteristic function. Since the total variation is bounded, its distributional derivative Du is bounded as well. By Riesz' representation theorem, we derive that it can equivalently be seen as a Radon measure, the norm of which is precisely the total variation. The definition of the reduced boundary follows.

Definition B.1.2 (Reduced boundary)**.** *Let $E \subset \Omega$ be a set with finite perimeter. Its reduced boundary ∂^* is the set of points $x \in \Omega$ at which the limit:*

$$\nu_E(x) = \lim_{\rho \downarrow 0} \frac{D_{\chi_E}(B_\rho(x))}{|D_{\chi_E}|(B_\rho(x))} \tag{B.2}$$

exists and has length equal to one.

One can show that this definition is more precise than an equivalent topological one, where the Hausdorff measure of its perimeter may be unnecessarily big. A more explicit definition of the distributional derivative of the characteristic function can be given as such:

$$D_{\chi_E} = \nu_E(x) \mathcal{H}^2 \llcorner \partial^* E$$

This definition of the reduced boundary also extends the Gauss-Green formula, confirming the geometric nature of the derivatives of the characteristic functions. Indeed, for any infinitely differentiable function

with compact support $\phi \in C_c^\infty(\Omega)$:

$$\int_E \text{div}\phi(x)dx = -\int_{\partial^* E} \phi \cdot \nu_E(x) d\mathcal{H}^2(x)dx. \tag{B.3}$$

The notion of a reduced boundary may actually be generalized to every functions of bounded variations. To see this, let us define the jump set.

Definition B.1.3 (Jump set)**.** *Let $u \in BV(\Omega)$. The jump set of u, J_u, is defined as the set of points x such as there exist $u_-(x), u_+(x) \in \mathbb{R}$ with $u_-(x) \neq u_+(x)$, and $\nu_u(x) \in \mathbb{R}^3$ a unit vector for which the following function:*

$$y \to u(x + \epsilon y)$$

converges for every $y \in B(0,1)$ as $\epsilon \to 0$ to the function:

$$y \to u_-(x) + (u_+(x) - u_-(x))\chi_{\{y \cdot \nu_u(x) \geq 0\}}.$$

The triplet (u_-, u_+, ν_u) is unique up to the permutation $(u_+, u_-, -\nu_u)$.

Then, one might show that $\partial^* E = J_{\chi_E}$ with $(\chi_E)_+(x) = 1$, $(\chi_E)_-(x) = 0$, and $\nu_{\chi_E}(x) = \nu_E$. Because we have this link between functions of bounded variations and finite perimeter sets, we may explicitly define the distributional derivative of a function of bounded variations in a kindred way. This is a natural extension of the Radon-Nikodym theorem.

Theorem B.1.1 (Radon-Nikodym theorem)**.** *Let (X, Σ) be a measurable space and μ, ν two measured on it. If ν is absolutely continuous with respect to μ, then there exists a Σ-measurable function $f : X \to [0, +\infty[$ such that:*

$$\nu(A) = \int_A f d\mu, \tag{B.4}$$

for any set $A \subset X$.

The Federer-Volpert theorem extends this fundamental result to the case of the Radon measure Du defined by the distributional derivative of a function of bounded variations u.

Theorem B.1.2 (Federer-Volpert)**.** *Let $u \in BV(\Omega)$. Then one has:*

$$Du = \nabla u(x)dx + Cu + (u_+(x) - u_-(x))\nu_u(x) d\mathcal{H}^2 \llcorner J_u.$$

We say that Cu is the Cantor part of Du, and is singular with respect to the Lebesgue measure.

In the case where $u \in W^{1,1}(\Omega)$, we have $Du = \nabla u(x)dx$. In our case, for instance, we wouldn't have this relation, since at the boundary of the nucleus the derivative witness a high change contained in the jump set as accounted in the last term of this equation. One may sense, although the proof is quite intricate, that the total variation of a function includes partly the gradient of this function on "smooth parts" and partly the discontinuities values contained at the jump sets, and therefore that it can be accounted through expressions of its level lines. This is what the co-area formula does.

Theorem B.1.3 (Co-area formula)**.** *Let $u \in BV(\Omega)$. For almost every $t \in \mathbb{R}$, the superlevel line $\{u > t\}$ is a set of finite perimeter. One further has:*

$$\text{TV}(u) = \int_\Omega |Du| = \int_{-\infty}^{+\infty} \text{Per}(\{u > t\}dt. \tag{B.5}$$

B.2 The Euler-Lagrange equations

We now establish the Euler-Lagrange equations of the following optical flow problem:

$$\min_{\mathbf{u}} \int_\Omega \left(\frac{\partial I}{\partial t} + \nabla I \cdot \mathbf{u}\right)^2 + \alpha(\mathrm{TV}(u) + \mathrm{TV}(v) + \mathrm{TV}(w)) \tag{B.6}$$

where $\mathbf{u} = (u, v, w) \in BV(\Omega, \mathbb{R}^3)$ and $(\mathbf{x}, t) \to I(\mathbf{x}, t)$ is a scalar valued function. One will see that this equation leaves valuable insights on the staircasing effect. Because the total variation is non-differentiable in the strong sense, one has to resort to the notions of subgradient.

Definition B.2.1 (Subgradient)**.** *Let X be a Hilbert space, $F : X \to]-\infty, +\infty]$ a convex function. The subgradient of F is the set operator ∂F defined by:*

$$\partial F(x) = \{v \in X \mid F(y) \geq F(x) + \langle v, y - x\rangle, \quad \forall y \in \Omega\},$$

for every $x \in \Omega$. In case F is differentiable, one naturally has $\partial F(x) = \{\nabla F(x)\}$.

Like with the usual gradient, the subgradient is stable against scaling with a scalar and addition. We showed in the previous section that the total variation admits a characteristic function as a natural Legendre-Fenchel conjugate. The set on which this characteristic function is defined bears properties of its own, exploited in modern higher order regularisation techniques such as the total generalized variation [319]. Denote $\mathcal{K}$ and K the following sets:

$$\begin{aligned} \mathcal{K} &= \left\{-\mathrm{div}\phi \mid \phi \in \mathcal{C}_c^\infty(\Omega, \mathbb{R}^3),\ \forall x \in \Omega,\ |\phi(x)| \leq 1\right\} \\ K &= \left\{-\mathrm{div} z \mid z \in L^\infty(\Omega, \mathbb{R}^3),\ -\mathrm{div}(z_{\chi_\Omega}) \in L^2(\mathbb{R}^3)\right\} \end{aligned} \tag{B.7}$$

where the last condition means that there exists $\gamma \in L^2(\Omega)$ such that $\int_\Omega \gamma u dx = \int_\Omega z \cdot \nabla u dx$ for all smooth u with compact support. K is the closure of $\mathcal{K}$ in $L^2(\Omega)$. Now, what is the subgradient of TV? For $u, v \in L^2(\Omega)$ and $p \in K$, one has:

$$\mathrm{TV}(v) = \sup_{p \in K} \int_\Omega u(x)q(x)dx \geq \int_\Omega p(x)u(x)dx = \mathrm{TV}(u) + \int_\Omega (v(x) - u(x))p(x)dx. \tag{B.8}$$

Conversely, if $p \in \partial\mathrm{TV}(u)$, $t > 0$ and $v \in \Omega$, the homogeneity of the total variation ensures us of the following relation:

$$t\mathrm{TV}(v) = \mathrm{TV}(tv) \geq \mathrm{TV}(u) + \int_\Omega p(x)(tv(x) - u(x))dx.$$

By taking the limit to infinity, then to 0, this shows the converse. We proved the following theorem.

Theorem B.2.1 (Subgradient of the Total Variation)**.** *For $u \in L^2(\Omega)$, the subgradient of the total variation is given at this point by:*

$$\partial\mathrm{TV}(u) = \left\{p \in K \mid \int_\Omega p(x)u(x)dx = \mathrm{TV}(u)\right\}$$

Like for the classical gradient, the subgradient fournishes a convenient characterization of the minimal of a convex function.

Theorem B.2.2 (Global minimum of a convex function)**.** *A point x_0 is the global minimum of a convex function F if and only if its subgradient contains* 0.

Pairing this property with the additivity of the subgradient, the differentiability of the data term, and the convexity of the whole optical flow energy functional, one gets the following Euler-Lagrange equations for the TV-L2 optical flow problem.

Theorem B.2.3 (Euler-Lagrange equations of the TV-L2 optical flow)**.** *The associated Euler-Lagrange equations of the following minimization problem:*

$$\underset{\mathbf{u}=(u,v,w)\in L^2(\Omega,\mathbb{R}^3)}{\text{argmin}} \quad ||\frac{\partial I}{\partial t} + \nabla I \cdot \mathbf{u}||_2^2 + \alpha(\text{TV}(u) + \text{TV}(v) + \text{TV}(w))$$

are given by the existence of three functions $z_x, z_y, z_z \in L^\infty(\Omega, \mathbb{R}^3)$ such that:

$$\begin{cases} -\alpha \text{div}(z_x(x)) + \left[I_x\left(\frac{\partial I}{\partial t} + \nabla I \cdot \mathbf{u}\right)\right](x) = 0, \quad \text{for} \quad x \in \Omega \\ -\alpha \text{div}(z_y(x)) + \left[I_y\left(\frac{\partial I}{\partial t} + \nabla I \cdot \mathbf{u}\right)\right](x) = 0, \quad \text{for} \quad x \in \Omega \\ -\alpha \text{div}(z_z(x)) + \left[I_z\left(\frac{\partial I}{\partial t} + \nabla I \cdot \mathbf{u}\right)\right](x) = 0, \quad \text{for} \quad x \in \Omega \\ |z_x(x)| \leq 1, \quad \forall x \in \Omega \\ |z_y(x)| \leq 1, \quad \forall x \in \Omega \\ |z_z(x)| \leq 1, \quad \forall x \in \Omega \\ z_x \cdot \nu = 0 \quad \text{on} \quad \partial\Omega \\ z_y \cdot \nu = 0 \quad \text{on} \quad \partial\Omega \\ z_z \cdot \nu = 0 \quad \text{on} \quad \partial\Omega \\ z_x \cdot Du = |Du| \\ z_y \cdot Dv = |Dv| \\ z_z \cdot Dw = |Dw| \end{cases} \tag{B.9}$$

Note that the functions z_x, z_y, z_z depend on the regularisation parameter α.

B.3 The equivalent level-sets problem, existence of the staircasing the effect

This section groups several theorems that we give as "claims", meaning their proofs remain yet to be established. They extend related theorems well established for the ROF problem (see figure B.1), and confirm the existence of a staircasing effect for TV-L2 optical flow. Since both problems are linear, we believe their veracity quite likely. We aim at proving them during the coming months.

We can attach to each superlevel set a variational problem of the following form.

Definition B.3.1 (OFs problem)**.** *Let $\lambda, s_x, s_y, s_z \in \mathbb{R}$. We denote (OFs) the following variational problem:*

$$\begin{aligned} \min_{E_x,E_y,E_z} \lambda(\text{Per}(E_x) + \text{Per}(E_y) + \text{Per}(E_z)) + \int_{E_x} I_x(I_x s_x + I_y s_y + I_z s_z)dx \\ + \int_{E_y} I_y(I_x s_x + I_y s_y + I_z s_z)dx \\ + \int_{E_z} I_z(I_x s_x + I_y s_y + I_z s_z)dx \end{aligned} \tag{B.10}$$

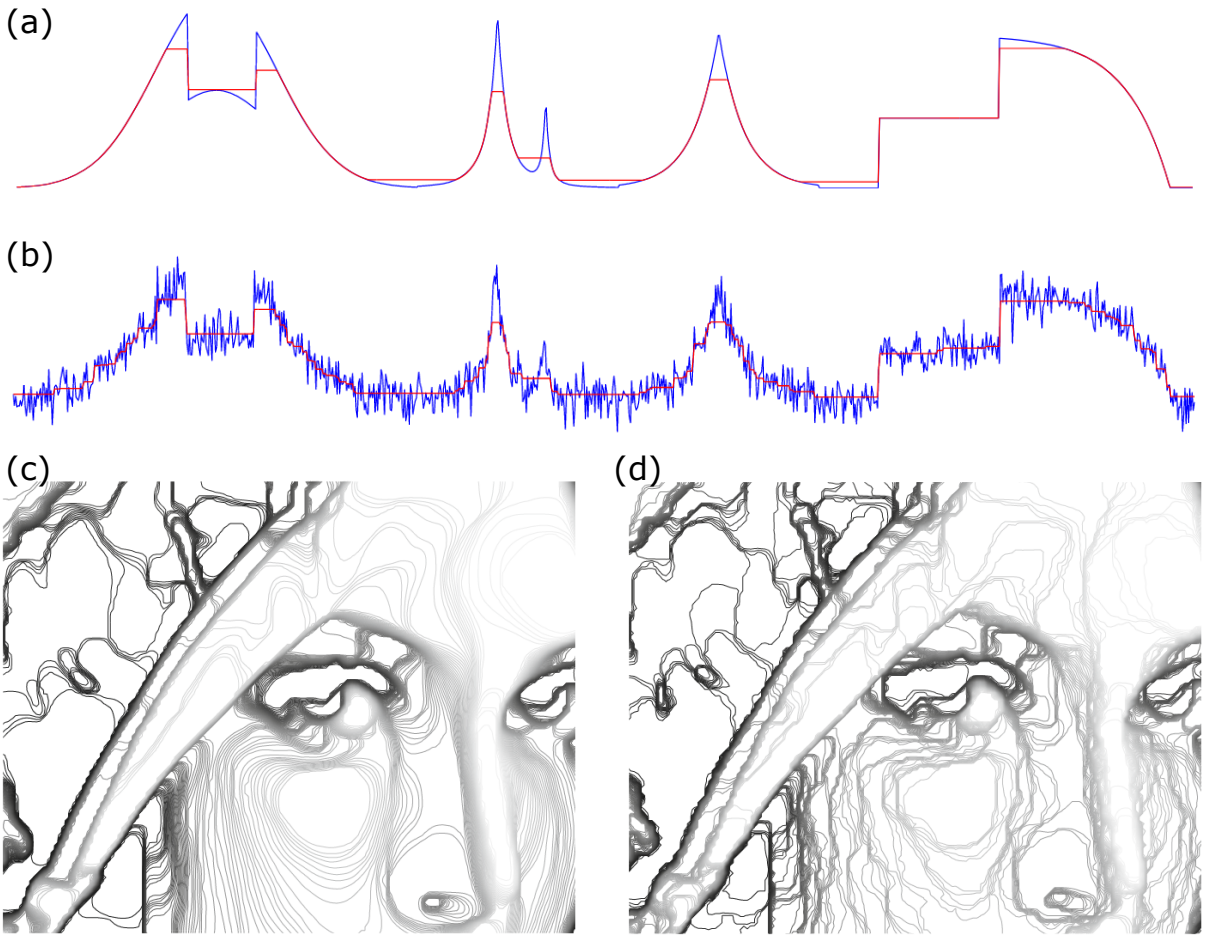

Figure B.1: Illustration of the staircasing effect with the Rudin-Osher-Fatemi problem. (a) True signal (blue) and reconstructed image (red) with the true image without noise as input. Notice that the reconstructed signal is constant around local extrema ; (b) When the inputted image is noisy, every point is a local extrema, therefore the reconstructed signal is almost everywhere constant ; (c) Level lines of a true 2D image ; (d) Level lines of the 2D image reconstruction with the ROF model, where the staircasing effect appears clearly again. (adapted from [248])

Based on the co-area formula stated in the previous section, we claim the following conjecture.

Claim B.3.1. *A function* $\mathbf{u} = (u, v, w)$ *is solution of the TV-L2 optical flow problem if and only for every* $s_x, s_y, s_z \in \mathbb{R}$*, the triplet of sets* $(\{u > s_x\}, \{v > s_y\}, \{w > s_z\})$ *solves problem (B.10).*

Our final claim states the existence of necessary staircasing for our problem.

Claim B.3.2 (Staircasing effect)**.** *Suppose the true displacement field warping the first image unto the second one belongs to* $L^\infty(\Omega, \mathbb{R}^3)$*. Then the solution* $\mathbf{u}$ *of the TV-L2 optical flow problem also belongs to* $L^\infty(\Omega, \mathbb{R}^3$ *and one has:*

$$|\{\mathbf{u} = \max \mathbf{u}\}| > 0. \tag{B.11}$$

where the maximum is taken in the sense of the infinity norm.

Appendix C

Adjoint method

We follow the plan adopted by Boquet in [214]. Denote $\mathcal{F}$ the functional such that $\mathcal{F}(\mathbf{u}, \mathbf{g}) = 0$ if and only the system of equation in (C.4) holds. We saw that both this functional and $J(\mathbf{u}(\mathbf{g}), \mathbf{g})$ are differentiable, so we may apply the chain rule to them:

$$\begin{aligned} \frac{dJ(\mathbf{u}(\mathbf{g}), \mathbf{g})}{d\mathbf{g}} &= \frac{\partial J}{\partial \mathbf{u}} \frac{d\mathbf{u}}{d\mathbf{g}} + \frac{\partial J}{\partial \mathbf{g}}, \\ \frac{\partial \mathcal{F}(\mathbf{u}, \mathbf{g})}{\partial \mathbf{u}} \frac{d\mathbf{u}}{d\mathbf{g}} &= -\frac{\partial \mathcal{F}(\mathbf{u}, \mathbf{g})}{\partial \mathbf{g}}. \end{aligned} \tag{C.1}$$

The second equation is the tangent linear system. The total derivatives involve three kinds of partial derivatives. The terms $\frac{\partial J}{\partial \mathbf{u}}$ and $\frac{\partial J}{\partial \mathbf{g}}$ admit a closed-form expression and thus are easy to compute. On the other hand the third term $\frac{d\mathbf{u}}{d\mathbf{g}}$ is a large and dense matrix that is defined implicitly only. To compute it directly would require as many finite element resolutions of the same partial differential equations as there are degrees of freedom. Instead we use the tangent linear system. A simple inversion would give for instance:

$$\frac{d\mathbf{u}}{d\mathbf{g}} = -\left(\frac{\partial \mathcal{F}(\mathbf{u}, \mathbf{g})}{\partial \mathbf{u}}\right)^{-1} \frac{\partial \mathcal{F}(\mathbf{u}, \mathbf{g})}{\partial \mathbf{g}} \tag{C.2}$$

But the inversion of the first term would require too many computations as well. This is where the "adjoint" comes in. Inputting C.2 into C.1:

$$\frac{dJ(\mathbf{u}(\mathbf{g}), \mathbf{g})}{d\mathbf{g}} = -\frac{\partial J}{\partial \mathbf{u}} \left(\frac{\partial \mathcal{F}(\mathbf{u}, \mathbf{g})}{\partial \mathbf{u}}\right)^{-1} \frac{\partial \mathcal{F}(\mathbf{u}, \mathbf{g})}{\partial \mathbf{g}} + \frac{\partial J}{\partial \mathbf{g}} \tag{C.3}$$

and taking the Hermitian adjoint:

$$\frac{dJ^*(\mathbf{u}(\mathbf{g}), \mathbf{g})}{d\mathbf{g}} = -\frac{\partial \mathcal{F}^*(\mathbf{u}, \mathbf{g})}{\partial \mathbf{g}} \left(\frac{\partial \mathcal{F}(\mathbf{u}, \mathbf{g})}{\partial \mathbf{u}}\right)^{-*} \frac{\partial J^*}{\partial \mathbf{u}} + \frac{\partial J^*}{\partial \mathbf{g}} \tag{C.4}$$

We introduce the adjoint variable λ such that:

$$\lambda = \left(\frac{\partial \mathcal{F}(\mathbf{u}, \mathbf{g})}{\partial \mathbf{u}}\right)^{-*} \frac{\partial J^*}{\partial \mathbf{u}} \tag{C.5}$$

with which we can rewrite equations C.1:

$$\begin{aligned} \frac{dJ(\mathbf{u}(\mathbf{g}), \mathbf{g})}{d\mathbf{g}} &= -\lambda^* \frac{\partial \mathcal{F}(\mathbf{u}, \mathbf{g})}{\partial \mathbf{g}} + \frac{\partial J}{\partial \mathbf{g}} \\ \left(\frac{\partial \mathcal{F}(\mathbf{u}, \mathbf{g})}{\partial \mathbf{u}}\right)^* \lambda &= \frac{\partial J^*}{\partial \mathbf{u}} \end{aligned} \tag{C.6}$$

In C.1, the source terms depend on the control variable, but here λ depends solely on the functional. It is a vector of the same dimension of $\mathbf{u}$. Therefore, we can compute the derivative of J by first computing

λ through the adjoint equation, then taking the inner product of λ with $\partial\mathcal{F}/\partial\mathbf{g}$ and addition it with $\partial J/\partial\mathbf{g}$. The computation time is therefore equivalent to the resolution of a single PDE, instead of the resolution of as much PDEs as there are degrees of freedom of the control parameter.

We now give a second derivation scheme. Define the Lagrangian L as:

$$L = J - \lambda^* \mathcal{F} \tag{C.7}$$

Its perturbation is obtained by differentiation:

$$dL = \frac{\partial J}{\partial \mathbf{u}} d\mathbf{u} + \frac{\partial J}{\partial \mathbf{g}} d\mathbf{g} - \lambda^* \frac{\partial \mathcal{F}}{\partial \mathbf{u}} d\mathbf{u} - \lambda^* \frac{\partial J}{\partial \mathbf{g}} d\mathbf{g}. \tag{C.8}$$

Suppose the derivative with respect to the state variables is zero, and that the forward equation is satisfied. Then:

$$dL = \left(\frac{\partial J}{\partial \mathbf{g}} - \lambda^* \frac{\partial J}{\partial \mathbf{g}} \right) d\mathbf{g} = dJ \tag{C.9}$$

which is the first equation of C.1. On the other hand, if the state derivatives are to zero, then:

$$\frac{\partial J}{\partial \mathbf{g}} - \lambda^* \frac{\partial \mathcal{F}}{\partial \mathbf{g}} = 0, \tag{C.10}$$

which is the adjoint equation of C.1.

Finally we show how the adjoint method applies in the continuous setting. From thereon the partial derivatives refer to the Gâteaux derivatives. The adjoint operator of $(\partial\mathcal{F}/\partial\mathbf{u})$ is defined by duality as:

$$\int_\Omega \Lambda^* \left(\frac{\partial \mathcal{F}}{\partial \mathbf{u}} \right) \Theta d\mathbf{x} = \int_\Omega \left(\left(\frac{\partial \mathcal{F}}{\partial \mathbf{u}} \right)^* \Lambda \right)^* \Theta d\mathbf{x} \tag{C.11}$$

for all appropriate pair of functions Λ, Θ. Suppose we dispose of a λ such that $(\partial\mathcal{F}/\partial\mathbf{u})^*\lambda = (\partial J/\partial\mathbf{u})^*$ in the weak sense. Then the gradient comes as:

$$\int_\Omega \frac{\partial J}{\partial \mathbf{g}} \frac{d\mathbf{u}}{d\mathbf{g}} d\mathbf{x} = \int_\Omega -\lambda^* \frac{\partial \mathcal{F}}{\partial \mathbf{g}} d\mathbf{x}. \tag{C.12}$$

As in the discrete case, the Lagragian way is also valid.

French summary

C.1 Motivation

Les études en mécanobiologie prouvent depuis des décennies que les propriétés mécaniques du noyau influent directement sur son fonctionnement physiologique. Cela vient de ce que certains de ses éléments occupent non seulement un rôle structurel, mais aussi génomique. Pour le comprendre, il est utile d'étudier l'architecture nucléaire. Le noyau peut être séparé en deux parties : l'enveloppe et l'intérieur. Dans la première l'on trouve, entre autres constituants, les membranes nucléaires internes et externes, les pores nucléaires, et la lamine, un maillage de filaments intermédiaires de type V sous-tendant la membrane. Les filaments intermédiaires sont, des trois composants du cytosquelette, ceux se déformant le moins facilement, et de nombreuses études montrent qu'en leur absence, le noyau se distend et perd en rigidité. Par ailleurs, l'invalidation génique des gènes LMNA et LMNB codant ses constituants occasionne de sévères affections, parmi lesquelles les dystrophies musculaires d'Emery Dreifuss, le syndrome d'Hutchinson-Gilford (ou progéria), ou certaines cardiomyopathies. Car la lamine, en plus de structurer le noyau, intervient en bonne part dans la régulation épigénétique. Dans l'intérieur nucléaire sont les corps nucléaires, comme le nucleolus, les corps Cajal, ou la chromatine. Cette dernière est la structure condensée par laquelle se présente l'ADN. Tout comme pour la lamine, son rôle est également ambivalent. Nous connaissons deux régions bien distinctes de la chromatine : l'hétérochromatine et l'euchromatine. L'hétérochromatine est dense et transcriptionnellement inactive. L'euchromatine est relâchée et transcriptionnellememt active. Selon que l'une ou l'autre se trouve en plus ou moins grande proportion, l'activité génomique du noyau varie, et avec elle sa dureté. Tout comme pour la lamine, certaines anomalies structurelles de la chromatine apportent leur lot de maladies graves, parmi lesquelles des cancers. Si les liens entres les propriétés mécaniques du noyau et le bon fonctionnement physiologique de la cellule sont attestés, ceux-ci s'avèrent singulièrement complexes, et mettent en jeu l'interaction de nombreuses protéines, parmi lesquelles le complexe LINC. Pour l'heure, aucune synthèse théorique exhaustive ne semble possible. Il est cependant envisageable de proposer, au niveau microscopique, des modèles physiques satisfaisants.

On peut supposer le noyau tel un milieu continu, dont les propriétés mécaniques de l'enveloppe sont dictées par la lamine, et celles de l'intérieur par la chromatine. De part leurs nombreuses interactions protéiques, l'enveloppe peut être supposée solidement attachée à l'intérieur. De nombreuses expérimentations prouvent que la lamine, tout comme la chromatine, peuvent être vus sans trop de préjudice comme des matériaux viscoélastiques. Les biologistes et les biophysiciens recourent à trois niveaux de modélisation de ces constituants, allant du plus simple au plus complexe (voir Figure C.1). Le premier niveau est constituté des modèles 1D, pour lesquels les constituants nucléaires sont représentés par un assemblage de ressorts (simulant ainsi la dureté) et d'amortisseurs (pour la viscosité). Dans le second, nous trouvons les modèles de mécanique des milieux continus, où le domaine nucléaire est délimité par une forme géométrique 2D ou 3D, et étudiée (le plus souvent) par une méthodologie recourant aux éléments finis. Enfin, au niveau le plus élevé d'exactitude l'on trouve les méthodes dites de "dynamisme moléculaires", qui vont jusqu'à modéliser les interactions au niveau protéique : l'on simule alors chaque

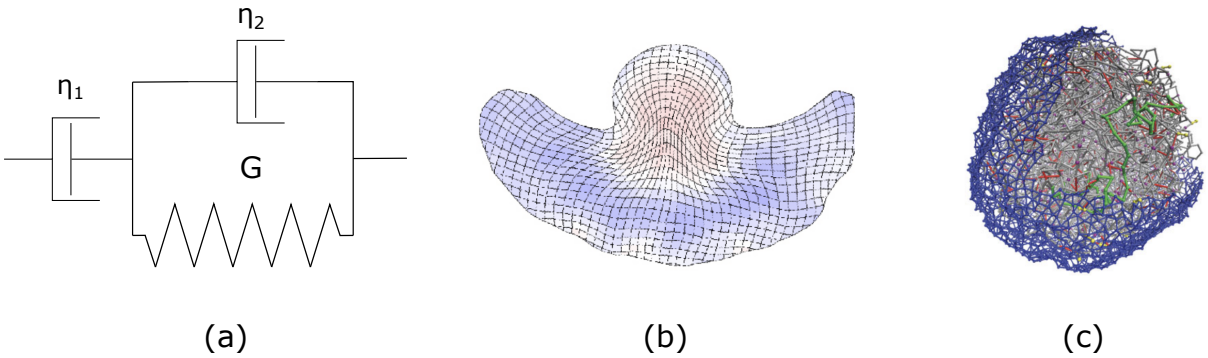

Figure C.1: Différents niveaux de modélisation mécanique des noyaux. (a) Modèle 1D de Jeffrey d'un noyau, où les ressorts et les amortisseurs sont assemblés en série ou en parallèle pour donner une représentation viscoélastique ; (b) Modélisation en mécanique des milieux continus, où la géométrie de la cellule est précisément déterminée par segmentation, puis maillée par une triangulation, et où les grandeurs physiques d'intérêt sont calculées le plus souvent par les éléments finis ; (c) .

force reliant chaque ensemble protéique, puis un assemblage numérique suivi d'une résolution nous livrent les propriétés mécaniques globales du noyau.

Les biologistes recourent constamment à ces modèles dans des dispositifs expérimentaux pour calculer les propriétés mécaniques du noyau. Parmi ces dispositifs, l'on dénombre les méthodes de sondage (Atomic Force Microscopy, micromanipulation, optical tweezers, magnetic tweezers, etc.), les méthodes de confinement (aspiration par micropipette, compression par plaque, migration confinée, etc.), ou les méthodes de suspension (modification d'environnement, déformation du substrat, suspension, etc.). Indépendamment du choix retenu, la plupart de ces méthodes souffrent de limitations bien connues des expérimentateurs : les déformations ne s'appliquent qu'*in vitro*, la définition du tenseur de déformation est souvent simplifiée, et de fortes contraintes doivent être appliquées pour que les mesures sont fiables, ce qui peut indésirablement déclencher une réorganisation nucléaire par mécanotransduction.

Nous proposons dans cette thèse d'apparier les modélisations physiques du noyau en mécanique des milieux continus à des méthodes novatrices en analyse d'images pour contourner ces problèmes. Nous définissons précisément les problèmes à résoudre au chapitre suivant, consacré à la modélisation du noyau.

C.2 Modélisation du noyau cellulaire

Nous avons donné une modélisation physique du noyau au chapitre précédent. Nous en donnons une modélisation mathématique dans ce chapitre. En supposant que le noyau occupe une région Ω à bord régulier Γ de l'espace $\mathbb{R}^3$, nous pouvons établir, en invoquant le principe de contrainte d'Euler et Cauchy, le système d'équations d'équilibre des forces en jeu. À ce système est joint un ensemble d'équations dites constitutives, qui lient les contraintes aux déformations internes par des relations mettant en jeu les constantes de rigidité E et de Poisson ν. Lorsque les forces qui compriment ou tendent le noyau sont supposées quasistatiques et faibles, comme c'est le cas dans de nombreux régimes d'intérêt où les précédentes méthodes biophysiques ne trouvent pas leur emploi, le noyau obéit aux équations différentielles suivantes :

$$\begin{cases} \nabla \cdot \varsigma = 0, & \text{in } \Omega \\ \varsigma(\mathbf{u}) = \lambda \mathrm{tr}(\varepsilon(\mathbf{u}))\mathbb{1} + 2\mu\varepsilon(\mathbf{u}), & \text{in } \Omega \\ \varepsilon(\mathbf{u}) = \frac{1}{2}(\nabla\mathbf{u} + \nabla\mathbf{u}^{\mathrm{T}}), & \text{in } \Omega \\ \mathbf{u} = \mathbf{0}, & \text{on } \Gamma_u \\ \varsigma \cdot \mathbf{n} = \mathbf{T}, & \text{on } \Gamma_t, \end{cases}$$

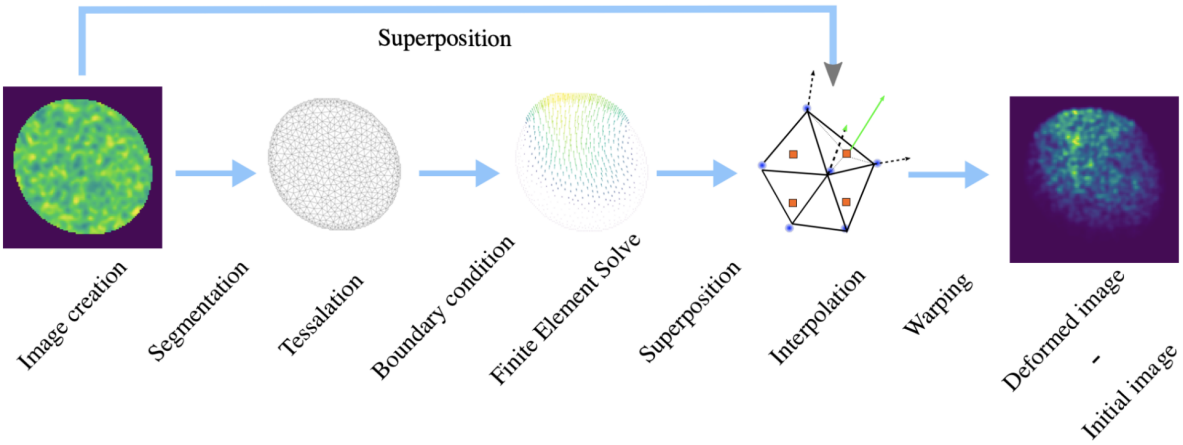

Figure C.2: Illustration des étapes de création de données synthétiques à partir des équations d'élasticité régissant le noyau.

où $\mathbf{u}$ est le champ de déplacement, ε le tenseur de déformation, ς le tenseur de contrainte, $\mathbf{T}$ les forces de traction au bord, $\mathbf{n}$ un vecteur unité normal au bord, Γ_u la portion du bord où les conditions sont de Dirichlet, Γ_t la portion du bord où les conditions sont de Neumann, et λ et μ sont les paramètres de Lamé, dépendant du module de Young E et de la constante de Poisson ν.

Puisque le bord Γ est régulier, que le LINC complex est homogènement réparti dans la membrane nucléaire, que les techniques de microscopie par fluorescence s'appliquent au niveau microscopique, et que les membranes internes et externes du noyau sont séparés, nous montrons, par simples propriétés de Schauder des opérateurs elliptiques, que les solutions de ces équations appartiennent nécessairement à l'espace de Sobolev $H^2(\Omega, \mathbb{R}^3)$. Cette contrainte à l'esprit, nous établissons les trois problèmes que les outils développés dans les chapitres suivants devront résoudre :

- **Problème 1**. Ayant deux images par fluorescence d'un noyau, une avant déformation, l'autre après, calculer le champ de déplacement $\mathbf{u}$ et le tenseur de déformation $\varepsilon(\mathbf{u})$.
- **Problème 2**. Ayant deux images par fluorescence d'un noyau, une avant déformation, l'autre après, ainsi que la valeur de la constante de Poisson, calculer la valeur relative du module de Young ou, dans le cas où les forces au bord sont connues, les valeurs absolues.
- **Problème 3**. Ayant le module de Young E, la constante de Poisson ν, et deux images par fluorescence d'un noyau, une avant déformation, l'autre après, calculer les tenseurs de contrainte ς et les forces de traction au bord $\mathbf{T}$.

Pour les évaluations futures, nous proposons une méthodologie de création d'images de noyaux se déformant, fondées sur les équations établies, avec les vraies valeurs physiques de référence les sous-tendant (voir Figure C.2). Elle se base sur la méthode des éléments finis : après avoir aléatoirement généré une image de noyau, nous définissions les forces de traction au bord, ainsi qu'une approximation en dimension finie des équations d'élasticité ; nous résolvons les déplacements occasionnés, que nous superposons à l'image initiale afin de la déformer par simple warping.

C.3 Mesure des déplacements à partir d'images

Nous recourons à une méthode bien connue en analyse d'images : le flux optique. Elle consiste à calculer, à partir d'images qui se suivent, le mouvement apparent d'objets qui s'y trouvent. Il ne s'agit

pas, à tout point de vue, du mouvement réel. Prenez par exemple un disque de même couleur, faites-le tournoyer autour de l'axe central, éclairez-le d'une lumière homogène, et contemplez-le de face : vous le croirez immobile. Son mouvement apparent est nul, quoique son mouvement réel ne le soit pas. Nous prétendons toutefois que, en microscopie à fluorescence, ils se correspondent. Cela tient d'une part à la propriété des fluorophores qui, hors cas de saturation, rendent une texture variée à chaque objet biologique marqué. Et d'autre part à la singulière disposition des montages optiques qui obtiennent, par le jeu de filtrage et de réflexion, une simple projection 3D, point par point, de l'objet réel. Les méthodes de flux optique se fondent sur une hypothèse irréfragable : la conservation de l'intensité lumineuse au cours du temps. De la sorte, l'intensité lumineuse de chaque pixel agit comme une "carte d'identité" du matériel sous-jacent : si la valeur d'un pixel change, cela tient non pas d'un changement d'illumination, mais d'un mouvement d'advection. L'on comprendra, au vu des réflexions du chapitre 1, que le photobleaching peut s'avérer désastreux dans le calcul de flux optique. Mais nous avons vu aussi qu'il advient homogènement et, par conséquent, peut être réglé par une simple technique de normalisation par rappot au temps. En notant $(\mathbf{x}, t) \to I(\mathbf{x}, t)$ la fonction d'intensité lumineuse de chaque image à l'instant t, la conservation de l'intensité lumineuse admet une formulation mathématique: $I(\mathbf{x} + \mathbf{u}, t + 1) = I(\mathbf{x}, t)$. Ici, $\mathbf{u}$ désigne le mouvement d'advection du matériel biologique sous-tendant l'image, et si on le suppose suffisamment petit, nous pouvons linéariser cette équation pour en obtenir celle du flux optique:

$$\mathrm{OF}(\mathbf{u}, I) = \frac{\partial I}{\partial t} + \mathbf{u} \cdot \nabla \mathbf{u} = 0.$$

Cette équation ne peut se résoudre telle qu'elle se présente : c'est le problème de l'ouverture (*aperture problem*). Il faut, pour déterminer un unique champ de déplacement, admettre des hypothèses supplémentaires, par exemple concernant la régularité du champ de déplacement voulu. Une stratégie communément adoptée consiste à transformer cette équation en un problème variationnel de la forme:

$$\tilde{\mathbf{u}} = \underset{\mathbf{u}}{\operatorname{argmin}}\ \Phi(\mathrm{OF}(\mathbf{u}, I)) + \alpha E_{\text{reg}}(\mathbf{u})$$

où Φ et E_{reg} désignent des fonctions coercives, semi continues inférieurement, et généralement convexes. Par exemple, la méthode de Horn-Schunck choisit la norme de L_2 pour $\Phi = ||\cdot||_2$, et le carré de la norme de Frobenius pour le terme de régularisation $E_{\text{reg}}(\mathbf{u}) = ||\nabla \mathbf{u}||^2_{S_2}$. Comme ces termes sont différentiables, le problème variationnel correspondant admet des équations d'Euler-Lagrange définissant des gradients exacts. De ces équations d'Euler-Lagrange sont tirées un schéma itératif, selon la méthode de Jacobi, pour calculer le champ de déplacement désiré. Remarquez que les équations du flux optique ne s'appliquent que pour des déplacements faibles. En un cas plus général, l'on recourt à une méthode "coarse-to-fine" dans laquelle les images initiales sont floutées et échantillonnées dans un schéma pyramidal: la méthode variationnelle est d'abord appliquée aux images les plus petites, dans lesquelles les déplacements sont au plus d'un pixel, avant d'être appliquée aux étages inférieurs, avec les déplacements obtenus à l'étage supérieure en initialisation. La simplicité de la méthode de Horn-Schunck en a fait son attrait durant de nombreuses années. Mais les termes quadratiques par lesquels elle pénalise les contraintes de régularisation et de flux optique obligent le champ de déplacement calculé à appartenir à $W^{1,2}(\Omega, \mathbb{R}^3)$. Par conséquent, il est continu absolument selon tout hyperplan de l'espace $\mathbb{R}^3$. Ainsi, la reconstitution du champ de déplacement tend à être "floutée" au bord des noyaux. Pour obvier à ce soucis, de très nombreuses méthodes remplacent les fonctions pénalisées par $\Phi = ||\cdot||_1$ et $E_{\text{reg}}(\mathbf{u}) = \mathrm{TV}(u) + \mathrm{TV}(v) + \mathrm{TV}(w)$ où $\mathbf{u} = (u, v, w)$ et où $\mathrm{TV}(u) = \sup\{\int_\Omega u \mathrm{div}\phi dx : \phi \in \mathcal{C}^\infty_c(\Omega, \mathbb{R}^3),\ ||\phi||_\infty \leq 1\}$. On parle de flux optique TV-L1. Contrairement au cas de Horn-Schunck, cette méthode contraint le champ de déplacement à appartenir à l'espace des fonctions à variations bornées, qui admettent des discontinuities selon les hyperplans. Depuis lors ce terme de régularisation connaît une vogue jamais démentie. La méthode LDOF (Large Displacement Optical Flow) l'utilise à son profit aussi. Soucieuse de restituer les déplacements de petits objets, qui tendent à être éliminés lors du floutage pyramidale, elle inclut, en plus des termes de régularisation TV et L1, des termes de pénalisation contraignant un "matching" de zones pré-segmentées

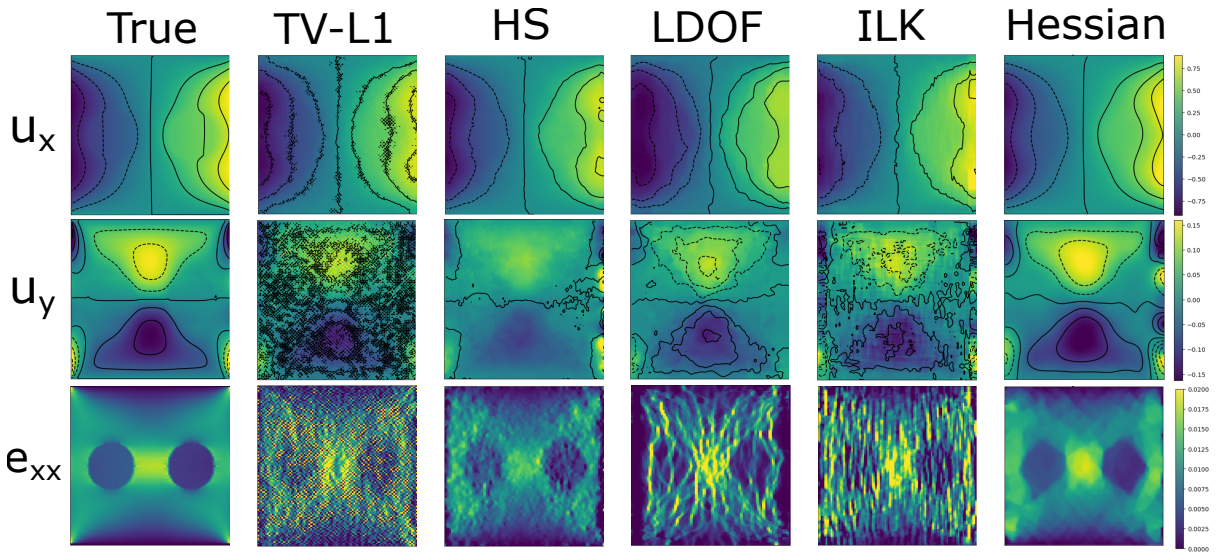

Figure C.3: Comparaison des méthodes de flux optique dans le calcul des déplacements et de la déformation axiale.

dans les images. D'autres méthodes, telle que eFOLKI, s'appuient sur des contraintes locales, suivant l'exemple de la méthode Lukas-Kanade, afin de gagner en vitesse d'exécution. Enfin, dernièrement, avec le développement des méthodes de deep-learning, de nombreuses méthodes de flux optique incorporent l'apprentissage supervisé et non supervisé dans l'estimation des déplacements. Ces méthodes peuvent s'accommoder des formulations variationnelles, pour lesquelles alors leur apprentissage sert essentiellement à remplacer l'intensité des images par des "features" extraits selon différentes modalitées, ou les rejeter complètement et d'opter pour un calcul direct des déplacements ("end-to-end"). Cependant, les méthodes de deep learning dépendent en bonne part du jeu de donnée sur lesquelles elles vont s'entraîner. Hors, à ce jour, seules des données de déplacement de mouvement 3D macroscopique existent. Ce type de mouvement est très différent des mouvements non rigides rencontrés en imagerie biologique et, de façon générale, ces méthodes de flux optique obtiennent des résultats insatisfaisants dans notre cas.

Les méthodes varitionnelles de flux optique, de par leur terme de pénalisation, contraignent le champ de déplacement à appartenir à $W^{1,s}(\Omega, \mathbb{R}^3)$, $s \geq 1$, ou $BV(\Omega, \mathbb{R}^3)$. Hors, la modélisation effectuée lors du chapitre 2 montre clairement que les déplacements élastiques à l'intérieur du noyau appartiennent à $H^2(\Omega, \mathbb{R}^3)$. De plus, les déplacements souffrent de ce qu'on nomme "l'effet de l'escalier", qui rend les déplacements constants par morceaux selon certains axes. Ces inexactitudes rendent très difficiles le calcul de valeurs physiques d'intérêt, comme la déformation, la contrainte ou la force de traction au bord. Pour éviter ces écueils, nous proposons un terme de régularisation fondée sur la norme nucléaire du Hessien. Le Hessien du champ de déplacement est un champ de tenseur d'ordre 3. La norme nucléaire est définie pour chaque tenseur $\mathcal{T}$ par:

$$||\mathcal{T}||_* = \inf \left\{ \sum_{i=1}^{r} |\lambda_i| \mid \mathcal{T} = \sum_{i=1}^{r} \lambda_i u_{1,i} \otimes u_{2,i} \otimes u_{3,i},\ ||u_{k,i}||_2 = 1,\ r \in \mathbb{N} \right\}.$$

Malheureusement, la norme nucléaire est NP-difficile à calculer, semicontinue supérieurement (et non inférieurement, ce qui peut causer des problèmes d'existence dans nos problèmes de minimisation), et non invariante par rotation (ce qui, pour la description de tout système physique, est rédhibitoire). Chacun de ces problèmes disparaissent cependant lorsque la norme nucléaire est calculée pour des tenseurs d'ordre 2, car elle devient dès lors la norme Schatten d'ordre 1 définie par $||A||_{\mathcal{S}_1} = \sum_k |\sigma_k|$ où $(\sigma_k)_k$ désigne l'ensemble des valeurs propres de A. Par ailleurs, il est prouvé que la norme $||\mathcal{H}\mathbf{u}||_*$ peut être

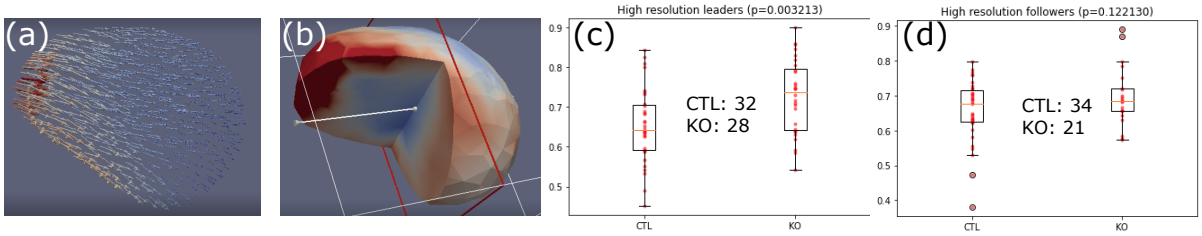

Figure C.4: Application des méthodes de flux optique dans l'étude de l'influence des filaments intermédiaires dans la migration des glioblastomes. (a) Champ de déplacement d'un noyau de glioblastome ; (b) Norme de Frobenius du tenseur de déformation du même champ de déformation ; (c) Comparaison de la déformation des noyaux de glioblastomes meneurs, avec ou sans filaments intermédiaires, avec une différence dans la moyenne significative ; (d) Comparaison de la déformation des noyaux de glioblastomes suiveurs, avec ou sans filaments intermédiaires, sans différence significative de la moyenne.

approximée avec un facteur $\sqrt{3}$ par $||(||\mathcal{H}u||_*, ||\mathcal{H}v||_*, ||\mathcal{H}w||_*)||_1$. Ainsi, nous proposons notre propre méthode de flux optique comme étant la solution au problème variationnel suivant:

$$\underset{\mathbf{u}=(u,v,w)}{\operatorname{argmin}} ||\frac{\partial I}{\partial t} + \nabla I \cdot \mathbf{u}||^{\#} + \int_{\Omega} (\alpha_u ||\mathcal{H}u||_{S_1} + \alpha_v ||\mathcal{H}v||_{S_1} + \alpha_w ||\mathcal{H}w||_{S_1}) \,,$$

où $|| \cdot ||^{\#}$ peut être prise égale à $|| \cdot ||_1$ ou $|| \cdot ||_2$. La méthode directe dans le calcul des variations montre que ce problème admet une solution dans $W^{2,1}(\Omega, \mathbb{R}^3)$ lorsque le domaine Ω est compact, et dans l'espace des fonctions à Hessien borné autrement. Nous pouvons, pour la résoudre, recourir aux méthodes ADMM ou APGD, selon que le terme de flux optique est pris égal à $|| \cdot ||_1$ ou à $|| \cdot ||_2$. Dans ce dernier cas, il existe un majorant satisfaisant de la constante de Lipschitz du gradient du terme de flux optique, avec laquelle une résolution rapide est possible. Les deux configurations requièrent néanmoins le calcul du proximal du terme de régularisation. Malheureusement, celui-ci n'admet pas de formualtion explicite. Il peut cependant être approximé rapidement par une méthode d'optimisation d'un problème primal-dual impliquant les projections sur la boule unité selon les normes Schatten. Notre méthode de flux optique a été numériquement comparée aux autres méthodes de flux optique selon la méthodologie exposée au chapitre 2 (voir Figure C.3). Elle est non seulement plus exacte selon le critère de la RMSE, mais ses lignes de niveau sont bien plus ressemblantes de celles de déplacements élastiques. Par ailleurs, elle ne présente pas d'effets de l'escalier et, enfin, les champs de déformation qui en résultent par simple dérivation par filtrage sont bien plus exactes que celles de ses homologues, quoique la méthode de Horn Schunck soit honorable en soi. Nous l'avons d'ailleurs utilisée à une époque où notre propre méthode du flux optique n'était pas encore au point pour un problème biologique d'intérêt : le calcul des déformations du noyau de cellules de glioblastomes lors d'invasion (voir Figure C.4). Les glioblastomes sont des cellules cancéreuses développées à partir des cellules gliales du cerveau. Leur très grande léthalité vient de leur métastase rapide appuyée sur une efficace migration. Il est supposé que les filaments intermédiaires du noyau jouent un rôle important dans la migration de cellules meneuses. Pour cela, une population de glioblastomes sans ces filaments intermédiaires fut filmée par imagerie par fluorescence lors d'invasion du tissu extracellulaire. En utilisant le flux optique de Horn-Schunck, nous avons calculé, pour chaque noyau, une valeur de "déformation" définie comme la moyenne, selon le temps et l'espace, de la norme de Frobenius du tenseur de déformation. Ces valeurs ont été comparées à une population de contrôle, de quoi il ressort très clairement que les glioblastomes meneurs sans filaments intermédiaires se déforment nettement plus que lorsqu'il en ont, alors que les suiveurs non.

C.4 Calcul des champs physiques à partir des déplacements

Des trois problèmes formulés au chapitre 2, le chapitre 3 n'apporte les solutions qu'au premier, mais sert de point de départ aux deux autres. L'un de ces deux problèmes est plus communément connu sous le nom d'élastographie. Il consiste à calculer, à partir d'images de sa déformation, la carte des modules de Young, ou dureté, du noyau. Nous avons entrevu au chapitre 1 l'intérêt que pouvait revêtir une telle technique en mécanique des noyaux : l'activité génomique étant directement corrélée au degré de compacité de sa chromatine (l'hétérochromatine est dense mais non active, l'euchromatine relâchée mais active), la dureté du noyau est dans de nombreux cas un marqueur intéressant de cette même activité, et parfois de son désordre, comme pour les cancers, par exemple. Curieusement, la dureté des tissues est de même un marqueur très fiable de la présence de certaines maladies (au premier rang desquelles les tumeurs, possiblement malignes), et est la raison pour laquelle les techniques d'imagerie médicale ont longuement perfectionné leurs propres méthodes d'élastographie. Cependant, leurs modalités d'imagerie et de déformation diffèrent grandement du cadre biologique. L'élastographie à ultrason, par exemple, envoie de part en part des ultrasons de longueur d'onde connues, en récupère la vitesse par imagerie B-scan, et inverse les équations de propagation des ondes pour obtenir la dureté du milieu traversé. Un raisonnement similaire tient avec des excitations par résonnance magnétique. Leur utilité est dorénavant attestée de longue date en imagerie médicale, mais ces modalités ne sont pas aisément transposables à notre configuration. Il est par exemple très peu coûteux (et indolore) de soumettre des ultrasons à un patient en qui l'on suspecte une tumeur, mais bien qu'il existe dorénavant des "acoustic reporter genes" et quelques techniques de microscopie à très haute résolution temporelle, ces dispositifs demeurent coûteux et peu répandus en imagerie biologique. Par ailleurs, nous connaissons trop peu les réactions mécaniques du noyau à des hautes fréquences sinusoïdales pour espérer exploiter proprement une équation des ondes adaptée. Bien qu'il existe en imagerie médicale des méthodes d'élastographie opérant avec des déformations quasistatiques, celles-ci requièrent des calculs plus complexes, et exploitent, pour être suffisamment précises, les propriétés d'incompressibilité du tissu : hors une telle propriété ne peut être supposée dans notre cas. À cause de ces nombreuses difficultés techniques, les biologistes se sont contentés jusqu'alors de méthodes plus rudimentaires pour calculer le module de Young du noyau. Toutes se fondent sur une représentation 0D de sa mécanique. Quoiqu'elles diffèrent quant au détail, le principe sous-jacent reste le même : on applique une force connue au noyau, on mesure, grâce à des marqueurs de forme obtenues par imagerie, une grandeur simplifiée de sa déformation, puis nous relions cette force et cette déformation via une formule par laquelle ressort une unique valeur du module de Young du noyau. On devine les limites de cette approche : simplification, inexactitude dans la modélisation géométrique, aucune connaissance *in fine* de l'hétérogénéité du module de Young dans le noyau, inapplicabilité *in vivo*. Nous proposons deux méthodes d'élastographie pour surmonter ces écueils. Dans la première, nous supposons connues les forces de déformation au bord, et calculons les valeurs absolues du module de Young à l'intérieur de la cellule et du noyau. Dans la seconde, nous ne disposons pas de ces forces de déformation, mais nous calculons néanmoins les valeurs relatives du module de Young.

Une première façon d'attaquer ces problèmes serait d'adapter les méthodes d'élastographie quasistique développées en imagerie médicale. Nous pouvons les regrouper en deux catégories : les méthodes directes et les méthodes indirectes. La première recourt à la méthode des éléments finis. Après discrétisation du domaine nucléaire, nous choisissons une base Lagrangienne d'interpolation comme sous-espaces de dimensions finis des espaces variationnels sous-tendants les équations d'élasticité linéaires. Nous réécrivons ces équations dans cette base de dimension finie, pour aboutir à un système d'équations très creux $\mathbf{K}\hat{\mathbf{u}} = \mathbf{t}$, où $\hat{\mathbf{u}}$ et $\mathbf{t}$ sont les vecteurs, ordonnées selon la méthode d'assemblage, de chaque valeurs des déplacements et de forces de traction aux noeuds de notre triangulation, et $\mathbf{K}$ est la matrice de dureté, dépendant linéairement du vecteur $\mathbf{e}$ regroupant le module de Young de chaque élément. Par linéarité, il est possible de ré-arranger ce système d'équation en un autre $\mathbf{De} = \mathbf{t}$ où cette fois la variable

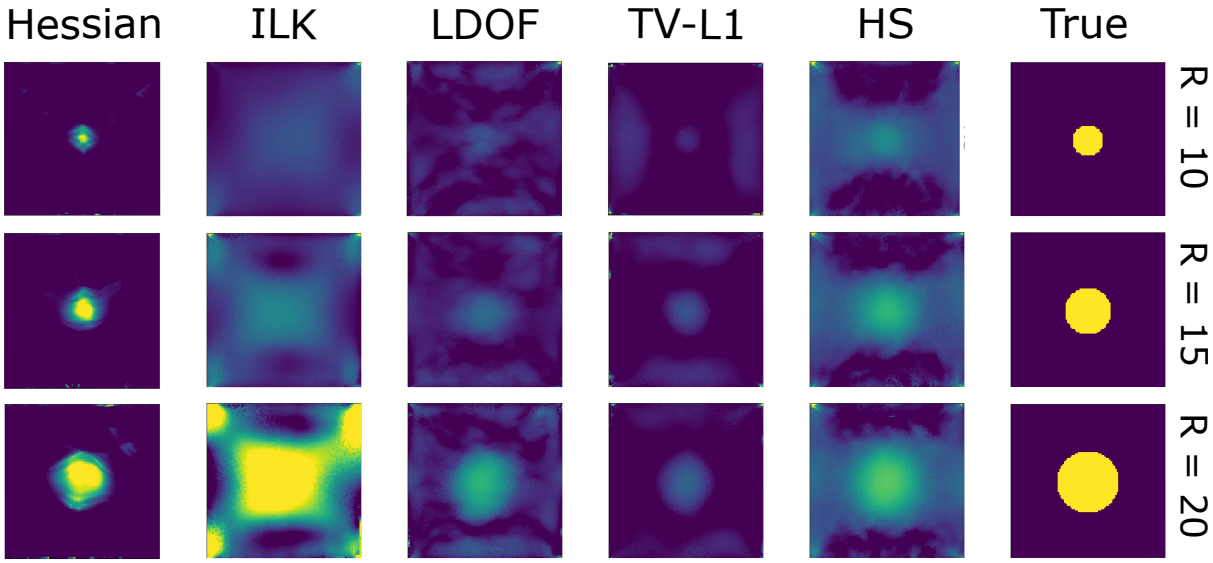

Figure C.5: Reconstitution de la valeur absolue du moduel de Young du noyau. Chaque ligne indique une simulation de déformation de noyau, avec des rayons de noyaux grandissants. Chaque colonne indique la méthode de flux optique utilisée. Les méthodes de flux optique de l'état de l'art sont appariées avec une méthode indirecte pour uen meilleure stabilité dans la reconstitution. Notre méthode de flux optique (Hessian) est appariée à une méthode d'élastographie directe. Non seulement la reconstruction est plus exacte dans notre cas, mais beaucoup plus rapide.

serait les modules de Young de chaque élément de notre triangulation. Puisque ce système d'équation est très creux, nous pouvons aisément l'invertir pour en obtenir la carte de dureté du noyau. Malheureusement, ce système d'équations est mal conditionné, et de légères erreurs de calculs des déplacements, par exemple ceux dûs aux effets de l'escalier, suffisent à gâter complètement la reconstitution. D'ordinaire, les champs de déplacement sont affinés en introduisant l'hypothèse d'incompressibilité, donnant ainsi un moyen d'interpoler les déplacements latéraux, plus brouillés ; mais, comme annoncé, cette hypothèse ne peut être prise dans notre cas. Les méthodes d'élastographie indirecte sont quant à elles plus stables face aux erreurs dans le calcul du champ de déplacement, mais plus coûteuses en calcul. Elles résolvent un problème variationnel sous contrainte d'équations différentielles partielles, comme la suivante :

$$\begin{aligned} \arg\min_{\mathbf{u},E} \quad & J(\mathbf{u},E) = ||\mathbf{u} - \tilde{\mathbf{u}}_{|\Omega}||^2_{\Omega,2} + \beta G(E) \\ & \text{subject to Eq. } (C.2), \end{aligned} \tag{C.13}$$

où $\tilde{\mathbf{u}}$ est le champ de déplacement calculé à partir des images, β une constante positive et G une fonction de E. Un choix classique du terme de régularisation serait $G(E) = E^2$. Pour chaque module de Young E, nous pouvons résoudre l'équation (C.2) et obtenir le champ de déplacement correspondant $\mathbf{u}$. Autrement dit, par le théorème des fonctions implicites, $\mathbf{u}$ est une fonction de E, et J une fonction de E uniquement. Ce problème peut donc être reformulé comme un problème sans contrainte d'équations différentielles. Il admet une résolution par descente itérative, par exemple la méthode L-BFGS. Comme le calcul du gradient requiert de coûteuses résolutions d'équations différentielles partielles, il est d'usage d'utiliser la méthode adjointe pour en limiter le calcul. Malgré cela, la résolution de ce genre de problème reste coûteuse et peut être beaucoup trop longue pour être utilisée dans des images volumineuses.

La méthode indirecte est suffisamment stable pour être appariée à n'importe quelle méthode de flux optique précédemment présentée. Nous prétendons que notre méthode est suffisamment précise pour être utilisée de conserve avec une méthode directe. Nous simulons une cellule prise entre deux plaques de compression comme illustrée. En multipliant les expériences, tantôt avec différentes forces de traction au bord, tantôt avec différentes tailles de noyau, tantôt avec différents module de Young de

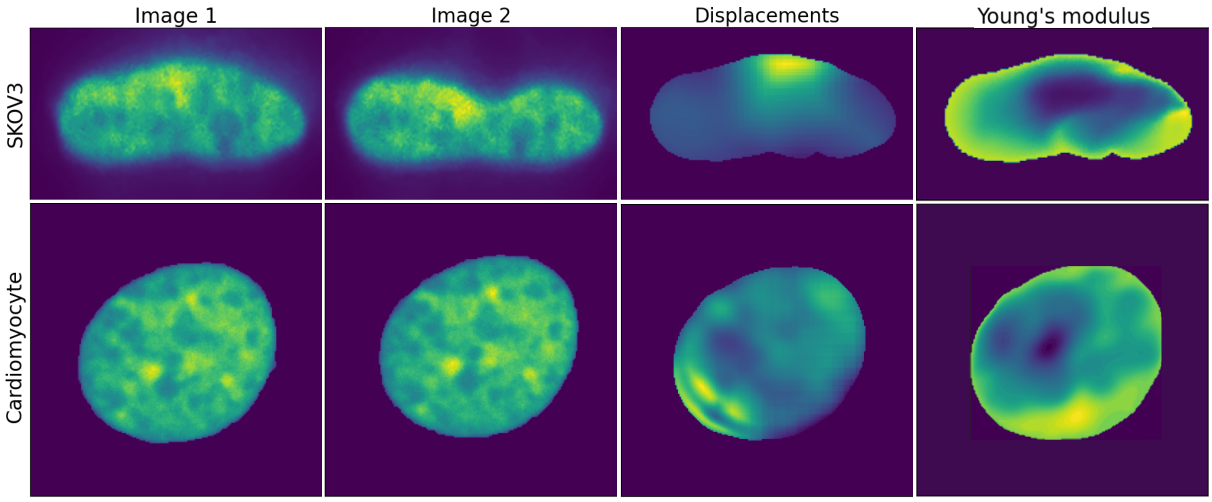

Figure C.6: Application à des données réelles de notre méthode d'élastographie relative.

noyau, nous montrons que non seulement apparier notre méthode de flux optique avec une méthode d'élastographie directe reconstitue incomparablement plus rapidement le module de Young qu'avec les autres méthodes, mais que cette reconstruction est par ailleurs très fidèle à la distribution envisagée (voir Figure C.5).

Cependant, il est dans la plupart du temps très difficile de connaître les forces de traction au bord, y compris dans des cas où celles-ci sont issues de dispositifs expérimentaux, ne serait-ce que parce que la surface d'application de ces forces est difficilement déterminée avec précision. Nous proposons une méthode d'élastographie inédite pour recouvrer les modules de Young relatifs à l'intérieur du noyau. Nous pouvons la considérer comme une méthode directe, en ce qu'elle consiste à réarranger les équations d'élasticité linéaires pour mettre le terme E en inconnue, avec pour condition au bord $E = 1$. Cette dernière condition peut aisément s'admettre dans la mesure où l'enveloppe nucléaire est sous-tendu par de la lamine, et a donc une valeur de rigidité homogène. Notons que ce réarrangement n'est pas neuf, et il a été montré par le passé que les différentes équations qui peuvent en ressortir sont toutes hyperboliques. Malheureusement, les équations hyperboliques sont connues pour être sensibles aux conditions au bord, comme représentantes d'une propagation d'onde. Pour les stabiliser, nous ajoutons délibérément un terme elliptique de second ordre, qui donne l'équation suivante :

$$\mathcal{A}\nabla \ln(E) + \mathcal{B} = \mathcal{F},$$

où $\mathcal{A}$ dépend du tensor de déformation et de la constante de Poisson et où $\mathcal{B} = (\gamma_1 \Delta \ln(E), \gamma_2 \Delta \ln(E))^T$. Ce problème d'équations différentielles partielles admet une formulation variationnelle, dite faible, qui peut être rapidement résolue par une méthode d'éléments mixtes finis GMRES avec préconditionnement ILU. Nous évaluons l'efficacité de cette méthode d'élastographie en deux étapes. D'abord, nous mesurons l'acuité de sa reconstruction pour des valeurs théoriques exactes du champ de déplacement. En ce cas, nous remarquons que notre méthode d'élastographie est bien supérieure aux méthodes directes et indirectes de reconstruction, tout en restant plus rapide. Ensuite, nous l'évaluons sur des simulations de noyaux se déformant, en l'appariant avec notre méthode de flux optique, et avec les autres méthodes de flux optique. Nous remarquons que les meilleurs résultats sont obtenus lorsque nous la combinons avec notre flux optique. Puisqu'elle est validée numériquement, nous l'appliquons pour calculer les valeurs relatives du module de Young dans deux configurations d'intérêt (voir Figure C.6). Dans la première, un noyau de SKOV3 se déforme sous AFM ; nous remarquons que la dureté du noyau se trouve essentiellement au bord, là où la fibronectin l'attache sur la plaque. Dans la seconde, un noyau de cardiomyocyte se déforme sous les battements de tissu. Ici, les résultats que nous obtenons confirment ceux obtenus précédemment par des méthodes plus invasives.

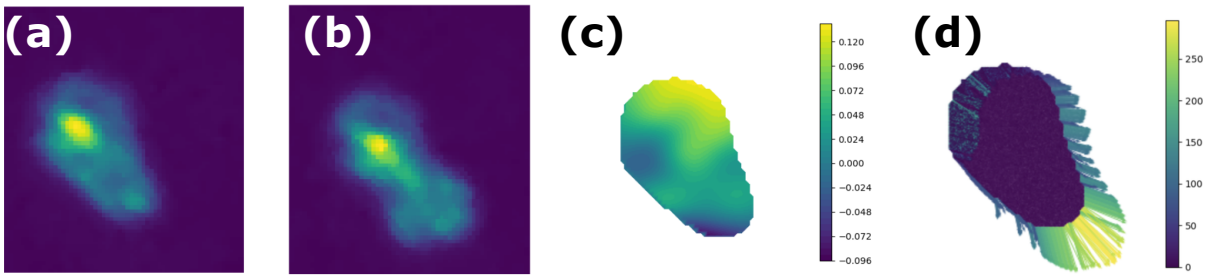

Figure C.7: Application de notre méthodologie pour le calcul des déformations déviatoriques et des forces de traction au bord d'un noyau de Toxoplasma gondii durant l'invasion. (a) Première image de l'invasion ; (b) Seconde image de l'invasion ; (c) Champ du tenseur de déformation déviatorique ; (d) Forces de traction au bord.

Enfin, pour résoudre le dernier problème que nous nous sommes fixés, nous traitons le champ de déplacement obtenu par flux optique $\tilde{\mathbf{u}}$

$$
\begin{aligned}
\underset{\mathbf{u},\mathbf{g}}{\operatorname{argmin}} \quad J(\mathbf{u},\mathbf{g}) := \int (\mathbf{u}-\hat{\mathbf{u}})^2 + \beta\,(\nabla\mathbf{g}\cdot n_\perp)^2\, d\Omega, & \\
\text{s.t.} \quad \nabla\cdot\varsigma = 0, & \quad \text{in } \Omega, \\
\varsigma(\mathbf{u}) := \lambda \mathrm{tr}(\varepsilon(\mathbf{u}))I + 2\mu\varepsilon(\mathbf{u}) & \quad \text{in } \Omega, \\
\varepsilon(\mathbf{u}) := \frac{1}{2}(\nabla\mathbf{u} + \nabla\mathbf{u}^T) & \quad \text{in } \Omega, \\
\lambda = \lambda_l,\ \mu = \mu_l & \quad \text{on } \Gamma, \\
\lambda = \lambda_c,\ \mu = \mu_c & \quad \text{in } \Omega\setminus\Gamma, \\
\mathbf{u} = \mathbf{g} & \quad \text{on } \Gamma,
\end{aligned}
$$

où $\lambda_l, \mu_l, \lambda_c, \mu_c$ désignent les valeurs des paramètres de Lamé sur le domaine de la lamine et de la chromatine, respectivement, et $\mathbf{g}$ est le déplacement au bord du noyau. Comme pour les méthodes indirectes en élastographie, ce problème variationnel peut être reformulé en un problème non contraint, résolu par L-BFGS avec méthode adjointe. L'idée est de projeter les déplacements obtenus par la méthode du flux optique sur l'espace des solutions des équations du noyau. L'évaluation numérique de cette méthode montre que les forces de traction au bord et le tenseur de contrainte recouvré sont bien plus exactes que si nous avions procédé au flux optique seulement. Nous employons ensuite cette méthodologie à l'étude de l'invasion de *Toxoplasma gondii* dans une cellule hôte (voir Figure C.7). Comme nous pouvons le constater, les déformations déviatoriques du noyau sont les plus fortes au milieu de l'invasion, alors que le noyau prend une forme de "8". Aussi, les forces de traction vont toujours de la droite à la gauche, ce qui s'explique par l'organisation ellipsoïdale, vers la gauche, du noyau du parasite.

C.5 Conclusion et perspective

Nous avons développé une batterie de méthodes computationnelles pour caractériser les propriétés mécaniques du noyau à partir d'images de sa déformation. Par là nous entendons le calcul en deux ou trois dimensions de grandeurs physiques d'intérêt telles que le champ de déplacement, de déformation, de contrainte, de module de Young, et de forces de traction au bord. Toutes se fondent sur une méthodologie en deux étapes, où nous calculons d'abord le champ de déplacement par flux optique, puis la valeur physique en question par traitement du signal obtenu. Bien que ces approches aient apporté des réponses satisfaisantes à de nombreux problèmes biologiques, certaines questions demeurent.

Discussion sur la modélisation mécanique du noyau. Il se peut, quoique le cas soit mal déterminé et les applications délicates, que le noyau obéisse non pas à une équation d'élasticité linéaire, mais non-linéaire. Les propriétés de régularité édictées au chapitre 2 tiennent toujours, dans la mesure où l'on peut considérer le noyau comme un matériau hyperélastique, et les méthodes développées devraient pouvoir s'appliquer avec de minimes aménagements. Si les déformations ne sont plus quasistatiques, mais périodiques, ou isssues de fluages ou de relaxations, le noyau montre des comportements visceux en plus. En ce cas il faudra supposer une régularité temporelle supplémentaire des champs de déplacements. Cependant, la validation numérique sera plus difficile, étant donné qu'au lieu d'une seule image, nous devrons en créer plusieurs, par déformation successive d'une image initiale : les erreurs dans le processus de déformation ne peuvent que s'accumuler. Une idée serait de considérer un système de pixels liés par des ressorts et des amortisseurs, de résoudre ce problème pour calculer de façon explicite la position de chacun de ces pixels dans le temps. Dans ce cas, les propriétés globales du noyau devront être vérifiées avec précaution.

Discussion sur l'estimation du champ de déplacement. Si le noyau est supposé viscoélastique, nous devrons améliorer la régularisation temporelle du déplacement, par exemple via une méthode de fusion comme il est déjà suggéré dans plusieurs méthodes de flux optique. Notre résolution numérique peut être par ailleurs accélérée pour en élargir l'accès à des biologistes, par exemple sur la plateforme Icy. Une idée serait d'escamoter la stratégie "coarse-to-fine", en offrant une initialisation rapide du flux optique, par exemple avec des "dense inverse search". De plus, il serait utile de comparer notre méthode de flux optique avec d'autres méthodes impliquant des termes de régularisation d'ordre 2 ou plus, comme BV2, TV2, Hessian-TV, ou TGV. Enfin, nous devons considérer une stratégie pour améliorer le calcul de petites zones de fortes déformations, peut-être en incorporant des descripteurs.

Discussion sur l'estimation de grandeurs physiques. Nous devons offrir une méthode d'élastographie dans le cas non-linéaire. Il serait aisé d'offrir une méthode indirecte en ce sens, mais le défi consiste à en trouver une méthode directe, qui se base en grande partie sur la possibilité de réarranger les équations de linéarité pour mettre le module de Young en inconnue. Une idée serait d'utiliser une méthode "coarse-to-fine", où nous linéarisons les équations d'élasticité à chaque niveau, pour y employer notre méthode : mais cela demanderait des vérifications sur la convergence d'une telle stratégie. Un deuxième défi consiste à savoir lorsque les problèmes d'élastographie sont des problèmes "bien posés". Nous savons que, lorsque la déformation est faible et localisée, on ne peut espérer une reconstruction complète du noyau : reste à formaliser cette idée dans un cadre mathématique précis. Enfin, il serait profitable d'étendre les méthodes obtenues à l'estimation de la constante de Poisson, peut–être en formulant une équation différentielle partielle elliptique à deux variables. En ce qui concerne l'estimation du tenseur de contrainte et des forces de traction au bord, le plus grand défi consiste à obtenir des paramètres de Lamé du noyau. Ce problème est entre les mains des biophysiciens. Par ailleurs, pour corriger les éventuelles pertes de flux dans des modélisations 2D, nous pouvons recourir à un terme additionel de flux sortant dans l'équation de contrainte.

Bibliography

[1] LS Beale. "Examination of sputum from a case of cancer of the pharynx and the adjacent parts". In: *Arch Med* 2.44 (1860), pp. 1860–1861.

[2] Albert K Harris, Patricia Wild, and David Stopak. "Silicone rubber substrata: a new wrinkle in the study of cell locomotion". In: *Science* 208.4440 (1980), pp. 177–179.

[3] Zhong-Wei Zhang et al. "Red blood cell extrudes nucleus and mitochondria against oxidative stress". In: *IUBMB life* 63.7 (2011), pp. 560–565.

[4] Graham J Burton and Carolyn JP Jones. "Syncytial knots, sprouts, apoptosis, and trophoblast deportation from the human placenta". In: *Taiwanese Journal of Obstetrics and Gynecology* 48.1 (2009), pp. 28–37.

[5] Odd-Arne Olsen. "Nuclear endosperm development in cereals and Arabidopsis thaliana". In: *The Plant Cell* 16.suppl_1 (2004), S214–S227.

[6] Predrag Jevtić et al. "Sizing and shaping the nucleus: mechanisms and significance". In: *Current opinion in cell biology* 28 (2014), pp. 16–27.

[7] Mingjuan L Zhang, Alan X Guo, and Christopher J VandenBussche. "Morphologists overestimate the nuclear-to-cytoplasmic ratio". In: *Cancer Cytopathology* 124.9 (2016), pp. 669–677.

[8] Maria Lucia Lombardi and Jan Lammerding. "Altered mechanical properties of the nucleus in disease". In: *Methods in cell biology* 98 (2010), pp. 121–141.

[9] Jan Lammerding. "Mechanics of the nucleus". In: *Comprehensive physiology* 1.2 (2011), p. 783.

[10] Monika Zwerger, Chin Yee Ho, and Jan Lammerding. "Nuclear mechanics in disease". In: *Annual review of biomedical engineering* 13 (2011), pp. 397–428.

[11] Colin Dingwall and Ronald Laskey. "The nuclear membrane". In: *Science* 258.5084 (1992), pp. 942–947.

[12] John F Nagle and Stephanie Tristram-Nagle. "Structure of lipid bilayers". In: *Biochimica et Biophysica Acta (BBA)-Reviews on Biomembranes* 1469.3 (2000), pp. 159–195.

[13] Dipen Rajgor and Catherine M Shanahan. "Nesprins: from the nuclear envelope and beyond". In: *Expert reviews in molecular medicine* 15 (2013), e5.

[14] Lei Lu, Mark S Ladinsky, and Tom Kirchhausen. "Cisternal organization of the endoplasmic reticulum during mitosis". In: *Molecular biology of the cell* 20.15 (2009), pp. 3471–3480.

[15] Stefan Pfeffer et al. "Structure and 3D arrangement of endoplasmic reticulum membrane-associated ribosomes". In: *Structure* 20.9 (2012), pp. 1508–1518.

[16] Hugh RB Pelham. "Control of protein exit from the endoplasmic reticulum". In: *Annual review of cell biology* 5.1 (1989), pp. 1–23.

[17] Alex B Novikoff. "The endoplasmic reticulum: a cytochemist's view (a review)." In: *Proceedings of the National Academy of Sciences* 73.8 (1976), pp. 2781–2787.

[18] Michael L Watson. “The nuclear envelope: Its structure and relation to cytoplasmic membranes”. In: *The Journal of biophysical and biochemical cytology* 1.3 (1955), p. 257.

[19] Mariana Juliani do Amaral et al. “The perinuclear region concentrates disordered proteins with predicted phase separation distributed in a 3D network of cytoskeletal filaments and organelles”. In: *Biochimica et Biophysica Acta (BBA)-Molecular Cell Research* 1869.1 (2022), p. 119161.

[20] Alayne Senior and Larry Gerace. “Integral membrane proteins specific to the inner nuclear membrane and associated with the nuclear lamina.” In: *The Journal of cell biology* 107.6 (1988), pp. 2029–2036.

[21] Laura I Davis. “The nuclear pore complex”. In: *Annual review of biochemistry* 64.1 (1995), pp. 865–896.

[22] André Hoelz, Erik W Debler, and Günter Blobel. “The structure of the nuclear pore complex”. In: *Annual review of biochemistry* 80 (2011), pp. 613–643.

[23] Susan R Wente and Michael P Rout. “The nuclear pore complex and nuclear transport”. In: *Cold Spring Harbor perspectives in biology* 2.10 (2010), a000562.

[24] Marie-Therese Mackmull et al. “Landscape of nuclear transport receptor cargo specificity”. In: *Molecular systems biology* 13.12 (2017), p. 962.

[25] Imke Baade and Ralph H Kehlenbach. “The cargo spectrum of nuclear transport receptors”. In: *Current opinion in cell biology* 58 (2019), pp. 1–7.

[26] Ueli Aebi et al. “The nuclear lamina is a meshwork of intermediate-type filaments”. In: *Nature* 323.6088 (1986), pp. 560–564.

[27] Nana Naetar, Simona Ferraioli, and Roland Foisner. “Lamins in the nuclear interior- life outside the lamina”. In: *Journal of cell science* 130.13 (2017), pp. 2087–2096.

[28] Yosef Gruenbaum and Roland Foisner. “Lamins: nuclear intermediate filament proteins with fundamental functions in nuclear mechanics and genome regulation”. In: *Annual review of biochemistry* 84 (2015), pp. 131–164.

[29] David AD Parry and Peter M Steinert. “Intermediate filament structure”. In: *Current opinion in cell biology* 4.1 (1992), pp. 94–98.

[30] Takeshi Shimi et al. “Structural organization of nuclear lamins A, C, B1, and B2 revealed by superresolution microscopy”. In: *Molecular biology of the cell* 26.22 (2015), pp. 4075–4086.

[31] David Lourim and Georg Krohne. “Membrane-associated lamins in Xenopus egg extracts: identification of two vesicle populations.” In: *The Journal of cell biology* 123.3 (1993), pp. 501–512.

[32] Jordi Camps, Michael R Erdos, and Thomas Ried. “The role of lamin B1 for the maintenance of nuclear structure and function”. In: *Nucleus* 6.1 (2015), pp. 8–14.

[33] Veronika Butin-Israeli et al. “Nuclear lamin functions and disease”. In: *Trends in genetics* 28.9 (2012), pp. 464–471.

[34] IAEW Van Loosdregt et al. “Lmna knockout mouse embryonic fibroblasts are less contractile than their wild-type counterparts”. In: *Integrative Biology* 9.8 (2017), pp. 709–721.

[35] Tim Pollex and Edith Heard. “Nuclear positioning and pairing of X-chromosome inactivation centers are not primary determinants during initiation of random X-inactivation”. In: *Nature genetics* 51.2 (2019), pp. 285–295.

[36] Cátia S Janota, Francisco Javier Calero-Cuenca, and Edgar R Gomes. “The role of the cell nucleus in mechanotransduction”. In: *Current opinion in cell biology* 63 (2020), pp. 204–211.

[37] Ezequiel Nazer. "To be or not be (in the LAD): emerging roles of lamin proteins in transcriptional regulation". In: *Biochemical Society Transactions* 50.2 (2022), pp. 1035–1044.

[38] Ashraf N Malhas, Chiu Fan Lee, and David J Vaux. "Lamin B1 controls oxidative stress responses via Oct-1". In: *The Journal of cell biology* 184.1 (2009), pp. 45–55.

[39] Nadir M Maraldi et al. "Laminopathies and lamin-associated signaling pathways". In: *Journal of cellular biochemistry* 112.4 (2011), pp. 979–992.

[40] Matilde Murga et al. "Global chromatin compaction limits the strength of the DNA damage response". In: *The Journal of cell biology* 178.7 (2007), pp. 1101–1108.

[41] Arvind Babu and Ram S Verma. "Chromosome structure: euchromatin and heterochromatin". In: *International review of cytology* 108 (1987), pp. 1–60.

[42] Sarah CR Elgin and Shiv IS Grewal. "Heterochromatin: silence is golden". In: *Current Biology* 13.23 (2003), R895–R898.

[43] Niall Dillon. "Heterochromatin structure and function". In: *Biology of the Cell* 96.8 (2004), pp. 631–637.

[44] Anton Wutz. "Gene silencing in X-chromosome inactivation: advances in understanding facultative heterochromatin formation". In: *Nature Reviews Genetics* 12.8 (2011), pp. 542–553.

[45] Nehmé Saksouk, Elisabeth Simboeck, and Jérôme Déjardin. "Constitutive heterochromatin formation and transcription in mammals". In: *Epigenetics & chromatin* 8 (2015), pp. 1–17.

[46] Jun-ichi Nakayama et al. "Role of histone H3 lysine 9 methylation in epigenetic control of heterochromatin assembly". In: *Science* 292.5514 (2001), pp. 110–113.

[47] Olivia Morrison and Jitendra Thakur. "Molecular complexes at euchromatin, heterochromatin and centromeric chromatin". In: *International Journal of Molecular Sciences* 22.13 (2021), p. 6922.

[48] Aniek Janssen et al. "A single double-strand break system reveals repair dynamics and mechanisms in heterochromatin and euchromatin". In: *Genes & development* 30.14 (2016), pp. 1645–1657.

[49] Andrew J Einstein et al. "Fractal characterization of chromatin appearance for diagnosis in breast cytology". In: *The Journal of Pathology: A Journal of the Pathological Society of Great Britain and Ireland* 185.4 (1998), pp. 366–381.

[50] Luay M Almassalha et al. "The global relationship between chromatin physical topology, fractal structure, and gene expression". In: *Scientific reports* 7.1 (2017), p. 41061.

[51] Konradin Metze. "Fractal dimension of chromatin: potential molecular diagnostic applications for cancer prognosis". In: *Expert review of molecular diagnostics* 13.7 (2013), pp. 719–735.

[52] Patricia Yang Liu et al. "Cell refractive index for cell biology and disease diagnosis: past, present and future". In: *Lab on a Chip* 16.4 (2016), pp. 634–644.

[53] HG Schwarzacher, A-V Mikelsaar, and W Schnedl. "The nature of the Ag-staining of nucleolus organizer regions: electron-and light-microscopic studies on human cells in interphase, mitosis, and meiosis". In: *Cytogenetic and Genome Research* 20.1-6 (1978), pp. 24–39.

[54] Thoru Pederson. "The plurifunctional nucleolus". In: *Nucleic acids research* 26.17 (1998), pp. 3871–3876.

[55] HG Schwarzacher and F Wachtler. "Nucleolus organizer regions and nucleoli". In: *Human genetics* 63 (1983), pp. 89–99.

[56] Sibdas Ghosh. "The nucleolar structure". In: *International Review of Cytology* 44 (1976), pp. 1–28.

[57] Valentina Sirri et al. “Nucleolus: the fascinating nuclear body”. In: *Histochemistry and cell biology* 129 (2008), pp. 13–31.

[58] Wongwarut Boonyanugomol et al. “Endoplasmic Reticulum Stress and Impairment of Ribosome Biogenesis Mediate the Apoptosis Induced by Ocimum x africanum Essential Oil in a Human Gastric Cancer Cell Line”. In: *Medicina* 58.6 (2022), p. 799.

[59] David L Spector and Angus I Lamond. “Nuclear speckles”. In: *Cold Spring Harbor perspectives in biology* 3.2 (2011), a000646.

[60] Cyrille Girard et al. “Post-transcriptional spliceosomes are retained in nuclear speckles until splicing completion”. In: *Nature communications* 3.1 (2012), p. 994.

[61] Vidisha Tripathi et al. “SRSF1 regulates the assembly of pre-mRNA processing factors in nuclear speckles”. In: *Molecular biology of the cell* 23.18 (2012), pp. 3694–3706.

[62] Joseph G Gall. “Cajal bodies: the first 100 years”. In: *Annual review of cell and developmental biology* 16.1 (2000), pp. 273–300.

[63] Stephen C Ogg and Angus I Lamond. “Cajal bodies and coilin—moving towards function”. In: *The Journal of Cell Biology* 159.1 (2002), p. 17.

[64] Karla M Neugebauer. *Special focus on the Cajal Body*. 2017.

[65] Salah Mahmoudi et al. “WRAP53 is essential for Cajal body formation and for targeting the survival of motor neuron complex to Cajal bodies”. In: *PLoS biology* 8.11 (2010), e1000521.

[66] DJ Battle et al. “The SMN complex: an assembly machine for RNPs”. In: *Cold Spring Harbor symposia on quantitative biology*. Vol. 71. Cold Spring Harbor Laboratory Press. 2006, pp. 313–320.

[67] A Gregory Matera and Zefeng Wang. “A day in the life of the spliceosome”. In: *Nature reviews Molecular cell biology* 15.2 (2014), pp. 108–121.

[68] Valérie Lallemand-Breitenbach et al. “PML nuclear bodies”. In: *Cold Spring Harbor perspectives in biology* 2.5 (2010), a000661.

[69] Katherine LB Borden. “Pondering the promyelocytic leukemia protein (PML) puzzle: possible functions for PML nuclear bodies”. In: *Molecular and cellular biology* (2002).

[70] Yuki Takahashi et al. “PML nuclear bodies and apoptosis”. In: *Oncogene* 23.16 (2004), pp. 2819–2824.

[71] Mathieu Vernier et al. “Regulation of E2Fs and senescence by PML nuclear bodies”. In: *Genes & development* 25.1 (2011), p. 41.

[72] Mei Kuen Tang et al. “Promyelocytic leukemia (PML) protein plays important roles in regulating cell adhesion, morphology, proliferation and migration”. In: *PLoS One* 8.3 (2013), e59477.

[73] Tobias Ulbricht et al. “PML promotes MHC class II gene expression by stabilizing the class II transactivator”. In: *Journal of Cell Biology* 199.1 (2012), pp. 49–63.

[74] Roger D Everett and Mounira K Chelbi-Alix. “PML and PML nuclear bodies: implications in antiviral defence”. In: *Biochimie* 89.6-7 (2007), pp. 819–830.

[75] Dmitri Negorev and Gerd G Maul. “Cellular proteins localized at and interacting within ND10/PML nuclear bodies/PODs suggest functions of a nuclear depot”. In: *Oncogene* 20.49 (2001), pp. 7234–7242.

[76] Stephen A Adam. “The nucleoskeleton”. In: *Cold Spring Harbor Perspectives in Biology* 9.2 (2017), a023556.

[77] David G Capco, Katherine M Wan, and Sheldon Penman. “The nuclear matrix: three-dimensional architecture and protein composition”. In: *Cell* 29.3 (1982), pp. 847–858.

[78] Patricia M Davidson and Bruno Cadot. "Actin on and around the Nucleus". In: *Trends in Cell Biology* 31.3 (2021), pp. 211–223.

[79] Jesse R Dixon, David U Gorkin, and Bing Ren. "Chromatin domains: the unit of chromosome organization". In: *Molecular cell* 62.5 (2016), pp. 668–680.

[80] Thoru Pederson and Ueli Aebi. "Actin in the nucleus: what form and what for?" In: *Journal of structural biology* 140.1-3 (2002), pp. 3–9.

[81] C-A Schoenenberger et al. "Conformation-specific antibodies reveal distinct actin structures in the nucleus and the cytoplasm". In: *Journal of structural biology* 152.3 (2005), pp. 157–168.

[82] Ildikó Kristó et al. "Actin, actin-binding proteins, and actin-related proteins in the nucleus". In: *Histochemistry and cell biology* 145 (2016), pp. 373–388.

[83] Pavel Hozák et al. "Lamin proteins form an internal nucleoskeleton as well as a peripheral lamina in human cells". In: *Journal of cell science* 108.2 (1995), pp. 635–644.

[84] Yong Li, Patrick Lang, and Wolfgang A Linke. "Titin stiffness modifies the force-generating region of muscle sarcomeres". In: *Scientific reports* 6.1 (2016), p. 24492.

[85] Michael S Zastrow et al. "Nuclear titin interacts with A-and B-type lamins in vitro and in vivo". In: *Journal of cell science* 119.2 (2006), pp. 239–249.

[86] Lan King and Chun-Ru Jhou. "Nuclear titin interacts with histones". In: *Chang Gung Med. J* 33.2 (2010), pp. 201–210.

[87] Xavier Fant, Andreas Merdes, and Laurence Haren. "Cell and molecular biology of spindle poles and NuMA." In: *International review of cytology* 238 (2004), pp. 1–57.

[88] Katri Kivinen, Pekka Taimen, and Markku Kallajoki. "Silencing of Nuclear Mitotic Apparatus protein (NuMA) accelerates the apoptotic disintegration of the nucleus". In: *Apoptosis* 15 (2010), pp. 936–945.

[89] Zhen Zheng et al. "Cell cycle–regulated membrane binding of NuMA contributes to efficient anaphase chromosome separation". In: *Molecular biology of the cell* 25.5 (2014), pp. 606–619.

[90] Rui Zhang et al. "Spectrin: structure, function and disease". In: *Science China Life Sciences* 56 (2013), pp. 1076–1085.

[91] Kevin G Young and Rashmi Kothary. "Spectrin repeat proteins in the nucleus". In: *Bioessays* 27.2 (2005), pp. 144–152.

[92] Deepa M Sridharan, Laura W McMahon, and Muriel W Lambert. "αII-Spectrin interacts with five groups of functionally important proteins in the nucleus". In: *Cell biology international* 30.11 (2006), pp. 866–878.

[93] Christophe Leterrier and Pramod A Pullarkat. "Mechanical role of the submembrane spectrin scaffold in red blood cells and neurons". In: *Journal of Cell Science* 135.16 (2022), jcs259356.

[94] Joel A Lefferts et al. "The SH3 domain of αII spectrin is a target for the Fanconi anemia protein, FANCG". In: *Biochemistry* 48.2 (2009), pp. 254–263.

[95] Sathya D Unudurthi et al. "Spectrin-based pathways underlying electrical and mechanical dysfunction in cardiac disease". In: *Expert review of cardiovascular therapy* 16.1 (2018), pp. 59–65.

[96] A Wayne Orr et al. "Mechanisms of mechanotransduction". In: *Developmental cell* 10.1 (2006), pp. 11–20.

[97] Maria L Lombardi et al. "The interaction between nesprins and sun proteins at the nuclear envelope is critical for force transmission between the nucleus and cytoskeleton". In: *Journal of Biological Chemistry* 286.30 (2011), pp. 26743–26753.

[98] Celine M Denais et al. “Nuclear envelope rupture and repair during cancer cell migration”. In: *Science* 352.6283 (2016), pp. 353–358.

[99] Martin W Hetzer. “The nuclear envelope”. In: *Cold Spring Harbor perspectives in biology* 2.3 (2010), a000539.

[100] Aya Sato et al. “Cytoskeletal forces span the nuclear envelope to coordinate meiotic chromosome pairing and synapsis”. In: *Cell* 139.5 (2009), pp. 907–919.

[101] Erin C Tapley and Daniel A Starr. “Connecting the nucleus to the cytoskeleton by SUN–KASH bridges across the nuclear envelope”. In: *Current opinion in cell biology* 25.1 (2013), pp. 57–62.

[102] Melissa Crisp et al. “Coupling of the nucleus and cytoplasm: role of the LINC complex”. In: *The Journal of cell biology* 172.1 (2006), pp. 41–53.

[103] Dae In Kim, Birendra KC, and Kyle J Roux. “Making the LINC: SUN and KASH protein interactions”. In: *Biological Chemistry* 396.4 (2015), pp. 295–310.

[104] Natalie E Cain and Daniel A Starr. “SUN proteins and nuclear envelope spacing”. In: *Nucleus* 6.1 (2015), pp. 2–7.

[105] Qiang Wang et al. “Characterization of the structures involved in localization of the SUN proteins to the nuclear envelope and the centrosome”. In: *DNA and cell biology* 25.10 (2006), pp. 554–562.

[106] Santharam S Katta, Christine J Smoyer, and Sue L Jaspersen. “Destination: inner nuclear membrane”. In: *Trends in cell biology* 24.4 (2014), pp. 221–229.

[107] Daniel A Starr and Janice A Fischer. “KASH’n Karry: The KASH domain family of cargo-specific cytoskeletal adaptor proteins”. In: *Bioessays* 27.11 (2005), pp. 1136–1146.

[108] Wenshu Lu et al. “Nesprin interchain associations control nuclear size”. In: *Cellular and Molecular Life Sciences* 69 (2012), pp. 3493–3509.

[109] Marina Meyerzon et al. “UNC-83 is a nuclear-specific cargo adaptor for kinesin-1-mediated nuclear migration”. In: (2009).

[110] Kevin Wilhelmsen et al. “Nesprin-3, a novel outer nuclear membrane protein, associates with the cytoskeletal linker protein plectin”. In: *The Journal of cell biology* 171.5 (2005), pp. 799–810.

[111] Gunes Uzer, Clinton T Rubin, and Janet Rubin. “Cell mechanosensitivity is enabled by the LINC nuclear complex”. In: *Current molecular biology reports* 2 (2016), pp. 36–47.

[112] Gregory R Fedorchak, Ashley Kaminski, and Jan Lammerding. “Cellular mechanosensing: getting to the nucleus of it all”. In: *Progress in biophysics and molecular biology* 115.2-3 (2014), pp. 76–92.

[113] Susanna Mlynarczyk-Evans and Anne M Villeneuve. “Time-course analysis of early meiotic prophase events informs mechanisms of homolog pairing and synapsis in Caenorhabditis elegans”. In: *Genetics* 207.1 (2017), pp. 103–114.

[114] Alexandre Méjat. “LINC complexes in health and disease”. In: *Nucleus* 1.1 (2010), pp. 40–52.

[115] Charles T Halfmann et al. “Repair of nuclear ruptures requires barrier-to-autointegration factor”. In: *Journal of Cell Biology* 218.7 (2019), pp. 2136–2149.

[116] Malini Mansharamani and Katherine L Wilson. “Direct binding of nuclear membrane protein MAN1 to emerin in vitro and two modes of binding to barrier-to-autointegration factor”. In: *Journal of Biological Chemistry* 280.14 (2005), pp. 13863–13870.

[117] Brian A Sosa et al. “How lamina-associated polypeptide 1 (LAP1) activates Torsin”. In: *Elife* 3 (2014), e03239.

[118] Daniela Dorner et al. "Lamina-associated polypeptide 2α regulates cell cycle progression and differentiation via the retinoblastoma–E2F pathway". In: *The Journal of cell biology* 173.1 (2006), pp. 83–93.

[119] Pietro Cortelli et al. "Nuclear lamins: functions and clinical implications". In: *Neurology* 79.16 (2012), pp. 1726–1731.

[120] Annachiara De Sandre-Giovannoli et al. "Lamin a truncation in Hutchinson-Gilford progeria". In: *Science* 300.5628 (2003), pp. 2055–2055.

[121] RL Pollex and Robert A Hegele. "Hutchinson–Gilford progeria syndrome". In: *Clinical genetics* 66.5 (2004), pp. 375–381.

[122] Scott A Heller et al. "Emery-Dreifuss muscular dystrophy". In: *Muscle & nerve* 61.4 (2020), pp. 436–448.

[123] Christina G Fiorenza, Sharon H Chou, and Christos S Mantzoros. "Lipodystrophy: pathophysiology and advances in treatment". In: *Nature Reviews Endocrinology* 7.3 (2011), pp. 137–150.

[124] Usha Kant Misra, Jayantee Kalita, and Pradeep P Nair. "Diagnostic approach to peripheral neuropathy". In: *Annals of Indian Academy of Neurology* 11.2 (2008), pp. 89–97.

[125] Qiuping Zhang et al. "Nesprin-1 and-2 are involved in the pathogenesis of Emery–Dreifuss muscular dystrophy and are critical for nuclear envelope integrity". In: *Human molecular genetics* 16.23 (2007), pp. 2816–2833.

[126] Megan J Puckelwartz et al. "Disruption of nesprin-1 produces an Emery Dreifuss muscular dystrophy-like phenotype in mice". In: *Human molecular genetics* 18.4 (2009), pp. 607–620.

[127] Elizabeth A Booth-Gauthier et al. "Hutchinson–Gilford progeria syndrome alters nuclear shape and reduces cell motility in three dimensional model substrates". In: *Integrative Biology* 5.3 (2013), pp. 569–577.

[128] Miron Prokocimer, Rachel Barkan, and Yosef Gruenbaum. "Hutchinson–Gilford progeria syndrome through the lens of transcription". In: *Aging Cell* 12.4 (2013), pp. 533–543.

[129] Juergen Scharner et al. "Mapping disease-related missense mutations in the immunoglobulin-like fold domain of lamin A/C reveals novel genotype–phenotype associations for laminopathies". In: *Proteins: Structure, Function, and Bioinformatics* 82.6 (2014), pp. 904–915.

[130] Merel Stiekema et al. "Structural and mechanical aberrations of the nuclear lamina in disease". In: *Cells* 9.8 (2020), p. 1884.

[131] MM Speeckaert et al. "Pelger-Huët anomaly: a critical review of the literature". In: *Acta haematologica* 121.4 (2009), pp. 202–206.

[132] Rita Colella and Sandra C Hollensead. "Understanding and recognizing the Pelger-Huët anomaly". In: *American journal of clinical pathology* 137.3 (2012), pp. 358–366.

[133] Robert A Weinberg. "How cancer arises". In: *Scientific American* 275.3 (1996), pp. 62–70.

[134] Leopold G Koss. "The Papanicolaou test for cervical cancer detection: a triumph and a tragedy". In: *Jama* 261.5 (1989), pp. 737–743.

[135] Mikel Gray and Terran W Sims. "NMP-22 for bladder cancer screening and surveillance." In: *Urologic Nursing* 24.3 (2004).

[136] Piia-Riitta Karhemo et al. "An extensive tumor array analysis supports tumor suppressive role for nucleophosmin in breast cancer". In: *The American journal of pathology* 179.2 (2011), pp. 1004–1014.

[137] Yongyu Yang et al. "Lamin B1 is a potential therapeutic target and prognostic biomarker for hepatocellular carcinoma". In: *Bioengineered* 13.4 (2022), pp. 9211–9231.

[138] IM Alhudiri et al. “Expression of Lamin A/C in early-stage breast cancer and its prognostic value”. In: *Breast cancer research and treatment* 174 (2019), pp. 661–668.

[139] Youxiang Ding et al. “c-Fos separation from Lamin A/C by GDF15 promotes colon cancer invasion and metastasis in inflammatory microenvironment”. In: *Journal of Cellular Physiology* 235.5 (2020), pp. 4407–4421.

[140] Tomer Meirson and Hava Gil-Henn. “Targeting invadopodia for blocking breast cancer metastasis”. In: *Drug Resistance Updates* 39 (2018), pp. 1–17.

[141] Mattia La Torre et al. “Combined alteration of lamin and nuclear morphology influences the localization of the tumor-associated factor AKTIP”. In: *Journal of Experimental & Clinical Cancer Research* 41.1 (2022), pp. 1–17.

[142] Terumi Kohwi-Shigematsu et al. “Genome organizing function of SATB1 in tumor progression”. In: *Seminars in cancer biology*. Vol. 23. 2. Elsevier. 2013, pp. 72–79.

[143] Daniele Zink, Andrew H Fischer, and Jeffrey A Nickerson. “Nuclear structure in cancer cells”. In: *Nature reviews cancer* 4.9 (2004), pp. 677–687.

[144] Chad M Hobson and Andrew D Stephens. “Modeling of cell nuclear mechanics: classes, components, and applications”. In: *Cells* 9.7 (2020), p. 1623.

[145] Jan Lammerding et al. “Lamins A and C but not lamin B1 regulate nuclear mechanics”. In: *Journal of Biological Chemistry* 281.35 (2006), pp. 25768–25780.

[146] Oren Wintner et al. “A unified linear viscoelastic model of the cell nucleus defines the mechanical contributions of lamins and chromatin”. In: *Advanced Science* 7.8 (2020), p. 1901222.

[147] Anat Vivante, Irena Bronshtein, and Yuval Garini. “Chromatin viscoelasticity measured by local dynamic analysis”. In: *Biophysical journal* 118.9 (2020), pp. 2258–2267.

[148] Paolo Caldarelli et al. “Self-organized tissue mechanics underlie embryonic regulation”. In: *bioRxiv* (2021), pp. 2021–10.

[149] Andrew D Stephens et al. “Chromatin and lamin A determine two different mechanical response regimes of the cell nucleus”. In: *Molecular biology of the cell* 28.14 (2017), pp. 1984–1996.

[150] Nikolay V Dokholyan et al. “Identifying the protein folding nucleus using molecular dynamics”. In: *Journal of molecular biology* 296.5 (2000), pp. 1183–1188.

[151] Ashkan Vaziri, Arvind Gopinath, and Vikram Deshpande. “Continuum-based computational models for cell and nuclear mechanics”. In: *Journal of Mechanics of Materials and Structures* 2.6 (2007), pp. 1169–1191.

[152] Michael J Sanderson et al. “Fluorescence microscopy”. In: *Cold Spring Harbor Protocols* 2014.10 (2014), pdb–top071795.

[153] Robert Prevedel et al. “Brillouin microscopy: an emerging tool for mechanobiology”. In: *Nature methods* 16.10 (2019), pp. 969–977.

[154] Giuseppe Antonacci et al. “Recent progress and current opinions in Brillouin microscopy for life science applications”. In: *Biophysical Reviews* 12 (2020), pp. 615–624.

[155] Claire L Curl et al. “Quantitative phase microscopy: a new tool for investigating the structure and function of unstained live cells”. In: *Clinical and experimental pharmacology and physiology* 31.12 (2004), pp. 896–901.

[156] Marko Tscherepanow et al. “Automatic segmentation of unstained living cells in bright-field microscope images”. In: *Advances in Mass Data Analysis of Images and Signals in Medicine, Biotechnology, Chemistry and Food Industry: Third International Conference, MDA 2008 Leipzig, Germany, July 14, 2008 Proceedings 3*. Springer. 2008, pp. 158–172.

[157] Elnaz Fazeli et al. "Automated cell tracking using StarDist and TrackMate". In: *F1000Research* 9 (2020).

[158] Kurt Thorn. "A quick guide to light microscopy in cell biology". In: *Molecular biology of the cell* 27.2 (2016), pp. 219–222.

[159] Chad M Hobson, Michael R Falvo, and Richard Superfine. "A survey of physical methods for studying nuclear mechanics and mechanobiology". In: *APL bioengineering* 5.4 (2021), p. 041508.

[160] Franz J Giessibl. "Advances in atomic force microscopy". In: *Reviews of modern physics* 75.3 (2003), p. 949.

[161] Steen M Willadsen. "Micromanipulation of embryos of the large domestic species". In: *Mammalian egg transfer*. CRC press, 2018, pp. 185–210.

[162] Robert M Hochmuth. "Micropipette aspiration of living cells". In: *Journal of biomechanics* 33.1 (2000), pp. 15–22.

[163] JP McGarry. "Characterization of cell mechanical properties by computational modeling of parallel plate compression". In: *Annals of biomedical engineering* 37 (2009), pp. 2317–2325.

[164] Leslie Y Yeo et al. "Microfluidic devices for bioapplications". In: *small* 7.1 (2011), pp. 12–48.

[165] Hong-Chen Chen. "Boyden chamber assay". In: *Cell migration: developmental methods and protocols* (2005), pp. 15–22.

[166] Sangmyung Rhee and Frederick Grinnell. "Fibroblast mechanics in 3D collagen matrices". In: *Advanced drug delivery reviews* 59.13 (2007), pp. 1299–1305.

[167] Edda Klipp et al. "Integrative model of the response of yeast to osmotic shock". In: *Nature biotechnology* 23.8 (2005), pp. 975–982.

[168] Chao-Min Cheng, Robert L Steward Jr, and Philip R LeDuc. "Probing cell structure by controlling the mechanical environment with cell–substrate interactions". In: *Journal of biomechanics* 42.2 (2009), pp. 187–192.

[169] JP McGarry, BP Murphy, and PE McHugh. "Computational mechanics modelling of cell–substrate contact during cyclic substrate deformation". In: *Journal of the Mechanics and Physics of Solids* 53.12 (2005), pp. 2597–2637.

[170] Alar Ainla, Gavin Jeffries, and Aldo Jesorka. "Hydrodynamic flow confinement technology in microfluidic perfusion devices". In: *Micromachines* 3.2 (2012), pp. 442–461.

[171] Tie Yang, Francesca Bragheri, and Paolo Minzioni. "A comprehensive review of optical stretcher for cell mechanical characterization at single-cell level". In: *Micromachines* 7.5 (2016), p. 90.

[172] Brett R Blackman, Kenneth A Barbee, and Lawrence E Thibault. "In vitro cell shearing device to investigate the dynamic response of cells in a controlled hydrodynamic environment". In: *Annals of biomedical engineering* 28 (2000), pp. 363–372.

[173] Philippe G Ciarlet. *Three-dimensional elasticity*. Elsevier, 1988.

[174] CRISTINEL MARDARE. *Méthodes mathématiques en élasticité*.

[175] Jerrold E Marsden and Thomas JR Hughes. *Mathematical foundations of elasticity*. Courier Corporation, 1994.

[176] Melvyn S Berger. *Nonlinearity and functional analysis: lectures on nonlinear problems in mathematical analysis*. Vol. 74. Academic press, 1977.

[177] Gaetano Fichera. "Existence theorems in elasticity". In: *Linear Theories of Elasticity and Thermoelasticity: Linear and Nonlinear Theories of Rods, Plates, and Shells*. Springer, 1972, pp. 347–389.

[178] Pablo Pedregal. *Variational methods in nonlinear elasticity*. SIAM, 2000.

[179] JL Ericksen and RS Rivlin. "Large elastic deformations of homogeneous anisotropic materials". In: *Collected Papers of RS Rivlin: Volume I and II*. Springer, 1954, pp. 467–487.

[180] Olgierd Cecil Zienkiewicz and PB Morice. *The finite element method in engineering science*. Vol. 1977. McGraw-hill London, 1971.

[181] Oleg R Musin. "Properties of the Delaunay triangulation". In: *Proceedings of the thirteenth annual symposium on Computational geometry*. 1997, pp. 424–426.

[182] Steven Fortune. "Voronoi diagrams and Delaunay triangulations". In: *Handbook of discrete and computational geometry*. Chapman and Hall/CRC, 2017, pp. 705–721.

[183] Der-Tsai Lee and Bruce J Schachter. "Two algorithms for constructing a Delaunay triangulation". In: *International Journal of Computer & Information Sciences* 9.3 (1980), pp. 219–242.

[184] Wiesław Rokicki and Ewelina Gawell. "Voronoi diagrams–architectural and structural rod structure research model optimization". In: *MAZOWSZE Studia Regionalne* 19 (2016), pp. 155–164.

[185] Simena Dinas and José María Banon. "A review on Delaunay triangulation with application on computer vision". In: *Int. J. Comput. Sci. Eng* 3 (2014), pp. 9–18.

[186] Samuel Rippa. "Minimal roughness property of the Delaunay triangulation". In: *Computer Aided Geometric Design* 7.6 (1990), pp. 489–497.

[187] Barry Joe. "Delaunay versus max-min solid angle triangulations for three-dimensional mesh generation". In: *International Journal for Numerical Methods in Engineering* 31.5 (1991), pp. 987–997.

[188] The CGAL Project. *CGAL User and Reference Manual*. 5.6. CGAL Editorial Board, 2023. URL: `https://doc.cgal.org/5.6/Manual/packages.html`.

[189] Rex A Dwyer. "A faster divide-and-conquer algorithm for constructing Delaunay triangulations". In: *Algorithmica* 2.1-4 (1987), pp. 137–151.

[190] Ivana Kolingerová. "On triangulations". In: *International Conference on Computational Science and Its Applications*. Springer. 2004, pp. 544–553.

[191] Cyrill W Hirt, Anthony A Amsden, and JL Cook. "An arbitrary Lagrangian-Eulerian computing method for all flow speeds". In: *Journal of computational physics* 14.3 (1974), pp. 227–253.

[192] Henning Braess and Peter Wriggers. "Arbitrary Lagrangian Eulerian finite element analysis of free surface flow". In: *Computer methods in applied mechanics and engineering* 190.1-2 (2000), pp. 95–109.

[193] M Souli and JP Zolesio. "Arbitrary Lagrangian–Eulerian and free surface methods in fluid mechanics". In: *Computer methods in applied mechanics and engineering* 191.3-5 (2001), pp. 451–466.

[194] Klaus-Jürgen Bathe. "The inf–sup condition and its evaluation for mixed finite element methods". In: *Computers & structures* 79.2 (2001), pp. 243–252.

[195] Jean-Claude Nédélec. "Mixed finite elements in 3". In: *Numerische Mathematik* 35 (1980), pp. 315–341.

[196] Ivo Babuška and Manil Suri. "On locking and robustness in the finite element method". In: *SIAM Journal on Numerical Analysis* 29.5 (1992), pp. 1261–1293.

[197] Gabriel N Gatica. "A simple introduction to the mixed finite element method". In: *Theory and Applications. Springer Briefs in Mathematics. Springer, London* (2014).

[198] Philippe G Ciarlet. *The finite element method for elliptic problems*. SIAM, 2002.

[199] Robert C Kirby et al. "Common and unusual finite elements". In: *Automated Solution of Differential Equations by the Finite Element Method: The FEniCS Book*. Springer, 2012, pp. 95–119.

[200] Martin Alnæs et al. "The FEniCS project version 1.5". In: *Archive of numerical software* 3.100 (2015).

[201] Sebastian Mitusch, Simon Funke, and Jørgen Dokken. "dolfin-adjoint 2018.1: automated adjoints for FEniCS and Firedrake". In: *Journal of Open Source Software* 4.38 (2019), p. 1292.

[202] Anders Logg, Kent-Andre Mardal, and Garth Wells. *Automated solution of differential equations by the finite element method: The FEniCS book*. Vol. 84. Springer Science & Business Media, 2012.

[203] Berthold KP Horn and Brian G Schunck. "Determining optical flow". In: *Artificial intelligence* 17.1-3 (1981), pp. 185–203.

[204] Sandrine Etienne-Manneville. "Intermediate filaments promote glioblastoma cell invasion by controlling cell deformability and mechanosensitive gene expression". In: (2023).

[205] James J Gibson. "The perception of the visual world." In: (1950).

[206] Hengli Wang et al. "End-to-end interactive prediction and planning with optical flow distillation for autonomous driving". In: *Proceedings of the IEEE/CVF Conference on Computer Vision and Pattern Recognition*. 2021, pp. 2229–2238.

[207] Wang Hongwei et al. "The optical flow method research of particle image velocimetry". In: *Procedia Engineering* 99 (2015), pp. 918–924.

[208] Zheng Yongguang et al. "Advances in techniques of monitoring, forecasting and warning of severe convective weather". In: 26.6 (2015), pp. 641–657.

[209] Min Liu and Tobi Delbruck. "Block-matching optical flow for dynamic vision sensors: Algorithm and FPGA implementation". In: *2017 IEEE International Symposium on Circuits and Systems (ISCAS)*. IEEE. 2017, pp. 1–4.

[210] David G Lowe. "Object recognition from local scale-invariant features". In: *Proceedings of the seventh IEEE international conference on computer vision*. Vol. 2. Ieee. 1999, pp. 1150–1157.

[211] Dianyuan Han. "Comparison of commonly used image interpolation methods". In: *Conference of the 2nd International Conference on Computer Science and Electronics Engineering (ICCSEE 2013)*. Atlantis Press. 2013, pp. 1556–1559.

[212] Chi-Cheng Cheng and Hui-Ting Li. "Feature-based optical flow computation". In: *International Journal of Information Technology* 12.7 (2006), pp. 82–90.

[213] John L Barron et al. "Performance of optical flow techniques". In: *Proceedings 1992 IEEE Computer Society Conference on Computer Vision and Pattern Recognition*. IEEE Computer Society. 1992, pp. 236–237.

[214] Aleix Boquet Pujadas. "Variational approaches in inverse problems for image-based characterisation of cellular dynamics". PhD thesis. Sorbonne Université, 2019.

[215] Anshuman Agarwal, Shivam Gupta, and Dushyant Kumar Singh. "Review of optical flow technique for moving object detection". In: *2016 2nd international conference on contemporary computing and informatics (IC3I)*. IEEE. 2016, pp. 409–413.

[216] Thomas Brox, Christoph Bregler, and Jitendra Malik. "Large displacement optical flow". In: *2009 IEEE Conference on Computer Vision and Pattern Recognition*. IEEE. 2009, pp. 41–48.

[217] Enric Meinhardt-Llopis and Javier Sánchez. "Horn-schunck optical flow with a multi-scale strategy". In: *Image Processing on line* (2013).

[218] Antonin Chambolle and Thomas Pock. "A first-order primal-dual algorithm for convex problems with applications to imaging". In: *Journal of mathematical imaging and vision* 40 (2011), pp. 120–145.

[219] Thorsten Hohage and Carolin Homann. "A generalization of the Chambolle-Pock algorithm to Banach spaces with applications to inverse problems". In: *arXiv preprint arXiv:1412.0126* (2014).

[220] R Tyrrell Rockafellar. *Convex analysis*. Vol. 11. Princeton university press, 1997.

[221] Bryan Catanzaro et al. "Efficient, high-quality image contour detection". In: *2009 IEEE 12th International Conference on Computer Vision*. IEEE. 2009, pp. 2381–2388.

[222] Thomas Brox and Jitendra Malik. "Large displacement optical flow: descriptor matching in variational motion estimation". In: *IEEE transactions on pattern analysis and machine intelligence* 33.3 (2010), pp. 500–513.

[223] Aurélien Plyer, Guy Le Besnerais, and Frédéric Champagnat. "Massively parallel Lucas Kanade optical flow for real-time video processing applications". In: *Journal of Real-Time Image Processing* 11 (2016), pp. 713–730.

[224] Simon Baker and Iain Matthews. "Lucas-kanade 20 years on: A unifying framework". In: *International journal of computer vision* 56 (2004), pp. 221–255.

[225] Guy Le Besnerais and Frédéric Champagnat. "Dense optical flow by iterative local window registration". In: *IEEE International Conference on Image Processing 2005*. Vol. 1. IEEE. 2005, pp. I–137.

[226] Pengpeng Liu et al. "Selflow: Self-supervised learning of optical flow". In: *Proceedings of the IEEE/CVF conference on computer vision and pattern recognition*. 2019, pp. 4571–4580.

[227] Andreas Geiger, Philip Lenz, and Raquel Urtasun. "Are we ready for autonomous driving? the kitti vision benchmark suite". In: *2012 IEEE conference on computer vision and pattern recognition*. IEEE. 2012, pp. 3354–3361.

[228] Simon Baker et al. "A database and evaluation methodology for optical flow". In: *International journal of computer vision* 92 (2011), pp. 1–31.

[229] D. J. Butler et al. "A naturalistic open source movie for optical flow evaluation". In: *European Conf. on Computer Vision (ECCV)*. Ed. by A. Fitzgibbon et al. (Eds.) Part IV, LNCS 7577. Springer-Verlag, Oct. 2012, pp. 611–625.

[230] Zachary Teed and Jia Deng. "Raft: Recurrent all-pairs field transforms for optical flow". In: *Computer Vision–ECCV 2020: 16th European Conference, Glasgow, UK, August 23–28, 2020, Proceedings, Part II 16*. Springer. 2020, pp. 402–419.

[231] Junhwa Hur and Stefan Roth. "Optical flow estimation in the deep learning age". In: *Modelling Human Motion: From Human Perception to Robot Design* (2020), pp. 119–140.

[232] Tak-Wai Hui, Xiaoou Tang, and Chen Change Loy. "Liteflownet: A lightweight convolutional neural network for optical flow estimation". In: *Proceedings of the IEEE conference on computer vision and pattern recognition*. 2018, pp. 8981–8989.

[233] David Gadot and Lior Wolf. "PatchBatch: A batch augmented loss for optical flow". In: *Proceedings of the IEEE Conference on Computer Vision and Pattern Recognition*. 2016, pp. 4236–4245.

[234] Christian Bailer, Kiran Varanasi, and Didier Stricker. "CNN-based patch matching for optical flow with thresholded hinge embedding loss". In: *Proceedings of the IEEE Conference on Computer Vision and Pattern Recognition*. 2017, pp. 3250–3259.

[235] Fatma Güney and Andreas Geiger. "Deep discrete flow". In: *Computer Vision–ACCV 2016: 13th Asian Conference on Computer Vision, Taipei, Taiwan, November 20-24, 2016, Revised Selected Papers, Part IV 13*. Springer. 2017, pp. 207–224.

[236] A. Dosovitskiy et al. "FlowNet: Learning Optical Flow with Convolutional Networks". In: *IEEE International Conference on Computer Vision (ICCV)*. 2015. URL: `http://lmb.informatik.uni-freiburg.de/Publications/2015/DFIB15`.

[237] Alexey Dosovitskiy et al. "Flownet: Learning optical flow with convolutional networks". In: *Proceedings of the IEEE international conference on computer vision*. 2015, pp. 2758–2766.

[238] Anurag Ranjan and Michael J Black. "Optical flow estimation using a spatial pyramid network". In: *Proceedings of the IEEE conference on computer vision and pattern recognition*. 2017, pp. 4161–4170.

[239] Eddy Ilg et al. "Flownet 2.0: Evolution of optical flow estimation with deep networks". In: *Proceedings of the IEEE conference on computer vision and pattern recognition*. 2017, pp. 2462–2470.

[240] Deqing Sun et al. "Pwc-net: Cnns for optical flow using pyramid, warping, and cost volume". In: *Proceedings of the IEEE conference on computer vision and pattern recognition*. 2018, pp. 8934–8943.

[241] Junhwa Hur and Stefan Roth. "Iterative residual refinement for joint optical flow and occlusion estimation". In: *Proceedings of the IEEE/CVF conference on computer vision and pattern recognition*. 2019, pp. 5754–5763.

[242] Gengshan Yang and Deva Ramanan. "Volumetric correspondence networks for optical flow". In: *Advances in neural information processing systems* 32 (2019).

[243] Pengpeng Liu et al. "Flow2stereo: Effective self-supervised learning of optical flow and stereo matching". In: *Proceedings of the IEEE/CVF conference on computer vision and pattern recognition*. 2020, pp. 6648–6657.

[244] Dongzhen Piao, Prahlad G Menon, and Ole J Mengshoel. "Computing probabilistic optical flow using markov random fields". In: *Computational Modeling of Objects Presented in Images. Fundamentals, Methods, and Applications: 4th International Conference, CompIMAGE 2014, Pittsburgh, PA, USA, September 3-5, 2014 4*. Springer. 2014, pp. 241–247.

[245] Deqing Sun et al. "Learning optical flow". In: *Computer Vision–ECCV 2008: 10th European Conference on Computer Vision, Marseille, France, October 12-18, 2008, Proceedings, Part III 10*. Springer. 2008, pp. 83–97.

[246] Wei-Sheng Lai, Jia-Bin Huang, and Ming-Hsuan Yang. "Semi-supervised learning for optical flow with generative adversarial networks". In: *Advances in neural information processing systems* 30 (2017).

[247] Tongtong Che et al. "SDOF-GAN: Symmetric dense optical flow estimation with generative adversarial networks". In: *IEEE Transactions on Image Processing* 30 (2021), pp. 6036–6049.

[248] Khalid Jalalzai. "Some remarks on the staircasing phenomenon in total variation-based image denoising". In: *Journal of Mathematical Imaging and Vision* 54 (2016), pp. 256–268.

[249] Shmuel Friedland and Lek-Heng Lim. "Nuclear norm of higher-order tensors". In: *Mathematics of Computation* 87.311 (2018), pp. 1255–1281.

[250] Zhening Li. "Bounds on the spectral norm and the nuclear norm of a tensor based on tensor partitions". In: *SIAM Journal on Matrix Analysis and Applications* 37.4 (2016), pp. 1440–1452.

[251] Alexandre Grothendieck and A Grothendieck. *Produits tensoriels topologiques et espaces nucléaires*. Vol. 16. American Mathematical Society Providence, 1955.

[252] Shengke Xue et al. “Low-rank tensor completion by truncated nuclear norm regularization”. In: *2018 24th International Conference on Pattern Recognition (ICPR)*. IEEE. 2018, pp. 2600–2605.

[253] Stamatios Lefkimmiatis, John Paul Ward, and Michael Unser. “Hessian Schatten-norm regularization for linear inverse problems”. In: *IEEE transactions on image processing* 22.5 (2013), pp. 1873–1888.

[254] Shayan Aziznejad, Joaquim Campos, and Michael Unser. “Measuring complexity of learning schemes using Hessian-Schatten total variation”. In: *SIAM Journal on Mathematics of Data Science* 5.2 (2023), pp. 422–445.

[255] Luigi Ambrosio et al. “Linear Inverse Problems with Hessian-Schatten Total Variation”. In: *arXiv preprint arXiv:2210.04077* (2022).

[256] Françoise Demengel. “Fonctions à hessien borné”. In: *Annales de l’institut Fourier*. Vol. 34. 2. 1984, pp. 155–190.

[257] Norman G Meyers. “Quasi-convexity and lower semi-continuity of multiple variational integrals of any order”. In: *Transactions of the American Mathematical Society* 119.1 (1965), pp. 125–149.

[258] Patrick L Combettes and Jean-Christophe Pesquet. “Proximal splitting methods in signal processing”. In: *Fixed-point algorithms for inverse problems in science and engineering* (2011), pp. 185–212.

[259] Amir Beck and Marc Teboulle. “A fast iterative shrinkage-thresholding algorithm for linear inverse problems”. In: *SIAM journal on imaging sciences* 2.1 (2009), pp. 183–202.

[260] Suvrit Sra. “Fast projections onto 1, q-norm balls for grouped feature selection”. In: *Machine Learning and Knowledge Discovery in Databases: European Conference, ECML PKDD 2011, Athens, Greece, September 5-9, 2011, Proceedings, Part III 22*. Springer. 2011, pp. 305–317.

[261] Javier Sánchez Pérez, Enric Meinhardt-Llopis, and Gabriele Facciolo. “TV-L1 optical flow estimation”. In: *Image Processing On Line* 2013 (2013), pp. 137–150.

[262] Arabel Vollmann-Zwerenz et al. “Tumor cell invasion in glioblastoma”. In: *International journal of molecular sciences* 21.6 (2020), p. 1932.

[263] Alexandre Dufour et al. “Automated quantification of cell endocytosis using active contours and wavelets”. In: *2008 19th International Conference on Pattern Recognition*. IEEE. 2008, pp. 1–4.

[264] Alexandre Dufour et al. “3-D active meshes: fast discrete deformable models for cell tracking in 3-D time-lapse microscopy”. In: *IEEE transactions on image processing* 20.7 (2010), pp. 1925–1937.

[265] Yekta Kesenci et al. “Probing Intracellular Elasticity with Minimal-Hessian Registration”. In: *2023 IEEE 20th International Symposium on Biomedical Imaging (ISBI)*. IEEE. 2023, pp. 1–5.

[266] Yekta Kesenci et al. “PDE-Constrained Optimization for Nuclear Mechanics”. In: *2022 IEEE International Conference on Image Processing (ICIP)*. IEEE. 2022, pp. 2192–2195.

[267] MM Knight et al. “Cell and nucleus deformation in compressed chondrocyte–alginate constructs: temporal changes and calculation of cell modulus”. In: *Biochimica et Biophysica Acta (BBA)-General Subjects* 1570.1 (2002), pp. 1–8.

[268] Christopher L Gilchrist et al. “Measurement of intracellular strain on deformable substrates with texture correlation”. In: *Journal of biomechanics* 40.4 (2007), pp. 786–794.

[269] Rosa MS Sigrist et al. “Ultrasound elastography: review of techniques and clinical applications”. In: *Theranostics* 7.5 (2017), p. 1303.

[270] Pol Grasland-Mongrain et al. "Ultrafast imaging of cell elasticity with optical microelastography". In: *Proceedings of the National Academy of Sciences* 115.5 (2018), pp. 861–866.

[271] Soham Ghosh et al. "Image-Based Elastography of Heterochromatin and Euchromatin Domains in the Deforming Cell Nucleus". In: *Small* 17.5 (2021), p. 2006109.

[272] Chad M Hobson et al. "Correlating nuclear morphology and external force with combined atomic force microscopy and light sheet imaging separates roles of chromatin and lamin A/C in nuclear mechanics". In: *Molecular biology of the cell* 31.16 (2020), pp. 1788–1801.

[273] Aleix Boquet-Pujadas and Jean-Christophe Olivo-Marin. "Multiple variational image assimilation for accessible micro-elastography". In: *Journal of Physics: Conference Series*. Vol. 1131. 1. IOP Publishing. 2018, p. 012014.

[274] Roch L Maurice et al. "Non-invasive high-frequency vascular ultrasound elastography". In: *Physics in Medicine & Biology* 50.7 (2005), p. 1611.

[275] Xiaochang Pan et al. "A regularization-free elasticity reconstruction method for ultrasound elastography with freehand scan". In: *Biomedical engineering online* 13.1 (2014), pp. 1–17.

[276] Assad A Oberai, Nachiket H Gokhale, and Gonzalo R Feijóo. "Solution of inverse problems in elasticity imaging using the adjoint method". In: *Inverse problems* 19.2 (2003), p. 297.

[277] Aleix Boquet-Pujadas, Jean-Christophe Olivo-Marin, and Nancy Guillén. "Bioimage analysis and cell motility". In: *Patterns* 2.1 (2021), p. 100170.

[278] Paul E Barbone and Jeffrey C Bamber. "Quantitative elasticity imaging: what can and cannot be inferred from strain images". In: *Physics in Medicine & Biology* 47.12 (2002), p. 2147.

[279] Yanning Zhu, Timothy J Hall, and Jingfeng Jiang. "A finite-element approach for Young's modulus reconstruction". In: *IEEE transactions on medical imaging* 22.7 (2003), pp. 890–901.

[280] Aleix Boquet-Pujadas and Jean-Christophe Olivo-Marin. "Reformulating optical flow to solve image-based inverse problems and quantify uncertainty". In: *IEEE Transactions on Pattern Analysis and Machine Intelligence* (2022).

[281] Aleix Boquet-Pujadas et al. "4D live imaging and computational modeling of a functional gut-on-a-chip evaluate how peristalsis facilitates enteric pathogen invasion". In: *Science Advances* (2022).

[282] Lorenz T Biegler et al. *Large-scale PDE-constrained optimization: an introduction*. Springer, 2003.

[283] Dong C Liu and Jorge Nocedal. "On the limited memory BFGS method for large scale optimization". In: *Mathematical programming* 45.1-3 (1989), pp. 503–528.

[284] Aleix Boquet-Pujadas et al. "BioFlow: a non-invasive, image-based method to measure speed, pressure and forces inside living cells". In: *Scientific reports* 7.1 (2017), p. 9178.

[285] Otger Campàs et al. "Quantifying cell-generated mechanical forces within living embryonic tissues". In: *Nature methods* 11.2 (2014), pp. 183–189.

[286] Robert W Style et al. "Traction force microscopy in physics and biology". In: *Soft matter* 10.23 (2014), pp. 4047–4055.

[287] Davide Ambrosi. "Cellular traction as an inverse problem". In: *SIAM Journal on Applied Mathematics* 66.6 (2006), pp. 2049–2060.

[288] Nils Klughammer et al. "Cytoplasmic flows in starfish oocytes are fully determined by cortical contractions". In: *PLoS computational biology* 14.11 (2018), e1006588.

[289] Michael D Huber and Larry Gerace. "The size-wise nucleus: nuclear volume control in eukaryotes". In: *The Journal of cell biology* 179.4 (2007), pp. 583–584.

[290] Chikayoshi Sumi, A Suzuki, and K Nakayama. "Estimation of shear modulus distribution in soft tissue from strain distribution". In: *IEEE Transactions on Biomedical Engineering* 42.2 (1995), pp. 193–202.

[291] AR Skovoroda, SY Emelianov, and M O'donnell. "Tissue elasticity reconstruction based on ultrasonic displacement and strain images". In: *IEEE transactions on ultrasonics, ferroelectrics, and frequency control* 42.4 (1995), pp. 747–765.

[292] Andrei R Skovoroda et al. "Reconstructive elasticity imaging for large deformations". In: *IEEE transactions on ultrasonics, ferroelectrics, and frequency control* 46.3 (1999), pp. 523–535.

[293] Chikayoshi Sumi and Kiyoshi Nakayama. "A robust numerical solution to reconstruct a globally relative shear modulus distribution from strain measurements". In: *IEEE transactions on medical imaging* 17.3 (1998), pp. 419–428.

[294] Per Christian Hansen. "The L-curve and its use in the numerical treatment of inverse problems". In: (1999).

[295] Andreas Hilfinger, Amit K Chattopadhyay, and Frank Jülicher. "Nonlinear dynamics of cilia and flagella". In: *Physical Review E* 79.5 (2009), p. 051918.

[296] Antonio Barragan and L David Sibley. "Transepithelial migration of Toxoplasma gondii is linked to parasite motility and virulence". In: *The Journal of experimental medicine* 195.12 (2002), pp. 1625–1633.

[297] Georgios Pavlou. "Toxoplasma gondii, a super fast runner and cell invader. Studying motion and forces". PhD thesis. Université Grenoble Alpes [2020-....], 2020.

[298] Georgios Pavlou et al. "Coupling polar adhesion with traction, spring, and torque forces allows high-speed helical migration of the protozoan parasite toxoplasma". In: *ACS nano* 14.6 (2020), pp. 7121–7139.

[299] Maksim V Sednev, Vladimir N Belov, and Stefan W Hell. "Fluorescent dyes with large Stokes shifts for super-resolution optical microscopy of biological objects: a review". In: *Methods and applications in fluorescence* 3.4 (2015), p. 042004.

[300] Howard R Petty. "Fluorescence microscopy: established and emerging methods, experimental strategies, and applications in immunology". In: *Microscopy research and technique* 70.8 (2007), pp. 687–709.

[301] Firas Mualla, Marc Aubreville, and Andreas Maier. "Microscopy". In: *Medical imaging systems: An introductory guide* (2018), pp. 69–90.

[302] Stephen R Meech. "Excited state reactions in fluorescent proteins". In: *Chemical Society Reviews* 38.10 (2009), pp. 2922–2934.

[303] Takako Kogure et al. "Fluorescence imaging using a fluorescent protein with a large Stokes shift". In: *Methods* 45.3 (2008), pp. 223–226.

[304] Darren M Reynolds. "The principles of fluorescence". In: *Aquatic organic matter fluorescence* (2014), pp. 3–34.

[305] Marc Zimmer. "Green fluorescent protein (GFP): applications, structure, and related photophysical behavior". In: *Chemical reviews* 102.3 (2002), pp. 759–782.

[306] Christopher W West et al. "Excited state dynamics of the isolated green fluorescent protein chromophore anion following UV excitation". In: *The Journal of Physical Chemistry B* 119.10 (2015), pp. 3982–3987.

[307] IB Nielsen, L Lammich, and LH Andersen. "S 1 and S 2 excited states of gas-phase Schiff-base retinal chromophores". In: *Physical review letters* 96.1 (2006), p. 018304.

[308] R Šípoš and J Šima. "Jablonski diagram revisited". In: *Revista cubana de física* 37.2 (2020), pp. 125–130.

[309] Danuta Frackowiak. "The jablonski diagram". In: *Journal of Photochemistry and Photobiology B: Biology* 2.3 (1988), p. 399.

[310] Olivier Braem et al. "A femtosecond fluorescence study of vibrational relaxation and cooling dynamics of UV dyes". In: *Physical Chemistry Chemical Physics* 14.10 (2012), pp. 3513–3519.

[311] Claire M Brown. "Fluorescence microscopy-avoiding the pitfalls". In: *Journal of cell science* 120.10 (2007), pp. 1703–1705.

[312] Joseph R Lakowicz. *Principles of fluorescence spectroscopy*. Springer, 2006.

[313] Takao Itoh. "Fluorescence and phosphorescence from higher excited states of organic molecules". In: *Chemical reviews* 112.8 (2012), pp. 4541–4568.

[314] Malcolm H Levitt. "Long live the singlet state!" In: *Journal of Magnetic Resonance* 306 (2019), pp. 69–74.

[315] Alberto Diaspro et al. "Photobleaching". In: *Handbook of biological confocal microscopy* (2006), pp. 690–702.

[316] Fred WD Rost. *Fluorescence microscopy*. Vol. 2. Cambridge University Press, 1992.

[317] Rafael Yuste. "Fluorescence microscopy today". In: *Nature methods* 2.12 (2005), pp. 902–904.

[318] Antonin Chambolle et al. "An introduction to total variation for image analysis". In: *Theoretical foundations and numerical methods for sparse recovery* 9.263-340 (2010), p. 227.

[319] Kristian Bredies, Karl Kunisch, and Thomas Pock. "Total generalized variation". In: *SIAM Journal on Imaging Sciences* 3.3 (2010), pp. 492–526.